PhD-FSTM-2021-037
The Faculty of Sciences, Technology and Medicine

DISSERTATION

Defence held on 22/06/2021 in Luxembourg

to obtain the degree of

DOCTEUR DE L'UNIVERSITÉ DU LUXEMBOURG

EN BIOLOGIE

by

Yolanda Sofia Pires Afonso
Born on 13th of July 1990 in Andorra (Andorra)

TUMOUR-ASSOCIATED MICROGLIA/MACROPHAGE HETEROGENEITY IN GLIOBLASTOMA

Dissertation defense committee

Dr Alessandro Michelucci, dissertation supervisor
Group Leader, Neuro-Immunology Group, Luxembourg Institute of Health, Luxembourg

Dr Gregor Hutter
Professor, University of Basel, Switzerland

Dr Michel Mittelbronn, Chair
Professor, Université du Luxembourg
Head of the National Center of Pathology, Laboratoire National de Santé, Luxembourg

Dr Rainer Glass
Professor, Munich University Hospital, Germany

Dr Simone Niclou, Vice Chair
Group Leader, Neuro-Oncology Laboratory, Luxembourg Institute of Health, Luxembourg

Dissertation Supervisors

Dr Alessandro Michelucci
Neuro-Immunology Group,
Luxembourg Institute of Health, Luxembourg

Prof. Dr Simone Niclou
NORLUX Neuro-Oncology Laboratory
Luxembourg Institute of Health, Luxembourg

The work presented in this thesis was conducted at the:

Neuro-Immunology Group
NORLUX Neuro-Oncology Laboratory
Luxembourg Institute of Health

The work presented in this thesis was supported by:

CANBIO Doctoral Training in Cancer Biology
Luxembourg National Research Fund

Fonds National de la Recherche Luxembourg
PRIDE15/10675146/CANBIO

Doctoral School in Systems and Molecular Biomedicine (DS_SMB)
Doctoral School in Science and Engineering
University of Luxembourg

Fondation du Pélican de Mie et Pierre Hippert-Faber
under the aegis of Fondation de Luxembourg

AFFIDAVIT

I hereby confirm that the PhD thesis entitled **"TUMOUR-ASSOCIATED MICROGLIA/MACROPHAGE HETEROGENEITY IN GLIOBLASTOMA"** has been written independently and without any other sources than cited. All necessary ethical approvals have been obtained in accordance with the law (on the use of clinical samples and on the Care and Use of laboratory animals, where applicable).

Luxembourg, May 13, 2021 Yolanda Sofia Pires Afonso

I would like to dedicate my thesis in loving memory of my father, Manuel Joaquim Afonso Gordo, who lost his battle against cancer sixteen years ago. His enthusiasm, knowledge and courage were the drivers to embark on this beautiful journey, my PhD. I will always remember your love and constant guidance throughout my life. I love you!

ACKNOWLEDGMENTS

I am very grateful to everyone that helped to arrive here and I would like to thank every person for helping me along the way.

I would like to start by thanking my supervisor, Dr. Alessandro Michelucci. First of all, thank you for giving me the opportunity to embark on this journey. After 4 years of work and looking back, I have enjoyed every moment of my PhD. Secondly, thank you for giving me the freedom to pursue my work and for your constant trust. It has been a challenging journey but we managed to reach my destination. It has been an incredible experience. I wish you all the best for your future projects and for providing me with the right set of tools for my next adventure.

I would like to express my gratitude to Prof. Dr. Simone Niclou from the NORLUX Neuro-Oncology laboratory. Thank you for your warm welcoming in my very first day to your lab and also for providing me with all the resources to develop my work. I am very grateful for all the advices that you gave me and for all the scientific discussions around my projects. In our meetings, you always brought insightful comments and a spark of enthusiasm. Not everything has gone as planned, but you were always there to keep me grounded.

To Prof. Dr. Michel Mittelbronn for your enthusiastic scientific discussions and for being part of my CET Committee. I have enjoyed and learned with all the discussions we had along my PhD. I will always remember the warmest memory of the ”Human brain dissection workshop” organized by you at the LNS in my early days as a PhD student. Your enthusiasm about discussing science in an informal way is contagious, making it a safe space to share ideas. Thank you for advocating this among young students.

A special thanks to Prof. Dr. Rainer Glass for always being present on our annual meetings. I will always remember your kindness and encouraging advices on every meeting we had. It has been a pleasure to discuss my project with you. I wish you all the best for your future personal and science-related endeavours.

A special thanks to the entire Neuro-Immunology Group team. Our team has grown recently and it has been a pleasure to have you on board. Your arrival brought me nostalgia about my first months at the LIH. Thank you Andrea, Frida, Rosanne and Ralph for your support and I wish you all the best for your personal and professional life. Also, I would like to thank Amandine for your help

during my last year. You were always willing to help me with a positive energy. It has been a pleasure to work with you and I still want to go to your hometown to see your daughter and visit the Belgian chocolates store, you once mentioned. Thank you Aurélie, which I know from my early days as PhD student and who has being supporting me in the last weeks of my PhD. Your energy is contagious and is good to have you around. Thanks for the discussions and personal advices you shared with me. You know whom to call to chit chat about the "why". Lastly, I would like to express my gratitude to Carole for helping me in the lab in my early days. It was a great time to have you and share bench work and late office hours. I will always remember the crazy nights in the lab and how important is to receive assistance when you need the most. I am glad that I was there to help you in this step of your life. Despite the distance, today you are giving me the support I need, I am very thankful for that.

To all NORLUX members, thank you for your help along my PhD journey. A special thanks to Anaïs and Virginie for always being available to help with the *in vivo* work. Your help was precious in many busy days I had in the lab. Also, thank you Anna for having the patience to show and teach me the FACS data analysis. I struggled a lot with it, but you were always there to take me forward. Thanks for all the advices and suggestions that you shared along these years regarding my PhD project. I would like to thank Anne Schuster and Virginie Neirinckx for helping me in the very first months with cell culture work and confocal imaging. We attended the Brain Tumour conference in Berlin in 2017, and I still keep warm memories of incredible days that we shared together.

A special thanks to the Quantitative Biology Unit. In particular, Arnaud for all your constant support with the scRNA-seq dataset analysis. It was a pleasure to discuss my work with you and understanding the bioinformatics point of view. Also, I want to thank Antonio Cosma and Thomas Cerutti for your help with my experiments and data analysis. Today, I laugh about my days coming to you and asking for a spot on the FACS Aria for "my precious samples". Thomas, we have spent endless hours together in front of the machine and overall, it became a pleasant time to chat and share life experiences with you. I want to express a big thanks to Antonio for the long working hours we have spent together around the Tableau software. It was a quite challenging task, but we succeeded in figuring out ways to visualize the scRNA-seq results. These days have taught me to look and think differently about my project and, with your help, I was able to conduct my analysis in an independent way.

I would like to thank my friends and family that I got the chance to know at the LIH. Starting by the very first ones that joined the LIH at same time as me: Andrés, Moha and Miriam. Thank you for the awesome evenings we spent at the Liquid (oh yeah, I miss my Guinness) while listening Blues and Jazz. And what about the crazy nights at De Gudde Wëllen? I have missed all these good times. The family grew up with the arrival of fresh PhD students, slightly before the Christmas party. Lia and Carina, these memories are remarkable and how much cold did we have that night? Only the alcohol could save us ^^. I cannot express how much grateful I am for your constant friendship and support along these years. Ladies, you became my safe arm when I needed the most, thank you! Malina, you are an incredible friend. It has been a pleasure to share my time with you and all the trips that we engaged on. Well, speaking about that, we still need to arrange the big one (you know which one I am talking about^^). This brings us to Eva, our trip companion. It was great to have you in Luxembourg. One of the best moments goes back to the Mullerthal trip. It looked like we were in the Koh-Lanta TV show. Despite only having one black Kinder Bueno as our sugar source, we arrived to the final line. New members joined the family and I would like to thank Yahaya, Hugo and Rédouane. Thank you for your kind heart and soul guys. Yahaya, you are a bright person and it has been a pleasure to work alongside in our projects. You have been always supportive and a friend. I enjoyed so much the time we spent together in Berlin while attending the conference. Huguito, my flower. Thank you for your hearted smile and the positive vibe. We shared few memorable moments and I promise that I will come to visit you in the garden. Rédouane, I am so grateful for all the amazing days and weekends we spent in the lab. You are a great friend, always there to listen and support. I am looking forward to the moment where we can all meet for drinks and enjoy as we used to do. Lastly, I cannot forget the friends with whom I have shared the office during my first months at the LIH. Thank you Victoria and Abhishek for all the good laughs and experiences we shared together.

To the other family that I had the opportunity to share my life with in Luxembourg. My life became much funnier with all of you, with all of your unique traits. I want to thank Stephan for the very good moments we shared upon my arrival to Luxembourg. Despite your busy schedule, you took the time to help me out in my very first days in Luxembourg. The adaptation was much easier with you. Hopefully, we will find the right time, once possible, to meet you in Brussels. Marina and JP, thank you for being incredible hosts during my first 6 months in Mamer. You introduced me to the Italian community, where fun was always present. Amandine, thank you for all the ecstatic karaoke sessions we got into. Your vibration is so energetic and in the last months your help was vital to arrive at this point of my life. Thank you Fabrice and Paolo for your friendship and for showing me the fancy restaurants (before COVID) in Luxembourg. I will always remember the weekend we

spent together in Les Vosges to celebrate my return to skiing. I want to thank you, Yaiza for letting me crash over your place during the winter holidays in Andorra. This last minute trip arrangement was one of the best adventures I could ever imagine in my life. Definitely I will come back to visit the peaceful white mountains from Pas de la Casa. The place where I learned to sky and where still feels like home. Thank you all for being there and making my life brighter.

I would like to express my gratitude to my therapists Marcela and Tiago. You gave me the support I needed to keep fighting until the end. For some time I have been in the hole and you helped to come out of it. Thank you so much.

To my closest family, mother and sister. Mother, you became the foundation of our family and despite all the struggles that we had to embrace, you always advocated for what matters most in life: education and respect! I don't have enough words to express my gratitude for all the hard work you have been through in order to grow-up two daughters. Many times life was bitter, but we managed to overcome all the difficulties. To my lovely sister, Jennifer, whom I admire more than anything. You have always been my companion in life. I have missed you so much in these last 4 years. Unfortunately, due to the COVID situation, we couldn't see each other as often as we planned. Along my PhD journey, you helped me when I needed the most and I will be forever grateful. Currently, you are finishing your master and I am so proud of the person you became. Hopefully, very soon we can plan our dream trip and enjoy life together in the beach. Mum and sis, you are simply the best.

"One love, one Life". Nathan, you tremendously helped me to reach this point. The last two years have been an incredible journey next to you. Better than anyone, you know that I have been facing the biggest personal battle of my life. Despite all the struggles, you always brought the light I needed the most. Without asking, you became my personal caregiver. You became my balance on every aspect of my life. Thank you from the heart and I am looking forward to all the adventures ahead with you. *Je t'aime, mon amour.*

Lastly, this achievement would not have been possible without the support of the funding agencies. I would like to thank the Fonds National de la Recherche Luxembourg, the CANBIO Doctoral Training in Cancer Biology, the Doctoral School in Systems and Molecular Biomedicine from the University of Luxembourg and the Fondation du Pélican de Mie et Pierre Hippert-Faber for supporting my research work and educational training.

LIST OF ABBREVIATIONS

A

AC-like: Astrocytic-like

ACOD1: Aconitate decarboxylase 1

ATP: Adenosine triphosphate

ANXA2: Annexin A2

B

BAMs: Border-associated macrophages

BBB: Blood Brain Barrier

BSA: Bovine Serum Albumin

C

CD44: CD44 Molecule

CDK4: Cyclin Dependent Kinase 4

CDKN2A/B: Cyclin-dependent kinase inhibitor 2A/B

CL: Classical

CNS: Central Nervous System

CTL: Cytotoxic T lymphocyte

D

DCs: Dendritic cells

DNA: Deoxyribonucleic acid

E

EGFR: Epidermal growth factor receptor

Ezh2: Enhancer of zeste homolog 2

G

GBM: Glioblastoma

GFAP: Glial fibrillary acidic protein

GITR: Glucocorticoid-induced TNFR-related protein

GO: Gene ontology

GPNMB: Transmembrane glycoprotein NMB

H

H&E: Hematoxylin and Eosin

HIF1α: Hypoxia Inducible Factor 1α

HGG: High-grade gliomas**I**

IDH: Isocitrate dehydrogenase

IDH1/2: Isocitrate dehydrogenase 1/2

IFN-γ: Interferon gamma

IL-4: Interleukin 4

IL-10: Interleukin 10

I

IRG1: Immunoresponsive gene 1

K

KEAP1: Kelch-like ECH-associated protein 1

KO: Knock-out

L

LDHA: Lactate Dehydrogenase A

LGG: Low-grade gliomas

LPS: Lipopolysaccharide

M

MES-like: Mesenchymal-like

MDSCs: Myeloid-derived suppressor cells

MHC-II: Major histocompatibility complex, class II

MGMT: O-6-Methylguanine-DNA Methyltransferase

MIF: Macrophage migration inhibitory factor

MRI: Magnetic Resonance Imaging

mRNA: Messenger Ribonucleic Acid

N

NF1: Neurofibromin 1

NK: Natural killer

NL: Neural

NPC-like: Neural precursor cell-like

NRF2: Nuclear factor erythroid 2-related factor 2

O

OPC: Oligodendrocyte precursor cell

OXPHOS: Oxidative phosphorylation

P

PBS: Phosphate Buffered Saline

PCR: Polymerase Chain Reaction

PAMPs: Pathogen-associated molecular patterns

PDGFRA: Platelet-derived growth factor receptor, alpha polypeptide

PN: Proneural

PTEN: Phosphatase and tensin homologue deleted on chromosome 10

S

scRNA-seq: Single-cell RNA-sequencing

SEM: Standard Error of the Mean

SOX2: Transcription factor SOX-2

T

TAMs: Tumour-associated microglia/macrophages

TCA: Tricarboxylic acid

TCGA: The Cancer Genome Atlas

TERT: Telomerase reverse transcriptase

TGF-β: Transforming growth factor beta

TGFBI: Transforming Growth Factor Beta Induced

TLR: Toll like receptor

TME: Tumour microenvironment

TP53: Tumour Protein P53

Tregs: Regulatory T cells

V

VEGF: Vascular Endothelial Growth Factor

VIM: Vimentin

W

WHO: World Health Organization

WT: Wildtype

SUMMARY

Glioblastoma (GBM) is the most common and aggressive primary brain tumour in adults, characterized by high degrees of both inter- and intra-tumour heterogeneity. GBM cells secrete numerous factors promoting the recruitment and infiltration of cellular players to the local tumour microenvironment. Tumour-associated microglia/macrophages (TAMs) represent the major cell type of the stromal compartment in GBM playing important roles along tumour development. Along GBM progression, these cells are supposed to be geared towards a tumour-supportive phenotype, therefore TAMs are pursued as key targets for the development of novel strategies aimed at re-educating them towards anti-tumour phenotypes. However, it is yet unclear how these immune suppressive properties are acquired and whether TAM subsets may phenotypically and functionally differently contribute to tumour development. Hence, the main goal of the present PhD project was to elucidate TAM diversity under defined temporal and spatial settings in GBM. Taking advantage of the GBM GL261 syngeneic and patient-derived orthotopic xenograft mouse models, we comprehensively studied the cellular and transcriptional heterogeneity of TAMs by combining single-cell RNA-sequencing, multicolour flow cytometry, immunohistological and functional analyses. We demonstrated that, as observed in patients, the myeloid compartment is the most affected and heterogeneous stromal compartment, with microglia and macrophage-like cells acquiring key transcriptional differences and rapidly adapting along GBM progression. Specifically, we uncovered that TAM transcriptional programmes converge over time, suggesting a context-dependent symbiosis mechanism characterized by decreased antigen-presenting cell signatures at late tumour stages. In the absence of *Acod1/Irg1*, a key gene involved in the metabolic reprogramming of macrophages towards an anti-inflammatory phenotype, we detected higher TAM diversity in the TME displaying increased immunogenicity and correlating with increased lymphocytic recruitment to the tumour site. Additionally, we uncovered that TAMs exhibit niche-specific functional adaptations in the tumour microenvironment, with microglia in the invasive landscapes displaying higher immune reactive profiles when compared to the corresponding cells in the angiogenic tumour phenotypes. Taken together, our data provide insights into the spatial and molecular heterogeneity of TAMs dynamically adapting along tumour progression or across specific tumour sites and revealing potential reactive anti-tumorigenic cell subsets that may be harnessed for therapeutic intervention in GBM.

TABLE OF CONTENTS

CHAPTER 1

INTRODUCTION

I. Diffuse gliomas of adulthood

1.1. General overview

Adult diffuse gliomas represent a heterogeneous group of tumours of the central nervous system (CNS) accounting for approximately 80% of the CNS malignancies (Xu et al., 2020). Approximately, six cases per 100,000 individuals are worldwide diagnosed with diffuse gliomas (Bray et al., 2018; Weller et al., 2021). The majority of gliomas are sporadic without major known risk factors. However, some exogenous risk factors such as exposure to radiation, have been associated with an increased risk of brain tumour development (Ohgaki and Kleihues, 2005).

The vast majority of gliomas are diagnosed upon the appearance of clinical symptoms, such as new-onset epilepsy, focal deficits (e.g. paresis or sensory disturbances), neurocognitive impairment, and symptoms associated with increased intracranial pressure (Weller et al., 2021; Wen et al., 2020). As such, the evolution of neurological symptoms enables the estimation of glioma growth dynamics. As a first preoperative imaging diagnostic choice, brain magnetic resonance imaging (MRI) is the golden standard method for brain tumours detection. Moreover, surgical resection, whenever feasible is commonly performed with both diagnostic and therapeutic intent (Weller et al., 2021). Regarding the diagnostic part, tissue analysis is performed upon surgery by assessing histological and molecular markers relevant for disease prognosis and treatment decisions.

The classification and tumour grading of diffuse gliomas were originally defined by histological diagnosis following the World Health Organization (WHO) of CNS tumour classification (Louis et al., 2016). However, thanks to new technological advances of next-generation sequencing, there have been important advances that contributed to a better understanding of the biology and molecular pathogenesis of diffuse gliomas in adults. This knowledge enabled the adoption of an integrated diagnosis not only based on histological features, but also taking into account several molecular signatures for better classification, diagnosis, and management of adult patients with diffuse gliomas (Brat et al., 2020; Brat et al., 2018; Capper et al., 2018; Ellison et al., 2019; Louis et al., 2016; Louis et al., 2020).

Recently, in order to provide the clinical and scientific communities with a source of reference for the diagnosis and clinical management of gliomas, the European Association of Neuro-Oncology (EANO) released new guidelines, which integrate major changes through the revision of the four editions from the WHO classification system (Weller et al., 2021). In this context, the classification

of diffuse gliomas should follow the most recent WHO criteria (Louis et al., 2016), complemented with the Consortium to Inform Molecular and Practical Approaches to CNS Tumor Taxonomy (cIMPACT-NOW) recommendations (Brat et al., 2020; Brat et al., 2018; Louis et al., 2020). Today, an integrated histomolecular analysis of diffuse gliomas, including tumour typing and grading as well as analysis of molecular markers (**Table 1**), is essential for the classification of diffuse gliomas (**Figure 1**) (Weller et al., 2021).

Table 1. A list of the recommended 2016 WHO system and cIMPACT-NOW molecular markers for the diagnosis and classification of diffuse gliomas. Adapted from (Weller et al., 2020).

Molecular Marker	Biological Function	Diagnostic Role
IDH1 R132 or IDH2 R172 mutation	Gain- of- function mutation	Distinguishes diffuse gliomas with IDH mutation from IDH-wildtype GBM and other IDH- wildtype gliomas
1p/19q codeletion	Inactivation of tumour suppressor genes such as *FUBP1* and *CIC*	Distinguishes oligodendroglioma, IDH- mutant and 1p/19q- codeleted from astrocytoma, IDH-mutant
Loss of nuclear ATRX	Role in proliferation and alternative lengthening of telomeres	Loss of nuclear ATRX in an IDH-mutant glioma is diagnostic for astrocytic lineage tumours
Histone H3 K27M mutation	*H3F3A* or *HIST1H3B/C* missense mutation affecting epigenetic regulation of gene expression	Defining molecular feature of diffuse midline glioma, H3 K27M- mutant
Histone H3.3 G34R/V mutation	Histone mutation affecting epigenetic regulation of gene expression	Defining molecular feature of diffuse hemispheric glioma, H3.3 G34- mutant
***MGMT* promoter methylation**	DNA repair	None, but is a predictive biomarker of benefit from TMZ in patients with IDH-wildtype Glioblastoma
Homozygous deletion of CDKN2A/CDKN2B	Regulators of Rb1 and p53-dependent signalling	A marker of poor outcome and WHO grade 4 disease in IDH-mutant astrocytomas
***EGFR* amplification**	Cell proliferation, invasion and resistance to induction of apoptosis	*EGFR* amplification occurs in ~40–50% of GBM, IDH-wildtype.
***TERT* promotor mutation**	Cell proliferation; increasing TERT expression	TERT promoter mutation occurs in ~70% of Glioblastoma, IDH-wildtype and >95% of oligodendroglioma, IDH- mutant and 1p/19q-codeleted.
+7/–10 cytogenetic signature	Gain of chromosome 7 combined with loss of chromosome 10	Molecular marker of Glioblastoma, IDH wildtype.
$BRAF^{V600E}$ mutation	Oncogenic driver mutation leading to MAPK pathway activation	Rare in adult diffuse gliomas but amenable to pharmacological intervention

On the basis of the 2016 WHO classification and cIMPACT-NOW recommendations, the following molecular biomarkers are key to categorize diffuse gliomas in adults: *IDH* mutation, ATRX, 1p/19q co-deletion, homozygous deletions on 9p21 involving the *CDKN2A* and *CDKN2B* gene loci, *TERT*, *EGFR* amplification, chromosome 7 gain combined with chromosome 10 loss, histone H3.3 G34R/V mutation and histone H3 K27M mutation (**Figure 1**) (Weller et al., 2021).

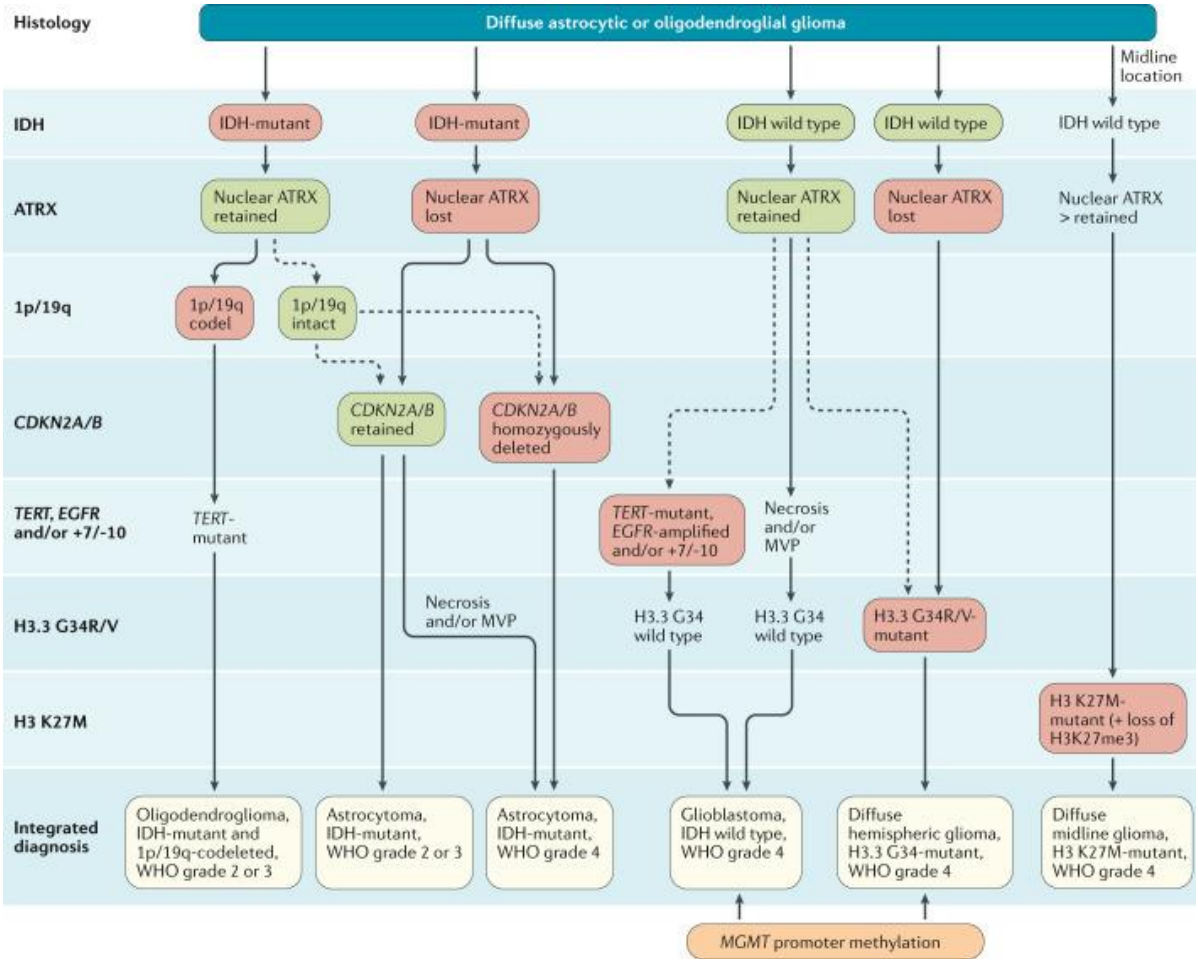

Figure 1. Adult diffuse gliomas diagnostic algorithm for an integrated histomolecular classification. Tissue biopsies are routinely evaluated for the assessment of molecular markers relevant for the diagnosis of adult diffuse gliomas by immunohistochemistry. This diagram displays the central molecular biomarkers for its categorisation: *IDH* mutation, ATRX, 1p/19q co-deletion, homozygous deletions on 9p21 involving the *CDKN2A* and *CDKN2B* gene loci deletion, TERT promoter mutation, EGFR gene amplification, chromosome 7 gain combined with chromosome 10 loss (the +7/-10 signature), histone H3.3 G34R/V mutation and histone H3 K27M mutation. Figure from (Weller et al., 2021). Abbreviations: IDH, Isocitrate dehydrogenase; ATRX, ATRX Chromatin Remodeler, *CDKN2A/B*, Cyclin Dependent Kinase Inhibitor 2A/B; *TERT*, Telomerase Reverse Transcriptase, *EGFR*, Epidermal Growth Factor Receptor; H3.3, H3.3 Histone A.

1.2. Isocitrate dehydrogenase-mutant gliomas

Isocitrate dehydrogenase (IDH) is a key rate-limiting enzyme in the Krebs cycle that plays an important role in cellular metabolism. IDH is involved in a number of cellular processes, including mitochondrial oxidative phosphorylation, glutamine metabolism, lipogenesis, glucose sensing, and regulation of cellular redox status (Huang et al., 2019). Specifically, IDH catalyses the oxidative decarboxylation of isocitrate to alpha-ketoglutarate (α-KG) and $NADP^+$ to NADPH.

The heterozygous point mutations resulting from the substitution of the amino acid arginine (R) in codon 132 of isocitrate dehydrogenase 1 (IDH1) or codon 172 of isocitrate dehydrogenase 2 (IDH2) are the molecular signatures defining IDH-mutant astrocytomas and oligodendrogliomas. Mutations of the metabolic enzyme IDH1/2 are observed in the vast majority of low grade gliomas and secondary high grade gliomas (Cohen et al., 2013). Precisely, molecular investigation of IDH1 R132 or IDH2 R172 mutation enables to distinguish diffuse gliomas with IDH mutation from IDH-wildtype Glioblastomas and other IDH-wildtype gliomas (Weller et al., 2021). IDH mutations lead to a gain of function enzyme that produces the oncometabolite 2-hydroxyglutarate (2-HG) (Cohen et al., 2013). In fact, 2-HG reduces the NADPH pool, which has an important function to protect the cells against oxidative damage (Pramono et al., 2020; Tedeschi et al., 2015). Moreover, the accumulation of 2-HG impairs the activity of α-KG–dependent dioxygenases, such as histone and DNA demethylases (eg, TET enzymes) and, thus being associated with cytosine-phosphate-guanine (CpG) island methylator phenotype (CIMP) (Malta et al., 2018). Importantly, patients carrying G-CIMP+ are younger at the time of diagnosis and exhibit better prognosis than those not carrying that phenotype (G-CIMP−) (Ceccarelli et al., 2016; Noushmehr et al., 2010). For therapeutic purposes, subtyping the G-CIMP status (-low and –high) might help for a better patient stratification, as G-CIMP-high tumours can emerge as G-CIMP-low at recurrence (Ceccarelli et al., 2016).

Astrocytoma and oligodendroglioma are classified as WHO grade 2 or 3. The characteristics of these tumours include necrosis, high microvascular proliferation and low levels of global DNA methylation (G-CIMP-low), which are associated with poor prognosis in patients (Brat et al., 2020). When ATRX is retained, the evaluation of 1p/19q codeletion is necessary to distinguish astrocytoma from oligodendroglioma, as 1p/19q codeletion remains exclusive to this type of diffuse gliomas (Louis et al., 2016). Other molecular characteristics present in astrocytomas include CDK4 amplification and homozygous deletion of RB1, which together can be considered as strong predictors of poor patient prognosis (Brat et al., 2020).

1.3. Isocitrate dehydrogenase-wildtype gliomas

Gliomas with wildtype status of IDH are classified as WHO grade 4 and further subtype classification can be evaluated by assessing *ATRX* and histone H3.3 status. Paediatric and young adult patients exhibit *ATRX* and *OLIG2* loss (90% of cases) together with histone variant H3.3-G34 mutation (missense mutations substituting glycine (G) with arginine (R) or valine (V) at position 34 of H3 histone family 3 (H3.3) encoded by *H3F3A***)** (Louis et al., 2020). On the other hand, diffuse midline glioma location subtype retains nuclear ATRX localization and presents H3 K27M mutation (replacing lysine (K) to methionine (M) at position 27 of H3 histone family 3 (H3.3)) (Louis et al., 2016). Gliomas with IDH, *ATRX* and histone H3.3 wildtype status are classified as WHO grade 4 Glioblastomas (GBMs) (Louis et al., 2016). IDH-wildtype GBMs represent approximately 90% of the cases and, most frequently, they represent primary or de novo GBMs in patients aged over 55 years (Ohgaki and Kleihues, 2013).

II. Glioblastoma

1.4. Clinical overview

Glioblastoma (GBM) is the most common and aggressive malignant brain tumour in adults, which is exemplified by its very poor prognosis. GBM accounts for 70-75% of all diffuse gliomas and has an incidence rate of approximately 3.2/ 100,000 cases per year (Tamimi and Juweid, 2017). GBM patients, on average, show the highest age at diagnosis (median 59 years) and the worst prognosis (Molinaro et al., 2019).

Common GBM symptoms comprise increased intracranial pressure, headache, neurologic deficits or seizures and focal or progressive neurologic deficits (Davis, 2016). Unfortunately, they almost systematically appear when the tumour is already well developed and limited therapeutic options are available for those patients. The initial diagnosis relies on MRI and an example of a regular MRI picture of a GBM patient using peripheral enhancement with gadolinium contrast injection shows a dark and hypo-intense centre corresponding to necrosis (**Figure 2**) (Davis, 2016).

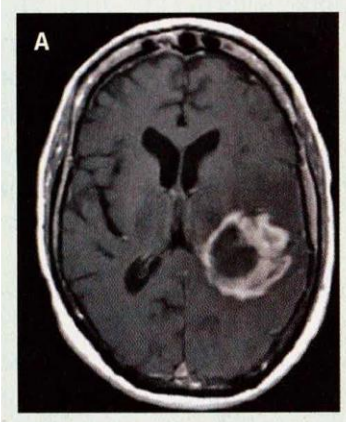

Figure 2. Magnetic resonance imaging of primary Glioblastoma. T1 post- gadolinium contrast (white) with dense rim enhancement. Picture from (Davis, 2016).

GBM surgery should involve maximal resection (Molinaro et al., 2020), however due to the high degree of invasiveness of the neoplastic cells towards eloquent areas of the brain, including regions that control speech, motor function and the senses (Davis, 2016), major resection of the primary tumour is not entirely feasible.

Prior to 2005, the standard care of treatment was the combination of surgical resection and subsequent radiation therapy. A pivotal phase III trial demonstrated that the addition of concurrent and adjuvant temozolomide (TMZ) to a standard radiation schedule improved overall survival towards 15-18 months than radiation alone in newly diagnosed GBM patients (Stupp et al., 2005). However, beyond these treatments, there has been minimal progress in extending patient survival. Nevertheless, the survival advantage observed was later found to be attributed to the methylation status of the O^6-methylguanine-DNA methyltransferase (*MGMT*) gene, located on chromosome 10q26. MGMT codes for an enzyme involved in DNA repair and promoter methylation and MGMT methylation status has been shown to be associated with improved survival and TMZ sensitivity (Hegi et al., 2005). As a result, MGMT testing became part of routine assessment as a prognostic biomarker.

Nevertheless, GBM recurrence is commonly observed following therapy and it is largely accepted that remained radio- and chemo-resistant GBM cells are likely to contribute to this phenomenon (Louis et al., 2016; Weller et al., 2014). Moreover, GBM displays high levels of inter- and intra-tumour heterogeneity, therefore its cure remaining a clinical challenge.

1.5. Glioblastoma molecular heterogeneity

GBM tumours exhibit an important inter- and intratumoural heterogeneity both at the cellular and molecular level (Furnari et al., 2007; Lee et al., 2017). According to the latest diffuse gliomas classification, patients with immunohistochemical negativity for IDH1 R132H, retained ATRX nuclear localization, non-midline tumour location and without a pre-existing lower grade glioma are classified as IDH-wildtype GBMs (Weller et al., 2021). Besides the mentioned molecular markers, GBM frequently shows unique molecular signatures such as EGFR gene amplifications (occurs in approximately 40-50%), TERT promoter mutations (occurs in approximately 70%) and gain of chromosome 7 (harbouring genes encoding for PDGFA and EGFR, among others) and loss of chromosome 10 (harbouring genes including PTEN and MGMT) (Brat et al., 2018; Brennan et al., 2013; Louis et al., 2020).

Importantly, genetic heterogeneity represents an important hallmark of treatment resistance in GBM, thus efforts have been conducted to identify robust gene expression-based molecular classifications. As such, a multidimensional genomic data study taking advantage of whole-tumour RNA sequencing analysis from The Cancer Genome Atlas (TCGA) further sub-classified GBM into four molecular subtypes: classical, mesenchymal, proneural and neural (**Figure 3**) (Verhaak et al., 2010).

The classical subtype mainly displays *EGFR* amplification and *EGFR* point or vIII mutation co-occurring with homozygous deletion of *CDKN2A* and the absence of *TP53* mutations. Additionally, genes belonging to the Notch and Sonic hedgehog signalling pathways were specifically expressed in the classical subtype.

The mesenchymal subtype contains a neurofibromin 1 (NF1) hemizygous deletion, expresses mesenchymal markers (chitinase-3-like protein-1, CHI3L1, and hepatocyte growth factor receptor; HGFR) as well as genes implicated in tumour necrosis factor (TNF) and nuclear factor-kappa B (NF-kB) pathways. Additionally, it is associated with higher aggressiveness, invasiveness and myeloid recruitment (Brennan et al., 2013; Wang et al., 2017).

The proneural subtype is characterised by the amplification and higher platelet-derived growth factor receptor alpha (*PDGFRA*) gene expression. In addition, tumours belonging to the proneural subtype also display point mutations in IDH1 and include *TP53* mutations. Immune landscape analysis showed reduced immune infiltration in this subtype associated with a better prognosis (Martinez-Lage et al., 2019)

Lastly, the neural subtype includes tumours enriched with neuronal markers (e.g. *NEFL*, *GABRA1*, *SYT1* and *SLC12A5*) as well as associated with oligodendrocytic and astrocytic

differentiation. Importantly, the neural subtype, whose expression pattern was closely related to normal brain or the result of normal neural lineage contamination, has been excluded from the current IDH-wildtype GBM molecular classification (Wang et al., 2017).

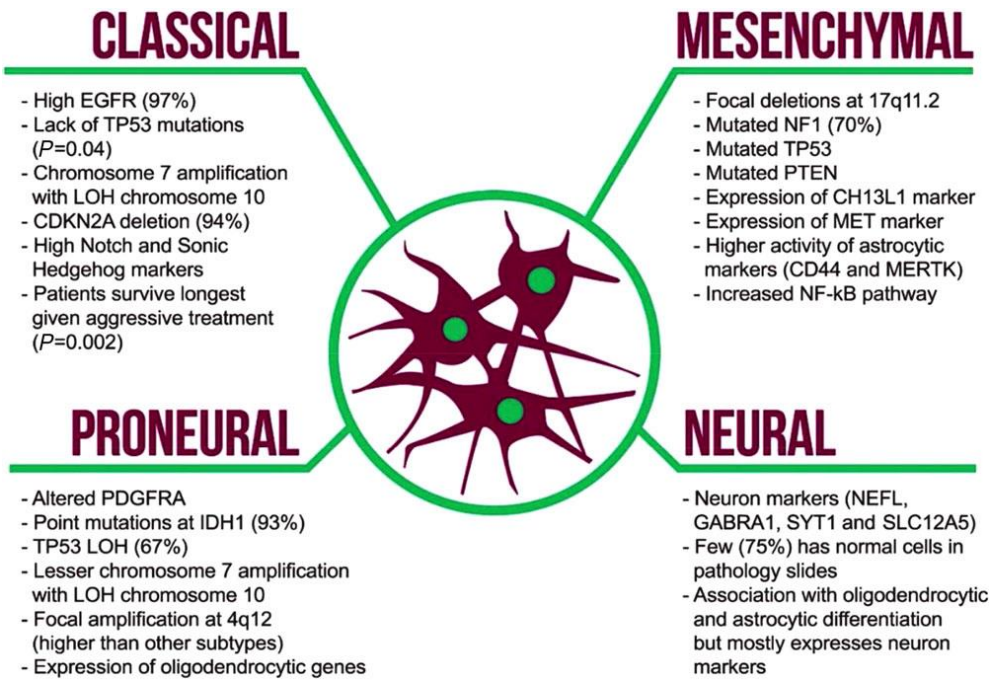

Figure 3. Schematic representation of the distinct molecular biomarkers across GBM subtypes. GBM molecular subtypes are classified as classical, proneural, mesenchymal and the neural molecular subtype according to the Verhaak classification. Work from *Wang et al 2017*, excludes the neural subtype from the classification. Figure from (Sasmita et al., 2018).

Important insights into GBM biology started to emerge with the advent of next-generation sequencing techniques. Here, tumour molecular and spatial characterization uncovered intra-tumour heterogeneity at the single-patient level, underlying variation in response to treatment (Sottoriva et al., 2013). Additionally, dynamic transcriptional program transitions were identified by *Patel et al 2014*, showing that a spectrum of GBM molecular subtypes co-exists in the tumour (Patel et al., 2014). Recently, taking advantage of single-cell RNA-sequencing (scRNA-seq) analyses, it was demonstrated that malignant cells in GBM exist in four main transcriptional cellular states. Three of them – neural stem cell (NPC)-like, oligodendrocyte progenitor cell (OPC)-like, and astrocyte (AC)-like – mirror cell types within a neurodevelopmental differentiation hierarchy, while the fourth cell state, termed mesenchymal (MES)-like does not seem to represent a specific cell type (Neftel et al., 2019), suggesting the influence of stromal cells in the tumour microenvironment (TME). In this

context, *NF1* deactivation correlated with increased infiltration of allograft inflammatory factor 1 (*AIF1*) myeloid cells at the tumours site (Wang et al., 2017).

Interestingly, at the transcriptional level GBM cells can span across the four main cellular states, as observed by the co-occurrence of combinatorial distinct cellular modules, such as AC-like/MES-like, NPC-like/OPC-like and AC-like/OPC-like (Neftel et al., 2019). It remains to be elucidated whether these transcriptional cellular states predict tumour progression and/or therapy response. Alternatively, the composition of the current microenvironment can dictate the dominance of a specific transcriptional state in GBM, as the presence of *AIF1* myeloid cells have shown to regulate the proneural-to-mesenchymal transition in GBM (Bhat et al., 2013; Wang et al., 2017).

Genome instability equips tumour cells with the potential to adapt to new environments and a combination of genetic, epigenetic, and microenvironmental cues influences cellular programmes and drive GBM heterogeneity. A better understanding of the multiple sources of heterogeneity in GBM and of their inter-relationships with the unique cellular components of the TME, may contribute to the development of more targeted therapies for GBM patients.

1.6. Glioblastoma immunosuppressive environment

Given GBM poor prognosis, there is a great interest in applying immunotherapy as a mechanism to overcome the immunoresistance of tumour cells and promote their eradication. Immune checkpoint inhibitors (ICIs) have changed the treatment landscape of many solid tumours and demonstrated remarkable improvements in melanoma, renal cell carcinoma and non-small cell lung cancer (Motzer et al., 2015; Paz-Ares et al., 2018; Ribas et al., 2015). A classification scheme has been proposed on the basis of clinical responses to ICIs. In this context, GBM has been characterized as an immunologically unresponsive or “cold” tumour (Woroniecka et al., 2018), thus showing poor response to current therapies. To date, phase III clinical studies with ICIs for GBM have been disappointing, as a short median overall survival of 7.3 months has been achieved upon treatment (Brahm et al., 2020). These prominent failures are, at least partially, explained by a low tumour mutational burden (Hodges et al., 2017), as well as by a local and systemic immunosuppression (Razavi et al., 2016). Precisely, systemic immunosuppression has been associated with sequestration of immune cells in the bone marrow in both pre-clinical models and GBM patients (Chongsathidkiet et al., 2018). Moreover, the paucity of T cells in the TME conferred GBM the status of “lymphocyte-depleted” tumour (Thorsson et al., 2018). The scarcity of T cells in

GBM is highly influenced by the distinct immunosuppressive populations as discussed below (**Figure 4**) (Grabowski et al., 2020).

In GBM, both neoplastic and non-neoplastic cells co-evolve in the TME. GBM-intrinsic factors have been shown to directly impact several cellular players, which collectively support the established immunosuppressive environment in GBM (**Figure 4**) (Grabowski et al., 2020). STAT3 was described as a key hub in mediating the secretion of immunosuppressive cytokines in GBM and higher expression of STAT3 was associated with mesenchymal subtype (Piperi et al., 2019). Classical immunosuppressive cytokines, such as transforming growth factor beta (TGF-β) and interleukin-10 (IL-10), largely contribute to the recruitment of immunosuppressive cell populations to the TME, which hampers local anti-tumour immune responses in GBM.

Regulatory T cells (Tregs)

Tregs play a significant role in inducing local immune dysfunction by suppressing anti-tumour immunity in human gliomas. While Tregs are rarely present in the normal brain tissue, they significantly increase in the TME of GBM, also compared to lower grade astrocytomas and oligodendroglial tumours (Heimberger et al., 2008; Wainwright et al., 2012). This population contributes to local immunosuppression by expressing the classical immune checkpoint markers, such as CTLA-4 and the programmed death-ligand 1 (PD-L1) on the cell surface, which bind to the co-stimulatory molecules on antigen presenting cells (e.g. CD80/86) and PD1 on effector T cells, respectively (Corse and Allison, 2012). Moreover, increased numbers of FoxP3+ Tregs over CD3+ and CD8+ T cells negatively impact the survival of primary GBM patients (Sayour et al., 2015). The recruitment of Tregs in GBM is, at least in-part, mediated through tumoral release of the cytokine TGF-β and upregulation of the enzyme indoleamine 2,3-dioxygenase (IDO) (Kaminska et al., 2013; Wainwright et al., 2012). Pre-clinical studies have demonstrated that the simultaneous targeting of immune checkpoints (e.g., CTLA-4 and PD-L1) and tryptophan catabolism decreases Treg numbers with improved T-cell-mediated long-term survival (Wainwright et al., 2014). Hence, these data suggest a combinatorial targeting of classical immune checkpoints together with metabolic pathways may bring potential value for future clinical trials in GBM patients.

Natural Killer (NK) cells

GBM-secreted TGF-β affects NK cell activity by downregulating the expression of NKG2D, an activating receptor important for NK cell-mediated killing of the target cell. This mechanism affects

NK cell activity by decreasing its cytotoxic immune response, thus contributing to GBM immune evasion mechanism (Crane et al., 2010). Despite NK cells make up a relatively small proportion of tumour-infiltrating cells in GBM, computational-based studies have recently demonstrated that activated NK cell transcriptional signatures correlate with improved prognosis in GBM patients (Barrow et al., 2018). For a summary of NK cell immunotherapy against CNS malignant tumours, please refer to the review by Sedgwick and co-workers (Sedgwick et al., 2020).

Myeloid-derived suppressor cells (MDSCs)

Higher numbers of MDSCs are detected in GBM compared to other tumours, such as melanoma, renal cell cancer and bladder cancer patients (Raychaudhuri et al., 2015). Precisely, a reduced intratumoural infiltration of MDSCs correlates with a better prognosis in GBM (Alban et al., 2018; De Leo et al., 2020) with subsequent increase of CD3+ and CD4+ T cell counts in both murine and human GBM patients (Raychaudhuri et al., 2015). MDSCs mediate immunosuppression by several mechanisms, including: 1) expression of arginase, which decreases the level of L-arginine necessary for T cell receptor chain expression and function; 2) secretion of nitric oxide and reactive oxygen species (ROS) inducing T cell suppression; 3) expression of PD-L1 contributing to T cell exhaustion (Dubinski et al., 2016; Nagaraj and Gabrilovich, 2007).

Tumour-associated microglia/macrophages (TAMs)

Increased myeloid gene expression in the mesenchymal subtype of GBM has been associated with a poor prognosis (Wang et al., 2017). Due to the local inflammation exerted by GBM cells, the majority of TAMs acquire an anti-inflammatory phenotype under the direct influence of tumour cells (Hambardzumyan et al., 2016). TAMs display high degree of plasticity in regards to their immune functions and other polarization phenotypes can be present in the TME, as discussed in **section III**. In the TME, TAMs are known to secrete anti-inflammatory cytokines such as IL-6, IL-10 and TGF-β, which further enhance immunosuppression in the TME leading to GBM growth and proliferation (Hambardzumyan et al., 2016)

It has been shown that TGF-β secretion by TAMs induces epithelial-to-mesenchymal transition and enhances CD133+ glioma stem cells invasion (Ye et al., 2012). Moreover, microglia-derived TGF-β is an important mediator of tumour–host interactions and a regulator of glioma invasion (Wesolowska et al., 2008). As innate immune cells, TAMs express Toll-like receptors (TLRs), which are pathogen recognition receptors playing important roles in tumour growth. TLR2

promotes TAM production of several matrix metalloproteinase (MMP), such as MMP2 and MMP9 which disrupts the ECM matrix potentiating GBM invasiveness (Hu et al., 2014; Ye et al., 2012). Additionally, TLR4 expression on TAMs which regulates IL-6 cytokine secretion, has been shown to increase glioma stem cell proliferation (Dzaye et al., 2016). TAMs also contribute to local angiogenesis by providing pro-angiogenic factors such as epidermal growth factor (EGF) and Vascular endothelial growth factor (VEGF) (Hambardzumyan et al., 2016; Zhu et al., 2017). Both murine and human TAMs show significant expression of transmembrane glycoprotein NMB (Gpnmb) and osteopontin (Spp1), which are respectively implicated in immunosuppression and tumour cell invasion, as well as are associated with poor prognosis in GBM patients (Szulzewsky et al., 2015). Additionally, GBM-secreted factors have been shown to downregulate the expression of major histocompatibility complex (MHC) surface molecules on microglia (Razavi et al., 2016), thus favouring local tumour immune evasion mechanisms. Lastly, peripheral blood macrophages from GBM patients exhibit higher PD-L1 expression compared to healthy control patients, which showed to suppress T cell activation *in vitro* (Bloch et al., 2013).

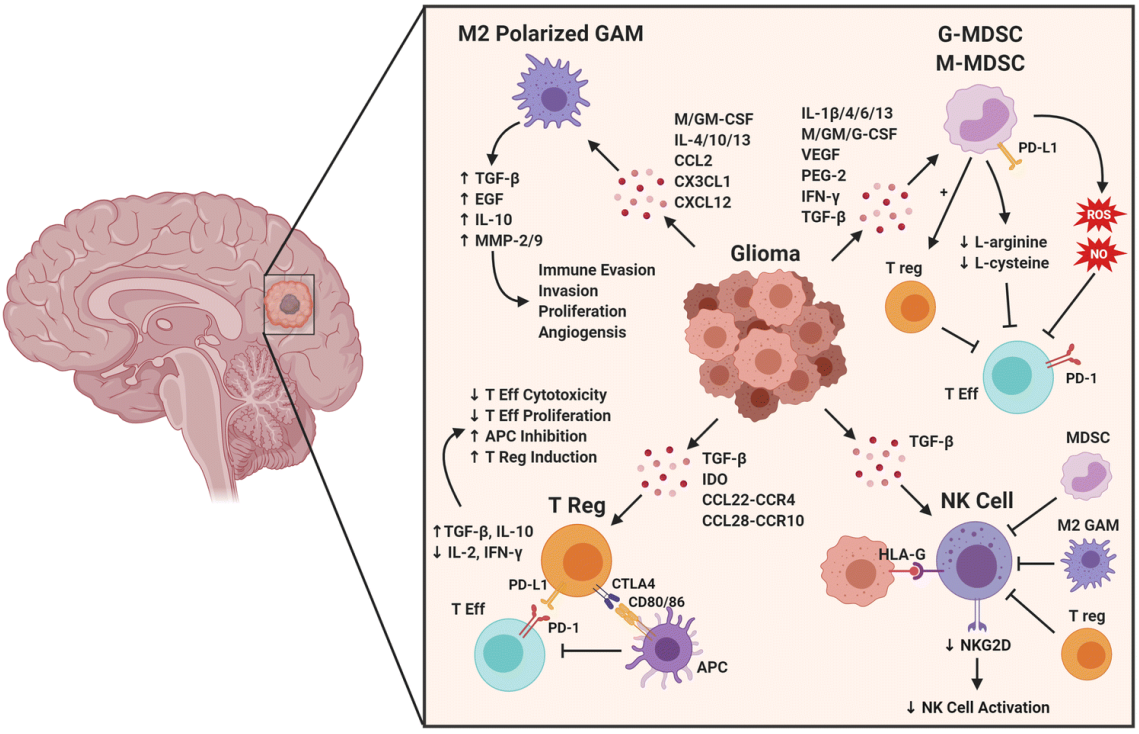

Figure 4. GBM-secreted factors recruit and modulate immune cell players in the TME towards an immunosuppressive phenotype contributing to immune evasion mechanisms. GBM cells secrete several soluble factors that contribute to the local immunosuppressive environment in GBM. Picture from (Grabowski et al., 2020).

Clinical studies have shown a correlation between the number of TAMs and poor prognosis for multiple cancer types, including brain tumours (Kowal et al., 2019). There has been considerable interest in targeting TAMs for GBM and therefore are being pursuit as key targets for the development of immune-based therapeutic approaches for GBM patients.

III. Tumour-associated microglia/macrophages

1.7. Ontogeny

TAMs constitute approximately 40% of the stromal compartment in GBM and include both tissue-resident microglia and monocyte-derived macrophages (Bowman et al., 2016; Hambardzumyan et al., 2016).

Parenchymal microglia are a unique immune cell population of the CNS (Sousa et al., 2017). Fate-mapping and lineage-tracing studies have identified immature yolk sac runt-related transcription factor 1 (Runx1) progenitors as the predominant source of brain microglia. The embryonic progenitors (between days 8.5 (E8.5) and E9.5) migrate from the yolk sac into the primitive brain, becoming the source of microglia in the adult brain (Ginhoux et al., 2010). Once in the CNS, microglia present limited self-renewal capacity (Ginhoux et al., 2010; Gomez Perdiguero et al., 2015) and they live for about 15 months on average, almost equalling the life span of post-mitotic neurons (Fuger et al., 2017). It has been debated for some time weather blood peripheral progenitors could contribute to the pool of adult microglia after birth. Recent fate-mapping studies confirmed the presence of non-parenchymal macrophages at CNS interfaces (called border-associated macrophages, BAMs) and indeed, they form a separate identity in terms of ontogeny, gene signature and contrary to microglia, they do not require TGF-β for their development (Utz et al., 2020).

The CNS parenchyma is mostly occupied by resident microglia, while in the context of tumour-bearing brain, there is a disruption of the BBB as a results of local inflammation and the growing tumour. This results in the infiltration of bone-marrow derived cells (BMDMs) from the circulation to the tumour site, where they differentiate into macrophages (Bowman et al., 2016; Hambardzumyan et al., 2016). In the TME, microglia and macrophages become morphologically similar in histological sections (**Figure 5**) (Buonfiglioli and Hambardzumyan, 2021). Naïve microglia display a highly ramified morphology aligned with its surveillance mode and once activated they rapidly modify their

morphology into an amoeboid shape. Monocyte-derived cells display a round-shape in the tissue and thus, making it challenging to distinguish from the resident activated microglia cells in GBM histological sections (**Figure 5**).

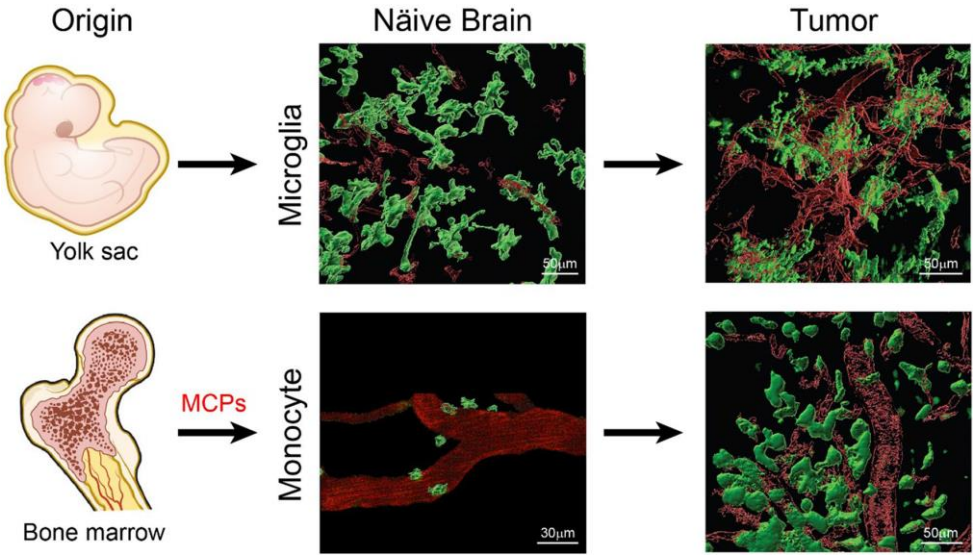

Figure 5. Myeloid cell lineage origin and respective morphological characterization in the healthy brain and GBM. Microglia arise from yolk sac progenitors in the embryonic stage and reside in the brain parenchyma. Microglia display a ramified morphology in the naïve brain, while they change towards a more amoeboid-like shape in GBM. In GBM, upon BBB disruption, BMDMs migrate from the circulation to the brain and differentiate into tissue-associated macrophages. These cells display a round-shape in circulation and upon infiltration to the tumour site become difficult to discriminate from the resident activated microglia cells. Picture from (Buonfiglioli and Hambardzumyan, 2021).

In GBM, when lineage-tracing models are not used, microglia cells were initially discriminated based on the expression of surface markers as CD11b+/CD45low (or CD45int), whereas BMDMs were characterized as CD11b+/CD45high population. However, this discrimination is inadequate since activated microglia can upregulate CD45 expression in pathological conditions (Muller et al., 2015). The combination of Ly6C and Ly6G markers were proposed to aid for discriminating microglia ($CD11b^{+}$ $CD45^{low}$ $Ly6C^{-}$ $Ly6G^{-}$) from macrophage ($CD11b^{+}$ $CD45^{high}$ $Ly6C^{low}$ Ly6G-) cells in murine GBM model (Chen et al., 2017). Several groups have used distinct genetically engineered GBM mouse models (GEMMs), such as the Flt3:Cre;Rosa26:mTmG or the *Cx3Cr1*$^{GFP/+}$;*Ccr2*$^{RFP/+}$ knock-in mice, which identified the contribution of peripheral cells to the overall TAM population. A meta-analysis using murine transcriptional databases identified *P2ry12, Tmem119, Slc2a5* and *Fcrls* as genes specifically expressed by microglial cells, and *Emilin2, Gda, Hp* and *Sell* being expressed by

BMDMs in murine gliomas (Haage et al., 2019). Recently, the glycoprotein Itga4 (CD49D) was reported to discriminate resident microglia from BMDMs in both humans and mice (Bowman et al., 2016; Klemm et al., 2020).

The combination of recent genome-wide and scRNA-seq technologies has revolutionized both the phenotypic and transcriptomic characterization of these two populations in GBM (**Figure 6**). For an exhaustive overview on this topic, please refer to our review (**Appendix**) (Pires-Afonso et al., 2020).

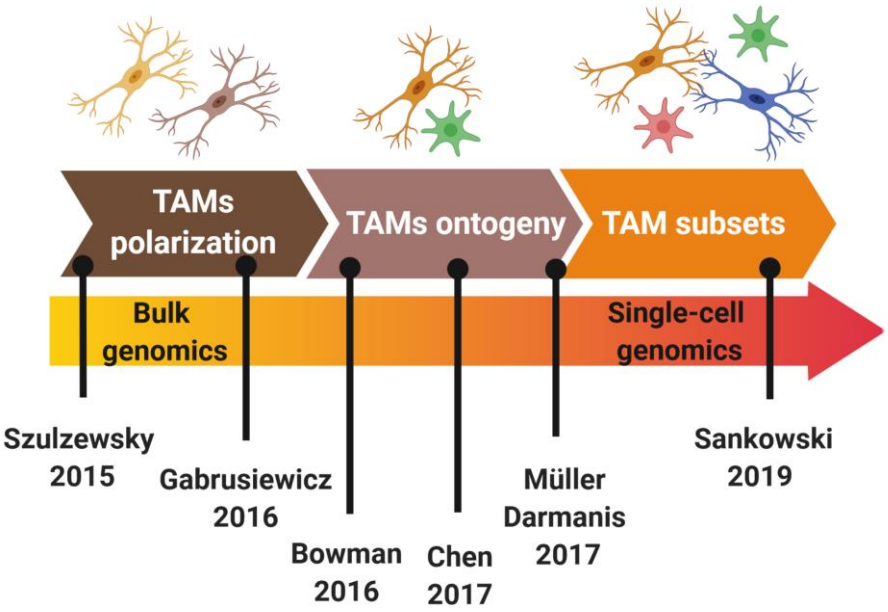

Figure 6. Chronology of the characterization of tumour-associated microglia/macrophages (TAMs) heterogeneity in glioblastoma (GBM). Key studies that have contributed to elucidate TAMs polarization, ontogeny and subsets in GBM mouse models and patients (Pires-Afonso et al., 2020).

The presence of both populations in GBM patients have been identified in recent scRNA-seq studies (Muller et al., 2017; Pombo Antunes et al., 2021). Despite the fact that TAMs are the most abundant immune cell type in GBM (Klemm et al., 2020), insight into the precise contribution of the two ontogenetically distinct TAM cell types is starting to emerge. Precisely, initial studies have shown that these two myeloid populations hold distinct transcriptional profiles.

The cytokine colony-stimulating factor-1 (CSF-1) critically supports TAMs survival and differentiation. Furthermore, inhibition of its receptor, CSF-1R, substantially gained attention for clinical approval. Despite promising strategy, it showed to contributed to tumour recurrence in more

than 50% of the mice through phosphoinositide 3-kinase (PI3K) signalling (Quail et al., 2016). Additionally, targeting the CSF-1/CSF-1R axis in phase II trial in recurrent GBM did not improved overall survival (Butowski et al., 2016). These studies are of relevance as TAMs heterogeneity impose limitations to non-selective immunotherapies and the identification of alternative markers may aid to a more targeted intervention for GBM patients.

1.8. Localization

TAMs exhibit differential localization at defined tumour regions. Recent studies have implied a dominance of BMDMs in the tumour core, while microglial cells are more prevalent in the invading edge in GBM patients (Darmanis et al., 2017; Muller et al., 2017). Whether this distinct *in situ* localization impacts the functional adaptation of microglia and BMDMs in the TME is starting to emerge. Leveraging from spatial transcriptomic technologies, Darmanis and colleagues showed, an enrichment of pro-inflammatory markers (e.g. IL1α and IL1β) in the periphery of the tumour, while an anti-inflammatory phenotype (e.g. IL1RN and TGFBI) was enhanced in the tumour core (**Figure 7**) in human GBM patients (Darmanis et al., 2017).

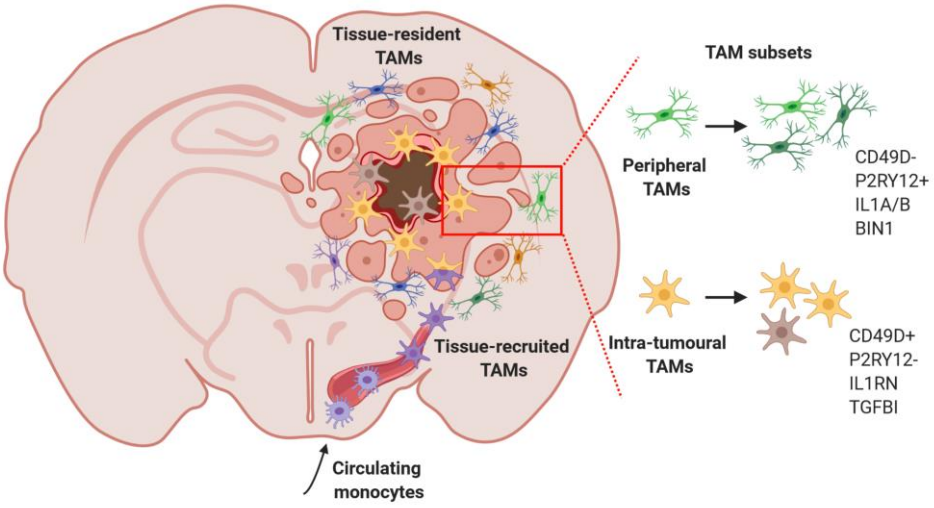

Figure 7. Discrimination of specific TAM subpopulations in GBM patients. TAMs present distinct features according to their ontogeny and spatial localization in specific tumour areas. Picture from (Pires-Afonso et al., 2020).

Recent work, further identified microglia enriched cells (IBA1+ CD163-) diffusely scattered thorough the section, while distinct macrophage subsets, CD163+, CD169+ and CD209+ were found in close proximity to blood vessels in gliomas (Friebel et al., 2020). Similarly, recent work also identified BMDMs dominance in close proximity to CD31+ vascular structures (Klemm et al., 2020). Respective tumour region occupancy can be partially mediated by differential migratory properties employed by TAMs. Morphological features combined with spatial characterization was evaluated by applying intravital two-photon microscopy imaging on GBM tumour sections (Chen et al., 2019). Precisely, they observed an enrichment of cells with a stationary profile characterized by larger surface area and branched morphology in the tumour periphery. In contrast, enrichment of amoeboid monocyte-derived macrophages was identified in the tumour core (Chen et al., 2019). Overall, these studies uncovered TAMs spatial heterogeneity in both murine and human GBM samples.

In order to elucidate TAMs functional dynamics in GBM, Chen and colleagues revealed that resident microglial cells display a pro-inflammatory cytokine-related signature compared to an enriched migratory signature in BMDMs (Chen et al., 2017). In line with this study, BMDMs were described to exhibited higher immunosuppressive potential in the tumour core compared to microglial cells from the tumour periphery in GBM patients (Pinton et al., 2019). Similarly, TAMs spatial-associated functions in GBM samples were linked to an increased activity of PD-1 signalling pathway in the tumour core, while an enrichment of NF-kB signalling was associated to the tumour periphery (Landry et al., 2020). Whether the PD-1 inhibition response correlates to the presence of TAM-enriched cells in the tumour core awaits further investigations.

Overall, TAMs spatial characterization and association with specific functional immune profiles are indicative of their high level of heterogeneity, a feature that should be taken into consideration for their specific targeting. Moreover, TAMs immunosuppressive capability further validates the rationale of potential targeting as a mean for intervention to modulate their activity and/or recruitment in GBM.

1.9. Polarization

The transcriptomic profile of TAMs can be shaped by numerous factors present in the GBM microenvironment. TAMs are recognized by having a significant degree of plasticity. Recent work has highlighted the role of the environment in governing tissue-specific education of macrophages. The role of epigenetic modifications as conduit for mouse tissue-specific macrophage identity and plasticity has been previously established (Lavin et al., 2014). Bowman and colleagues, showed that

the differential TAM education in the TME is regulated by epigenetic events, suggesting that TAMs might be poised to engage in distinct transcriptional programs based on initial enhancer selection (Bowman et al., 2016).

In general, tumours develop gradually and whether the tumour genotype instructs differential functional shifts on highly dynamic TAMs needs further investigations. The majority of these studies have been performed at late stage of GBM and therefore a dynamic adaptation of these cells along GBM progression is lacking. As such, we cannot exclude that differential ontogeny and regional heterogeneity might contribute for the distinct functional adaptation of TAMs in the TME.

In the tumour, TAMs are being categorised taking into account their activation/polarization profile. Previous work adopted the conventional *in vitro* binary system for the characterization of TAMs in the TME. Specifically, *in vitro* stimulation with interleukin 4 (IL-4) shifts macrophages towards the "M2 or alternative activation", while interferon gamma (IFN-γ) skew them towards the "M1 or classic activation" state (Mills et al., 2000). Distinct activated states correlate with differential properties, wherein M1 macrophages are capable of mounting an anti-tumour immune response by presenting antigens to adaptive immune cells, producing pro-inflammatory cytokines and phagocytosing tumour cells (Martinez et al., 2008). In contrast, M2 macrophages are considered pro-tumorigenic by promoting tissue remodelling, angiogenesis (Hambardzumyan et al., 2016; Zhou et al., 2015).

However, the traditional M1 and M2 nomenclature does not fully represent TAM heterogeneous activated states in GBM (Muller et al., 2017; Pires-Afonso et al., 2020). In brain malignancies, intermediate phenotypes exist as a putative M2c state has been identified and associated with immune regulation, matrix deposition and tissue remodelling (Roesch et al., 2018). Moreover, it has been described that TAMs in GBM exhibit a M0 state, as they exhibit an undifferentiated or non-polarized phenotype (Gabrusiewicz et al., 2016). Recent studies have unravelled that TAMs co-express the canonical M1 and M2 markers in traumatic brain injury (Kim et al., 2016) as well in human gliomas (Muller et al., 2017).

The MacSpectrum algorithm, a scRNA-seq based gene enrichment tool used to estimate the polarization index of TAMs in human GBM, enabled to uncover that TAMs display high heterogeneous activated states (Landry et al., 2020). Independently of the regional localization, the M2-like state dominated and showed no significant differences between tumour core and periphery (Landry et al., 2020).

It is becoming of urgent need to discriminate between the biological functions of microglia from macrophages in GBM and elucidate whether there is a redundancy of their functions in the TME.

1.10. Myeloid heterogeneity across Glioblastoma subtypes

GBM creates a proangiogenic and inflammatory microenvironment, which leads to an increased expression of adhesion molecules on endothelial cells and reduced tight junctions, thereby promoting a permeable blood-brain barrier (BBB) (Chen and Hambardzumyan, 2018). These changes support cellular infiltration to the tumour site. The presence of distinct immune-related cell infiltrates within the tumour significantly accounts for the gene expression variability observed in GBM patients. Therefore, the exact implication of immune infiltrates in distinct GBM subtypes are starting to emerge.

Across several cancers, myeloid cells are described as key determinant players for tumour progression and patient outcome (Cassetta and Pollard, 2018; DeNardo and Ruffell, 2019). In GBM, despite extensive correlative studies implying that TAMs may play differential roles across GBM subtypes, to date, there are still no systemic functional studies corroborating this hypothesis.

Clinically, GBM subtypes have not been established as predicative biomarkers for patient survival (Verhaak et al., 2010), although accumulating evidences indicate that subtype-specific treatment may preferentially benefit patients (Chen and Hambardzumyan, 2018). Tumour cells from the mesenchymal subtype frequently deactivate NF1 through genomic copy loss or somatic mutations (Verhaak et al., 2010) and it has been proposed that NF1 deficiency drives the recruitment of myeloid cells (Wang et al., 2017). Accordingly, the mesenchymal subtype exhibits the highest percentage of myeloid and lymphocyte infiltrates (Kaffes et al., 2019; Wang et al., 2017), making this subtype attractive for immune-based therapies. Tissue microarray analyses from a cohort of 98 GBM patients revealed that 80% of the mesenchymal subtype cellularity is composed by CD163 positive cells, which have been associated with poor prognosis (Martinez-Lage et al., 2019), thus supporting the rationale for the design of therapies directed against the myeloid component in the mesenchymal subtype.

Moreover, a proneural-mesenchymal transition (PMT) has been described in GBM patients and activation of the transcription factor signal transducer and activator of transcription 3 (STAT3) has been demonstrated to result in the transition to the mesenchymal profile (Piperi et al., 2019; Segerman et al., 2016). Precisely, the PMT transition has been associated with recurrent tumours with the emergence of chemotherapeutic and radiation resistance glioma-initiating cell clones harbouring gain in PMT transcriptomic patterns (Segerman et al., 2016). In this context, it was recently shown that the potential of clustering STAT3-high and STAT3-low gene signature as a mean for stratifying glioma patients to receive targeted therapy (Tan et al., 2019). Furthermore, elevated

levels of phosphorylated STAT3 have been shown to favour an anti- inflammatory phenotype in myeloid cells affecting their potential as antigen presenting cells, thus dampening their anti-tumour immune response (Piperi et al., 2019; Wang et al., 2004; Wu and Watabe, 2017).

Recent work demonstrated distinct TAM composition dependent on the tumour genotype. Precisely, IDH-mutant tumours exhibited a predominance of microglial cells in the TME, while IDH-wildtype tumours showed an increased invasion by monocyte-derived infiltrative cells (Friebel et al., 2020; Klemm et al., 2020).

IV. Therapeutic targeting of tumour-associated microglia/macrophages

Immunotherapy, and especially immune checkpoint inhibitors, have transformed the landscape of cancer treatment and improved patient survival in a number of different cancer types. However, no clinical benefit has been observed in GBM patients. Despite the general interest in targeting TAMs in GBM, only a few studies performed in preclinical models have taken into account the dual origin of the TAM population (Bowman et al., 2016; Chen et al., 2017). Nevertheless, due to their abundance in the TME, their genomic stability and phenotypic plasticity, several strategies are being pursued to target TAMs in GBM. Currently TAM-based strategies are mainly focused on two strategies: 1) blocking their infiltration to the tumour site and 2) strategies at reprogramming their function (De Leo et al., 2020).

1.11. Strategies targeting TAMs recruitment

The CCL2/CCR2 axis is essential for monocyte recruitment to the tumour site, and genetic ablation of *Ccl2* prolonged the survival of GBM-bearing mice (Chen et al., 2017). The involvement of CCL2 signalling in multiple diseases renders it an interesting therapeutic target, however caution should be taken as CCL2 shows pleiotropic effects on myeloid cells, including polarization, activation and survival (Gschwandtner et al., 2019). Although current targeting strategies have not met early expectations in the clinic, few clinical trials using antagonists for CCL2 and CCR2 to treat solid tumours, such as in metastatic pancreas cancer (PF-04136309, NCT02732938).

As previously mentioned, TAMs critically depend on CSF-1 for survival and differentiation, thus several approaches targeting either the CSF ligand or the receptor are substantially gaining attention for clinical approval. The use of CSF1R small-molecule inhibitors, such as BLZ945, was shown to

decrease glioma progression by polarizing TAMs into an anti-tumour phenotype in a proneural rodent model of GBM (Pyonteck et al., 2013). However, further pre-clinical trials studying the long-term administration of BLZ945 showed tumour rebound rapidly after a dormancy phase of 4 weeks (Quail et al., 2016). The resistance mechanism was shown to be mediated by TAMs, via the secretion of insulin growth factor 1 (IGF-1) and cognate interaction with IGF-1R on the surface of tumour cells, which in turn activated the phosphatidylinositol 3-kinase (PI3K) signalling pathway leading to tumour resistance and proliferation (Quail et al., 2016). The usage of another CSF-1R inhibitor, PLX3397, showed no efficacy advantage in recurrent GBM (Butowski et al., 2016).

Another promising target to block TAM recruitment is the stromal cell-derived factor 1 (SDF-1) receptor C-X-C chemokine receptor type 4 (CXCR4). Preclinical studies showed that after irradiation, tumour induces the recruitment of myeloid cells through the SDF-1/CXCR4 pathway (Liu et al., 2014; Walters et al., 2014). Several CXCR4 antagonists, such as peptide R or LY2510924, were shown to be beneficial in GBM mouse models (Mercurio et al., 2016; Peng et al., 2015). In newly diagnosed GBM patients, a phase I/II study showed that infusion of Plerixafor, the currently and only FDA approved CXCR4 antagonist, is well-tolerated as an adjuvant to chemo-radiation therapy, contributing to a median overall survival of 21.3 months (Thomas et al., 2019).

1.12. Strategies targeting TAM functions

Despite no significant improvements were observed in TAMs recruitment upon CSF1R blockade, the use of CSF1R inhibitor BLZ945 showed the potential to polarize TAMs into an anti-tumour phenotype in the proneural GBM mouse model (Pyonteck et al., 2013). Conversely, in the syngeneic GL261 GBM mouse model, stimulator of interferon gene (STING) agonists significantly increased IFN-γ production by TAMs. This lead to TAMs re-education towards a pro-inflammatory phenotype and subsequent recruitment and activation of T cells (Ohkuri et al., 2014).

A genetic reprogramming of macrophages to perform antitumor functions without causing systemic toxicity might be achieved using targeted nanocarriers that can deliver *in vitro*-transcribed mRNA encoding M1-polarizing transcription factors through the mannose receptor CD206. Infusion of nanoparticles containing mRNAs encoding interferon regulatory factor 5 (IRF5) in combination with its activating kinase IKKβ, not only inhibit the immunosuppressive state of TAMs, but also reprogram them to an anti-tumour phenotype, which contributed to tumour regression (Zhang et al., 2019).

Another compelling strategy to target TAMs is the use of nucleic acid-based therapies, such as microRNA. Reports showed that microRNAs can be transported from donor cells to recipient cells, serving as TLR signalling activators (Fabbri et al., 2012). In the study from Buonfiglioli and colleagues, s subset of the *Let-7* microRNA family members, was shown to induce microglial anti-tumour activity in TLR7 dependent manner, associated with increased inflammatory response and antigen presentation in GL261 syngeneic GBM model (Buonfiglioli et al., 2019).

A recent and promising treatment for GBM consists of oncolytic viruses (OVs). The oncolytic adenovirus Delta24-RGD, also known as DNX-2401, is designed to selectively replicate in cells harbouring the retinoblastoma gene. To access its efficacy as a treatment for recurrent malignant gliomas, 37 patients received an intra-tumoral injection of DNX-2401. The study showed long free survival of 26 months before a second tumour resection due to recurrence (Lang et al., 2018). Mechanistically, Delta24-RGD-infected tumour cells were detected by TLR9 on macrophages, via the MyD88–IRF5 pathway. Consequently, TLR9 skew TAMs towards a M1 polarizing phenotype, which is associated with enhanced tumour cell phagocytosis and leukocyte recruitment (van den Bossche et al., 2018). Despite the promising results, it remains to elucidate whether the TAM phenotypic shift is responsible for mediating tumour delayed in this cohort.

V. Macrophage immunometabolism

1.13. Metabolic reprogramming in innate immune cells

Otto Warburg, during his research on tumour cells, first identified a dramatic increase of glucose uptake and lactate by the cells in conjunction with reduced levels of oxidative phosphorylation (OXPHOS) in the presence of oxygen. Later, it has been coined as the “Warburg effect” or “Warburg metabolism” (Warburg et al., 1927). Contrary to tumour cells, which require high levels of energy to sustain their proliferation rate on site, metabolic rewiring of inflammatory macrophages evolved as an inducible and reversible phenotype (El Kasmi and Stenmark, 2015).

Over the last decade, the metabolism of immune cells is a rapidly expanding area of research. Immune cells react to their environment by flexibly reprogramming intrinsic metabolic pathways that subsequently alter immune function, in a process called immunometabolism. Thus, immunometabolism relates to the dynamic crosstalk between the immune cells and the metabolic pathways occurring upon stress and insults (Mathis and Shoelson, 2011; O'Neill et al., 2016).

Distinctive metabolic rewiring networks occur to sustain their phenotype and function in distinct contexts. For instance, to sustain a pro-inflammatory phenotype, macrophages mainly rely on glycolysis and the pentose phosphate pathway to meet their ATP requirements to sustaining the glycolytic metabolism, while the metabolic activity of anti-inflammatory macrophages is mainly characterized by enhanced OXPHOS and fatty acid oxidation (Mills et al., 2017).

Under homeostatic conditions, microglial favour oxidative metabolism to fuel the dynamic motility they exhibit in surveillance mode. In contrast, it was shown that primary microglia cultures increase their glycolytic flux in response to proinflammatory stimuli (Nair et al., 2019). Similarly, in neuroinflammatory conditions, microglia shift away from oxidative phosphorylation towards a more glycolytic profile necessary for cytokine production and phagocytosis, which is mediated by increased hypoxia-inducible factor 1-alpha (HIF-1α) and mTOR transcriptional control (Bernier et al., 2020).

In tumour context, local environment is characterized by high nutrient competition, low pH and limited oxygen. Under such conditions, myeloid cells undergo metabolic reprogramming by adjusting their phenotype and function in response to the local cues (Gosselin et al., 2014). In human gliomas, a decreased glycolytic metabolism in tumour-associated macrophages compared to tumour-associated microglia, is associated with increased immunosuppression in the TME and poor patient survival (Muller et al., 2017). These findings shed light on the potential of environmental factors mediating TAM-specific immunity. As discussed previously, microglia and macrophages preferentially occupy distinct regions in the tumour brain, thus exhibiting distinct metabolic profiles and adaptations, which ultimately may govern divergent functions in the TME. Whether these metabolic adaptations dictate TAM contribution to GBM progression awaits further investigation.

1.14. Immunoregulatory role of itaconate

Metabolic reprogramming of macrophages plays a predominant role in regulating their phenotype but also their plasticity. The discovery that intermediate metabolites of the trycarboxylic acid (TCA) cycle (such as succinate) and metabolites produced by their conversion (e.g. itaconate from cis-aconitate) possess immunological properties, led to the discovery that central metabolism can regulate immune cell functions and affect their responses (Michelucci et al., 2013; Tannahill et al., 2013).

Lipopolysaccharide (LPS) is a potent activator of monocytes and macrophages and the LPS-inducible gene, cis-aconitate decarboxylase or initially termed as immune-responsive gene 1 (ACOD1/IRG1), catalyses the decarboxylation of the TCA cycle intermediate cis-aconitate to produce itaconate (Strelko et al., 2011). Itaconate contributes to succinate accumulation in macrophages by acting as an endogenous succinate dehydrogenase (SDH) inhibitor (**Figure 8**) (Cordes et al., 2016).

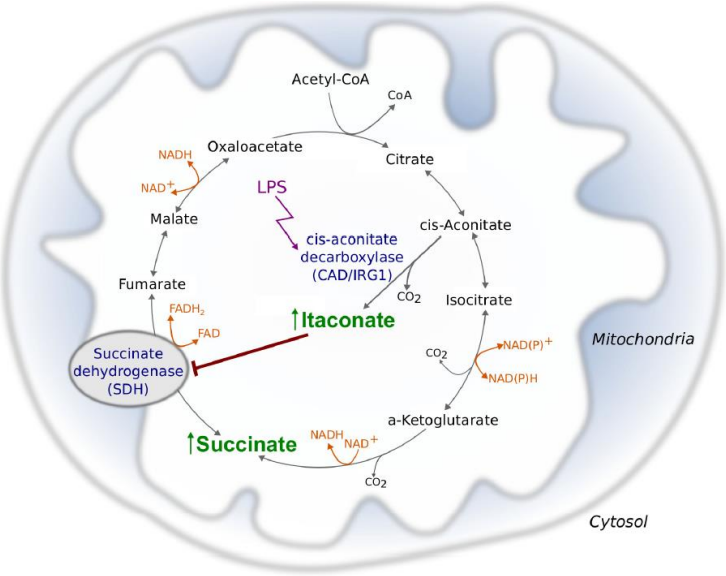

Figure 8. Itaconate produced in LPS-activated macrophages induces intracellular succinate accumulation. Under inflammatory conditions, such as LPS stimulation, IRG1 catalyses the decarboxylation of the TCA cycle intermediate cis-aconitate to produce itaconate. This metabolite contributes to succinate accumulation in macrophages by acting as an endogenous SDH inhibitor. Picture from (Cordes et al., 2016).

Itaconate ability to directly inhibit SDH comes from its structural similarity with succinate (O'Neill and Artyomov, 2019). Increasing succinate levels inhibit prolyl hydroxylase domain (PHD) enzyme activity, resulting in the stabilization of hypoxia-inducible factor 1-alpha (HIF-1α) leading to subsequent induction of HIF-1α-dependent genes, such as IL-1β during inflammation (Tannahill et al., 2013). The mechanism by which itaconate induces these metabolic and functional changes in LPS-activated macrophages has been recently elucidated (**Figure 9**) (Mills et al., 2018). Itaconate alkylates several cysteine residues on the protein Kelch-like ECH-associated protein 1 (KEAP1), enabling nuclear factor erythroid 2-related factor 2 (Nrf2) translocation to the nucleus, thus suppressing the pro-inflammatory downstream signalling pathway (**Figure 9**). Metabolic rewiring plays a crucial role and high levels of itaconate has the potential to skew macrophages towards an anti-inflammatory phenotype (**Figure 9**) (Mills et al., 2018)

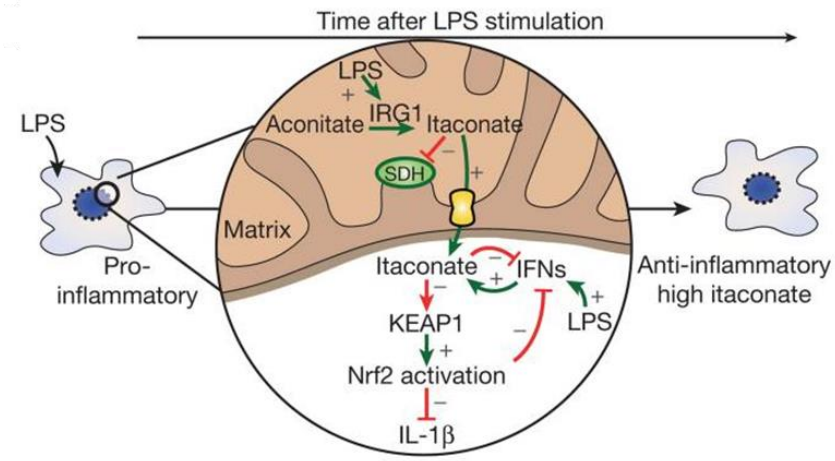

Figure 9. Schematic representation of the anti-inflammatory role of itaconate in LPS-stimulated macrophages. LPS-activated macrophages leads to the production of itaconate inside the cell. Itaconate alkylates several cysteine residues on the protein Kelch-like ECH-associated protein 1 (KEAP1) with subsequent suppression of the pro-inflammatory downstream signalling pathway, contributing to anti-inflammatory reprogramming. Picture from (Mills et al., 2018).

Previous studies showed that, itaconic acid display intrinsic antimicrobial properties by inhibiting isocitrate lyase, a key enzyme of the glyoxylate shunt, and fundamental for infectious bacterial survival (Williams et al., 1971). The effect of itaconate in host susceptibility to viral infections has also been elucidated following the observation that *Acod1* mRNA is strongly induced in the early stages of influenza A virus infection in mice (Preusse et al., 2013). Further protective effects of itaconate on neurons exposed to RNA viruses have also been reported (Daniels et al., 2019). Additional roles have been identified in septic shock patients where IRG1 expression levels are up-regulated in monocytes and correlate with the suppression of TLR-mediated production of pro-inflammatory cytokines (e.g. TNF, IL-6, and IFN-β) (Li et al., 2013b). This regulation is mediated by the inhibition of the NF-κB activation by A20 expression through a ROS-dependent manner (Li et al., 2013b). In the context of sepsis, itaconate synthesis contributed to immune tolerance in human monocytes (Dominguez-Andres et al., 2019). This effect was reverted by β-glucan, a fungal cell wall component that exerts a long-term upregulation of innate immune function. Precisely, β-glucan reverted monocytes immunoparalysis by preserving the SDH pathway (Dominguez-Andres et al., 2019).

Cellular metabolism is a key mechanism by which metabolic rewiring plays a role in the establishment of disease tolerance and the induction of immunoparalysis (O'Neill et al., 2016). Accumulating evidences have shown that the mammalian innate immune system can adapt its

functions following previous infections or vaccinations, a process termed as “trained immunity” (Netea et al., 2011). These results identify itaconate as a critical regulatory node linking metabolism with trained immunity and highlight the importance to modulate IRG1-itaconate-SDH axis as a mechanism to revert immune tolerance in disease.

1.15. Role of itaconate in cancer

Although the role of itaconate under inflammatory and infectious conditions are emerging, little work has yet been addressed regarding the function of the ACOD1/IRG1 axis in a tumour context, especially in GBM. Although its role in cancer is still unclear, itaconate is emerging as a critical metabolic component underlying the crosstalk between neoplastic cells and tumour-associated macrophages.

Acod1/Irg1 is highly expressed in mammalian macrophages during inflammation and in cancer. In cancer, microarrays analysis have shown that CD11b+ cells from the GL261 syngeneic models show significant increase of *Irg1* expression compared to naïve controls (Szulzewsky et al., 2015). Recent work has shown that itaconate metabolite is highly upregulated in peritoneal macrophages from tumour-bearing mice, which contributed to tumour progression (Weiss et al., 2018). By using a lentiviral shRNA approach that specifically targets *Irg1* expression on macrophages, they observed a drastic reduction of B16 tumour burden in the peritoneum. Mechanistically, they have shown that itaconate promotes tumour growth via OXPHOS-driven ROS expression on macrophages and concomitant ROS-mediated MAPK activation in tumour cells (Weiss et al., 2018).

In conclusion, itaconate metabolism represents a crucial regulatory node for therapeutic interventions focused on TAM reprogramming in the TME. Particularly in GBM, characterized by a highly immunosuppressive environment, targeting of ACOD1/IRG1-itaconate axis represents a promising alternative to modulate the immunosuppressive profile of myeloid cells.

CHAPTER 2

OBJECTIVES

GBM is the most common primary brain tumour in adults characterized by an extensive transcriptional heterogeneity. The management of newly diagnosed GBM patients has not changed since the introduction of TMZ in 2005 and, until today, GBM remains an incurable tumour. Thus, given its poor response to current standard treatments, GBM represents an attractive target for immunotherapy.

Within the tumour microenvironment (TME), TAMs are increasingly recognized as critical players in shaping the local microenvironment. In GBM, TAMs constitute up to 40% of the stromal compartment, outnumbering the infiltrating lymphocytes in the TME (Quail and Joyce, 2017). This scarcity of lymphocytes in the tumour microenvironment is in contrast with other tumour types, such as melanoma or lung cancer, therefore classifying GBM into the category of "cold tumours". Hence, due to their substantial number, genomic stability and their ability to infiltrate the tumour, TAMs are being pursued as key targets for the development of novel strategies for GBM patients.

In GBM, TAMs are mainly composed of resident microglia, which colonize the brain early during development giving rise to a unique immune population in the CNS (Ginhoux et al., 2010; Sousa et al., 2017), and monocyte-derived macrophages, which infiltrate the CNS as a result of BBB impairment due to the growing tumour (Hambardzumyan et al., 2016).

Due to significant advances on next generation sequencing techniques, it is currently emerging that these two myeloid cell populations possess different adaptations in the TME, thus immunotherapies which seek to target TAMs indiscriminately may be counterproductive. For example, as TAMs critically depend on CSF-1 for their survival, differentiation and proliferation, murine gliomas tumour burden can be reduced following CSF-1R blockade (Pyonteck et al., 2013). However, clinical trials in GBM patients targeting CSF-1R have not shown increased overall survival (Butowski et al., 2016), suggesting that subsets of TAMs are resistant to CSF-1R inhibition.

It has been shown that microglia and monocyte-derived macrophages react differently to various types of CNS insults (London et al., 2013). Notably, recent studies have uncovered distinct regional abundances of TAMs with a predominance of microglial cells in the invading edge of the tumour, while monocyte-derived macrophages are mainly located in the tumour core (Darmanis et al., 2017; Muller et al., 2017). Moreover, it is starting to emerge that differential *in situ* localization might be related with distinct functional adaptations of these cells in the TME. Recent work revealed that monocyte-derived macrophages are endowed with higher immunosuppressive potential in the tumour core compared to resident microglial cells (Pinton et al., 2019), thus suggesting distinct functional adaptations. Overall, these results are indicative of high levels of heterogeneity among

TAMs and harnessing their functional adaptive features is critical for the development of novel immune therapeutic strategies for GBM patients.

Further, the role of intermediate metabolites of the TCA cycle is emerging as immune modulators and metabolic reprogramming is emerging as a promising strategy to re-educate TAMs in the TME. Recently, ACOD1/IRG1 has been shown to link metabolism to immunity by catalysing itaconate production from cis-aconitate, a tricarboxylic acid (TCA) cycle intermediate (Michelucci et al., 2013). Additionally, it has been shown that itaconate has the potential to skew macrophages towards an anti-inflammatory phenotype (Mills et al., 2018). For example, in sepsis context, itaconate synthesis contributed to immune tolerance in human monocytes (Dominguez-Andres et al., 2019), while promoted tumour growth in peritoneal tumours (Weiss et al., 2018).

In this context, the work presented in this thesis focuses on elucidating TAM diversity in GBM, with a special focus on:

1. TAM education along GBM progression
2. TAM adaptation under ACOD1/IRG1 deficiency
3. TAM functional adaptation across GBM landscapes

Overall, our results contribute to elucidate the transcriptional diversity of TAMs and their diverse functional adaptations within the TME that might be taken into consideration for the design of novel anti-tumour immune strategies in GBM.

CHAPTER 3

MATERIALS & METHODS

3.1. Animals

Adult male and female 8–10 week old C57BL/6N mice (25–30g) and *Acod1* KO C57BL/6N mice were bred in house. For the experiments, heterozygote animals were crossed to generate homozygote *Acod1* KO mice and WT littermate controls, with their genotype confirmed by PCR. Immunodeficient *Nu/Nu Nude* adult females were obtained from Charles River Laboratories (France) and used to generate patient-derived orthotopic xenograft (PDOX) models. Animals were maintained under specific pathogen-free conditions, housed in 12 h light/dark cycle with *ad libitum* access to water and food. The handling of animals was performed in accordance to the Luxembourguish law (based on the European Directive 2010/63/EU) and all animal procedures were approved by the national authorities and the Animal Welfare Structure (AWS) at the LIH.

3.2. GL261 murine glioma cell line

Mouse glioma 261 (GL261) cells were cultured as adherent monolayers in DMEM containing 10% FBS (Gibco/Life Technologies), 2 mM L-Glutamine (ThermoFisher Scientific) and 100 U/ml Pen-Strep (100 U/ml/; Gibco/Life Technologies). Cells were maintained at 37°C in a humidified atmosphere containing 5% CO_2. Upon reaching 80% confluence, GL261 cells were trypsinized with 0.05% Trypsin-EDTA (Gibco/Life Technologies), and total cell number was measured using the Countess Automated Cell Counter (Thermo Scientific). Cell viability was assessed with trypan blue. GL261 cells were tested as mycoplasma free (MycoAlert PLUS Mycoplasma Detection Kit, Westburg, The Netherlands) before mice implantation. For *in vivo* orthotopic implantation, GL261 cells were re-suspended in serum-free medium.

3.3. GBM intracranial models

3.3.1. Syngeneic GL261 orthotopic model

Mice were intraperitoneally (i.p) anesthetized with a mixture of ketamine (100 mg/kg) and xylazine (10 mg/kg) and placed in a stereotactic frame. Subsequent subcutaneous administration of local anhestetic (Marcain 0.25% with Adrenalin) was slowly delivered before GL261 tumour cell

implantation. *In vivo* orthotopic implantation was performed by administrating 1 µl of 500 GL261 cells in the frontal cortex of the brain using a Hamilton syringe (Hamilton, Reno, NV, USA). Mice were monitored weekly for the first 2 weeks and daily from day 15 post-implantation, due to the fast growing tumour. Magnetic resonance imaging (MRI) was performed weekly upon 15 post-implantation to assess tumour volume. When tumours reached early (5-10 mm3), intermediate (20-25 mm3) and late (30-35 mm3) stage of tumour progression, wild type (WT) and age-matched ACOD1/IRG1 knock-out (KO) C57BL/6N mice were sacrificied and the brains isolated for the respective analyses.

3.3.2. Patient-derived orthotopic xenograft models

Human glioma biospies from P8 (invasive tumour phenotype) and P13 (angiogenic tumour phenotype) patients were obtained from Haukeland University Hospital (Bergen, Norway) upon approval of the local ethics committee. 3D organoids from patient biopsies were prepared as previously described (Bougnaud et al., 2016) and the correspondent biopsies were diagnosed as grade 4 GBM IDH wildtype. Tumour biopsies were mechanically minced without enzymatic digestion for the generation of organotypic spheroids, as previously published by the NORLUX Neuro-Oncology Laboratory (Golebiewska et al., 2013). Briefly, the minced tumour pieces were seeded on agar coated flasks, forming spheroids whithin 7-10 days in DMEM 4.5g/L glucose w/o L-glutamine (Lonza) supplemented with 10% Fetal Bovine Serum (FBS) (ThermoFisher Scientific), 10 000U/ml Penicillin and Streptomycin (Pen-Strep) (Sigma-Aldrich), 200mM UltraGlutamine I (Lonza) and 10mM Non-Essential Amino Acid Solution (Lonza). Ressuspended in serum-free medium, viable organoids of approximately 400 – 1000 µm size were collected and used for *in vivo* implantation (6 organoids per mouse) in the right frontal cortex of immunodeficient *Nu/Nu Nude* mice (Charles River Laboratories, France).

3.4. Tumour volume measurement

Tumour volume was measured by Magnetic Resonance Imaging (MRI) on a 3T preclinical horizontal bore scanner (MR Solutions, Guilford, UK), equipped with a quadrature volume coil designed for mouse head imaging. Animals were placed prone in the cradle and maintained asleep during the duration of the scans, using 2-3% isoflurane mixed with oxygen. The body temperature

was kept constant at 37°C and breathing was monitored throughout the scan sessions. Anatomical series were used to screen the animals and calculate tumour volumes. The Fast Spin Echo T2-weighted 2D sequence protocol was used with the following acquisition parameters: TE: 68 ms, TR: 3000 ms, echo train: 8, averages: 4, plane resolution: 256 µm, slice thickness: 1 mm, slices: 15, orientation: coronal. The total scanning time for T2 weighted scan took 6 minutes and 12 seconds. Tumour volume was measured on ImageJ software (NIH, Bethesda, MD, USA) using the polygon selection tool and the delineated area was measured by analysis tool. Tumour volume was measured as the sum of areas obtained by delineating the tumour in each slice and multiplying by slice thickness (1mm).

3.5. Survival analysis

Mice survival analyses were performed according to humane endpoints guidelines, including loss of locomotor activity, weight loss (up to 20%) and central nervous system symptoms. The survival time was measured from the day of tumour cell implantation to the day of euthanasia and median mouse survival time was calculated for each group.

3.6. Single cell RNA-sequencing using Droplet-Sequencing

3.6.1. Tissue collection and dissociation

Mice were deeply i.p anaesthetized with a mixture of ketamine (100 mg/kg) and xylazine (10 mg/kg) and transcardially perfused with ice-cold PBS. Brains were rapidly removed and further tissue processing was performed at 4°C. In sterile conditions, the olfatory bulbs and cerebellum were discarded and either full brain (naïve samples) and tumour core regions (with the exception of the invasive tumour phenotype) were minced with scalpels until few pieces were observed. The respective tissues were collected into 50ml tube containing HBSS w/o Ca2+/Mg2+ (Sigma-Aldrich).

For single cell RNA-sequencing (scRNA-seq) experiments, naïve and tumour-bearing mice from both syngeneic GL261 and GBM PDOX models were used (**Table 2**) and processed accordingly.

Table 2. List of samples used for scRNA-seq using the Droplet-seq methodology.

Syngeneic GL261	Mice strain	Tumour stage	Tumour volume
Naïve	C57BL/6N Immunocompetent mice	*NA*	*NA*
Early		Early	5-10 mm^3
Intermediate		Intermediate	20-25 mm^3
Late		Late	30-35mm^3
PDOX models	**Mice strain**	**Tumour stage**	**Tumour volume**
Naïve	Nu/Nu Immunocompromised mice	*NA*	*NA*
Invasive tumour phenotype		Late	Tumour present in both hemispheres
Angiogenic tumour phenotype		Late	40-50mm^3

NA: not applicable

To obtain a single cell suspension, tissues were dissociated using the Neural Dissociation Kit P (MACS Miltenyi Biotec) following the manufacturer's instructions. Briefly, cell pellets were resuspended in prewarmed EM1 solution (50µl of Enzyme P, 1900µl of Buffer X and 2,5µl of 2-mercaptoethanol) and incubated for 15 minutes at 37°C by reverting the tube every 5 minutes. Next, freshly prepared EM2 solution (20µl of Buffer Y and 10µl of Enzyme A) was added to the cell pellet and tissue was mechanically dissociated as described below.

For the syngeneic GL261 model, the cell suspension was loaded into the "C tubes" of the gentleMACS Dissociator (gentleMACS™ Octo Dissociator with Heaters, Miltenyi Biotec). The following 37C_ABDK_01 program was used to dissociate the brain tissue (>100 mg). Upon centrifugation, the myelin was removed using the Myelin removal beads kit (Myelin Removal Beads II, MACS Miltenyi Biotec) accordingly to the manufacturer's instruction (for 500 mg of tissue). Specifically, the cell suspension was resuspended in 1800 µL of MACS buffer and incubated with 200 µl of myelin Microbeads (MACS Miltenyi Biotec) at 4ºC for 15 min. Cells were washed, centrifuged for 10 min at 300g and suspended in MACS buffer (3 x 1000 µl/mouse brain). The cell suspension was applied into the LS columns (1000µl/each column) and the eluted fraction was collected in 2% of BSA RNAse free solution before Drop-seq loading.

For the GBM PDOX models, the cell suspension was manually dissociated using glass pipettes and incubated for 10 minutes at 37°C, by inverting the tube every 5 minutes. If pieces still remained visible, another mechanical dissociation was repeated and cells were washed with HBSS w/o Ca2+/Mg2+ (Sigma-Aldrich). To distinguish human tumour cells from host murine cells, PDOXs single suspension was FACS-sorted (for the invasive tumour phenotype) or MACS-purified (for the angiogenic tumour phenotype). Regarding the FACS-sorted samples, we separated hCD90 positive human tumour cells from hCD90 negative stromal cells. MACS-purified samples were obtained using

the Myelin removal beads kit (Myelin Removal Beads II, MACS Miltenyi Biotec) accordingly to the manufacturer's instruction, as described above. An additional step was performed using the mouse cell depletion kit (MACS Miltenyi Biotec) following the manufacturer's protocol. Specifically, this step allows for the enrichment of murine stromal cells over human patient tumour cells. Briefly, cell pellet was resuspended in 80µl of cold HBSS with 0.5% BSA (Sigma-Aldrich) and incubated with 20µl of cell depletion cocktail for $1x10^7$ total cells at 4ºC for 15 min. Cells were washed, centrifuged for 10 min at 300g, applied to the LS columns (500µl/each column) and the eluted fraction was collected in 2% BSA RNA-free solution before Drop-seq loading.

Prior to cell loading on the Drop-seq microchips, cellular viability was assessed. All samples analysed in this work had a cell viability above 90-95%. Microfluidic devices were fabricated using a previously published design (Macosko et al., 2015) and subsequent steps, such as cells handling, microfluidics fabrication, single cell droplet encapsulation and next-generation sequencing preparation for Drop-seq libraries were done as previously described (Sousa et al 2018).

3.6.2. Bioinformatic processing

The FASTQ files were assembled from the raw BCL files using Illumina's bcl2fastq converter and ran through the FASTQC codes [Babraham bioinformatics; https://www.bioinformatics.babraham.ac.uk/projects/fastqc/] to check for the consistency in the library qualities. The monitored quality assessment parameters were: a) quality per base sequence (especially for the read 2 of the gene); b) per base N content; c) per base sequence content and d) over-represented sequences. The libraries, which showed significant deviation, were re-sequenced. Then, the FASTQ files were merged and converted to binaries using PICARD's fastqtosam algorithm. We have applied the Drop-seq bioinformatics pipeline (Macosko et al., 2015). The sequencing reads were converted to digital gene expression (DGE) matrix. To normalize for the transcript loading between the beads, the averaged normalized expression levels (log2(TPM+1)) were calculated. To distinguish between cell-containing and empty beads, a cumulative function of the total number of transcripts per barcode was plotted. Then, a threshold was applied empirically on the resulting "knee plot" to estimate the beads exposed to the cell content. For each experimental batch, we retained top 1'000 cell barcodes based on the cumulative distribution, leading to 8'000 cells. We removed low-abundance genes and only genes that were expressed in at least 30 cells were considered for further analysis. We additionally removed cells expressing less than 1'000 genes. Lastly, we concatenated each batch in a single matrix of the following dimensions: 5'659 cells

x 18’338 genes. These pre-analytical filtering steps were processed using R environment with the tidyverse package. The tSNE projection was processed with the Rtsne package with a perplexity = 50, followed by a topological clustering with the library HDBSCAN (Hierarchical DBSCAN with a minimum of 19 points - cells - for a cluster to be considered). We conducted statistical analysis for significant expression between groups using pairwise Wilcoxon test, while p-values were adjusted with Benjamini Hochberg (BH) method.

Single cell trajectory inference analysis was done with Monocle 2 in R (version 3.6.3) using default parameters (Qiu et al., 2017; Trapnell et al., 2014). The branching method orders cells along a trajectory based on gene expression similarities. Monocle 2 uses reversed graph embedding to describe multiple fate decisions in a fully unsupervised manner. Branches in the trajectory represent cell fate decisions through a developmental process.

Data visualization and exploration were performed using the Tableau Desktop software (Seattle, USA). The respective digital gene expression (DGE) matrix generated was integrated into Tableau Prep Builder (Seattle, USA) and the workflow was design in order to generate the Tableau Data Extract hyper file for data visualization. For data dimensionality reduction and heat-maps representation, we used FlowSOM advanced analysis from Cytobank (Santa Clara, CA). Here, we selected the top 40 differentially expressed genes (p-value ≤ 0.01) across the corespondent comparisons, which was further merged in n = 49 clusters and n = 10 metaclusters. The output files were used for the generation of two-way hierarchical heat-maps using the Glucore (version 3.5, Lund, Sweden) software.

3.6.3. Gene Ontology analysis

The DAVID (The Database for Annotation, Visualization and Integrated Discovery) gene functional classification tool (http://david.abcc.ncifcrf.gov) was used to investigate and interpret the respective functional biological terms from the large gene lists of differentially expressed genes (DEGs). Representation of gene ontology (GO) terms enrichment was done on Cytoscape Software (National Institute of General Medical Sciences, https://cytoscape.org/). Each node represents a GO term and the size of each node is proportional to the number of genes from the correspondent query set with that term. Only nodes with p-value < 0.001 were chosen for network representation.

3.7. Adult CD11b+ myeloid cells isolation

Mice were deeply i.p anaesthetized with a mixture of ketamine (100 mg/kg) and xylazine (10 mg/kg) and transcardially perfused with ice-cold PBS. Brains were rapidly removed and the tissue was processed as previoulsy described. Upon tissue dissociation, cells were passed through a 70µm sterile filter and the total number of cells were counted using a hemocytometer. Myeloid cells were enriched by magnetic separation using CD11b+ beads (MACS Miltenyi Biotec). Briefly, 1×10^7 cells were resuspended in 90 µl of PBS supplemented with 0.5% BSA (Sigma-Aldrich) and 2 mM EDTA (MACS buffer) and incubated with 10 µl of CD11b beads (MACS Miltenyi Biotec). The cell suspension was incubated at 4°C for 20 min, washed and pelleted in 500 µl of MACS buffer at a density of 1×10^8 cells. The cell suspension was applied into the LS columns (MACS Miltenyi Biotec) and the CD11b+ fraction was eluted. The purity of CD11b+ isolated cells was analysed by flow cytometry.

3.7.1. Flow cytometry

Enriched CD11b+ populations from tumour-bearing mice were ressuspended in ice-cold flow buffer (HBSS with 2% FBS and 10 mM HEPES) at density of 1×10^6 cells in 100 µl volume. Cell pellets were blocked with Fc receptor binding inhibitor (anti-mouse CD16/CD32 monoclonal antibody; 1:100; eBioscience) for 15 min at 4ºC to reduce binding of non-specific Fc-gamma receptors. After incubation, cells were washed and subsequently stained with 1ug/ml of amine reactive fluorescent dye Zombie NIR (1:1000 dilution in PBS; Biolegend) for 30 minutes at room temperature for dead cell discrimination (with the exception for the unstained tube). Next, fluorochrome-conjugated antibodies were added in flow buffer at 4°C for 30 minutes in the dark (see **Table 3**). Before acquisition, the performance of the instrument was assessed using CS&T beads according to the manufacturer's instructions. Single-stain controls were prepared with UltraComp eBeads (eBioscience) following the manufacturer's instructions and thus used to calculate the compensation matrix. Samples were run on FACSAria Ilu SORP cytometer (Becton Dickinson) and flow cytometry data was analysed using FlowJo software (v. 10.6.1, Becton Dickinson).

Table 3. List of antibodies used for flow cytometry.

Epitope	Conjugate	Clone	Supplier	Dilution	Catalog
mLy6C	PB	HK1.4	Biolegend	0.5µl/test	128014
hCD90	BV605		Biolegend	5µl/test	
mLY6G	BV785	1A8	Biolegend	2.5ul/test	127645
mCD74	FITC	In-1	BD pharmigen	5µl/test	561941

mCD45	FITC	30-F11	eBioscience	1µl/test	
mCD11b	PERCPCY5.5	M1/70	eBioscience	5µl/test	550993
mP2RY12	PE	16007D	eBioscience	5µl/test	848003
mMHC-II	APC	F6-120,1	Biolegend	5µl/test	116418
mC206	APC	C068C2	Biolegend	2.5ul/test	141708
mCD16/CD32	NA	93	eBioscience	1µl/test	14-0161-82
Zombie NIR™ Fixable Viability Kit			Biolegend	0.5µl/test in PBS	23106

3.7.2. Cell proliferation

Ex vivo CD11b+ isolated cells from naïve and tumour-bearing mice were directly seeded in 96-well plate in DMEM-F12 containing 10% FBS (Gibco/Life Technologies) and 100 U/ml Pen-Strep (100 U/ml/; Gibco/Life Technologies). The plates were transferred into the Incucyte ZOOM (Essen Bioscience, MI USA) platform and cells were kept inside the cell incubator at 37°C/5% CO2 for 48h. Cell proliferation was quantified by applying a phase contrast mask enabling the identification of cells/per field. 10X objective was used for imaging acquisition.

3.8. *Ex vivo* functional assays

3.8.1. Transwell migration and invasion assays

Ex vivo CD11b+ migratory abilities were assessed using 8µm pore size boyden chambers (Thincert cell culture inserts, Greiner), fitting into 24-well plate. 100'000 cells were sedeed in the upper part of the boyden chambers in DMEM-F12 medium. Upon 48 hours, cells were fixed in 4% PFA for 15 minutes and washed briefly 2 times in PBS. Cells were stained with DAPI for 15 minutes and washed 2 times in PBS before imaging. Migratory cells were quantiifed by counting the number of cells on the lower side of the membrane under light microscope with a 20x magnifying objective (5 representative fields per membrane). Experiments were conducted in 3 biological replicates (each with 2 technical replicates). The data was normalized according to the respective proliferation index and is represented as percentage of cells that migrated relative to the initial number of cells.

3.8.2. Phagocytic assay

Ex vivo CD11b+ phagocytic abilities were measured using the pHrodo Red *E.coli* bioparticles (Essen Bioscience, MI USA), according to the manufacturer's instructions. Briefly, 100'000 CD11b+ freshly isolated cells were plated into the 96 well-plates in 100ul and left for 2h to adhere. pHrodo Red *E.coli* bioparticles were added at 1 µg/ml and the plates were transferred into the Incucyte ZOOM (Essen Bioscience, MI USA) platform. Four images per well from at least three technical replicates were taken every hour for 48 h using a 10× objective and then analyzed using the IncuCyte Basic Software. Red channel acquisition time was 800 ms and corresponding red channel background noise was subtracted with the Top-Hat method of background non-uniformity correction with a radius of 20 µm. Red fluorescence signal was quantified applying a mask and the parameter red object area was extracted for data analysis and visualization.

3.9. Differentiation of murine bone marrow-derived macrophages and co-culture experiments with GL261 cells

Bone-marrow cells were obtained by flushing the tibia and femurs of WT and *Acod1* KO adult mice. Briefly, mice were euthanized and their legs were removed. Bone marrow precursors were flushed out and cell suspension was further incubated with red blood cells hypotonic lysis buffer. After washing, cells were plated in DMEM media containing 10% FBS supplemented with 20% of L929 supernatant for seven days for full differentiation of bone marrow-derived macrophages (BMDMs).

GL261 and BMDMs were co-cultured in 1:1 mix in DMEM medium containing 10% FBS. GL261 cells were plated on top of 1 µm pore size Boyden chambers (Thincert, Greiner), whereas BMDMs were plated on the bottom of the 6-well plates. RNA was extracted from BMDMs at 0, 24 and 48 hours.

3.10. RNA extraction and RT-qPCR

Total RNA was extracted from BMDMs and freshly isolated CD11b+ cells from naïve and tumour-bearing mice at late stage using the RNeasy Mini Kit (Qiagen, Germantown, MD) according to the manufacturer's instructions. RNA concentration was quantified by NanoDrop (NanoDrop Technologies) and RNA quality was assessed by the quotient of the 28S to 18S ribosomal RNA electropherogram peak using a bioanalyser (Agilent 2100; Agilent Technologies). For cDNA

synthesis, RNA was reverse-transcribed using SuperScript™ III reverse transcriptase (10,000 U; Invitrogen/Life Technologies) with 1 µl (50µM)/reaction oligo(dT)20 (25 µM; Invitrogen/Life Technologies) as primer according to the manufacturer's instructions. Reverse transcription was performed at 50°C for 60 min. Gene expression reaction mixtures contained 2 µl of diluted cDNA, 10 µl of Fast SYBR Green Master Mix (Applied Biosystems/Thermo Fisher Scientific) and 0.5 µl of each 10 µM forward and reverse primers. PCRs were carried out in 384-well plates on a ViiA™ 7 real-time PCR system (Applied Biosystems/Thermo Fisher Scientific) using the following program: 95°C for 20 s, 40 cycles at 95°C for 1 s and 60°C for 20s. Samples were run in triplicates, and the mean Ct (threshold cycle) values were used to calculate the relative amount of product by the ΔΔCt method using 60S ribosomal protein *L27* (Rpl27) as housekeeping gene. The specific primer sequences are listed in **Table 4**.

Table 4. PCR primer pair sequences used in this work.

Gene	PCR primer sequenceS (5'-3')
Acod1	Forward: GCAACATGATGCTCAAGTCTG Reverse: TGCTCCTCCGAATGATACCA
Cd74	Forward: GACCCAGGACCATGTGATGC Reverse: TCCTGGCACTTGGTCAGTACTTTA
H2-Ab1	Forward: TCACTGTGGAGTGGAGGGCA Reverse: GGCAGTCAGGAATTCGGAGC
H2-Aa	Forward: TCTGTGGAGGTGAAGACGAC Reverse: AGGAGCCTCATTGGTAGCTGG
Irf1	Forward: ACTCGAATGCGGATGAGACC Reverse: GCTTTGTATCGGCCTGTGTG
Tyrobp	Forward: ATGCGACTGTTCTTCCGTGA Reverse: TTGTTTCCGGGTCCCTTCC
Trem2	Forward: CTTGCTGGAACCGTCACCAT Reverse: ACAGGATGAAACCTGCCTGGA
Itgax	Forward :TTTGGCTTCCCAGACTTGAAGA Reverse: TGCTGTCACACATGAGGTGC
L27	Forward: ACATTGACGATGGCACCTC Reverse: GCTTGGCGATCTTCTTCTTG

3.11. Immunofluorescence staining and confocal microscopy imaging

Naïve and tumour-bearing brains were isolated as previously described and immediately fixed in PFA for 2 days at room temperature. In order to cryopreserve the tissue quality for further imaging analysis, the brain tissue was further immerged in 30% sucrose solution for two days at room temperature and subsequently stored at -80C. Coronal sections of 12 µm tickness were prepared adopting the standard protocol with minor modifications (Buttini et al., 1999). Briefly,

sections were fixed with PFA 4% during 10 minutes and washed twice with PBS, permeabilised (PBS with 1.5% Triton X-100), blocked (PBS with 5% BSA) and incubated with the following primary antibodies (**Table 5**). Secondary antibodies against the appropriate species were incubated for 2h at room temperature. Cell nuclei were counterstained with Hoechst (1 mg/ml; Sigma). Sections were mounted on glass slides and cover slipped using FluoromountTM Aqueous Mounting Medium (Sigma-Aldrich).

Table 5. List of primary and secondary antibodies used in this study.

Primary	**Host**	**Clone**	**Company**	**Catalog**	**Dilution**
Anti-IBA1	Rabbit	N/A	Biocare Medical	CP 290A	1.1000
Anti-MHC-II	Rat	NIMR-4	Abcam	ab25333	1:00
Anti-CD11c	Mouse	3.9	Abcam	ab11029	1:200
Anti-CD74 FITC	Rat	In-1	BD Pharmingen	561941	1:50
Anti-Irf1	Mouse	E-4	Santa Cruz Biotechnology	sc-514544	1:100
Secondary	**Host**	**Conjugate**	**Company**	**Catalog**	**Dilution**
Anti-Rabbit IgG	Goat/IgG	Alexa Fluor 555	Thermo Fisher	A-11039	1:500
Anti-Mouse IgG	Goat/IgG	Alexa Fluor 647	Thermo Fisher	A-11037	1:500
Anti-Rat IgG	Goat/IgG	Alexa Fluor 488	Thermo Fisher	A-21244	1:500

Fluorescence imaging of the distinct tumour sections was performed by acquiring at least 5 random 40X or 63X confocal images along the tumour margin and the tumour core with a Zeiss LSM880 microscope (Jena, Germany). High-resolution XYZ stack images (1.024 x 1.024 pixels per Z step) were taken with a step size of 0.50 µm. Cell quantifications were peformed using NIH ImageJ software (Bethesda, United States). The number of IBA1 positive cells per field and respective IBA1 surface area were analysed. Surface area measurements were done on Fiji software by applying a threshold (min:40-50; max=255) and random cells per field were selected for surface area measurements. Otherwise mentioned, at least 3 mice per condition were analysed and data from single mouse is represented with a disticnt shape in the graphs. Hoechst staining was used as reference for tumour localization.

3.12. Raw data files

All relevant datasets were merged in a single supplementary file attached to the thesis. We deposited the raw scRNA-seq data from the GL261 analyses in Gene Expression Omnibus (GEO) database under the accession number GSE158016.

3.13. Statistical analysis

Data were analysed using the GraphPad Prism 8 software (GraphPad software, La Jolla, CA, USA) and R environment (R Core Team, Vienna, Austria). Unless otherwise indicated, all data are presented as mean ± standard error of the mean (SEM) of at least three independent biological experiments. Statistical analysis was carried out with GraphPad Prism 8 software (GraphPad software, La Jolla, CA, USA). Differences were considered significantly different at p value <0.05 and were annotated as follows: * $p< 0.05$, ** $p< 0.01$, *** $p< 0.001$ and ns > 0.05.

CHAPTER 4

RESULTS

I. Elucidating tumour-associated microglia/macrophage diversity along Glioblastoma progression and under aconitate decarboxylase 1 deficiency

4.1. Single-cell transcriptomics reveals cellular diversity in naïve and GL261 tumour-bearing wildtype and ACOD1/IRG1 KO mice

To investigate the heterogeneity of the TME in GBM, both at baseline and under ACOD1/IRG1 deficiency along tumour progression, we analysed brain tissue from naïve and GL261 tumour-bearing mice at early (5-10 mm3), intermediate (20-25 mm3) and late (30-35 mm3) stage in wildtype (WT) and age-matched ACOD1/IRG1 knock-out (KO) mice by single cell RNA-sequencing (scRNA-seq) (**Figure 10**). We took advantage of the GL261 syngeneic murine model as a widely used paradigm for immunotherapy studies in GBM (Oh et al., 2014). Importantly, this model allows investigating the TME in immunocompetent mice which, differently from the immunodeficient models, includes an intact lymphocytic compartment.

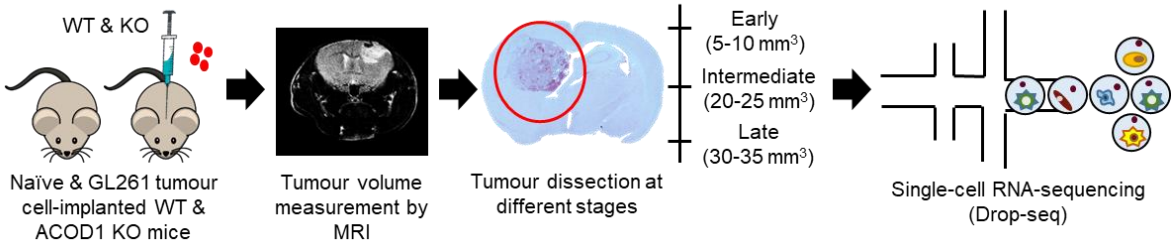

Figure 10. Flowchart depicting the overall design of the study. Naïve- and macro-dissected brain tumour regions from both WT and ACOD1/IRG1 KO mice were processed. Samples were collected at different time points (early: 5-10 mm3; intermediate: 20-25 mm3; late: 30-35 mm3) according to tumour volume measured by MRI. Respective samples were loaded using the Drop-seq methodology for scRNA-seq.

Following pre-analytical filtering of the scRNA-seq experiments, we obtained a matrix composed of 5'659 single cells (n = 18'338 genes). In order to reduce the dimensionality of the matrix, we applied t-Distributed Stochastic Neighbourhood Embedding followed by unsupervised topological clustering with DBSCAN on the 2D projection of the tSNE. We identified 12 cell clusters with distinct gene expression signatures, irrespective of the tumour burden and genotype (**Figure 11A**). We annotated 11 of them (n > 30 cells) based on cell type-specific gene markers (Cahoy et al., 2008; Tasic et al., 2016) and gene set enrichment analysis of up-regulated genes in the

correspondent clusters. Specifically, in addition to tumour cells (*Cd44*+, n = 3'332 cells), we identified 10 stromal clusters that we classified as pericytes (*Dbi*+, n = 61 cells), lymphocytes (*Trac*+, n = 178 cells), ependymal cells (*Ttr*+, n = 73 cells), endothelial cells (*Pecam1*+, n = 328 cells), astrocytes (*Slc1a2*+, n = 289 cells), oligodendrocytes (*Plp1*+, n = 365 cells), oligodendrocyte precursor cells (OPCs, *Pdgfra*+, n = 60 cells), neural stem cells (NSCs, *Meg3*+, n = 36 cells) and myeloid cells 1 and 2 (*Itgam+,* n = 836 cells) (**Figure 11B**).

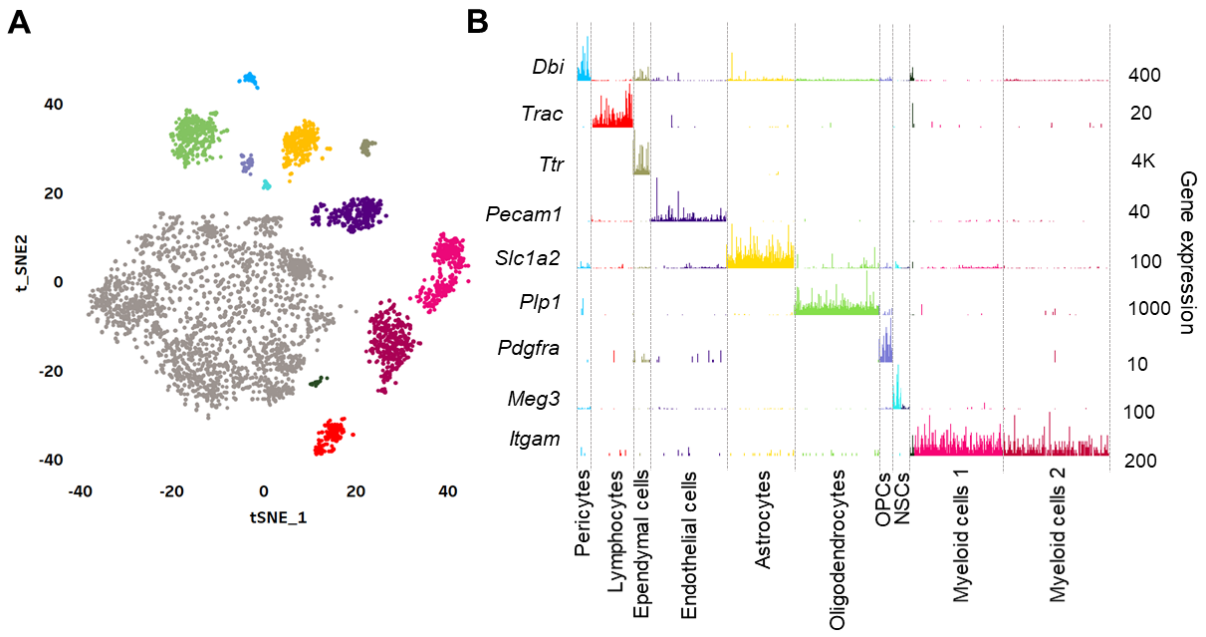

Figure 11. Stromal cell type diversity in naïve and GL261 tumour-bearing mice at different tumour stages, both from wildtype and ACOD1/IRG1 knock-out mice. (A) 2D-tSNE representation of all single cells included in the study (n = 5'659 cells) grouped within 12 cell clusters. **(B)** Cell type-specific markers allowing the identification of stromal cell types: pericytes (*Dbi*), lymphocytes (*Trac*), ependymal cells (*Ttr*), endothelial cells (*Pecam1*), astrocytes (*Slc1a2*), oligodendrocytes (*Plp*1), oligodendrocyte precursor cells (OPCs, *Pdgfra*), neural stem cells (NSCs, *Meg3*), myeloid cells 1 (*Itgam*) and 2 (*Itgam*). See **Figure 12** for additional cell type-specific markers used for clusters annotation.

Cells in the additional small subset (n = 20 cells) expressed myeloid markers (e.g. *Itgam, Aif1*), but clustered independently from the annotated main myeloid clusters (**Figure 11A**). Further, the analyses of additional specific markers provided robust molecular definitions of the major cell types present in the brain of naïve and tumour-bearing mice (**Figure 12**).

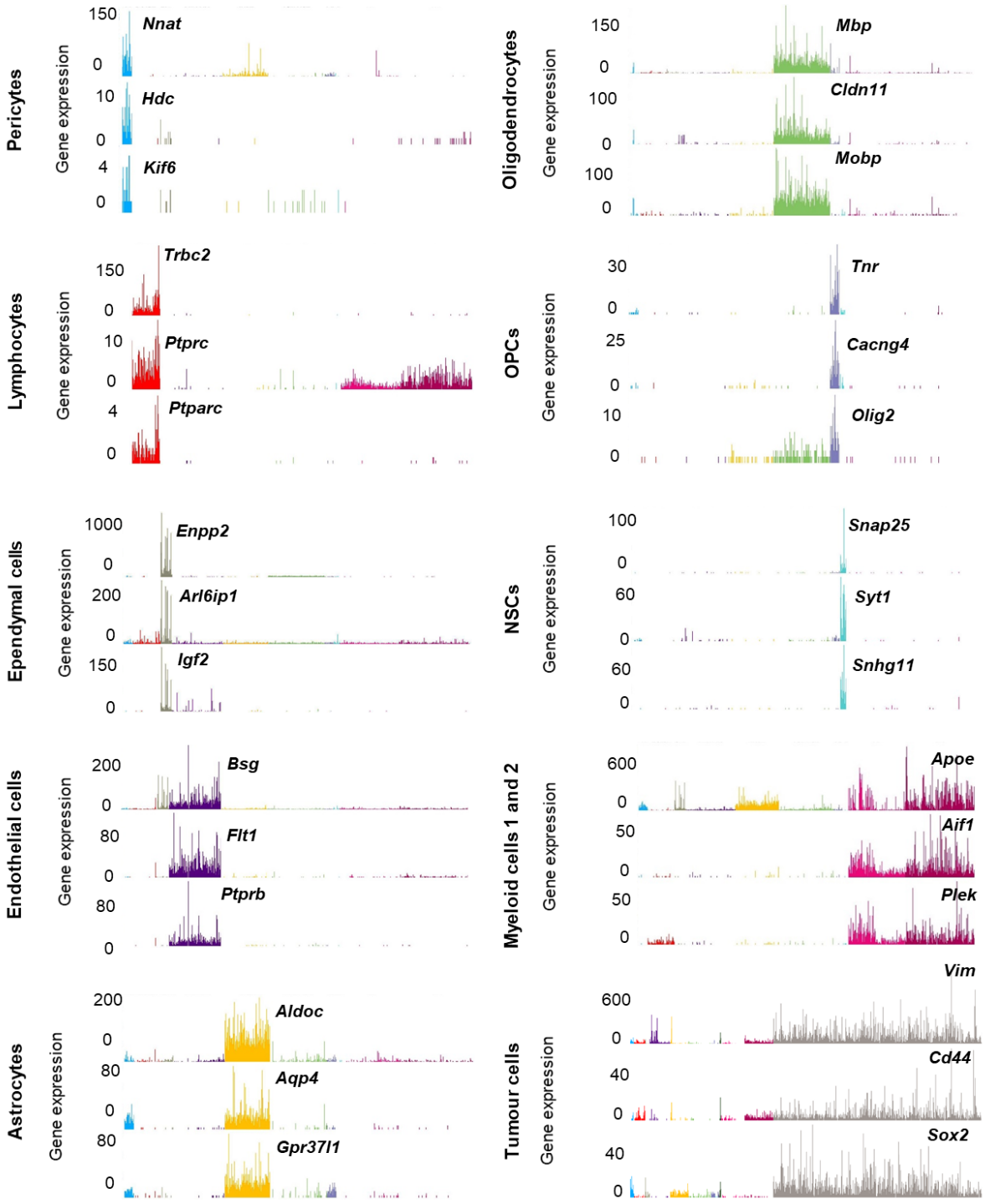

Figure 12. Gene expression levels of distinct cell-type specific markers analysed by scRNA-seq in the GL261 syngeneic murine model and naïve mice. Bar plots of additional cell type-specific markers. Pericytes (*Nnat, Hdc, Kif6*), lymphocytes (*Trbc2, Ptprc, Ptprcap*), ependymal (*Enpp2, Arl6ip1, Igf2*), endothelial (*Bsg, Flt1, Ptprb*), astrocytes (*Aldoc, Aqp4, Gpr37l1*), oligodendrocytes (*Mbp, Cldn11, Mobp*), OPCs (*Tnr, Cacng4, Olig2*), NSCs (*Snap25, Syt1, Snhg11*), myeloid cells 1 and 2 (*Apoe, Aif1, Plek*), tumour cells (*Vim, Cd44, Sox2*) Abbreviations: OPCs, Oligodendrocyte precursor cells; NSCs, Neural stem cells.

Finally, as GBM is an archetypal heterogeneous tumour characterized by a significant extent of common genetic alterations affecting tumour progression (Patel et al., 2014), we verified the expression levels of specific oncogenes in the GL261-implanted mice. In line with previous studies (Szatmari et al., 2006), *Myc* and *Trp53* were the main highly overexpressed genes in tumour cells compared to non-malignant cells (**Figure 13**).

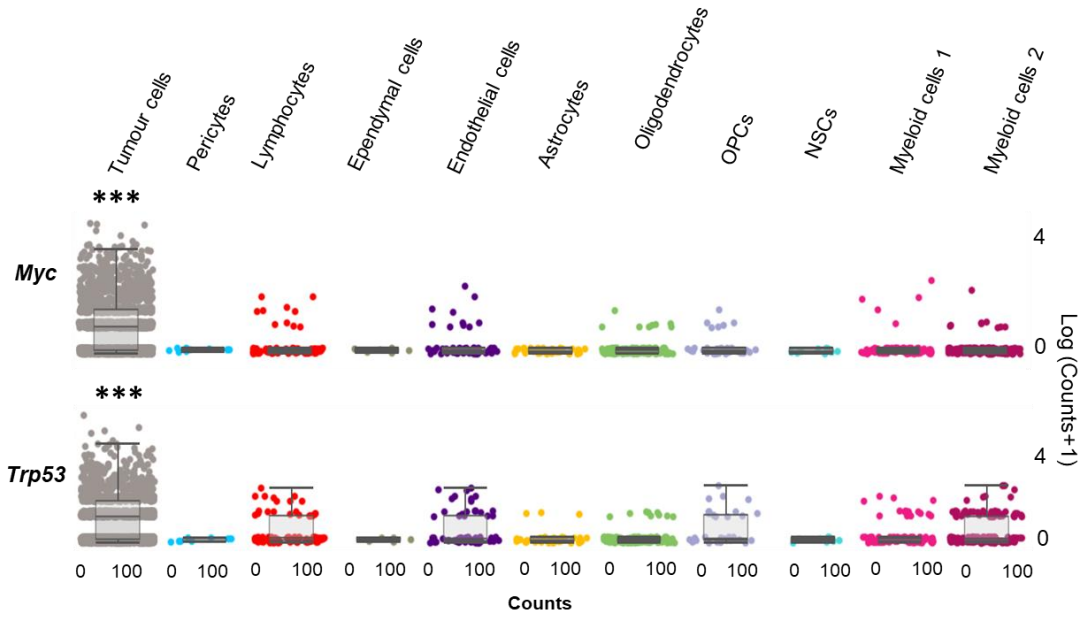

Figure 13. Expression levels of tumour cell oncogenes in the GL261 GBM murine model. *Myc* and *Trp53* gene expression levels across tumour cells and the main 10 stromal cell-types identified by scRNA-seq. Unpaired Student t test. Data are presented as mean ± SEM, *** $p < 0.001$.

Under homeostatic conditions, microglia, endothelial cells, astrocytes and oligodendrocytes represented 83.5% of all cells in the naïve CNS. Pericytes, ependymal cells, neural stem cells and resident macrophages composed the remaining 16.5% of the cells (**Figure 14A-B**). Focusing on the TME, we observed that lymphocytes, OPCs and a subset of myeloid cells were solely present in tumour-bearing mice (**Figure 14A**). Similar to GBM patients, the myeloid compartment constituted the biggest cluster, representing 39.3% in the TME of the GL261 GBM mouse model (**Figure 14B**).

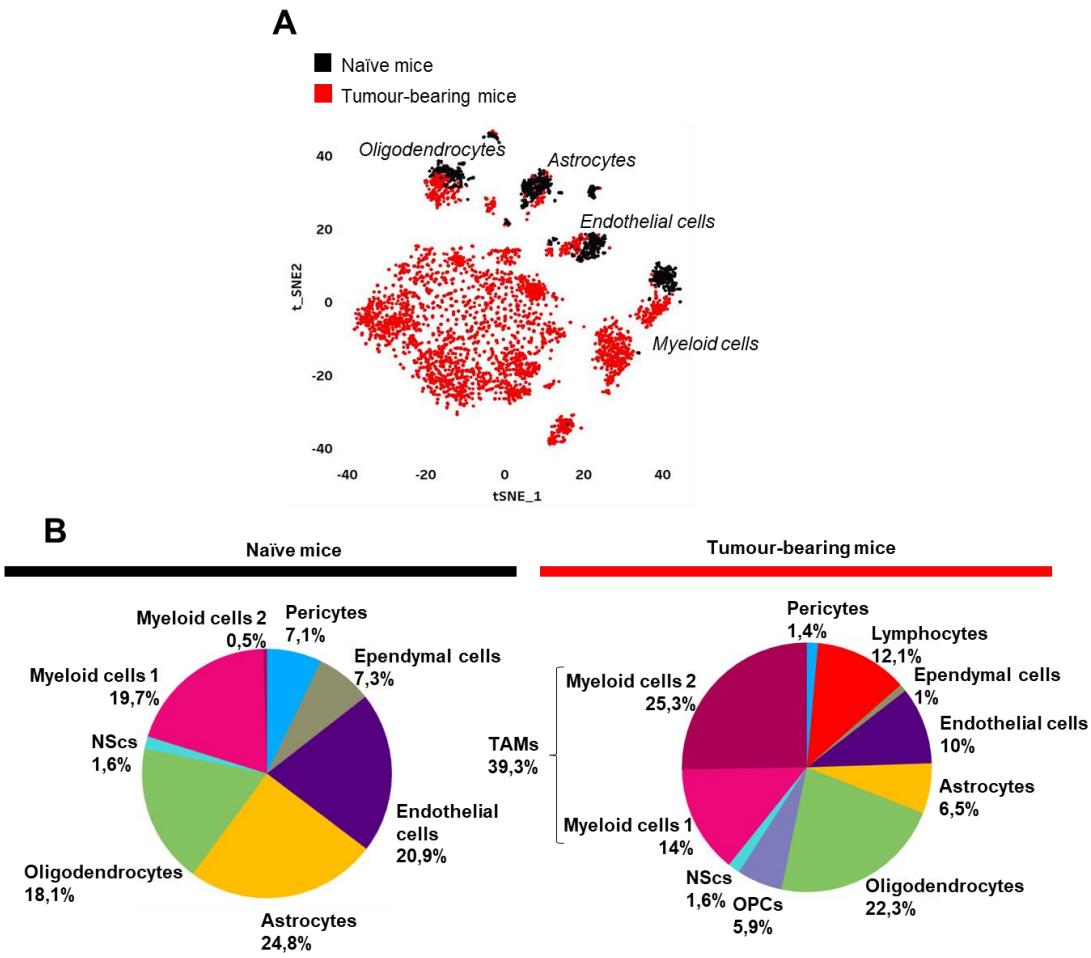

Figure 14. GBM induces the emergence of cells in the TME that are absent in the homeostatic CNS. (A) 2D-tSNE representation showing naïve (in black) and tumour-associated (in red) cells. **(B)** Pie charts representing cell-type proportions of 2'282 isolated cells from naïve mice and 3'377 isolated cells from tumour-bearing mice.

Next, a direct comparison of tumour-associated cells (myeloid cells, endothelial cells, oligodendrocytes and astrocytes) versus the corresponding cells in naïve mice enabled to identify differentially expressed genes (p value < 0.01; log FC > ± 0.5) (**Table S1**). Among them, myeloid cells displayed the highest number of up-regulated genes (n = 574) followed by endothelial cells (n = 178), oligodendrocytes (n = 18) and astrocytes (n = 7) (**Figure 15A**), thus indicating a prominent adaptation of the myeloid compartment in the TME of GBM. Similar findings have been described also in patients (Darmanis et al., 2017; Venteicher et al., 2017).

We detected cell-type specific up-regulated genes across the four CNS resident cells (**Figure 15B**). Notably, all four cell types displayed a shared antigen processing and presentation gene signature (e.g. *H2-D1, H2-K1 and B2m*) (**Table S1**).

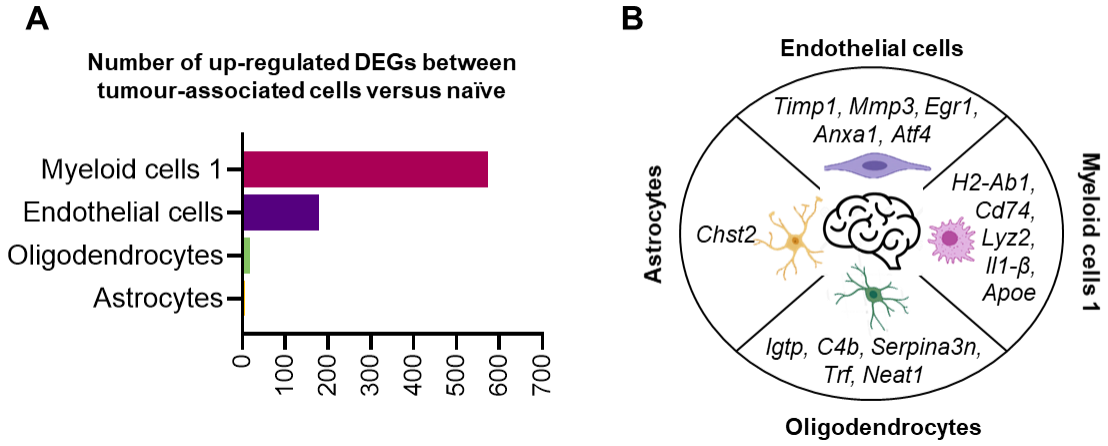

Figure 15. Myeloid cells display prominent transcriptional adaptation in the TME compared to tumour-associated endothelial cells, oligodendrocytes and astrocytes. (A) Up-regulated genes in tumour-associated clusters compared to corresponding naïve cell types (myeloid cells, endothelial cells, oligodendrocytes and astrocytes). (**B**) Examples of the most up-regulated genes (p value < 0.01, logFC > 0.5) per cell type in tumour-bearing mice.

Neo-angiogenesis is an important component of tumorigenesis in GBM and various roles of TAMs contributing to angiogenesis have been described (Zhu et al., 2017). Since TAMs are described to actively contribute to this process, we analysed common differentially expressed genes between myeloid and endothelial cells versus the correspondent naïve cells (**Table S2**). We observed common genes involved in angiogenesis (e.g., *Anxa2, Spp1*, *Gpx1, Itgb1, Ncl, Mmp14, Ptgs2, Nr4a1, Vim and Junb*), indicating that TAMs participate to local angiogenesis in GBM. Additionally, we observed that more than 90 genes (e.g. *Cd74, B2m, Calr, H2-K1, H2-d1, H2-Q7, Psmb1*, *Psmb8, Cd63* and *Junb*) were up-regulated in both tumour-associated endothelial and myeloid cells (**Table S2**), indicating that the endothelial compartment is also an active immune modulator of the TME in GBM.

4.2. Tumour-associated myeloid cells in Glioblastoma are heterogeneous and display distinct transcriptional programmes

In GBM, resident parenchymal microglia are difficult to segregate from peripheral infiltrative immune cells, which prevalently constitute the myeloid compartment of the TME. Thus, we took advantage of our scRNA-seq dataset obtained in WT mice to analyse the expression of known microglia and monocyte-derived macrophage markers across naïve and the two TAM subsets

identified by 2D-tSNE (**Figure 16A**). Naïve and TAM I clusters showed high expression levels of the microglia homeostatic genes (e.g. *Gpr34, Hexb, P2ry12, Siglech, Sparc*), while these genes were almost undetectable (except *Hexb*) in the TAM II cluster. Accordingly, the TAM II cluster exhibited high levels of macrophage markers (e.g. *Arg1, Ccr2, Ly6c2, Mrc1, Tgfbi*) (**Figure 16B**). These observations were supported by flow cytometry analyses of the macro-dissected tumour region to discriminate CD11b+ P2RY12+ from CD11b+ P2RY12-/low cells (**Figure 16C**). Compared to naïve mice, where more than 90% of CD11b+ cells were P2RY12+ resident microglial cells, the percentage of CD11b+ P2RY12+ cells in tumour-bearing mice was significantly reduced (mean 58.16 ± 5.6 %) (**Figure 16C-D**).

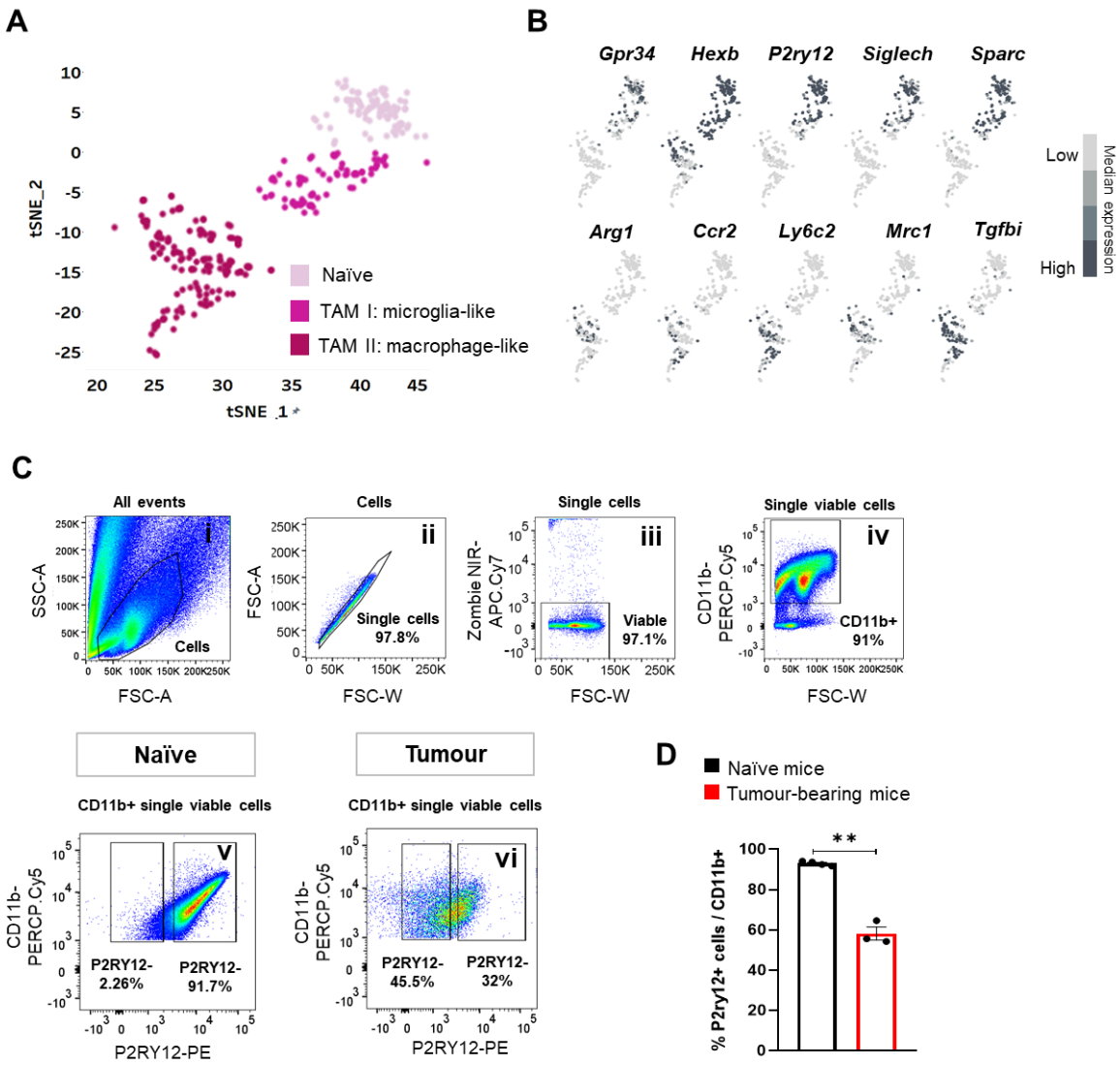

Figure 16. Microglia- (TAM I) and macrophage-like (TAM II) subsets identification in naïve and tumour-bearing mice. (A) Colour-coded 2D-tSNE representation showing three distinct myeloid

cell subsets in WT mice: naïve, TAM I and TAM II clusters. **(B)** 2D-tSNE representation showing the expression of microglia homeostatic genes (*Gpr34*, *Hexb*, *P2ry12*, *Siglech* and *Sparc*) and macrophage-like markers (*Arg1, Ccr2, Ly6c2, Mrc1 and Tgfbi*). **(C)** Representative flow cytometry gating strategy. (i) Cells of interest were gated based on forward (FSC) and side scatter (SSC). (ii) Doublets were excluded based on the forward scatter height (FSC-H) versus forward scatter 1016 area (FSC-A). (iii) Zombie NIR-APC.Cy7 was used to discriminate living cells. (iv) CD11b-PERCP.Cy5 was used to gate the myeloid compartment. Lastly, we gated P2RY12- and P2RY12+ expressing cells in (v) naïve and (vi) tumour samples. **(D)** Percentage of CD11b+ P2RY12+ cells in naïve (n = 4) and tumour-bearing mice (n = 3) quantified by flow cytometry in naïve (black) and tumour-bearing mice (red) (1 biological replicate). Bars represent mean ± SEM, ** $p < 0.01$.

The presence of heterogeneous TAM subsets in GBM was further supported by the overall higher number of differentially expressed genes between naïve microglia and tumour-associated monocytes/macrophages (up = 943 genes, down = 111 genes) compared to tumour-associated microglia (up = 574 genes, down = 17 genes) (**Figure 17A, Table S3**).

Hierarchical clustering based on the top 40 differentially expressed genes with the lowest p-value between naïve, microglia- and macrophage-like cells (**Table S4**) revealed, in agreement with their different ontogeny, a less pronounced difference between naïve and tumour-associated microglia compared to the monocyte/macrophage cluster (**Figure 17B**). In line with the decrease of homeostatic genes in microglia under inflammatory conditions (Sousa et al., 2018), TAM I cells displayed a decreased expression of these genes (e.g. *Siglech, P2ry12, Gpr34*, *Sparc, Mef2c, Olfml3*) in the tumour when compared to the naïve group (**Figure 17B**).

Notably, we further detected two subsets with distinct transcriptional profiles representing both TAM I and TAM II populations that we latterly attributed to different tumour stages. Specifically, the main difference between TAM I subsets relied on the differential expression of the microglia homeostatic genes, while TAM II subpopulations differently up-regulated genes associated with antigen presentation (e.g. *H2-Aa, Cd74*), positive regulation of angiogenesis (e.g. *Lgals3, Il1β, Cybb, Thbs1, Plek, Vim, Stat1*) and metabolic redox metabolism (e.g. *Cybb, Msrb1*) (**Figure 17B**). Overall, these results point towards the heterogeneous composition of TAMs and their distinct adaptation profiles in the TME of GBM.

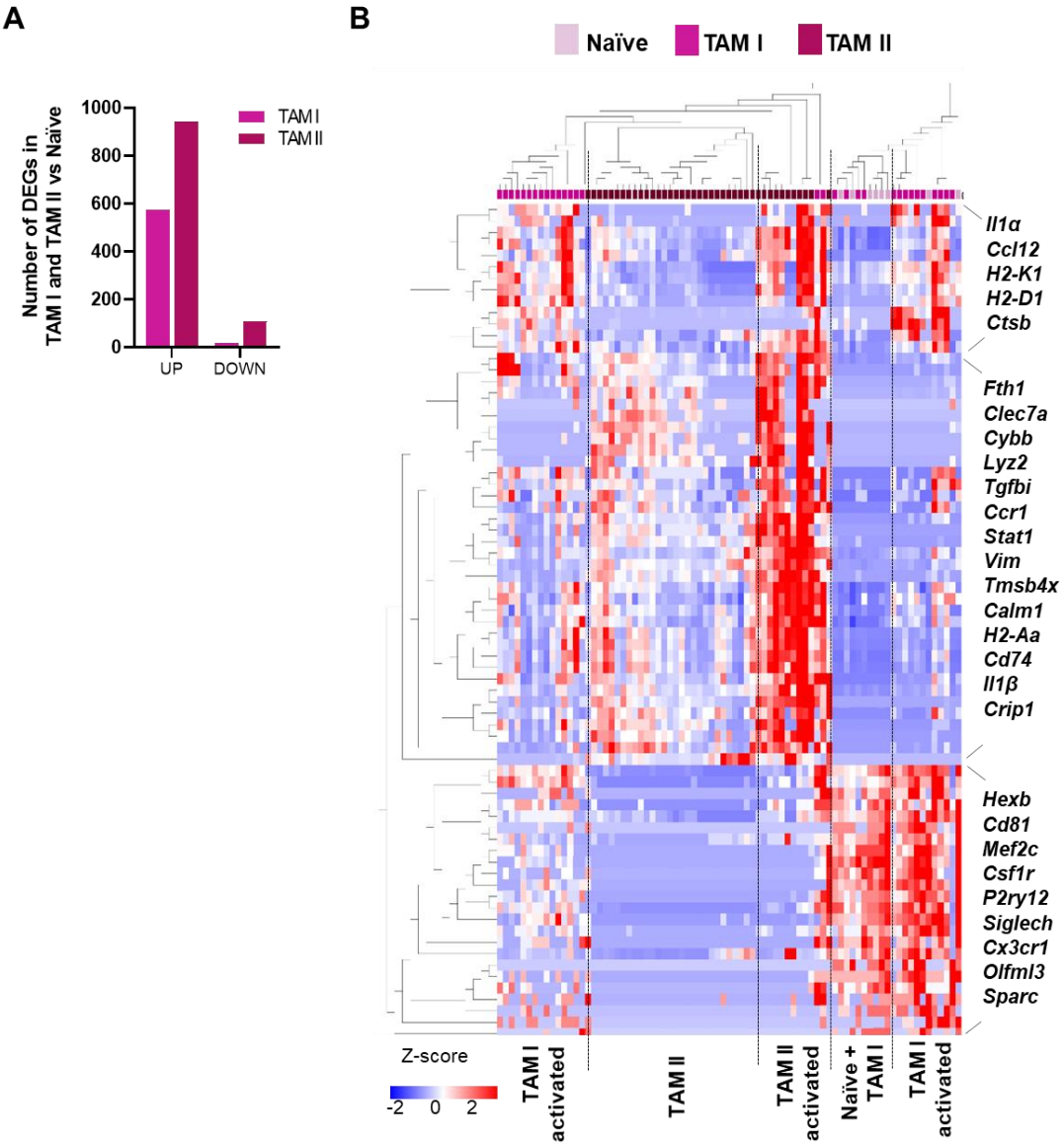

Figure 17. Myeloid cells display heterogeneous transcriptional adaptation in GBM. (A) Number of differentially expressed genes for TAM I versus naïve (n = 574 up-regulated; n = 17 down-regulated) and for TAM II versus naïve (n = 943 up-regulated; n = 110 down-regulated). **(B)** Heat-map representation of two-way hierarchical clustering analyses of the top 40 differentially expressed genes based on the p-value rank (rows) for each myeloid cluster: naïve, TAM I and TAM II (columns). Genes represented were present at least in one of the three comparisons (TAM I versus naïve; TAM II versus naïve and TAM I versus TAM II, **Table S4)**. Red: up-regulation; blue: down-regulation.

Gene set enrichment analysis of tumour-associated microglia or tumour-associated-monocyte/macrophage transcriptional programs revealed immunological terms shared by both cell types (e.g. inflammatory response and innate immune response). We also identified terms specifically associated with TAM I (e.g. positive regulation of phagocytosis and T cell mediated

cytotoxicity) or TAM II (e.g. positive regulation of cell migration and oxidation-reduction process), suggesting distinct ontogeny-based functional adaptations to the tumour (**Figure 18**).

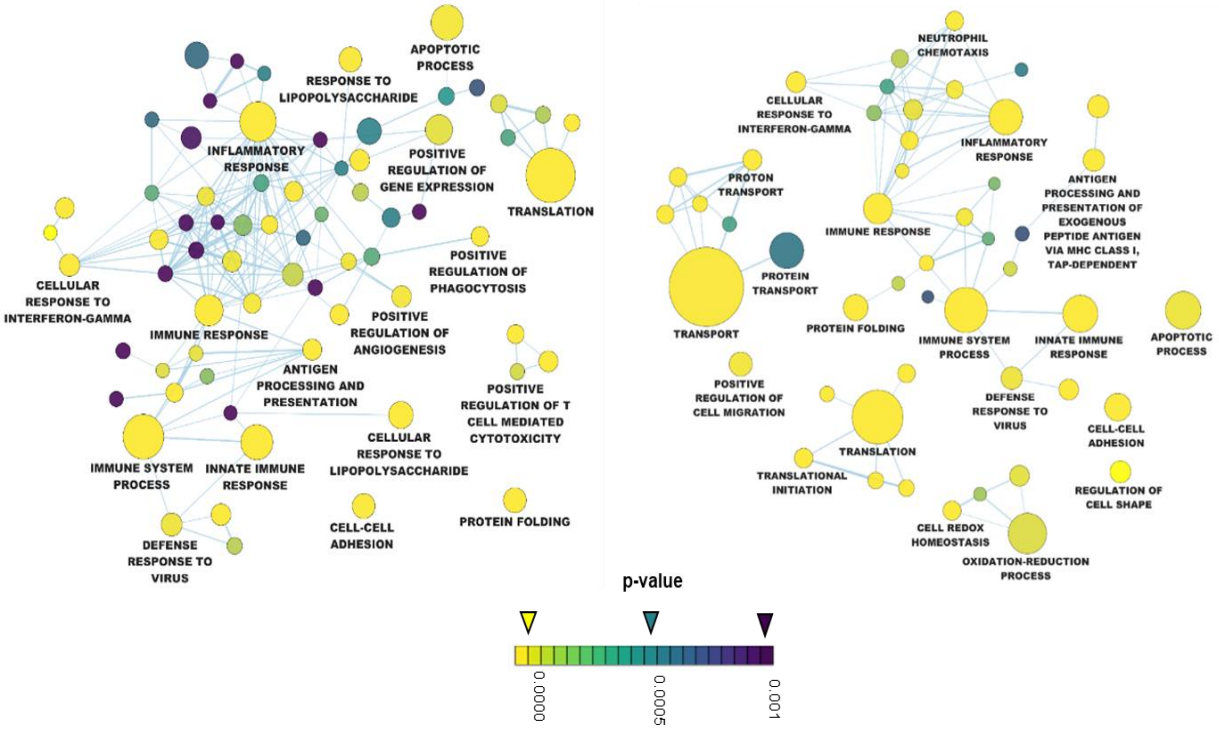

Figure 18. Microglia- (TAM I) and macrophage-like (TAM II) subsets display discrete functional adaptation in the GBM syngeneic GL261 murine model. Gene ontology functional network of TAM I (left graph) and TAM II (right graph) versus naïve microglia. Node size correlates to gene set numbers and annotated nodes were defined as containing ≥ 15 genes.

We take advantage of this critical distinction to separately characterizing tumour-associated microglia and macrophage subsets along GBM progression.

4.3. Tumour-associated microglia/macrophages rapidly infiltrate the tumour and adapt along Glioblastoma progression

By studying TAM heterogeneity along GBM progression in WT mice at single-cell resolution, we detected microglia-like and macrophage-like cell subsets across all the analysed tumour stages (i.e. early, intermediate and late time points), indicating that, in agreement with prior observations (Bowman et al., 2016), in this model the infiltration of monocyte-derived macrophages occurs early during tumour growth (**Figure 19A**). Notably, we observed a gradual decrease in the number of up-regulated genes (early n = 372, intermediate n = 291 and late n = 143) and a relatively constant

number of down-regulated genes (early n = 138; intermediate n = 110 and late n = 167) between macrophage-like and microglia-like cells along tumour stages. These results indicate that the transcriptional programs of microglia and peripheral infiltrated macrophages converge over time (**Figure 19B**), suggesting a context-dependent symbiosis mechanism along GBM progression. Overall, the ratios of microglia-like and macrophage-like cells in the GBM TME did not significantly change across early (TAM I: 29,35%; TAM II: 70,65%) and late (TAM I: 24,43%; TAM II: 75,57%) stages (**Figure 19C**).

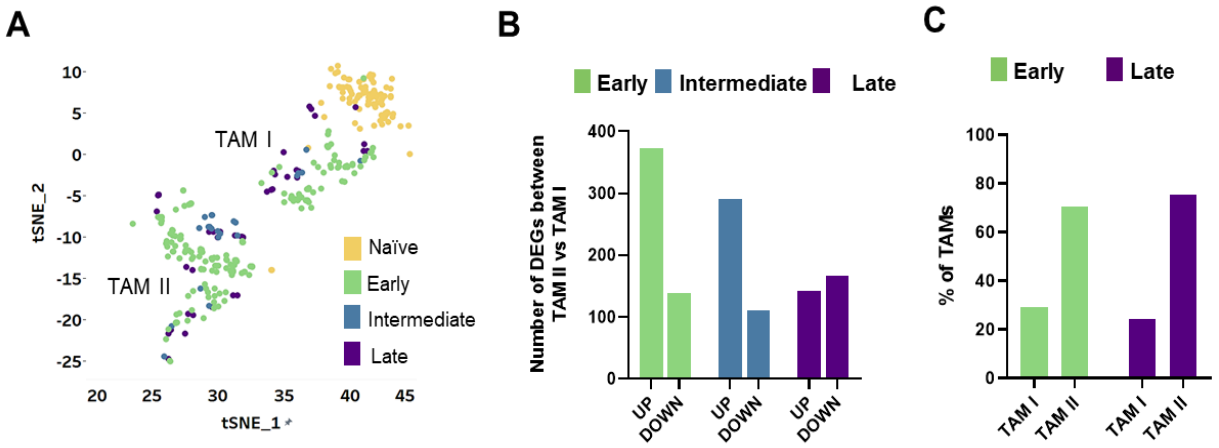

Figure 19. TAM subsets characterisation along Glioblastoma development. (A) tSNE plot showing myeloid cells along tumour progression (green: early; blue: intermediate; purple: late stage). **(B)** Number of up-regulated and down-regulated genes (p-value <0.01, FC > ± 0.5) between TAM II and TAM I along GBM progression. **(C)** Relative proportions of TAM I and TAM II subsets at early and late GBM stages obtained by scRNA-seq analysis.

Focusing on TAM I subset, hierarchical clustering based on the top 40 differentially expressed genes with the lowest p value across the tumour stages revealed three clusters mainly represented by naïve microglia, tumour-associated microglia at early/intermediate time points and a late-enriched group (**Figure 20A**, **Table S5**). Thus, we sought to investigate microglia-like cell transcriptional programmes along tumour progression separately, with a special focus at early and late stages (**Figure 20B and C**).

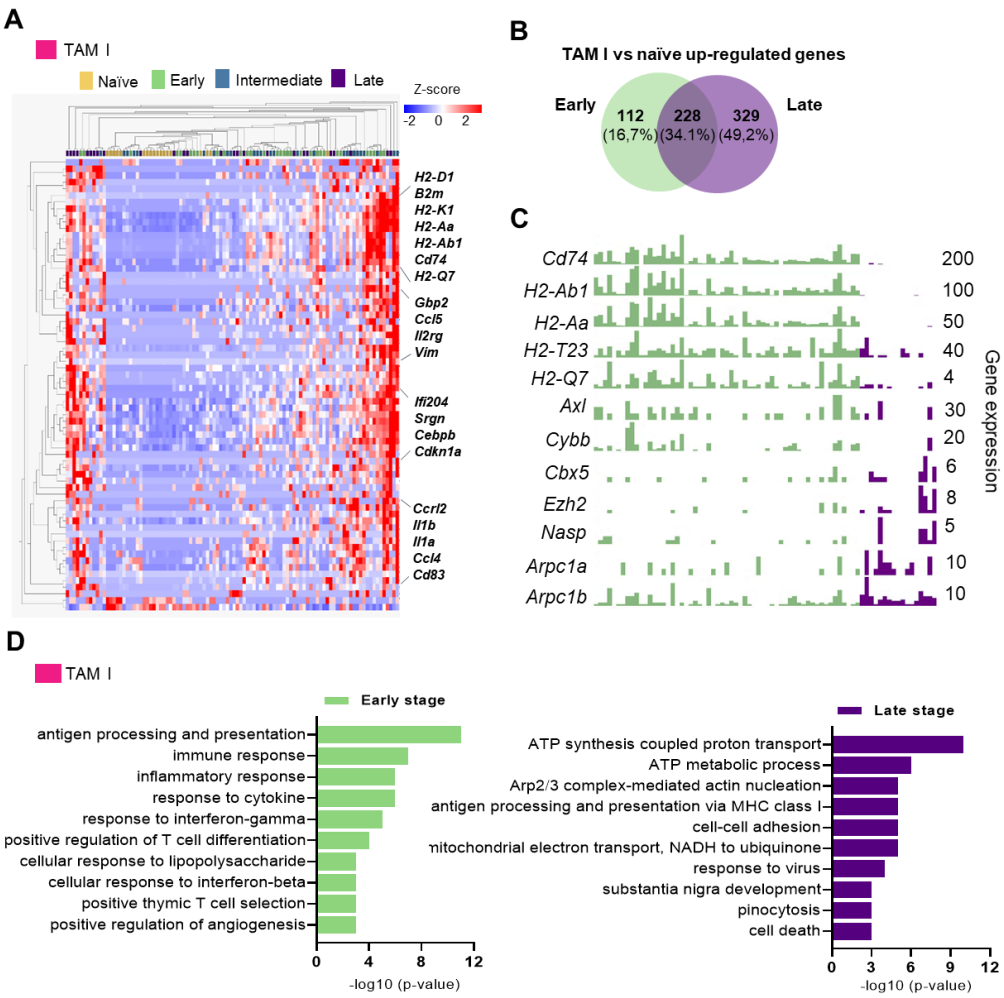

Figure 20. Differential microglia transcriptional adaptation along GBM progression. (A) Two-way hierarchical heat-map clustering analyses of the most differentially expressed genes (based on p-value rank) in TAM I along tumour progression. Red: up-regulation; blue: down-regulation. **(B)** Venn diagram representation showing TAM I shared (n = 228) and exclusively up-regulated genes at early (n = 112) and late (n = 329) stages versus naïve microglia. **(C)** Single-cell bar plots showing selected top differentially expressed genes in TAM I between early and late GBM stages. **(D)** Gene ontology terms of TAM I exclusive up-regulated genes at early (left) and late (right) GBM stages.

We found great overlap (34.1%) of genes expressed by microglia-like cells between the two stages (e.g. *H2-D1, H2-K1, Cd83, Il1b, Ccl12, Ccl4, Lyz2, Fth1, Ctsb, Atf3, Cst7, B2m, Cd52, Nfkbia*), indicating a core transcriptional programme maintained along GBM progression. When comparing the levels of specific differentially expressed genes between early (n = 112) and late (n = 329) tumour stages, markers associated with antigen processing and presentation (e.g. *Cd74, H2-Ab1, H2-Aa*) or T-cell activation and cytotoxicity (e.g. *H2-T23, H2-Q7*) and inflammatory response (e.g. *Axl, Cybb*) were largely decreased at later tumour stages (**Figure 20C-D**). In parallel, genes

associated with chromatin remodelling (e.g. *Cbx5, Ezh2, Nasp*) and actin nucleation/polymerization (e.g. *Arpc1a, Arpc1b*) were enhanced at later stages (**Figure 20C-D**).

Next, we conducted similar analyses for the macrophage-like subset. Unsupervised clustering of the top 40 differentially expressed genes along the tumour stages revealed a less pronounced separation of the clusters across tumour stages compared to microglia-like cells, probably due to the strong transcriptional differences between naïve microglia and the overall TAM II subset (**Figure 21A**, **Table S6**).

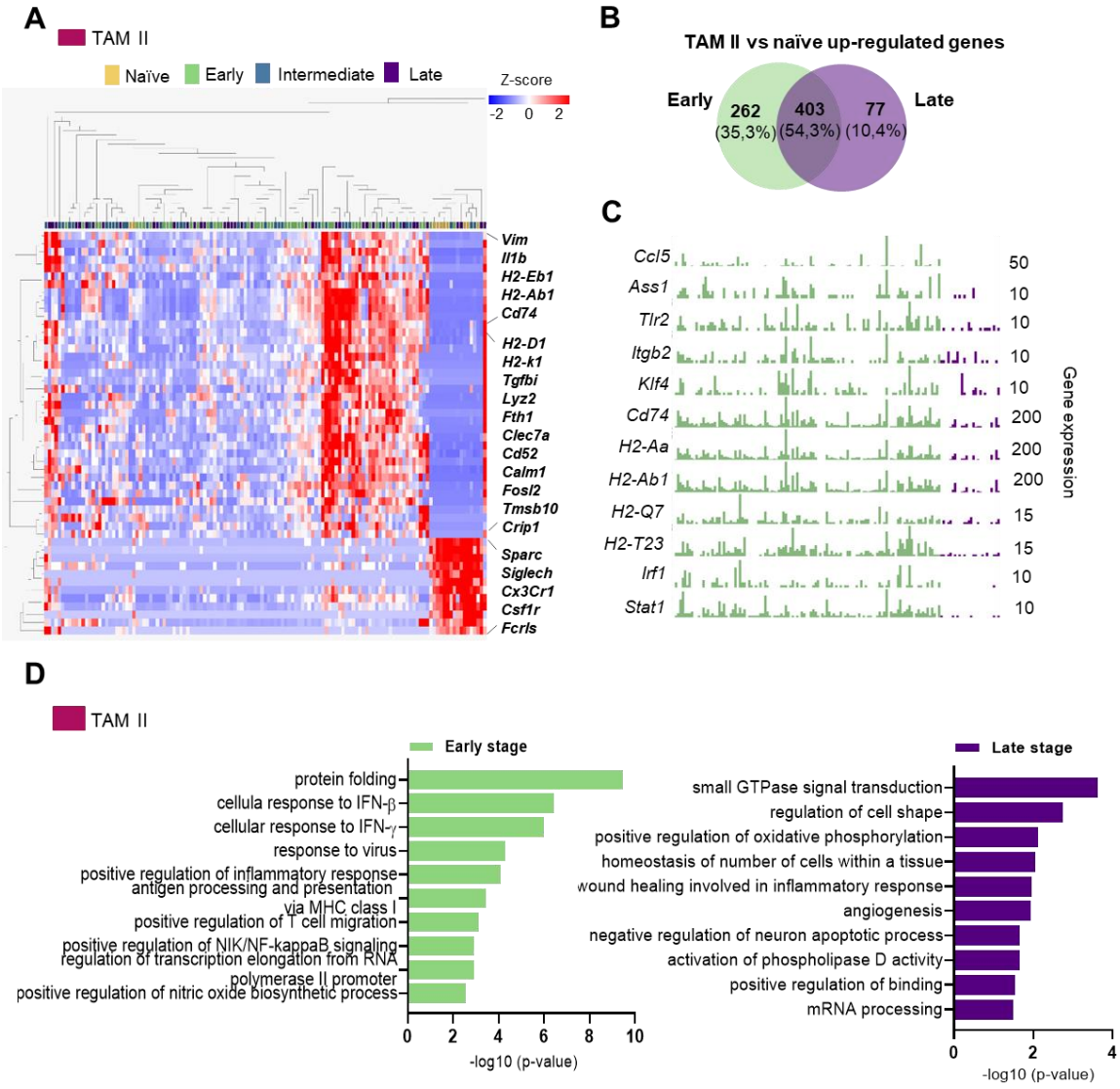

Figure 21. Differential macrophage transcriptional adaptation along GBM progression. (A) Two-way hierarchical heat-map clustering analyses of the most differentially expressed genes (based on p-value rank) in TAM II along tumour progression. Red: up-regulation; blue: down-regulation. **(B)** Venn diagram representation showing TAM II shared (n = 403) and exclusively up-regulated genes at early (n = 262) and late (n = 77) stages versus naïve microglia. **(C)** Single-cell

bar plots showing selected top differentially expressed genes in TAM II between early and late GBM stages. **(D)** Gene ontology terms of TAM II exclusive up-regulated genes at early (left) and late (right) GBM stages.

We found prominent overlap (54.3%) of genes up-regulated both at early and late tumour stages expressed by macrophage-like cells compared to naïve microglia (e.g. *Lyz2, Apoe, Fth1, Il1β, H2-K1, H2-D1, Vim, Cd14, Cybb, Tgfbi*) indicating, similarly to microglia-like cells, a main transcriptional programme preserved along GBM progression (**Figure 21B**). The comparison of the levels of specific differentially expressed genes between early and late tumour stages revealed the decrease of macrophage activation markers (e.g. *Ccl5, Ass1, Tlr2, Itgb2, Klf4*) as well as, similarly to microglia-like cells, the down-regulation of genes associated with antigen processing and presentation (e.g. *Cd74, H2-Ab1, H2-Aa*) and regulation of T-helper cells (e.g. *H2-Q7, H2-T23*). In addition, type I interferon genes (e.g. *Irf1, Stat1*) were drastically reduced at late stage (**Figure 21C-D**). Moreover, exclusive gene ontology (GO) terms associated with positive regulation of oxidative phosphorylation, wound healing together with angiogenesis were present at late stage (**Figure 21D**).

To corroborate these results at the protein level, we compared the expression levels of CD74 and MHC-II (encoded by *H2-Ab1*) at early and late stages in corresponding tissue sections. To discriminate brain-resident microglia and peripheral monocytes/macrophages in immunohistological analyses, we took advantage of the Ivy Glioblastoma Atlas Project to infer TAM spatial localization in laser-micro-dissected regions of GBM patients (Puchalski et al., 2018). Here, we observed an enrichment of microglia-like cells (expressing *BIN1, CX3CR1, P2RY12*) at the leading edge of the tumour, while macrophage-like cells (expressing *IL1RN, TGFBI, THBS1*) were mostly detected in the microvascular compartment (**Figure 22A**). Recent work applying 2-photon microscopy in murine GBM sections revealed two distinct cell types with different morphological properties composing TAMs. Specifically, reduced branching and increased surface area compared to naïve, resident parenchymal cells mainly accumulated at the tumour margins and represented tumour-associated microglia, while BMDMs displaying shrank surface area were mainly located in the tumour core (Chen et al., 2019). In agreement with this, we observed a significant reduction of the surface area of macrophage-like cells in the tumour core compared to larger and branched microglia-like enriched cells in the tumour margin independent of tumour stage (**Figure 22B-D**).

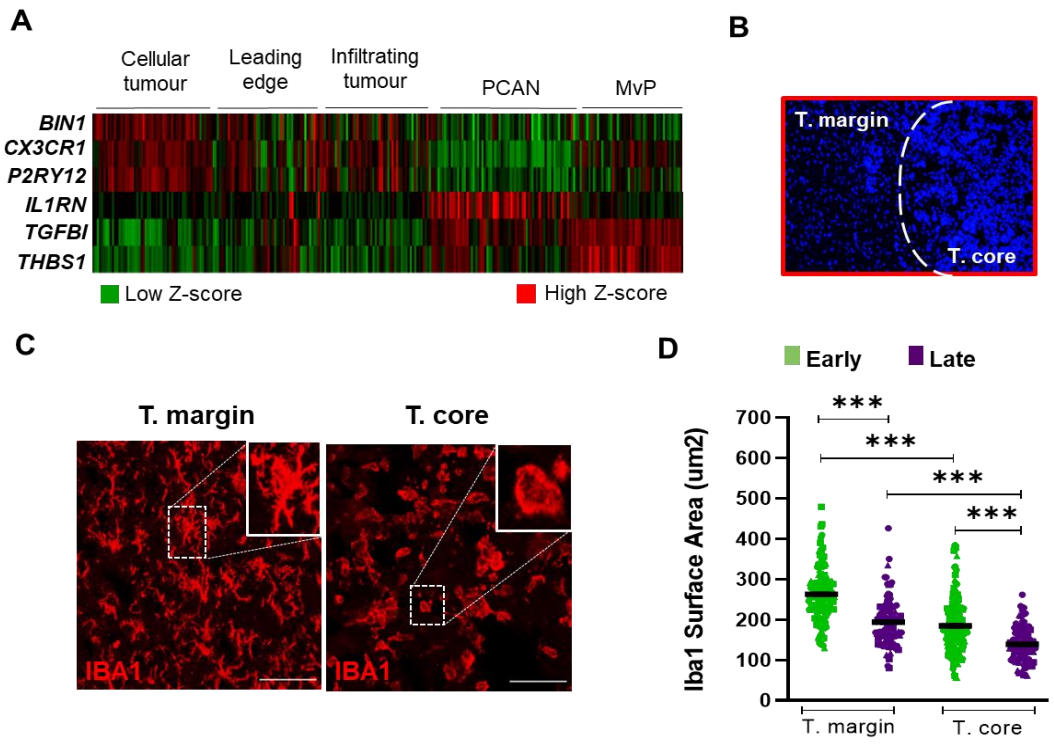

Figure 22. Spatial and temporal morphological characterization of microglia and macrophages in GBM. (A) RNA-seq profiles of laser-micro dissected regions of GBM patients for microglia (*BIN1, CX3CR1, P2RY12*) and peripheral monocyte-derived macrophage (*IL1RN, TGFBI, THBSI*) marker genes. Data extracted from the Ivy Glioblastoma Atlas Project (PCAN: pseudopalisading cells around necrosis; MvP: microvascular proliferation). **(B)** Picture representing Hoechst-stained nuclei used to discriminate tumour margin and core in mouse brain sections. **(C)** Representative immunofluorescence pictures of IBA1 positive cells in the tumour margin and core in murine brain sections. Scale bar = 50µm. **(D)** Quantification of IBA1 surface area in the tumour margin and tumour core at early (n = 3) and late (n = 3) stages. Two-way ANOVA with Sidak's multiple comparison corrections (1 biological replicate). Data are presented as mean ± SEM, *** $p < 0.001$.

In line with our scRNA-seq data, we observed a significant decrease of the antigen presenting cell markers MHC-II (**Figure 23A**) and CD74 (**Figure 23B**) at late GBM stage in both the tumour margin and core. These results further support the notion that TAMs at late stage show a reduced immune reactive profile.

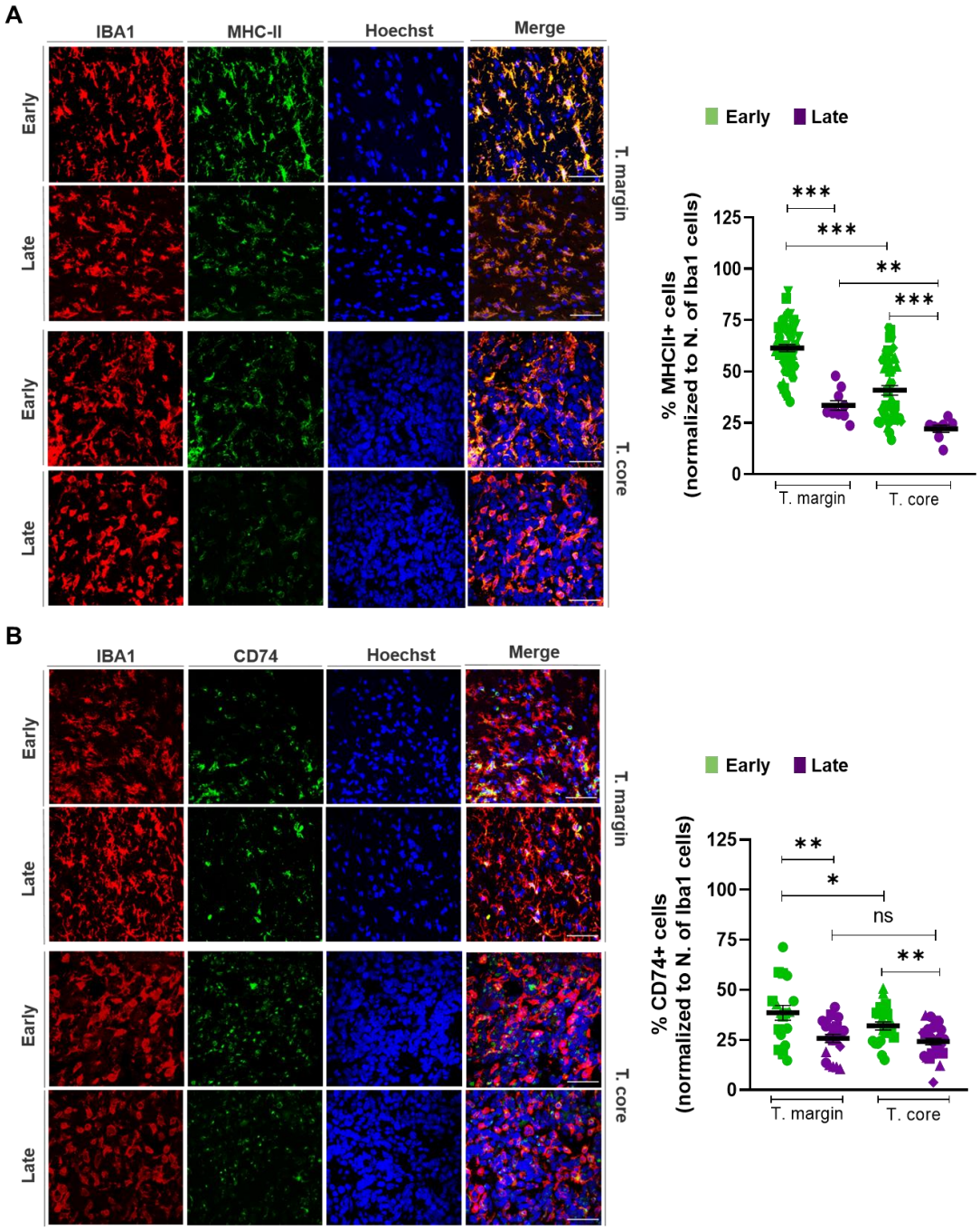

Figure 23. TAM subsets spatial and temporal characterisation along GBM development. (A-B) Representative immunofluorescence pictures and quantification for **(A)** MHC-II and **(B)** CD74 staining in the tumour margin and core at early ($n \geq 3$) and late (late $n = 4$) stages. Two-way ANOVA with Sidak's multiple comparison corrections (1 biological replicate). Data are presented as mean ± SEM, * $p < 0.05$; ** $p < 0.01$; *** $p < 0.001$; ns > 0.05. Scale bars in A and B = 50µm.

Notably, we observed a higher percentage of IBA1+ MHC-II+ cells in the tumour margin compared to tumour core both at early and late stages (**Figure 23A**), indicating that microglia-like

cells express higher levels of antigen presenting cell markers when compared to macrophage-like cells in the TME.

To strengthen our findings obtained in the GL261 syngeneic mouse model, we compared microglia-like (TAM I) and monocyte/macrophage-like (TAM II) transcriptional signatures with putative corresponding cell types recently described in GBM patients at single-cell resolution (Muller et al., 2017) (**Table S7**). Overall, 8.6% of up-regulated genes in TAM I ($p < 0.01$; Log FC > 0.5) were shared with tumour-associated microglia-like cells in GBM patients. In addition, 7% of differentially expressed genes characterizing TAM II ($p < 0.01$; Log FC > 0.5) were mutually up-regulated in blood monocyte-derived macrophage-like cells in GBM patients (**Figure 24A**).

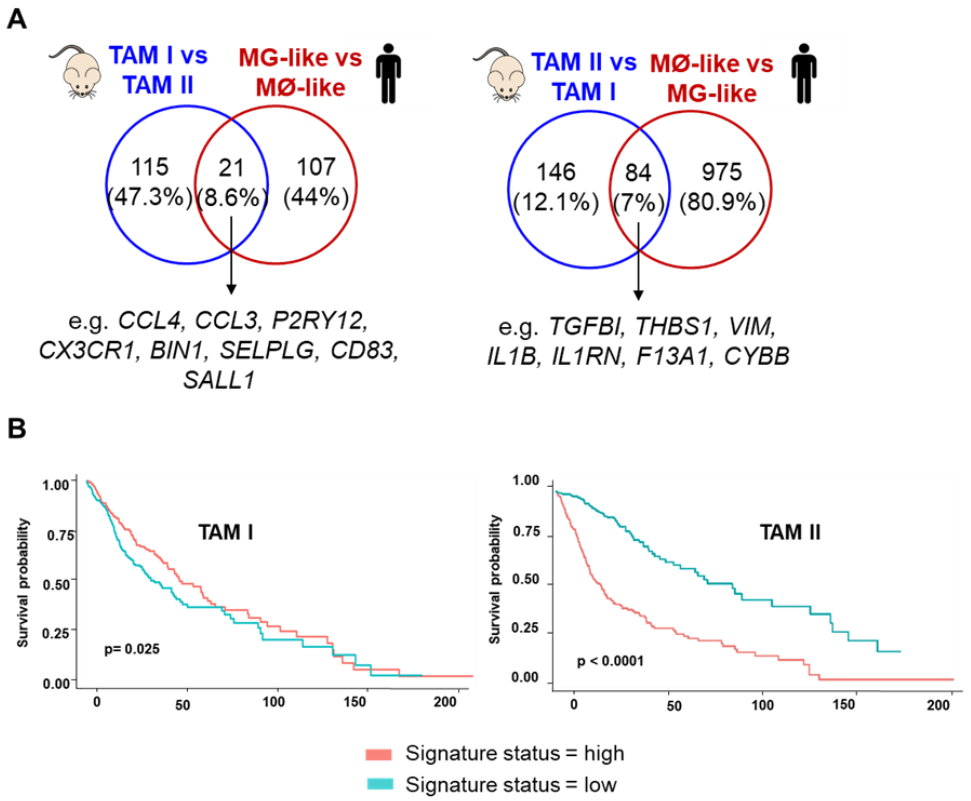

Figure 24. TAM transcriptional signatures predict GBM patient survival. (A) Comparison of up-regulated genes in microglia-like (TAM I) and macrophage-like (TAM II) cells with putative corresponding cell types described in GBM patients (Muller et al., 2017). Shared and unique genes are represented in Venn diagrams and a selection of genes is annotated (see **Table S7** for full gene lists). **(B)** Kaplan-Meier survival analysis in GBM patients (TCGA-LGG and TCGA-GBM databases) with high and low TAM I or TAM II enriched signatures.

This comparison enabled to identify robust transcriptional signatures maintained across the two species allowing discriminating tumour-associated microglia (e.g. *CCL4, CCL3, P2RY12,*

CX3CR1, BIN1, SELPLG, CD83, SALL1) and tumour-associated macrophages (e.g. *TGFBI, THBS1, VIM, IL1B, IL1RN, F13A1, CYBB*) both in the GBM syngeneic murine model and in patients (**Table S7**). We used the characterized transcriptional signatures to verify their prognostic value in GBM patients. For this, we took advantage of The Cancer Genome Atlas (TCGA) datasets allowing to link patient survival with corresponding bulk transcriptional data from two publicly available TCGA-databases (TCGA-GBM: high grade glioma and TCGA-LGG: low grade glioma). Notably, a macrophage-like-enriched signature correlated with a worse patient survival compared to a microglia-like-enhanced programme supporting the notion that tumour-associated microglia may possess effective immunological functionality, while tumour-associated macrophages display an immune-suppressed pro-tumorigenic phenotype (**Figure 24B**).

4.4. Tumour-associated microglia/macrophages display higher immunological reactivity under aconitate decarboxylase 1 deficiency affecting T cell recruitment

In mammals, immune-responsive gene 1 protein (IRG1), encoded by aconitate decarboxylase 1/immunoresponsive gene 1 (*Acod1/Irg1*), catalyses the production of itaconate from the decarboxylation of cis-aconitate, an intermediate metabolite of the TCA cycle (Cordes et al., 2016; Michelucci et al., 2013). Interestingly, it has been recently shown that low doses of itaconate inhibit inflammation, while itaconate promotes inflammation at high doses (Muri et al., 2020). Due to the emerging role of itaconate in macrophage reprogramming towards specific phenotypes, we sought to analyse the role of *Acod1/Irg1* in TAM adaptation along GBM progression and characterize TAM subsets under ACOD1 deficiency at single cell resolution.

Taking advantage of the Brain Tumour Immune Micro Environment dataset acquired in GBM patients by RNA-seq, we observed that *ACOD1/IRG1* expression was up-regulated in both CD49D^{low} microglial cells and CD49D^{high} macrophages. Additionally, higher expression levels were detected in IDH-wildtype compared to IDH-mutant gliomas (**Figure 25A**) (Klemm et al., 2020). In the GL261 model, we exclusively detected *Acod1/Irg1* induction across the myeloid compartment and, at a larger extent, within the macrophage-like subset (**Figure 25B**).

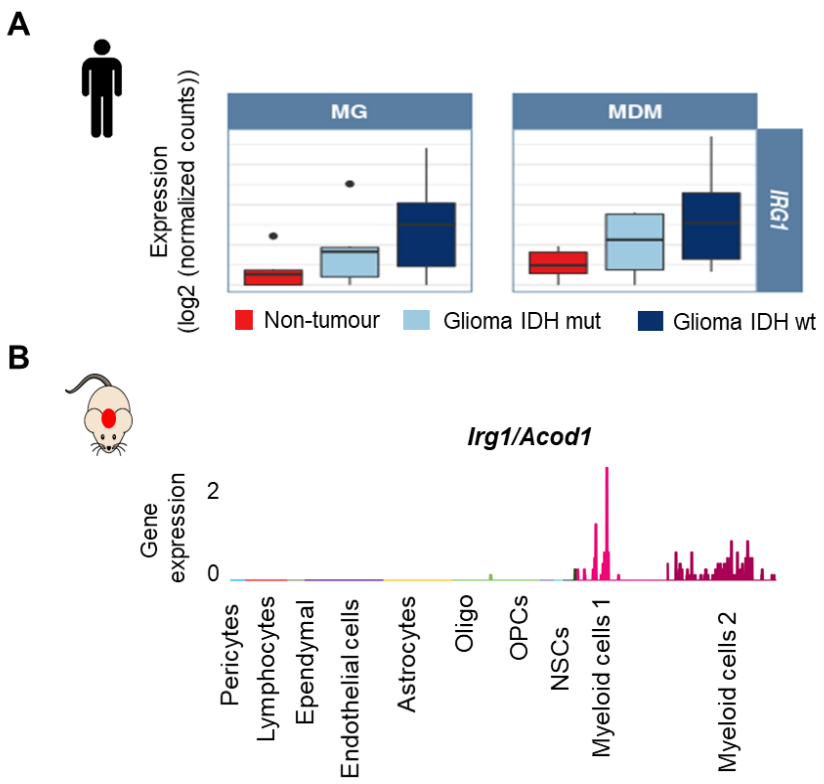

Figure 25. IRG1/ACOD1 expression is induced in myeloid cells of GBM patients and GL261 mouse model. (A) *IRG1/ACOD1* expression in both microglia (MG) and macrophages (MDM) in GBM patients from the Brain Tumor Immune Micro Environment dataset (Klemm et al., 2020). **(B)** *Irg1/Acod1* expression levels across the main 10 stromal cell-types identified by scRNA-seq.

In our hands, *Acod1/Irg1* was mainly induced by a subset of myeloid cells at early stages, while its expression was reduced at later tumour stages (**Figure 26A**), indicating a time-dependent expression of *Acod1/Irg1* in myeloid cells in GBM. BMDMs co-cultured with GL261 tumour cells *in vitro* showed time-dependent expression of *Acod1*, while its expression was undetectable in BMDMs obtained from *Acod1* KO mice (**Figure 26B**). Similarly to LPS stimulation (Dominguez-Andres et al., 2019; Michelucci et al., 2013), the expression of *Acod1/Irg1* was mainly induced at earlier (24h) compared to later (48h) time points (**Figure 26B**).

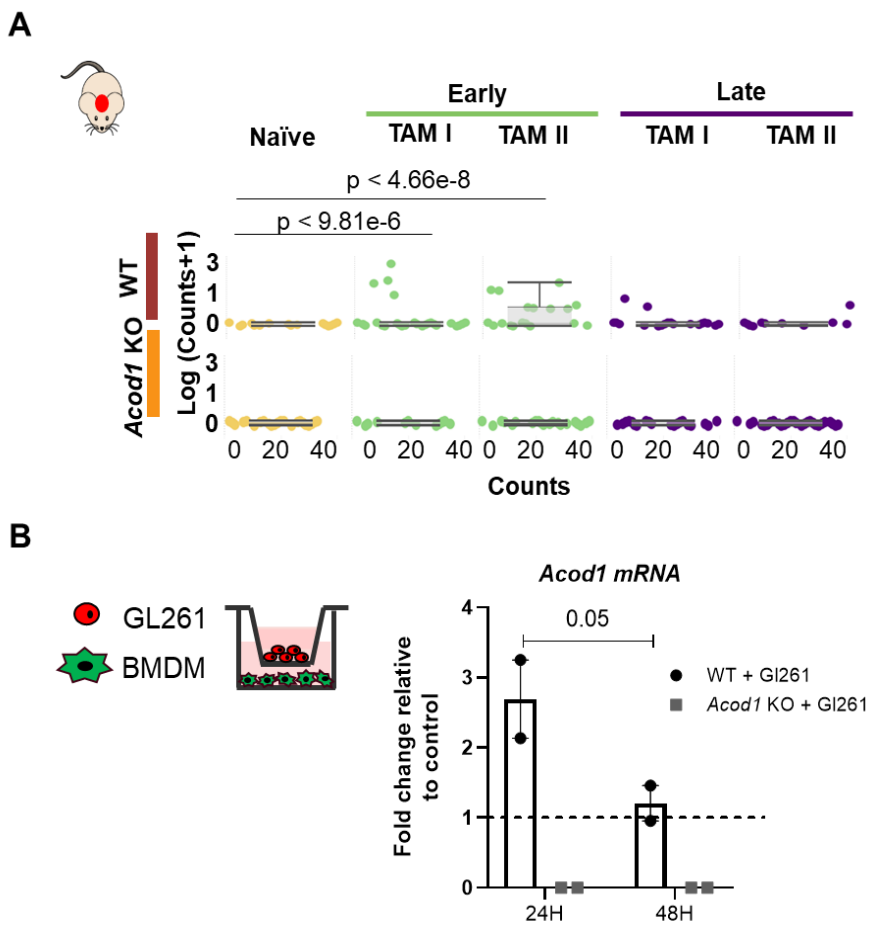

Figure 26. Time-dependent induction of *Acod1/Irg1* in myeloid cells in GBM. (A) *Acod1* expression levels in naïve and tumour-bearing TAM I (logFC 0,44) and TAM II (logFC 0,46) cells at early and late stage of GBM progression by scRNA-seq. **(B)** Expression levels of *Acod1* gene in BMDMs from WT and *Acod1* KO mice upon co-culture with GL261 tumour cells at 24 and 48h (WT = 2, *Acod1* KO n= 2) (1 biological replicate). Dash line represents baseline expression at time zero. Data are presented as mean ± SEM, ns > 0.05.

The analysis of TAM subsets by scRNA-seq suggested an over-representation of the macrophage-like population in *Acod1* KO mice (81.15%) compared to age-matched WT mice (63.11%) (**Figure 27A**). Albeit we did not detect differences in the total number of BMDM precursors between naïve WT and *Acod1* KO mice (**Figure 27B**), we observed an increase in the number of CD11b+ cells in tumour-bearing brain of *Acod1* KO compared to WT tumour-bearing mice (**Figure 27C**).

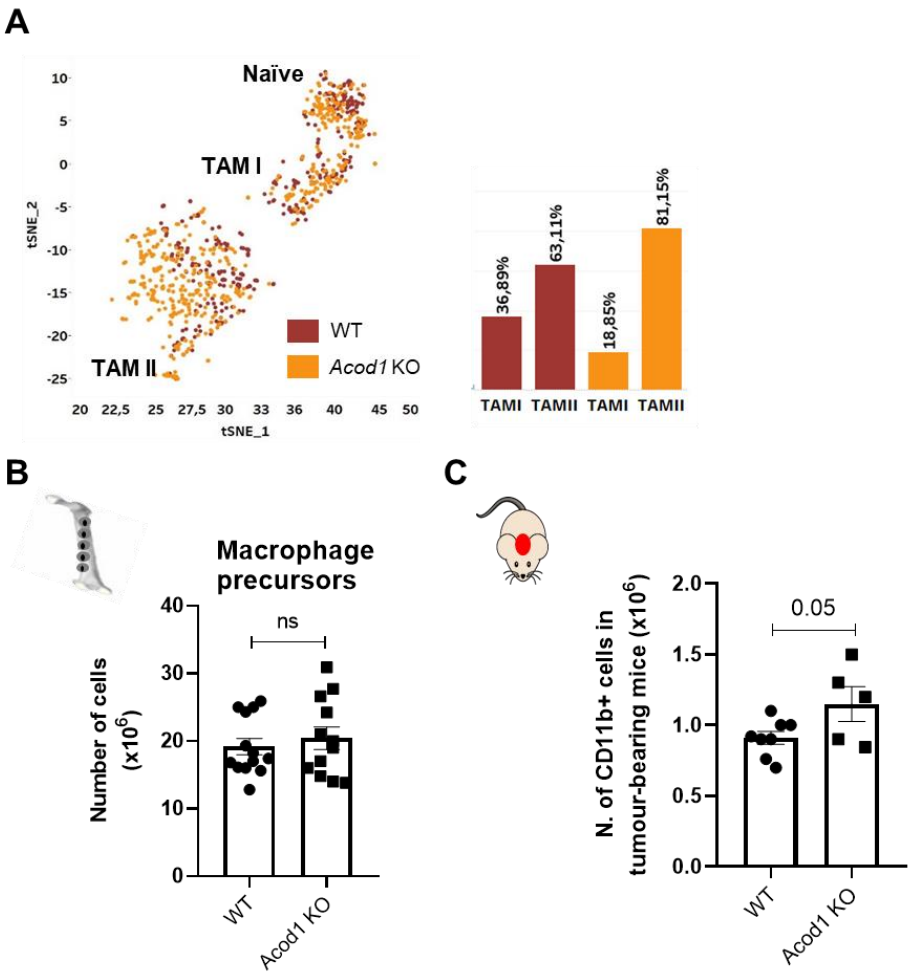

Figure 27. *Acod1*-deficient tumour-bearing mice display higher recruitment of TAMs. (A) tSNE plot showing colour coded (brown: WT; orange: *Acod1* KO) myeloid cells and respective percentages of microglia-like and macrophage-like cells according to the genotype. **(B)** Total number of bone marrow precursor cells flushed from the legs of WT (n = 13) and *Acod1* KO (n = 12) mice. Unpaired Student t test. **(C)** Total number of CD11b+ cells isolated from WT (n = 8) and *Acod1* KO (n = 5) tumour-bearing mouse brains at late stage. Unpaired Student t test (1 biological replicate). Data are presented as mean ± SEM, ns > 0.05.

Indeed, immunofluorescence analyses revealed a significant increase in the number of IBA1+ cells at early stages at both the tumour margin and core, thus confirming enhanced myeloid cells recruitment to the tumour site in *Acod1* KO mice (**Figure 28**).

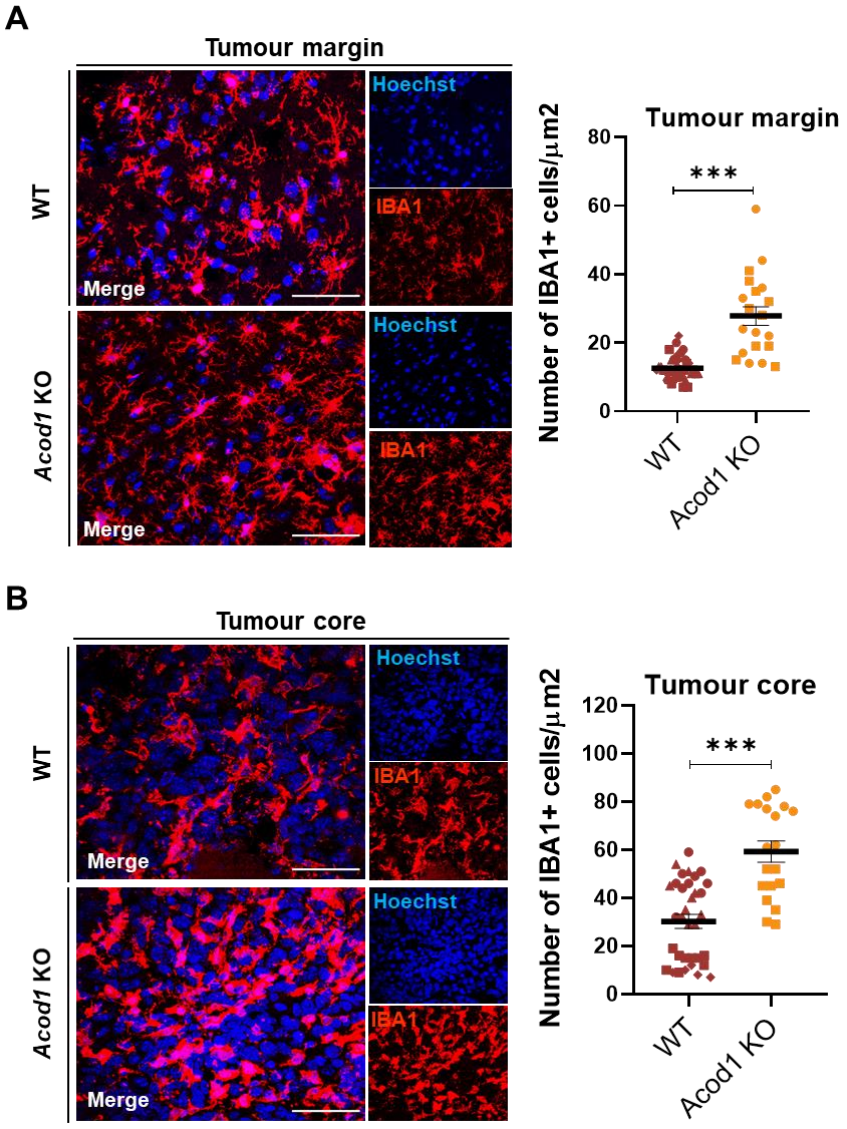

Figure 28. *Acod1* deficiency affects TAM recruitment to the tumour site. (A-B) Immunofluorescence pictures depicting IBA1 positive cells in **(A)** the tumour margin and **(B)** tumour core in tumour-bearing brain sections. Number of IBA1 positive cells were quantified in WT (n = 4) and *Acod1* KO (n ≥ 2) mice at early GBM stage. Unpaired Student t test (1 biological replicate). Data are presented as mean ± SEM. *** $p < 0.001$. Scale bars = 50µm.

Investigation of the exclusively up-regulated genes in microglia-like and macrophage-like cells at early stages in *Acod1* KO mice versus their corresponding counterparts in WT mice identified a major transcriptional effect on macrophage-like (n = 41 genes) compared to microglia-like (n = 3 genes) cells (**Figure 29A**, **Table S8**). Genes associated with TAM recruitment, such as *Ccr2, Mif, Ldha and Tspo*, were uniquely overexpressed in macrophage-like cells from *Acod1* KO mice (**Figure 29B**).

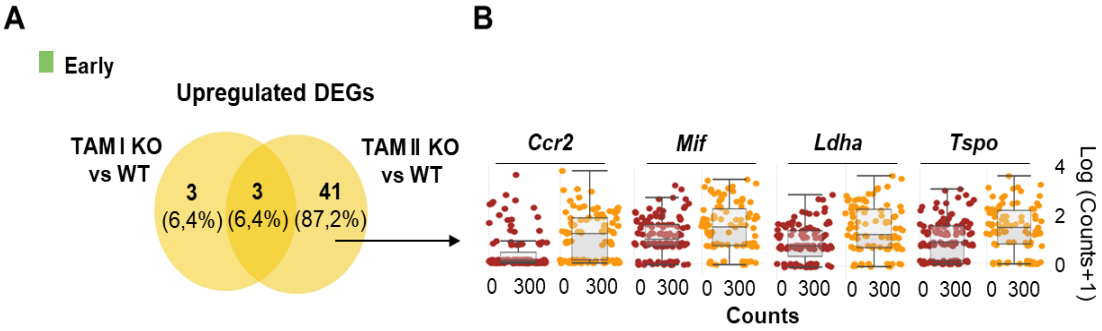

Figure 29. *Acod1* deficiency mainly affected the transcriptional programme of peripheral infiltrating macrophages compared to microglia at early stage. (A) Venn diagram representation showing shared and exclusive up-regulated genes in *Acod1* KO TAM I (n = 3) and TAM II (n = 41) at early stage versus their respective counterparts in age-matched WT cells. **(B)** Notch plot representation of selected genes exclusively up-regulated by TAM II in *Acod1* KO mice in comparison to WT mice at early stage (see **Table S8**).

Similarly to early stages, the number of exclusively up-regulated genes was higher in macrophage-like (n = 68 genes) compared to microglia-like (n = 9 genes) cells when comparing *Acod1* KO with WT tumour-bearing mice at late stage (**Figure 30A**, **Table S9**), confirming that the lack of *Acod1/Irg1* mainly affected the transcriptional programme of peripheral infiltrating macrophages compared to microglia. Gene set enrichment analysis of macrophage-like cell exclusively up-regulated genes at late GBM stage in *Acod1* KO compared to WT mice uncovered enrichment of terms associated with inflammation (e.g. *Irf1*), antigen processing and presentation via MHC class I (e.g. *H2-K1*) and T cell mediated cytotoxicity (e.g. *H2-T23*) (**Figure 30B**).

The common 15 microglia-like and macrophage-like cell up-regulated genes in *Acod1* KO compared to WT mice were associated with antigen presenting cell (e.g. *Cd74, H2-Ab1*) and inflammatory (e.g. *Stat1*) markers, reflecting an enhanced immune activation at late stage in *Acod1* KO mice. In agreement with these results at single-cell resolution, we detected a higher induction of antigen presentation (e.g. *Cd74, H2-Ab1, H2-Aa*) and inflammatory (e.g. *Irf1*) transcripts in *ex vivo* CD11b+ isolated TAMs from *Acod1* KO compared to WT tumour-bearing mice at late stages (**Figure 30C**).

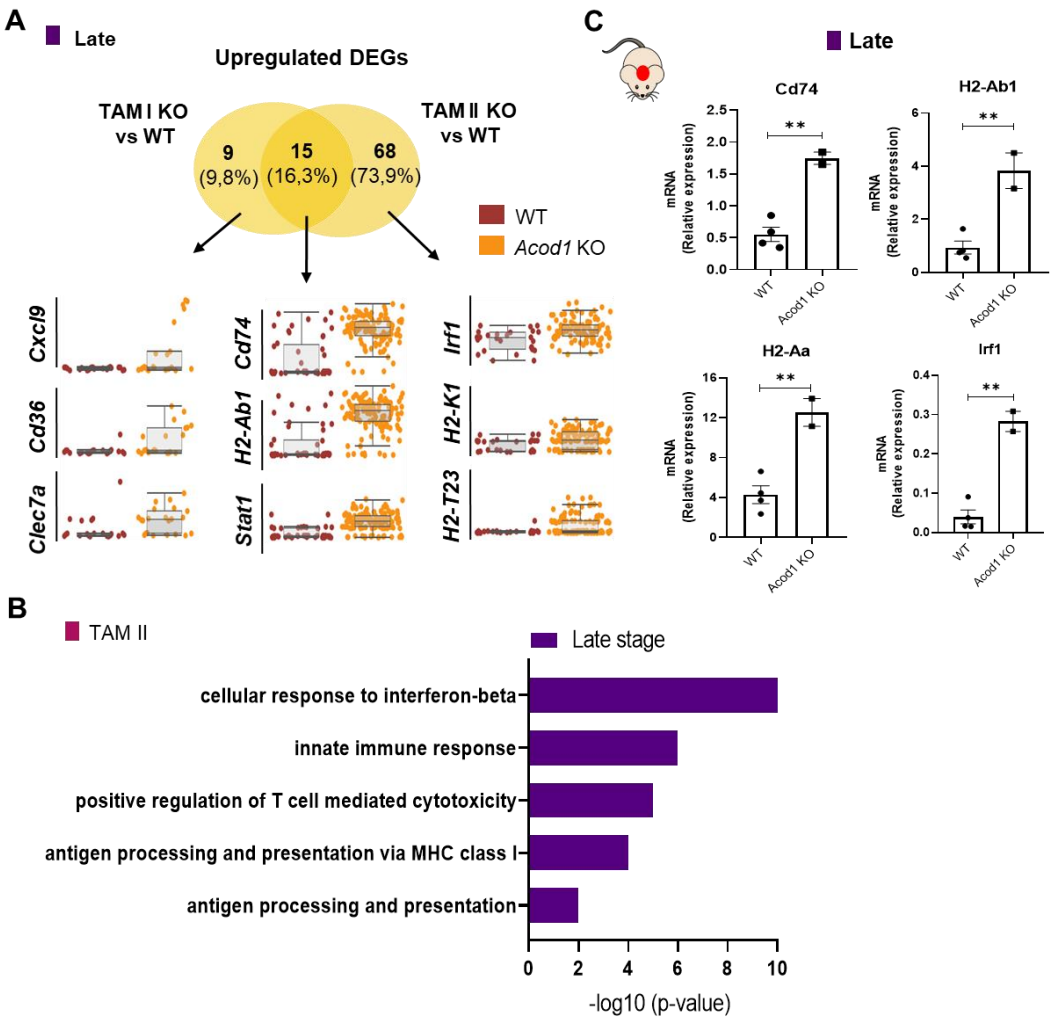

Figure 30. TAMs under *Acod1* deficiency display higher antigen presenting cell programmes. **(A)** Venn diagram representation showing shared (n = 15) and exclusive up-regulated genes in *Acod1* KO TAM I (n = 9) and TAM II (n = 68) at late stage versus their respective counterparts in age-matched WT cells (see **Table S9**). Corresponding notch plot representations of selected shared or unique genes up-regulated in TAM I and TAM II cells in *Acod1* KO mice compared to age-matched WT mice at late stage. **(B)** Gene set enrichment analysis of TAM II uniquely up-regulated genes in *Acod1* KO mice versus WT mice at late stages. **(C)** Expression levels of *Cd74, H2-Ab1, H2-Aa* and *Irf1* genes in CD11b+ cells isolated from WT (n = 4) and *Acod1* KO (n = 2) mice at late stages. Unpaired Student t test (1 biological replicate). Data are presented as mean ± SEM ** $p < 0.01$.

IRF family members play essential roles in regulating immune responses (Borden et al., 2007; Taniguchi et al., 2001) and seminal work has shown that *Irf1* KO mice exhibit impaired NK cell maturation and defective Th1 responses (Lohoff et al., 1997; Ogasawara et al., 1998). Additionally, IRF1 operates as a tumour suppressor and its inactivation was shown to significantly increase risk of malignancy (Alsamman and El-Masry, 2018). To investigate the expression of IRF1 at the protein level, we conducted immunofluorescence analysis and detected higher numbers of IBA1+IRF1+

positive cells in the tumour core in *Acod1* KO compared to WT mice (**Figure 31A**). Amongst the downstream targets of IRF1, we detected by flow cytometry an increased expression of MHC-II in TAMs isolated at late stage from *Acod1* KO compared to WT mice (**Figure 31B**). Additionally, in brain sections from *Acod1* KO tumour-bearing mice, we detected a significant increase of CD74 marker expressed by macrophage-like cells, which were enriched in the tumour core, compared to WT mice (**Figure 31C**).

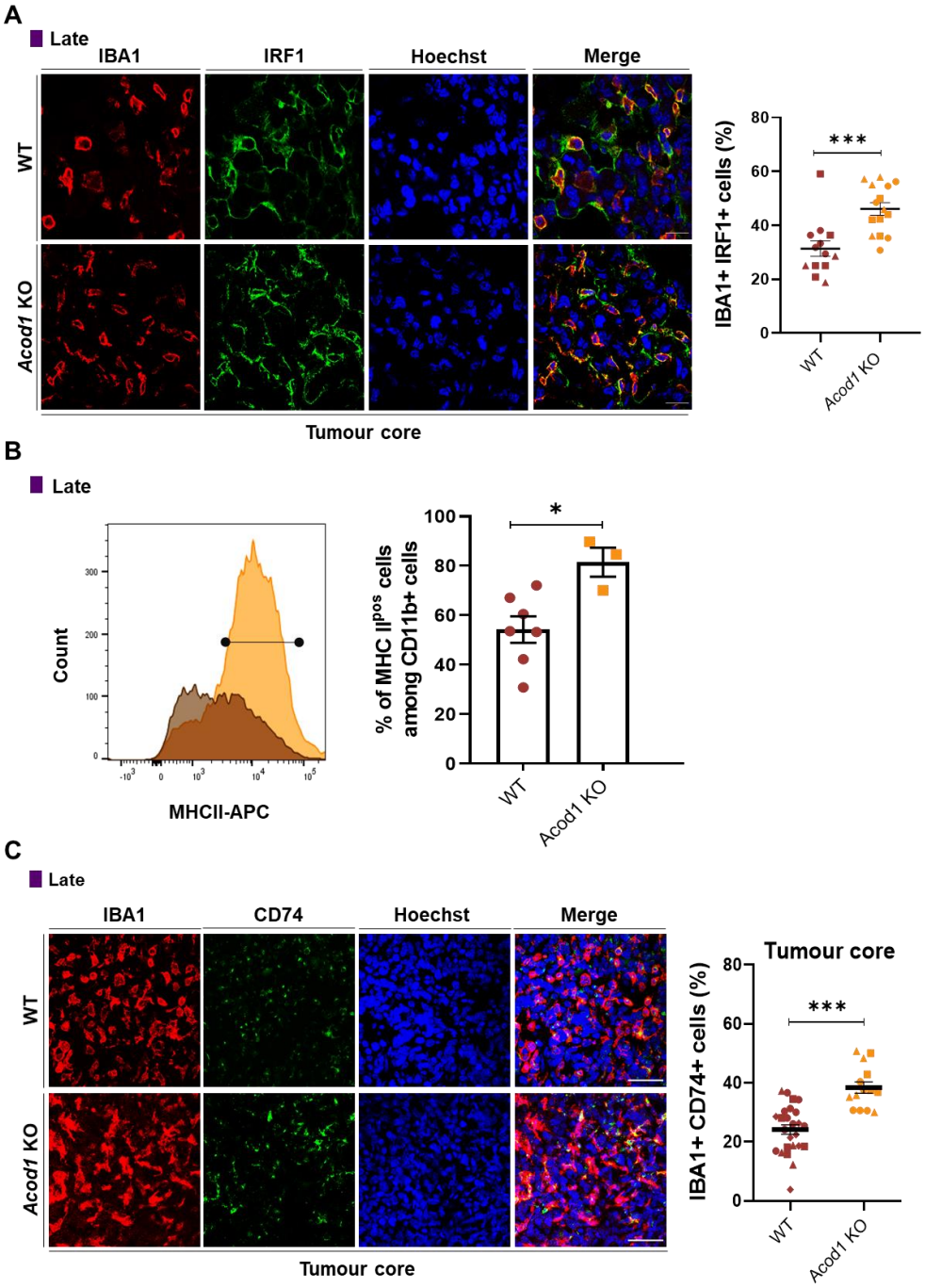

Figure 31. Up-regulation of IRF1 is associated with increased expression levels of antigen presenting cell markers by TAMs at late stage. (A) Immunofluorescence pictures (left) and quantification (right) of IRF1 expression in IBA1+ cells in the tumour core region at late stage in *Acod1* KO (n = 3) and WT (n = 3) mouse brain sections. Unpaired Student t test (1 biological replicate). **(B)** Representative overlay histogram (left) and quantification (right) of MHC-II expression in TAMs analysed in WT (n = 7) and *Acod1* KO (n = 3) mice at late stage by flow cytometry. Unpaired Student t test (1 biological replicate). **(C)** Immunofluorescence pictures (left) and quantification (right) of CD74 expression in IBA1+ cells in the tumour core region at late stage in *Acod1* KO (n = 3) and WT (n = 4) mouse brain sections. Unpaired Student t test (1 biological replicate). Data are presented as mean ± SEM, * $p < 0.05$; *** $p < 0.001$. Scale bars in A and C = 20µm.

Since gliomas are characterized as "immunologically silent" in IDH-mutant or "lymphocyte-depleted" in IDH-wildtype subtypes (Thorsson et al., 2018), we sought to investigate whether the ablation of *Acod1*, which induces an enhanced TAM immunogenic phenotype, could influence the recruitment of T cells to the tumour site. Therefore, we applied trajectory analysis to investigate TAM cellular states in the TME. We observed higher macrophage-like cell heterogeneity in *Acod1* KO compared to WT mice, suggesting that *Acod1* deficiency supports TAM II diversity in the TME (**Figure 32**).

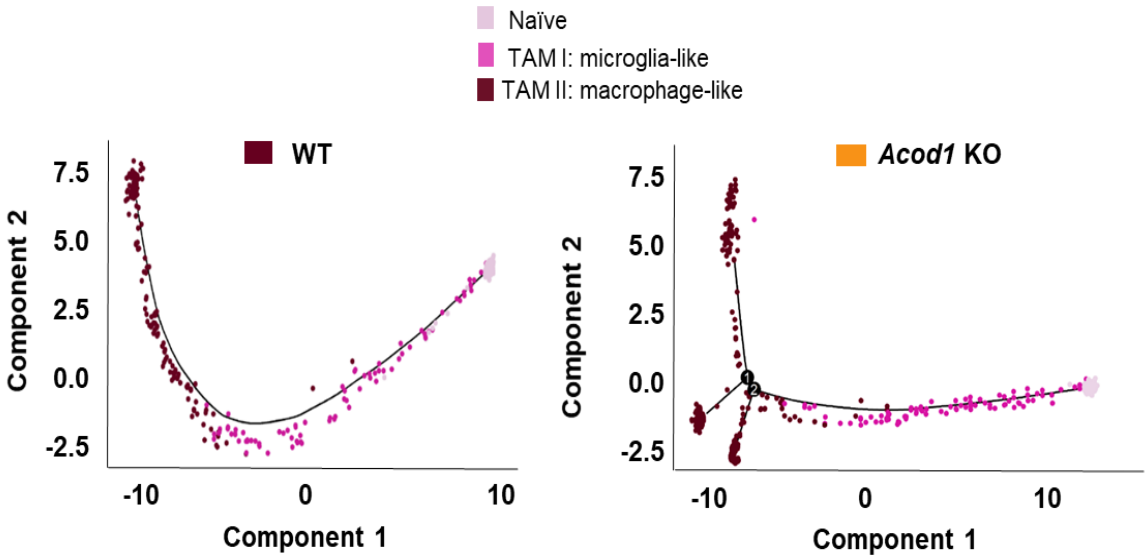

Figure 32. *Acod1* deficiency contributes to TAM II heterogeneity in GBM. Trajectory analysis of 335 myeloid cells from WT naïve and tumour-bearing mice (left graph) and 501 myeloid cells from *Acod1* KO naïve and tumour-bearing mice (right graph).

Moreover, we observed that *Acod1* TAM diversity in the TME occurs independently of the tumour stage (**Figure 33A**) and distinct cellular states were identified among the TAM II subset (**Figure 33B**).

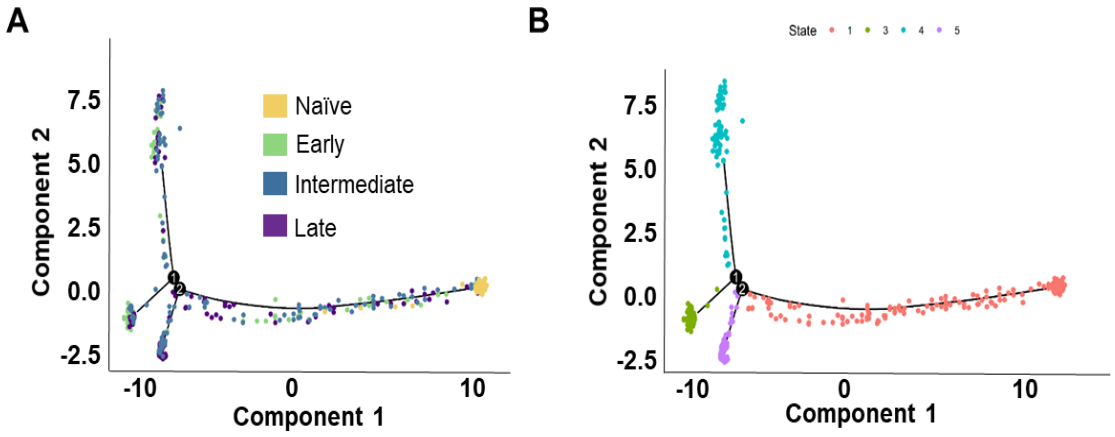

Figure 33. TAM II heterogeneous cellular states are maintained along GBM progression. (A) Trajectory analysis of 501 myeloid cells from *Acod1* KO naïve along GBM progression and **(B)** identification of four distinct cellular states across the myeloid compartment.

We further investigated the transcriptional set of cellular state 4 in macrophage-like cells in *Acod1* KO mice (**Figure 34**), as it showed the most prominent trajectory among the four cellular states. Interestingly, we identified a subset of TAMs in *Acod1* deficient mice involved in leukocyte migration and T cell activation and differentiation (e.g., *Ccl17, Ccl22*, *Ccr7, IL12b, Cd1d1*) as well as expressing serine proteinase inhibitors (e.g., *Serpinb9, Serpinb6b*) (**Figure 34*)***. In particular, serpins have been described to play a critical role in T lymphocyte mediated immunity (Ashton-Rickardt, 2013). These results show that a specific TAM II subset present in *Acod1*- deficient tumour bearing mice might support leukocyte migration to the tumour site.

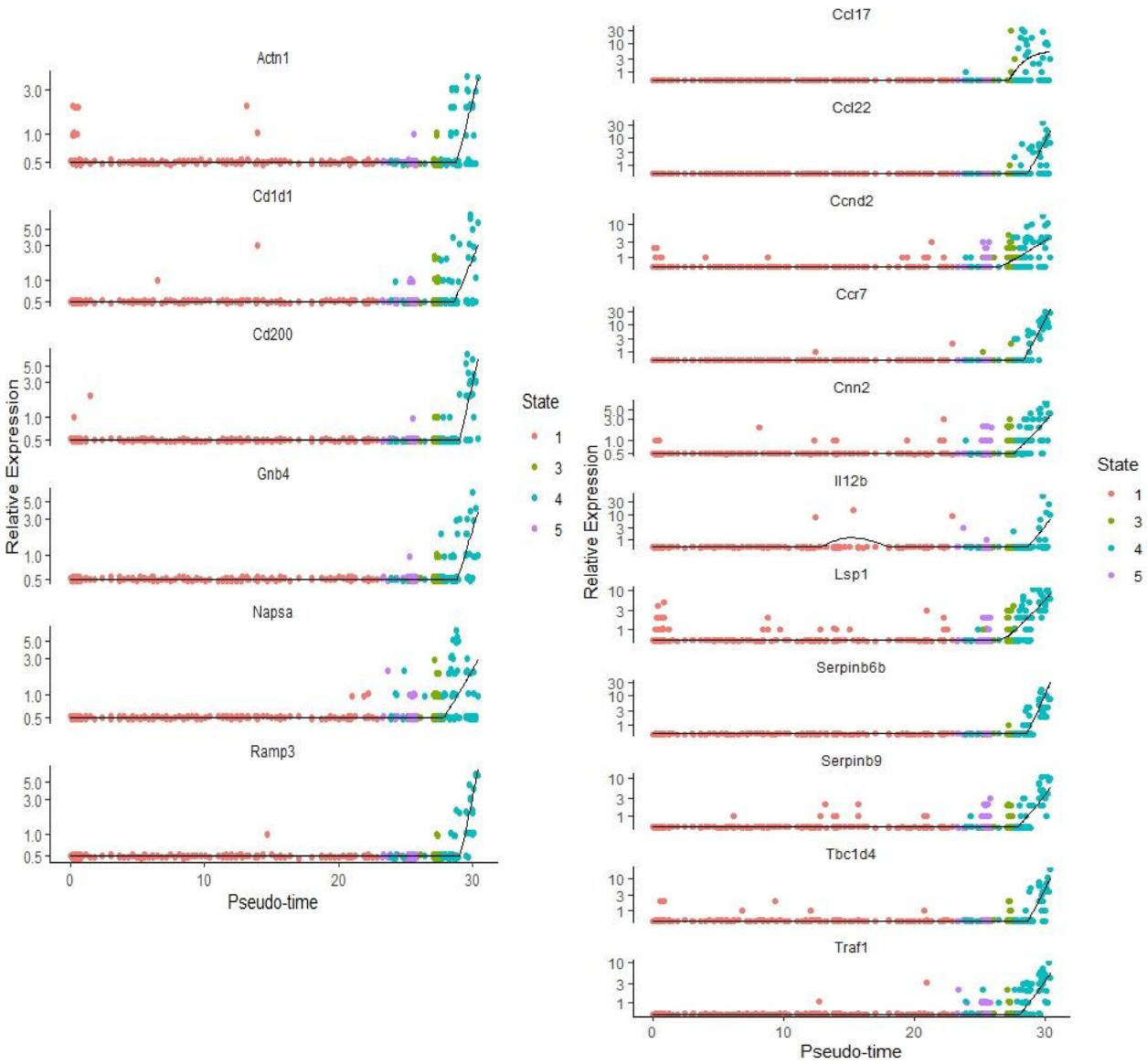

Figure 34. Pseudo-time dynamics of exclusive genes driving the cellular state 4 in TAM II subset under *Acod1* deficiency. Relative expression of genes driving the correspondent cellular state in TAM II subset. Abbreviations: *Actn1* (Actinin Alpha 1), *Cd1d1* (CD1d Molecule), *Cd200* (CD200 Molecule), *Gnb4* (G Protein Subunit Beta 4), *Napsa* (Napsin A Aspartic Peptidase), *Ramp3* (Receptor Activity Modifying Protein 3), *Ccl17* (C-C Motif Chemokine Ligand 17), *Ccl22* (C-C Motif Chemokine Ligand 22), Ccnd2 (Cyclin D2), *Ccr7* (C-C Motif Chemokine Receptor 7), Cnn2 (Calponin 2), *Il12b* (Interleukin 12B), *Lsp1* (Lymphocyte Specific Protein 1), *Serpinb6b* (Serpin Family B Member 6), *Serpinb9* (Serpin Family B Member 9), *Tbc1d4* (TBC1 Domain Family Member 4), *Traf1* (TNF Receptor Associated Factor 1).

Notably, in line with this notion, we observed a considerable increase of the lymphocytic population in *Acod1* KO compared to WT mice, both in our scRNA-seq dataset (**Figure 35A**) and by

flow cytometry (**Figure 35B-C**), suggesting an effective crosstalk between TAMs and the adaptive immune cell compartment.

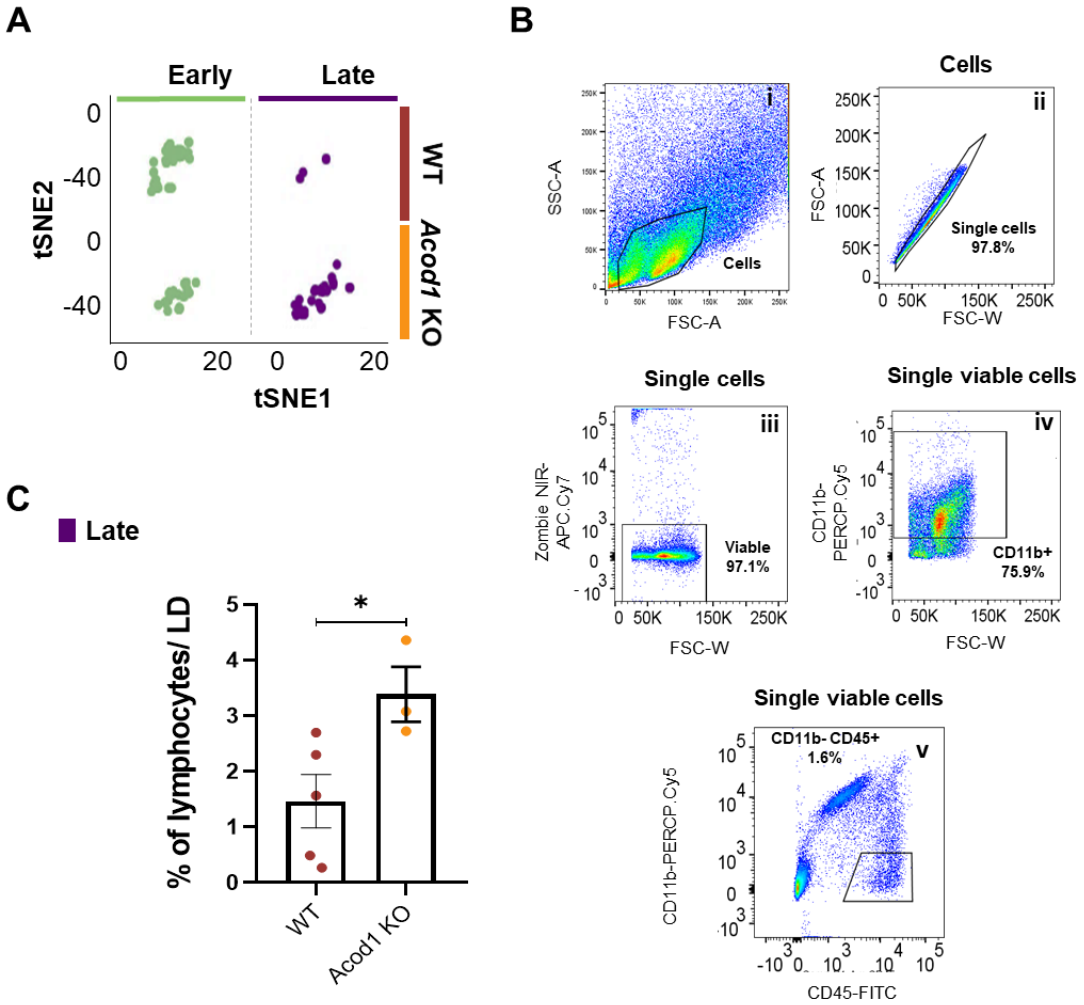

Figure 35. Enhanced TAM immunogenic phenotype under *Acod1* deficiency influences the recruitment of T cells to the tumour site. (A) tSNE representation of the lymphocytic population detected at early and late stage by scRNA-seq. **(B)** Flow cytometry gating strategy. (i) Cells of interest were gated based on forward (FSC) and side scatter (SSC). (ii) Doublets were excluded based on the forward scatter height (FSC-H) versus forward scatter (FSC-A). (iii) Zombie NIR-APC.cy7 was used to discriminate living cells. (iv) CD11b-PERCP.cy5 was used to gate the myeloid compartment. Lastly, we gated MHC-II expressing cells and lymphocytes (CD11b- CD45+). **(C)** Percentage of CD11b- CD45+ lymphocytes at late stage quantified by flow cytometry. Unpaired Student t test (WT n = 5, Acod1 KO n = 3) (1 biological replicate). Data are presented as mean ± SEM, * $p < 0.05$.

However, although *Acod1/Irg1* silencing in macrophages significantly reduced the peritoneal tumour burden (Weiss et al., 2018), the analysis of tumour growth did not show significant differences

between WT and *Acod1* KO in GL261 tumour-bearing mice (**Figure 36A**), neither we detected differences in the mouse survival (**Figure 36B**).

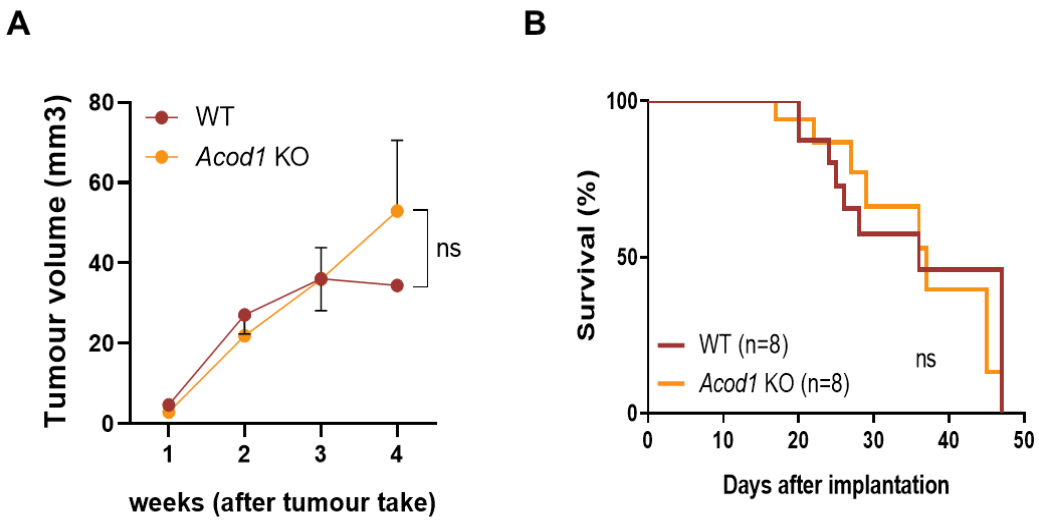

Figure 36. *Acod1* KO mice do not show improved survival. (A) Time course of tumour volume ratio in WT and *Acod1* KO mice. Tumour volume was normalized to the initial tumour take for each week. **(B)** Kaplan-Meier curves showing the survival rate in WT and *Acod1* KO mice.

II. Revealing tumour-associated microglia/macrophage heterogeneity across distinct Glioblastoma landscapes

4.5. Patient-derived orthotopic xenograft models recapitulate human Glioblastoma features

In order to elucidate TAM diversity across specific GBM tumour landscapes/niches, we took advantage of patient-derived orthotopic xenograft (PDOX) models as they preserve key histopathological features of patient tumours in immunocompromised mice. Specifically, we took advantage of previously characterized GBM PDOX models, established by the NORLUX Neuro-Oncology Laboratory (see Materials and Methods section). These models display distinct tumour landscapes depending on the origin of the tumour (Bougnaud et al., 2016). According to histopathological features, GBM PDOX models displayed a varying range of invasive and angiogenic features (Golebiewska et al., 2020). In our study, we selected two distinct paradigms of the disease to investigate microglia and macrophage-like cells in the TME and their specific functional adaptation across distinct GBM landscapes. Therefore, we conducted our analysis on the invasive tumour phenotype, characterized by a highly infiltrative growth pattern with an apparent normal brain

vasculature, and on the angiogenic tumour phenotype, displaying necrotic areas with large, dilated blood vessels and microvascular proliferation (Bougnaud et al., 2016).

In order to address the inherent capacity of distinct tumour phenotypes in modifying the various host immune and haematological components, we collected peripheral blood from naïve and the two distinct tumour phenotypes at late stage of GBM development. In this context, total white blood cell (WBC) counts were increased in the invasive compared to the angiogenic tumour phenotype and naïve mice (**Figure 37A**). Within the WBC counts, increased lymphocytes and granulocytes were observed in the peripheral blood of mice from the invasive tumour phenotype (**Figure 37A**), suggesting an increased production of WBC counts as response to the tumour. Moreover, we detected reduced numbers of red blood cells (RBC) and platelets in the angiogenic tumour phenotype compared to naïve and the invasive tumour phenotype (**Figure 37B-C**).

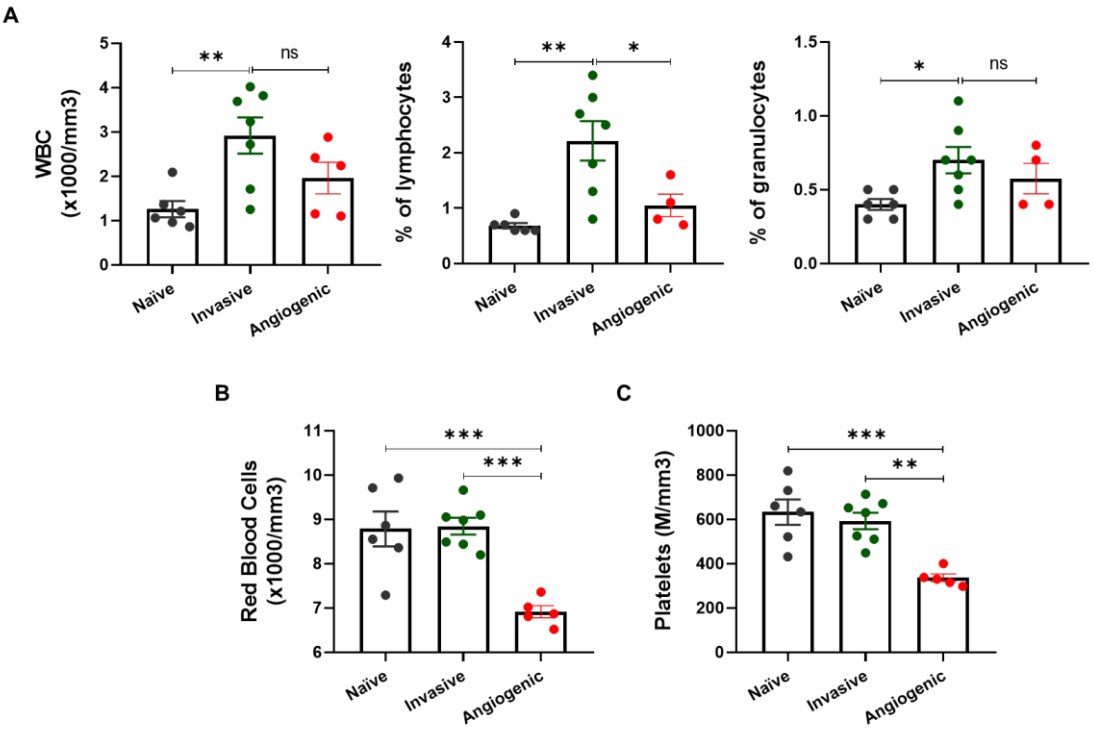

Figure 37. Peripheral blood analysis of naïve and GBM tumour-bearing mice at late stage. (A) WBC **(B)** RBC and **(C)** platelet counts in the blood of naïve and late stage tumour-bearing mice. One-way ANOVA followed by Tukey's multiple comparisons test (naïve brain, n = 6; invasive landscape, n = 7, angiogenic landscape, n = 5) (1 biological replicate). Data are represented as mean ± SEM, * p<0.05, ** p < 0.01, *** p< 0.001; ns > 0.05.

Overall, the association of thrombocytopenia with reduced mice survival demonstrates a more aggressive tumour phenotype characterizing the angiogenic tumour phenotype. These results show the relevance of using PDOX models recapitulating specific features of GBM disease.

Therefore, we took advantage of the invasive and angiogenic GBM paradigms to elucidate respective innate immune cells adaptation across naïve and GBM tumour-bearing mice.

4.6. Tumour-associated microglia/macrophages accumulate at the tumour site showing morphological heterogeneity across Glioblastoma landscapes

Having observed cellular differences in the peripheral blood, we next aimed to investigate whether distinct tumour landscapes would differently recruit immune cells to the tumour site. Thus, we performed immunohistochemistry analysis to investigate the number of IBA1 cells in both naïve and late stage GBM tumour sections (**Figure 38**). Microglia cells actively survey the environment by extending their protrusions. Functioning as a sensor unit in the brain, these cells display a ramified morphological phenotype, which was recapitulated in the naïve brain (**Figure 38A**). By measuring the surface area occupied per cell, we indeed confirmed that IBA1+ cells show an altered morphology associated with reduced branching in the tumour sections compared to naïve mice (**Figure 38B**). Remarkably, we detected a more heterogeneous IBA1 surface area in the angiogenic tumour phenotype, indicating heterogeneous TAM populations at the tumour site, in comparison to a more homogenous surface area population in the invasive tumour phenotype (**Figure 38B**). Preliminary analyses indicate increased numbers of IBA1 cells in the tumour in comparison to naïve mice (naïve: 9.14 ± 2.41; invasive tumour phenotype: 15.87 ± 5.52; angiogenic tumour phenotype: 19.45 ± 4.10), showing that independently of the tumour phenotype, GBM actively recruit TAMs to the tumour site (**Figure 38C**).

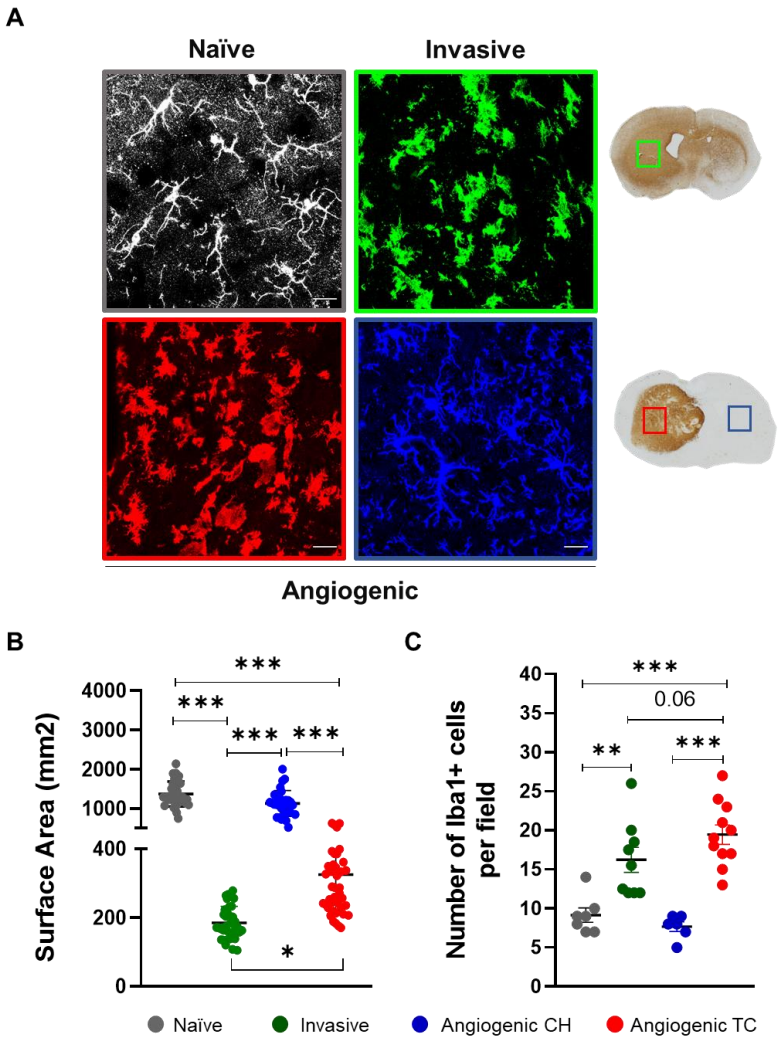

Figure 38. Naïve microglia and TAMs spatial morphological characterization at late stage of GBM development. (A) Immunofluorescence pictures depicting IBA1+ cells morphological features across distinct tumour landscapes: naïve (grey), invasive (green), angiogenic tumour core (red) and angiogenic contralateral hemisphere (blue). **(B)** IBA1 surface area measurements per cell across naïve and tumour-bearing sections. **(C)** Numbers of IBA1 positive cells per field. One-way ANOVA followed by Tukey's multiple comparisons test (naïve n = 1; invasive n = 2; angiogenic n = 2) (1 biological replicate). Data are presented as mean ± SEM, ** $p < 0.01$, *** $p < 0.001$, ns > 0.05. Scale bars = 50µm.

TAMs can assume different morphologies in GBM tumour bearing mice (Ricard et al., 2016). Specifically, the ramified phenotype is considered typical for a "resting" state, whereas the amoeboid phenotype is associated with a more activated state. However, how morphological changes relate to functional states in the TME is still poorly understood. Thus, we applied scRNA-seq analysis to investigate myeloid tumour-instructed transcriptional adaptation in the TME.

4.7. Glioblastoma-educated myeloid cells display major transcriptional adaptation across distinct landscapes

In order to investigate the heterogeneity of the TME in relevant PDOX models, we analysed brain tissue from naïve and GBM tumour-bearing mice at late stage by scRNA-seq. For this analysis, we took the whole brain for naïve and invasive tumour phenotype, while we dissected the tumour-containing hemisphere for the angiogenic tumour phenotype. Following pre-analytical filtering of the scRNA-seq experiments, we obtained a matrix composed of 6'641 single cells. In order to reduce the dimensionality of the matrix, we used unsupervised topological clustering uniform manifold approximation and projection (UMAP) (**Figure 39A**). Irrespective of the GBM tumour phenotype, we identified 17 stromal clusters that we annotated based on respective cell type-specific gene markers (**Figure 39B, Table 6**).

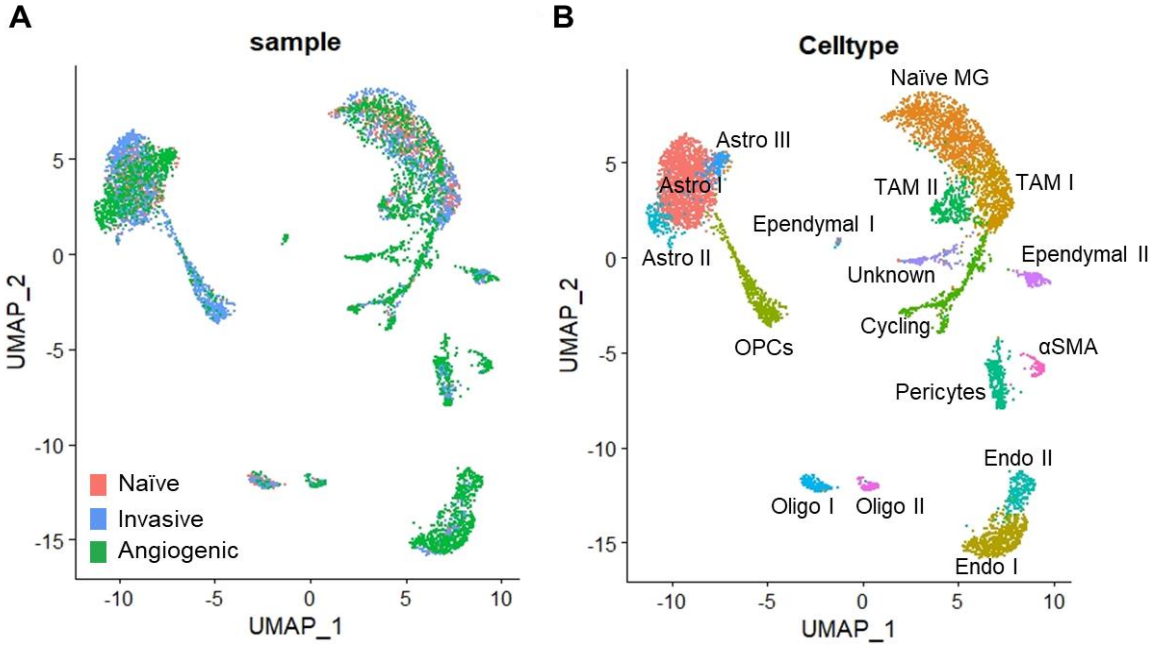

Figure 39. Stromal cell type diversity in naïve and PDOX models. (A) UMAP representation of all the cells included in the study from naïve (n = 1'692 cells) and tumour-bearing mice (invasive landscape, n = 2'193 cells and angiogenic landscape, n = 2'756 cells). **(B)** UMAP representation of all single cells included in the study grouped within 17 cell clusters. Cell type-specific markers allowing the identification of stromal cell types are summarized in **Table 6**. Abbreviations: MG: Microglia; TAM I: Microglia-like cells; TAM II: Macrophage-like cells; Astro: Astrocytes; Endo: Endothelial cells OPCs: Oligodendrocyte progenitor cell; Oligo: Oligodendrocytes; αSMA: alpha-smooth muscle actin.

Table 6. Cell type identification, related to Figure 39.

Cell type	Genes
Astro I: Astrocytes	*Gja1, Slc1a2, Slc4a4, Aqp4, Acsl3, Htra1, Aldoc, Vegfa, Gpr37l1, Timp3*
Naïve MG: Naïve microglia	*P2ry12, Cx3cr1, Hexb, Cst3, Gpr34, Csf1r, Siglech, Sparc, Itgam, Tmem119*
TAM I : Microglia-like cells	*P2ry12, Cx3cr1, Hexb, Ctss, Tyrobp, C1qa, Trem2, Hexb, C1qb, Cd68*
Endo I: Endothelial cells	*Pecam1, Ptprb, Nes, Vim, Flt1, Bsg, Spock2, Adgff5, Pltp, Prom1*
OPCs: Oligodendrocyte progenitor cells	*Cacng4, Pdgfra, Olig1, Vcan, Cntn1, Gap43, Ccnd1, Meg3, Olig2, Serpina3n*
Cycling cells	*Aif1, Mki67, Top2a, Cenpa, Cenpf, Cenpe, Ccnb2, Cenph, Cdkn1, Ccna2*
TAM II : Macrophage-like cells	*Aif1, Lyz2, Ms4a7, Ccr2, Cybb, Ptprc, Atf3, Ctss, Cyba, Cd14*
Pericytes	*Rgs5, Pdgfrb, Cspg4, Myl9, Gjc1, Mgp, Cygb, Itga1, Col4a2, Col3a1*
Endo II: Endothelial cells	*Pecam1, Kdr, Angpt2, Adgrl4, Tie1, Anxa2, Notch4, Icam2, Vim, Nes*
Astro II: Astrocytes	*Plpp3, Aldoc, Mt2, Mt1, Gfap, Aqp4, Gpr37l1, Vim, Scg3, Slc1a2*
Oligo I: Oligodendrocytes	*Plp1, Apod, Ptn, Frzb, Col5a2, Igf1, Timp3, Gja1, Ptgds, Mfap3l*
Astro III: Astrocytes	*Plpp3, Gria2, Slc1a2, Slc1a3, Acsl3, Aldoc, Malat1, Ptprz1, Neat1, Lsamp*
Unknown	*Ccdc153, Tmem212, Rsph1, Gm12346, Enkur, Mns1, Dbi, Rarres2, Ak7*
Ependymal I	*Vim, Acta1, Lgals1, Top2a, Hist1h1d, Tmsb4x, Nasp, Rack1, Atp5e, Gap43*
Oligo II: Oligodendrocytes	*Pdgfra1, Edn3, Ptgds, Apod, Igf2, Col1a2, Colec12, Pdgfra, Serpinh1, Anxa2*
αSMA	*Myh11, Acta2, Tpm2, Cald1, Crip1, Lmod1, Tpm1, Tagln, Myl9, Filip1l*
Ependymal II	*Calml4, Prlr, Igf2, Otx2, Folr1, Kcnj13, Vat1l, Tmem72, Ppp1r1b, Atp2b3*

Under homeostatic conditions, microglia, endothelial cells, astrocytes and oligodendrocytes represented 90.5% of all cells present in the brain of naïve nude mice. The remaining 9.5% were pericytes, ependymal cells, OPCs and cycling cells (**Figure 40A**). Focusing on the TME of the invasive landscape, we observed a prominent presence of OPCs (18.74%) compared to naïve brain (1.06%) and angiogenic landscape (1.71%) (**Figure 40B**). Moreover, in the TME of the angiogenic landscape we observed the emergence of additional cells, such one cluster composed by ependymal cells (Ependymal II: 2.18%) and a third cluster composed by astrocytes (Astro III: 5.59%) (**Figure**

40C). These results suggest that distinct tumour-intrinsic phenotypes might affect cell type diversity in the TME.

Focusing on the myeloid compartment, we were able to identify and annotate three distinct myeloid clusters (**Figure 40**), as detected in the GBM syngeneic model. Specifically, naïve and TAM I clusters showed gene markers of the microglia homeostatic genes (e.g., *P2ry12, Cx3cr1, Gpr34, Siglech, Sparc*), while these genes were not detected in the TAM II cluster (**Table 6**). Moreover, the TAM II cluster exhibited peripheral monocytic-derived macrophage gene markers (e.g., *Aif1, Lyz2, Ms4a7, Ccr2, Cybb, Ptprc)* (**Table 6**). Interestingly, the TAM morphological heterogeneity that we detected in the angiogenic tumour phenotype might be explained by the increased number of monocyte-derived macrophages when compared to the more homogeneous microglia population detected in the invasive landscape (**Figure 38B**). By scRNA-seq, we detected a small fraction of TAM-I like and TAM II-like cells in the naïve brain (**Figure 40A**). Recent work has demonstrated regional microglia heterogeneity in the naïve mouse brain (Silvin and Ginhoux, 2018; Stratoulias et al., 2019; Uriarte Huarte et al., 2021) and our results could explain its clustering with TAM I-like cells. Also, non-parenchymal macrophages, namely border-associated macrophages (BAMs), are present in the naïve brain, which most probably compose the identified TAM II-like cells (**Figure 40A**). In line with this notion, mannose receptor CD206 (coded by *Mrc1*) was expressed by this subset of cells, as observed by others (Goldmann et al., 2016). Additionally, in line with its angiogenic nature as previously described, by scRNA-seq we detected higher percentage of endothelial cells composing the TME of the angiogenic tumour phenotype (mean = 20.42%) in comparison to the naïve (mean = 2.48%) and invasive landscape (mean = 7.06%) (**Figure 40**).

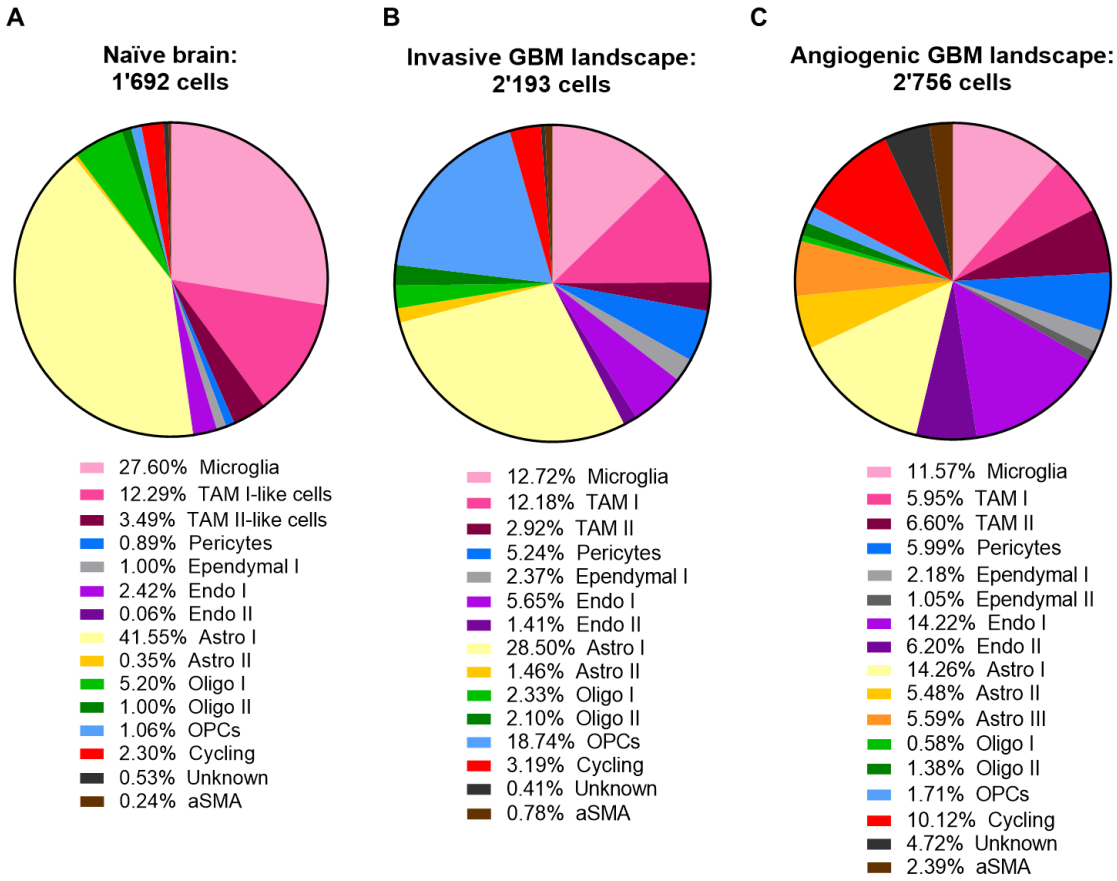

Figure 40. GBM-intrinsic tumour phenotype contributes to the emergence of specific cell types in the TME. (A-C) Pie chart representations of respective cell-type proportions for **(A)** 1'692 cells from naïve brain, **(B)** 2'193 cells from the invasive landscape and **(C)** 2'756 cells from the angiogenic landscape.

For our purposes, we focused our analysis on the myeloid compartment, which, similarly to the syngeneic model, also showed a prominent transcriptional adaptation in the TME of PDOX models (**Figure 41**). By analysing TAM heterogeneity across GBM landscapes at single-cell resolution, we detected microglia-like and macrophage-like cell subsets in tumour-bearing mice from the invasive (TAM I: 43.77%; TAM II: 10.49%) and angiogenic tumour landscape (TAM I: 24.66%; TAM II: 27.37%) (**Figure 41B-C**). Interestingly, we detected a smaller fraction of macrophage-like cells in the homeostatic conditions (TAM II: 8.04%) and the invasive landscape (TAM II: 10.49%) when compared to the angiogenic tumour phenotype (TAM II: 27.37%). Taking together, these results show that the invasive tumour phenotype is mainly composed by microglia-like cells in the TME, while the angiogenic tumour phenotype shows almost equal presence of both microglia and macrophage-like cells (**Figure 41B-C**).

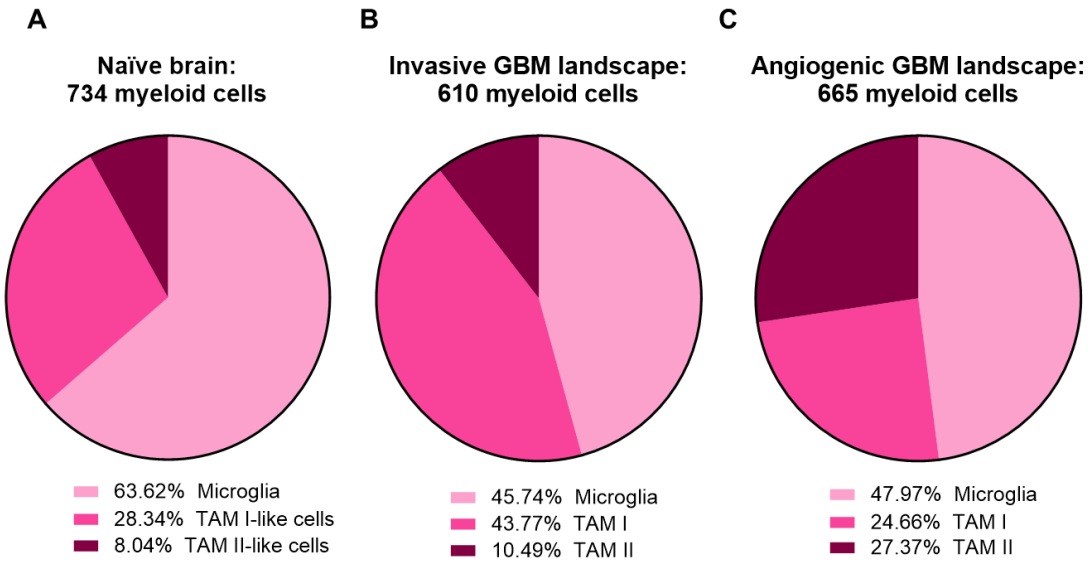

Figure 41. Microglia- (TAM I) and macrophage-like (TAM II) subsets identification in naïve and tumour-bearing mice. (A-C) Myeloid cells pie chart representations for respective proportions in **(A)** the naïve brain (n = 734 cells), **(B)** the invasive landscape (n = 610 cells) and **(C)** the angiogenic landscape (n = 665 cells).

Previous phenotypic characterization of the TME composition by flow cytometry identified distinct myeloid subtypes across GBM landscapes based on surface markers, such as CD11b, Ly6C, Ly6G and CD206 (**Figure 42A**). This strategy allowed for the identification of resting or activated microglia/macrophages (CD11b+Ly6C-Ly6G-CD206-), alternatively activated/perivascular macrophages (CD11b+Ly6C-Ly6G-CD206+) and infiltrative monocytes (CD11b+Ly6C+Ly6G-CD206-) (**Figure 42A**). In line with the scRNA-seq dataset, inflammatory monocytes were mainly found in the angiogenic tumour phenotype (7.7% of cells), indicating that peripheral monocytic infiltration was mainly present in the angiogenic tumour phenotype (**Figure 42B**). This observation correlates with BBB disruption as previously observed by MRI contrast imaging (Bougnaud et al., 2016).

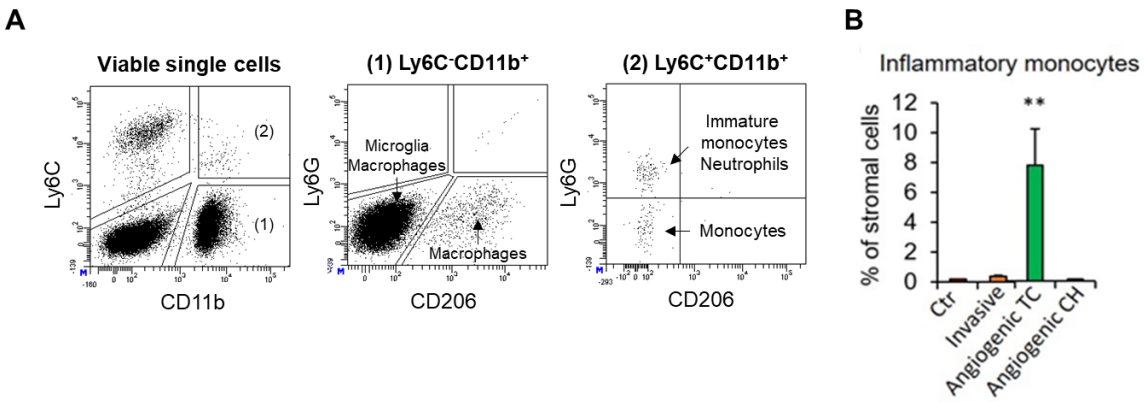

Figure 42. Peripheral monocytic infiltration is largely absent in GBM invasive compartments

(A) FACS gating strategy allowing to distinguish distinct myeloid cell types based on the differential expression of CD11b, Ly6C, Ly6G and CD206 markers: resting or activated microglia/macrophages (CD11b+Ly6C-Ly6G-CD206-), alternatively activated/perivascular macrophages (CD11b+Ly6C-Ly6G-CD206+) and monocytes (CD11b+Ly6C+Ly6G-). **(B)** Quantification of monocytes across naïve and GBM tumour phenotypes (TC: tumour core; CH: contralateral hemisphere). Two tailed Student's t-test, n=3. Data are presented as mean ± SEM, ** $p < 0.01$.

Next, we focused our analysis on GBM-educated microglia cells across the invasive and angiogenic GBM landscapes at late stage. A direct comparison of microglia-like cells (TAM I subset) from the invasive and angiogenic tumour phenotype versus the corresponding cells in naïve mice showed a distinct transcriptional adaptation across GBM landscapes (**Figure 43A**). This observation was supported by the overall higher number of differentially expressed genes between naïve microglia and TAM I subset from the angiogenic (up = 930 genes, down = 204 genes) compared to TAM I subset from the invasive tumour phenotype (up = 520 genes, down = 106 genes) (**Figure 43A)**. These results suggest tumour-intrinsic phenotype differently affects distinct transcriptional adaptation of resident microglia-like cells in the TME. We found partial overlap (21.3%) of genes expressed by TAM I subset across the two GBM landscapes versus naïve microglia (e.g. *Spp1, Lpl, Apoe, Lyz2, Fn1, Cst7, H2-D1, Ctsb, Ctsz, H2-K1, Axl, Cd14, Csf1, Ifg1, Vim, Atf3, Ifitm3*), indicating that microglia-like cells maintain a core transcriptional programme across the distinct GBM landscape (**Figure 43B**). Investigation of the exclusive up-regulated genes in microglia-like cells from the invasive landscape versus their correspondent counterparts in the angiogenic landscape, identified a major transcriptional effect on the angiogenic landscape (n = 675 genes) compared to the invasive landscape (n = 265 genes) (**Figure 43B**).

GO analysis of microglia-like cells exclusively up-regulated genes from the invasive landscape uncovered enrichment of terms associated with host immune response (e.g. positive regulation of cytokine secretion, response to oxidative stress, phagocytosis and positive regulation of MAPK

cascade) (**Figure 43C, Table S10**), thus reflecting their immune reactive profile in the TME. Focusing on microglia-like cells exclusively up-regulated genes from the angiogenic landscape, we also uncovered a reactive profile, although represented by different GO terms (e.g. positive regulation of nitric oxide biosynthetic process, ATP biosynthetic process and cellular response to interferon-alpha) (**Figure 43D, Table S11**). Taking together, these results support the notion that distinct tumour-intrinsic properties differentially affect microglia-like transcriptional programmes in the TME.

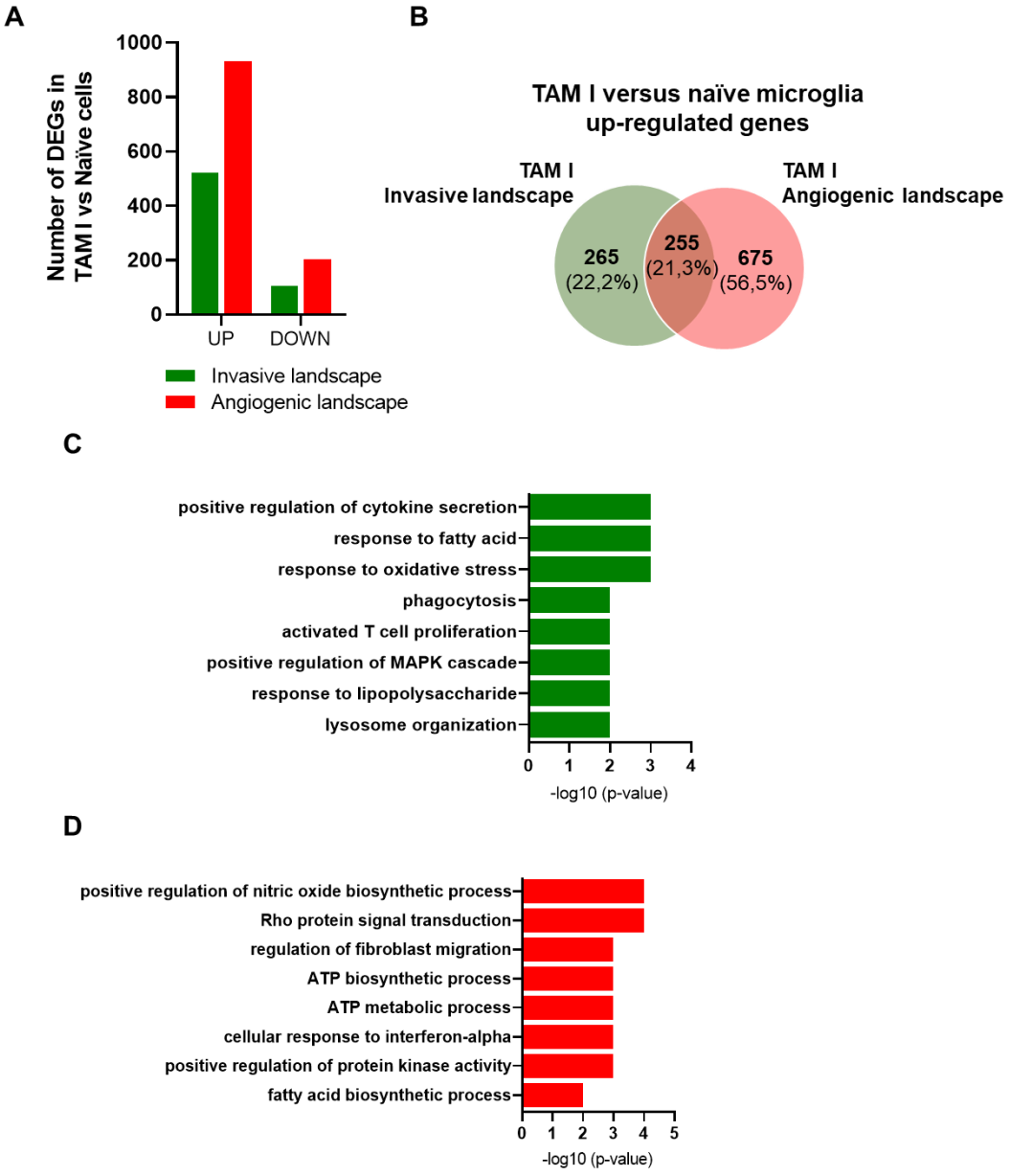

Figure 43. GBM-educated microglial cells display distinct transcriptional adaptations across GBM landscapes. (A) Number of differentially expressed genes for TAM I in the invasive (n = 520 up-regulated; n = 106 down-regulated) and angiogenic (n = 930 up-regulated; n = 204 down-regulated) tumour phenotypes versus naïve microglial cells. **(B)** Venn diagram representation

showing TAM I shared (n = 255) and exclusively up-regulated genes in the invasive (n = 265) and angiogenic (n = 675) tumour phenotypes versus naïve microglia. **(C-D)** Microglia-like cells gene ontology terms of exclusively up-regulated genes (**C**) in the invasive (**Table S10**) and **(D)** angiogenic (**Table S11**) tumour phenotypes versus correspondent naïve microglial cells.

We conducted similar analyses for the macrophage-like subset. A direct comparison of macrophage-like cells (TAM II subset) from the invasive and angiogenic tumour phenotype versus naïve microglia cells, showed a pronounced difference between tumour-associated macrophage cells from the angiogenic landscape compared to the invasive landscape (**Figure 44A**). This observation was supported by the overall higher number of differentially expressed genes between naïve microglia and TAM II subset from the angiogenic (up = 866 genes, down = 91 genes) compared to TAM II subset from the invasive tumour phenotype (up = 259 genes, down = 45 genes) (**Figure 44A**). Similar to TAM I subset, tumour-intrinsic phenotype differently mediated distinct transcriptional adaptation of macrophage-like cells across GBM landscapes. We observed that macrophage-like cells maintain a core transcriptional programme (e.g. *Spp1, Trem2, Cd83, Fn1, Ctsd, Plac8, Cxcl13, H2-K1, H2-Ab1, Ly6c2, Axl, Sparc, Mpeg1, Ramp1, Lat2, Icam1, H1f1α*) across GBM landscapes (**Figure 44B**). Additional investigation of the exclusive up-regulated genes in macrophage-like cells from the invasive landscape versus their correspondent counterparts in the angiogenic landscape, identified a major transcriptional effect on the angiogenic landscape (n = 725 genes) compared to the invasive landscape (n = 118 genes) (**Figure 44B**). Taken together, the angiogenic landscape contributed to a major transcriptional adaptation of both microglia and macrophage-like cells in the TME.

GO analysis of macrophage-like cells exclusively up-regulated genes from the invasive landscape uncovered enrichment of terms associated with migratory properties (e.g. leukocyte migration, cell-matrix adhesion and integrin-mediated signalling pathway) and immune response (e.g. positive regulation of inflammatory response and adaptive immune response) (**Figure 44C, Table S12**). Focusing on macrophage-like cells exclusively up-regulated genes from the angiogenic landscape, we mainly found enrichment of terms associated with chemotaxis (e.g. positive regulation of monocyte chemotaxis) and migration (e.g. positive regulation of T cell migration) (**Figure 44D, Table S13**).

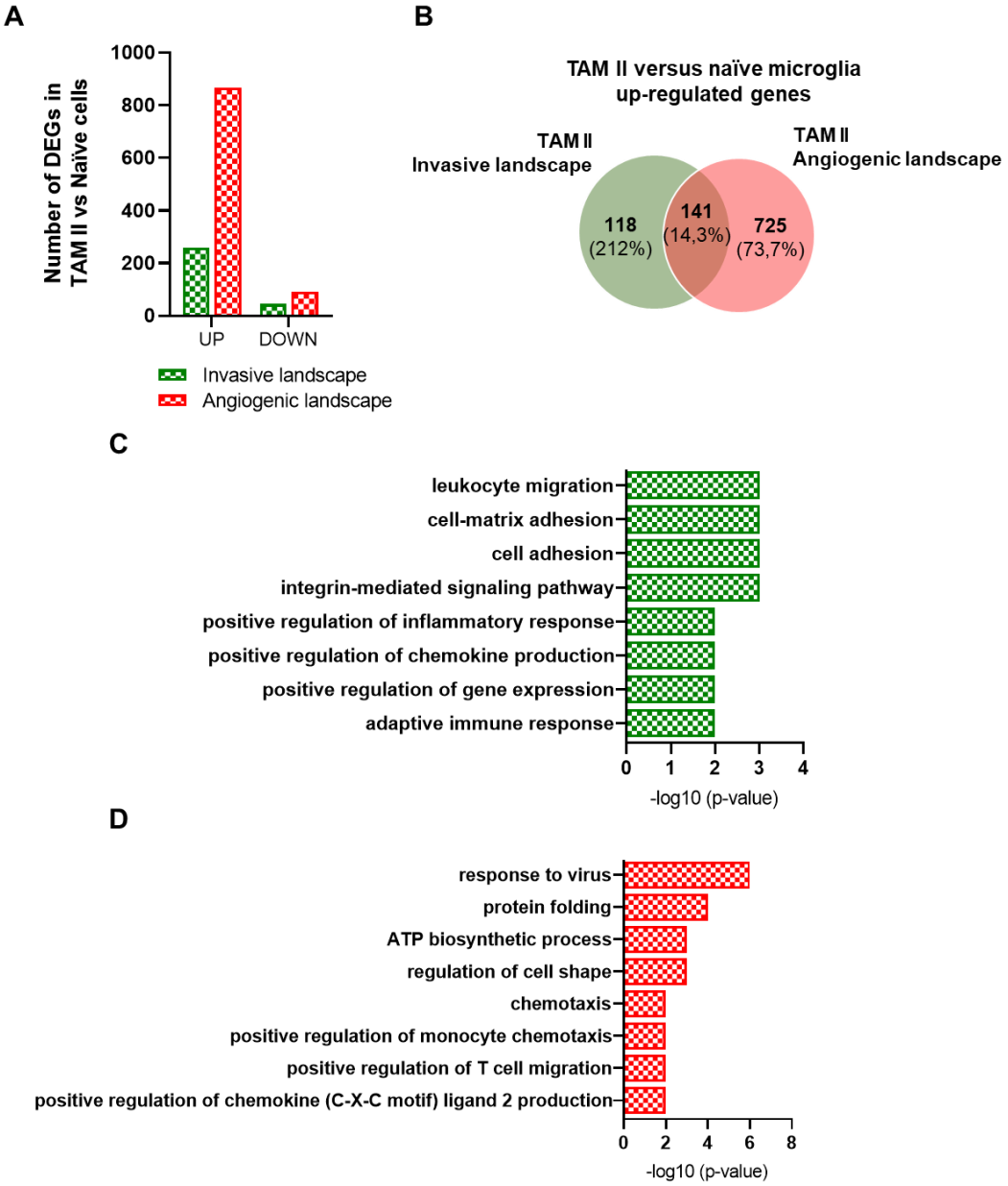

Figure 44. GBM-educated macrophages display distinct transcriptional adaptations across GBM landscapes. (A) Number of differentially expressed genes for TAM II in the invasive (n = 259 up-regulated; n = 44 down-regulated) and angiogenic (n = 866 up-regulated; n = 90 down-regulated) tumour phenotypes versus naïve microglial cells. **(B)** Venn diagram representation showing TAM II shared (n = 141) and exclusively up-regulated genes in the invasive (n = 118) and angiogenic (n = 725) tumour phenotypes versus naïve microglia. **(C-D)** Macrophage-like cells gene ontology terms of exclusively up-regulated genes **(C)** in the invasive (**Table S12**) and **(D)** angiogenic (**Table S13**) tumour phenotypes versus naïve microglia cells.

Overall, these results demonstrate that various tumour-intrinsic phenotypes induce specific transcriptional adaptations of microglia and macrophage-like cells in the TME of GBM.

4.8. Tumour-associated microglia/macrophages display niche-specific functional adaptation across Glioblastoma landscapes

TAMs phagocytic activity is emerging as a mechanism to improve innate anti-tumour immunity and to promote T-cell mediated adaptive immune responses. Taking our results, microglia-like cells from the invasive landscape showed enriched GO terms associated with phagocytosis and activated T cell proliferation (**Figure 43C**). Hence, we sought to investigate the phagocytic activity of *ex vivo* CD11b isolated cells from naïve and tumour-educated cells at late stage of GBM development.

Due to the high abundance of tumour cells in the tumour-bearing mice, prior to CD11b isolation we performed mouse cell depletion step in order to discriminate host murine cells from human patient tumour cells (see Materials and Methods section) (**Figure 45A-B**). Moreover, as TAMs accumulate at the tumour site, we dissected the tumour core region of the angiogenic landscape, while no dissection was done for the invasive landscape (**Figure 45B**). The purity of *ex vivo* CD11b isolated cells was assessed by flow cytometry after the mouse cell depletion step by quantifying the ratio between human $CD90^{+}$ cells versus murine myeloid $CD11b^{pos}$ cells (**Figure 45C**). Overall, we obtained high enrichment of $CD11b^{+}$populations across the invasive (96.90% ± 3.10) and the angiogenic (97.00% ± 1.85) tumour phenotypes (**Figure 45C**).

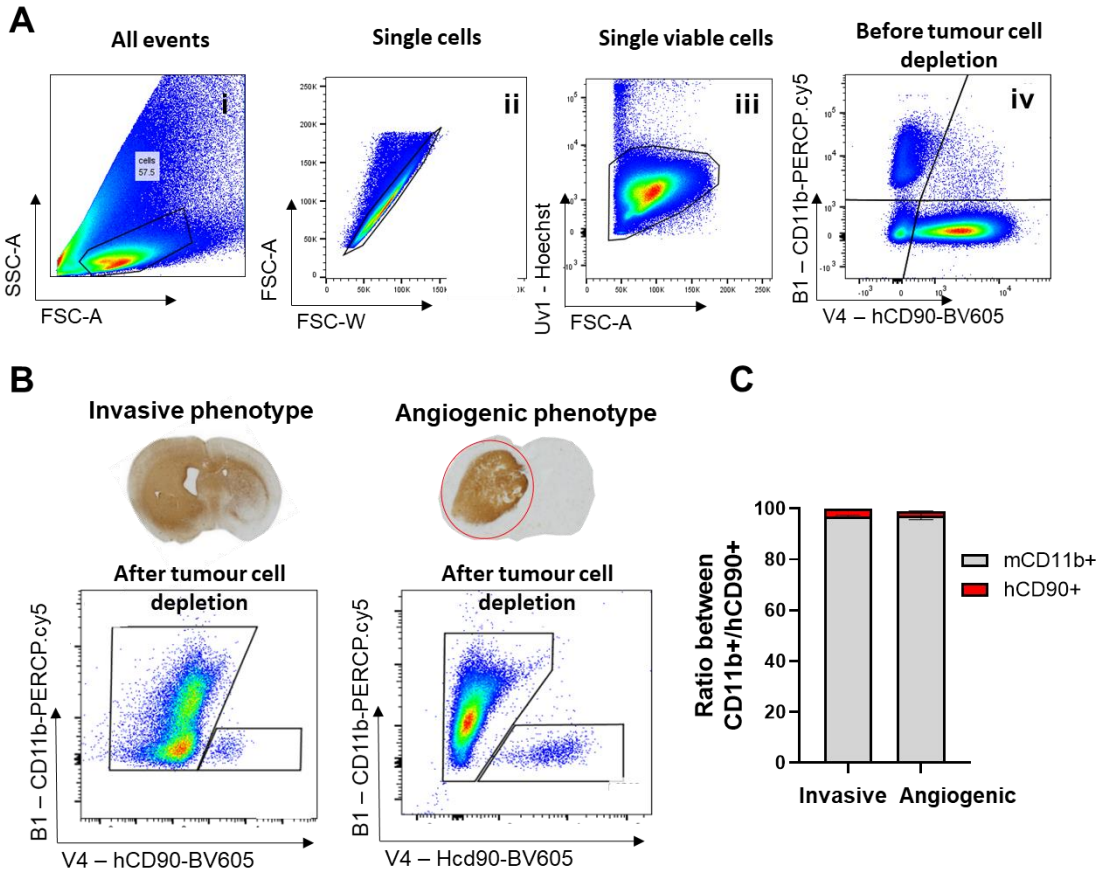

Figure 45. *Ex vivo* CD11b magnetic cell isolation of high viable CD11b+ TAMs in PDOX models. (A) Flow cytometry gating strategy. (i) Cells of interest were gated based on side scatter (SSC) and forward (FSC). (ii) Doublets were excluded based on the forward scatter height (FSC-H) versus forward scatter area (FSC-A). (iii) Hoechst was used to discriminate living cells. (iv) CD11b-PERCP.cy5 was used to gate the myeloid compartment and human CD90 BV605 to identify tumour cells. **(B)** Nestin immunohistochemistry staining depicting tumour mass and red circle denotes respective tumour core dissection. Bottom graphs depict CD11b enrichment population obtained for the invasive and angiogenic tumour phenotype upon tumour cell depletion step **(C)** Bar plots depicting the ratio between murine CD11b+ myeloid cells versus human CD90+ tumour cells obtained across the invasive (n = 2) and angiogenic (n = 2) tumour phenotypes after tumour cell depletion step (1 biological replicate).

In line with the scRNA-seq dataset, we detected an increased phagocytic ability of CD11b cells isolated from the invasive tumour phenotype compared to the corresponding cells harvested from the angiogenic phenotype and naïve mice (**Figure 46A, Table S14**). In line with these results, the expression of phagocytic markers (e.g. *Trem2* and *Tyrobp*) were significantly overexpressed on CD11b cells isolated from the invasive landscape when compared to the angiogenic landscape and naïve mice (**Figure 46B**). These results show higher phagocytic potential of microglia-like cells within the TME of the invasive tumour phenotype when compared to TAMs in the corresponding angiogenic

PDOX model. Whether macrophage-like cells have the potential to dampen the phagocytic capacity of resident microglia-like cells in the TME needs to be addressed.

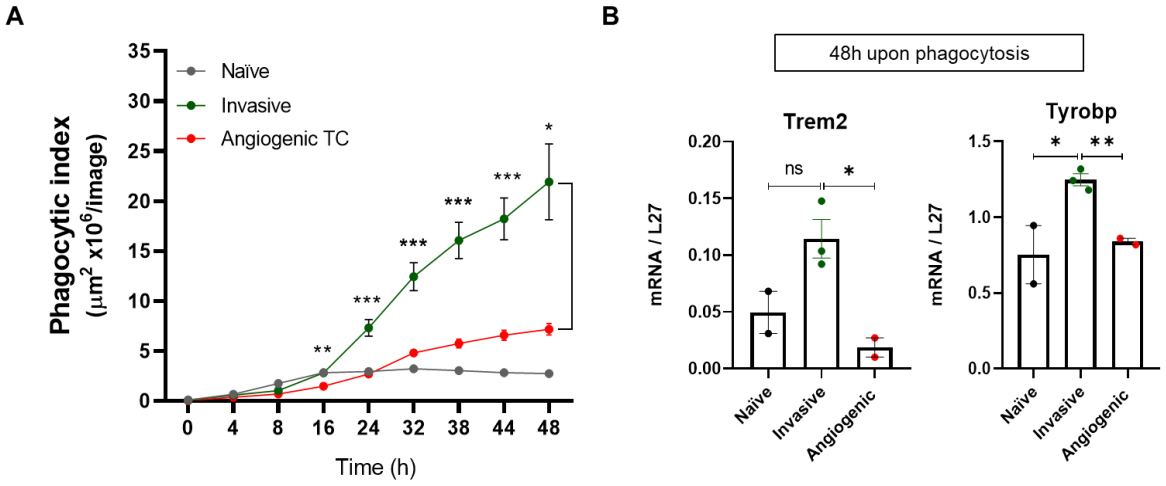

Figure 46. GBM-educated microglial cells display increased phagocytic capacity. (A) *Ex vivo* CD11b phagocytic uptake of pHrodo *E.coli* bioparticles from naïve and tumour-bearing mice. Two-way ANOVA followed by Tukey's multiple comparisons test (naïve n = 4, invasive n = 4 and angiogenic n = 4) (1 biological replicate) (**Table S14**). **(B)** Expression levels of the phagocytic markers *Trem2 and Tyrobp* from *ex vivo* CD11b cells 48h upon the phagocytic assay (naïve n = 2; invasive n = 3 and angiogenic n = 2) (1 biological replicate). Data are represented as mean ± SEM, * p <0.05, ** p <0.01, *** p <0.001, ns >0.05.

Phagocytosis is a mechanism employed by the cells, which leads to the proteolysis of exogenous antigens with the potential to display them on the cell surface via MHC class I and/or class II molecules (Mantegazza et al., 2013). Precisely, the cross-presentation of tumour antigens by TAMs is critical to initiate an adaptive immune response at the tumour site. Therefore, TAM phagocytic activity and antigen presentation to improve local anti-tumour response is a promising axis of investigation. In line with this notion, we further investigated antigen presentation cell markers, both at the gene and protein levels in tumour sections of the invasive tumour phenotype. The analysis of the relevant markers across our scRNA-seq datasets, showed that microglia-like cells exhibit an immunologically reactive signature associated with the down-regulation of the "homeostatic" genes (e.g. *P2ry12, Tmem119, Gpr34 and Hexb*) and the overexpression of antigen presenting cell markers (e.g. *Itgax, Igf1 and Cd74*) (**Figure 47A**). In the healthy brain, about 2–3% of the microglial cells are CD11c positive (Wlodarczyk et al., 2018). Preliminary immunofluorescence analyses, indicate that approximately 50% of the total activated IBA1 microglial cell population co-express MHC-II and CD11c (encoded by *Itgax*) in the invasive tumour phenotype (**Figure 47B-C**). Moreover, approximately 15% of IBA1 cells expressed CD11c independently of MHC-II molecules and

approximately 35% of IBA1 cells were CD11c negative and only 10% of them expressed MHC-II (**Figure 47C**). Overall, these results show differential activation states among GBM-educated microglia subsets and that distinct subsets differentially express antigen presenting cell markers within the tumour. CD11c is commonly used as a marker for dendritic cells specialized in antigen capture and MHC class II type antigen presentation to T cells. Whether different GBM-educated CD11c microglial subsets differently interact with T cell subpopulations in GBM would need to be further investigated.

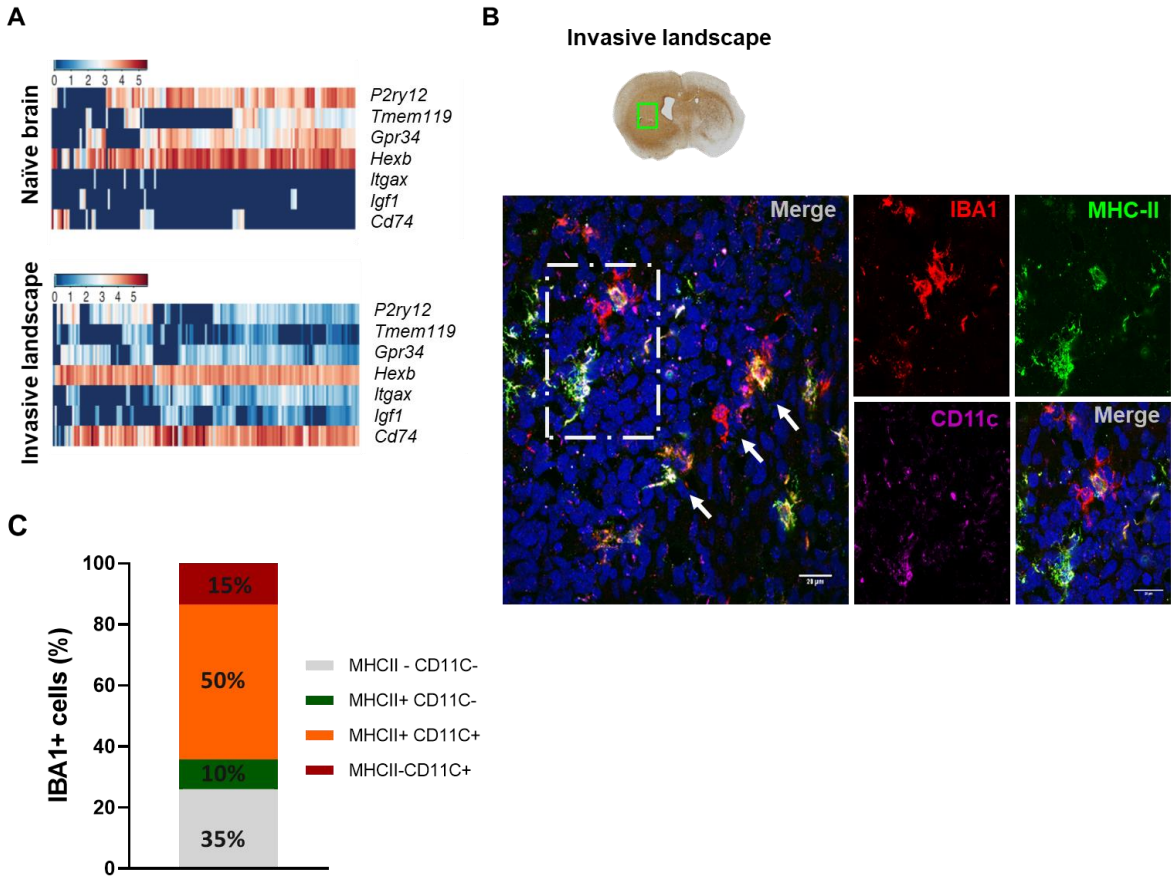

Figure 47. GBM-educated microglia subsets express antigen presenting cell markers. (A) Heat-map representation of microglia core genes (*P2ry12, Tmem119, Gpr34, Hexb*) and antigen presenting cell markers (*Itgax, Igf1, Cd74*) from scRNA-seq data from naïve mice and the invasive tumour phenotype **(B)** Representative immunofluorescence pictures depicting MHC-II and CD11c staining of IBA1 cells in the invasive tumour phenotype at late stage of GBM development. Scale bar = 20µm. **(C)** Percentage of IBA1 cells expressing MHC-II and/or CD11c in the tumour core of the invasive tumour phenotype at late stage (n = 2, 1 biological replicate).

One striking feature of microglia is their ability to actively sense the brain environment, thus they have the capacity to efficiently migrate to the sites of injury. Therefore, we evaluated the migratory capacities (see Materials and Methods section) of *ex vivo* CD11b cells from naïve and

tumour-bearing mice at late stage of GBM development (**Figure 48A**). As expected, tumour-educated CD11b cells showed higher migratory capacities compared to naïve CD11b cells (**Figure 48A**), independently of the GBM tumour phenotype. Moreover, in our experimental setting, *ex vivo* CD11b TAMs from the angiogenic phenotype displayed a less pronounced migratory ability in comparison to CD11b cells from the invasive tumour phenotype (**Figure 48A**), suggesting differential TAM-education profiles. By immunofluorescence, we confirmed that more than 99% of the migrated cells corresponded to IBA1 cells (IBA1: mean = 99.50% ± 0.52; HuNu: mean 2.51% ± 2.59) (**Figure 48B**).

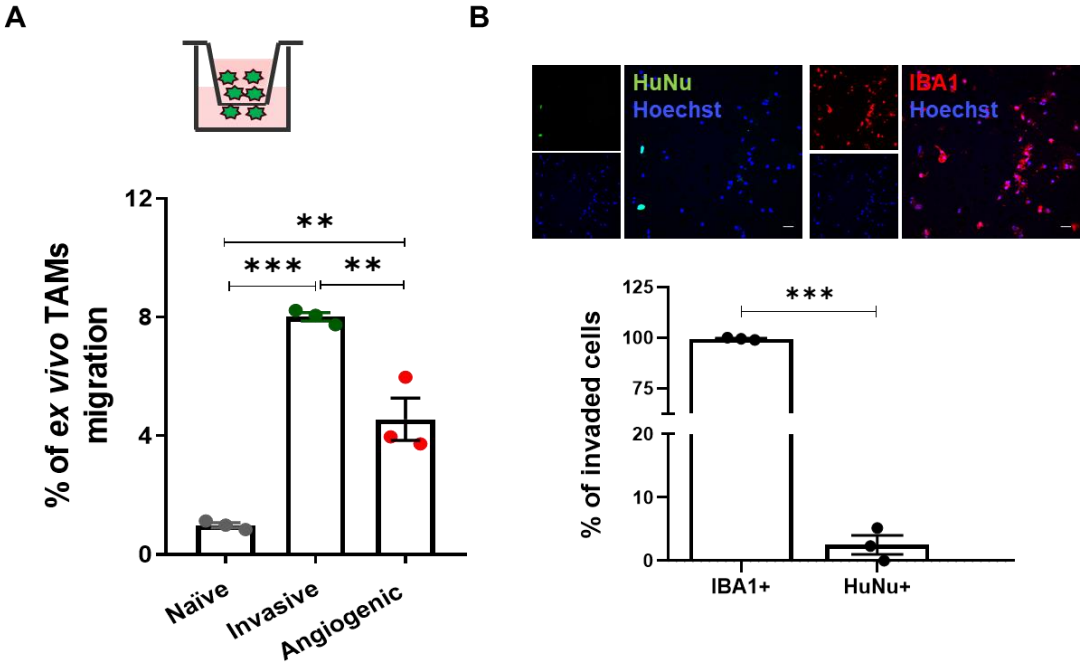

Figure 48. *Ex vivo* CD11b isolated cells display distinct migratory properties across GBM landscapes. (A) Percentage of migratory *ex vivo* CD11b cells from naïve (n = 3) and GBM tumour-bearing mice (invasive: n = 3; angiogenic: n = 3) (1 biological replicate) at late stage. Bars represent the mean ± SEM, ** $p < 0.01$, *** $p < 0.001$. **(B)** Immunofluorescence representative pictures depicting human nuclei (HuNu) and IBA1 cells upon the migration assay and respective quantification. Data are represented as mean ± SEM (1 biological replicate), *** $p < 0.001$.

GO analysis of microglia-like cells from the invasive tumour phenotype showed positive regulation of the MAPK cascade (**Figure 43C**). In fact, extracellular signal–regulated kinases (ERKs) or classical MAP kinases are known to play important roles in the signalling pathways that regulate microglia activation and chemotaxis. Therefore, we further investigated potential genes involved in microglial cellular migration. For this, we compared the up-regulated genes expressed by microglia-like cells from the invasive tumour phenotype versus naïve cells with the GO cell migration list extracted from the Mouse Genome Informatics (MGI) database (**Figure 49B, Table S15**). Here, we

specifically focused on various types of receptors expressed by the cells, such as integrin (e.g. *Itgax, Itgb1bp1, Itgb3, Itga5*), tyrosine kinases (e.g. *Flt1, Ptprc, Fgr, Ptk2b*) and surface receptors (e.g. P*tprc, Trem2, C3ar1, P2rx4, Tlr2, f2r, Nsmf, Itga5*) as potential modulators involved in microglia cellular migration to the tumour site (**Figure 49A**). Compared to naïve microglial cells, CD11b+ isolated cells from the invasive landscape showed increased gene expression levels of the integrin *Itgax* and the receptor *Trem2* compared to the counterparts of the angiogenic tumour phenotype (**Figure 49B**).

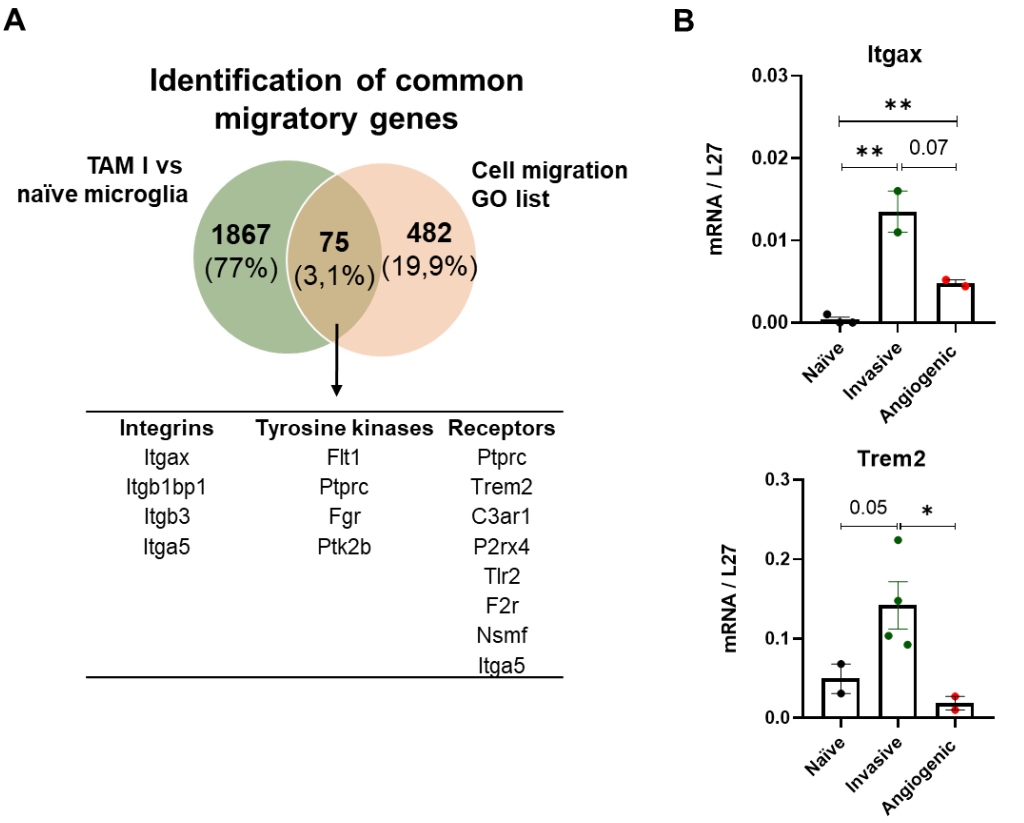

Figure 49. Tumour-associated microglia migratory genes investigation. (A) Venn diagram representation showing shared (n = 75) up-regulated genes in TAM I versus naïve microglia cells versus cell migration list extracted from the Mouse Genome Informatics and intersection shows a selection of integrin, tyrosine kinases and receptor genes involved in motility processes (see **Table S15**). **(B)** Expression levels of *Itgax* and *Trem2* in CD11b+ cells from naïve and tumour-bearing mice at later stages (naïve n = 2; invasive tumour phenotype n = 2 and angiogenic tumour phenotype n = 2) (1 biological replicate). Data are represented as mean ± SEM, * p <0.05, ** p <0.01, ns > 0.05.

Overall, we observed that distinct GBM landscapes differently educate and influence TAM functional adaptation in the TME.

CHAPTER 5

DISCUSSION

GBM is a highly heterogeneous tumour, and several cellular players co-exist and co-evolve together with the tumour cells. Within the TME, TAMs are increasingly recognized as critical players in shaping the local microenvironment, not only for being the most abundant cell population accounting for up to 40% of the stromal compartment, but also for their pro-tumorigenic phenotype contributing to tumour growth and progression (Hambardzumyan et al., 2016). Therefore, understanding TAMs plasticity and functional heterogeneity in GBM is imperative for the development of new therapeutic strategies. In particular, elucidating mechanisms contributing to distinct functional adaptations in the TME may be key to re-educate TAMs toward anti-tumour immune phenotypes in GBM.

I. Elucidating tumour-associated microglia/macrophage diversity along Glioblastoma progression and under aconitate decarboxylase 1deficiency

5.1. Resident microglia and peripheral monocytic-derived macrophages display discrete functional adaptation in Glioblastoma

We took advantage of the GL261 syngeneic mouse model as a widely used paradigm for immunotherapy studies in GBM (Oh et al., 2014). This model allows the engraftment of immortalized tumour cells from the same strain with low immune rejection, thus enabling the investigation of an immunocompetent TME in vivo, including functional T and B cells (Aslan et al., 2020; Fecci et al., 2007; Qian et al., 2018). Recent studies aiming at comparing datasets obtained in GBM patients with distinct GBM syngeneic mouse models, identified high correlation levels with both the 005 and GL261 models, thus serving as reliable preclinical models recapitulating several GBM patient features (Khalsa et al., 2020).

In GBM, resident parenchymal microglia are difficult to segregate from peripheral infiltrative immune cells, which prevalently constitute the myeloid compartment of the TME. Experimentally, approaches to distinguish resident microglia from other inflammatory immune cells entering the CNS have traditionally relied on CD45 expression to discriminate resident microglia (CD11b+CD45low cells) from peripheral monocyte-derived macrophages (CD11b+CD45high cells). However, this strategy has been challenged showing that glioma-associated microglia upregulate CD45 expression, thus limiting the effective discrimination of both populations in GBM (Muller et al., 2015). In recent years, the transcriptional signatures of microglia and macrophage-like cells in the TME has

been possible due to advances on single cell technologies (Darmanis et al., 2017; Muller et al., 2017; Ochocka et al., 2021).

In our dataset, we have shown that the myeloid compartment in tumour-bearing GL261 mice displays the highest number of differentially expressed genes compared to respective counterparts in naïve mice, indicating a prominent adaptation of the myeloid compartment in the TME. We have been able to discriminate at the transcriptional level microglia-like (e.g., *Gpr34, Hexb, P2ry12, Siglech, Sparc*) from macrophage-like (e.g., *Arg1, Ccr2, Ly6c2, Mrc1, Tgfbi*) cells in the GL261 syngeneic model. Similar findings have been reported by others using the GL261 syngeneic model (Bowman et al., 2016; Ochocka et al., 2021) and in GBM patients (Darmanis et al., 2017; Muller et al., 2017; Pombo Antunes et al., 2021; Venteicher et al., 2017). Additionally, in line with the decrease of homeostatic genes in microglia under inflammatory conditions (Sousa et al., 2017; Sousa et al., 2018) and human GBM (Pombo Antunes et al., 2021; Sankowski et al., 2019), microglia-like cells displayed a decreased expression of these genes (e.g. *Siglech, P2ry12, Gpr34*) in the GL261 syngeneic tumour-bearing mice when compared to the naïve mice.

Elegant genetic mouse models have demonstrated that microglia and BMDMs are both present in gliomas and possess distinct transcriptional states (Bowman et al., 2016). Notably, we uncovered high transcriptional heterogeneity within microglia- and macrophage-like populations in the TME. Specifically, the main difference between TAM I subsets relied on the differential expression of the microglia homeostatic genes and inflammatory genes (e.g. *Stat1, Il-1β*), while TAM II subpopulations differently up-regulated genes associated with antigen presentation (e.g. *H2-K1, H2-D1*, *H2-Aa, Cd74*), positive regulation of angiogenesis (e.g. *Lgals3, Il1β, Cybb, Thbs1, Plek, Vim, Stat1*) and metabolic redox metabolism (e.g. *Cybb, Msrb1*). Overall, these results highlight the presence of heterogeneous TAM populations and their diverse transcriptional adaptation profiles in the TME of the GL261 syngeneic GBM model.

Several studies have demonstrated the distinct roles of microglia and macrophages in CNS diseases (Ajami et al., 2011; Greenhalgh et al., 2018; Shemer and Jung, 2015). To date, the understanding of the individual roles of microglia and macrophages in GBM are only partially understood. We identified common immunological terms shared by both microglia- and macrophage-like cells (e.g. inflammatory response and innate immune response) in the TME of GL261 syngeneic murine model by performing gene set enrichment analysis. Additionally, we also uncovered exclusive terms for microglia-like cells (e.g., positive regulation of phagocytosis and T cell mediated cytotoxicity) and macrophage-like cells (e.g. positive regulation of cell migration and oxidation-reduction process), thus highlighting distinct ontogeny-based functional adaptations in the TME.

Nevertheless, we cannot exclude that diverse transcriptional adaptations of TAMs might also be influenced by the spatial localization of these cells and by specific GBM loco-niche cues.

Several studies point out that a higher presence of immunosuppressed monocyte-derived macrophages in the TME contributes to GBM progression. Precisely, immunosuppressive immune cell infiltrates increase from grade 2 to grade 4 (Pinton et al., 2019) and a reduced immune suppressive phenotype correlates with extended survival, as observed in LGG patients (Alban et al., 2018). In order to verify the prognostic value of microglia- and macrophage-like transcriptional signatures in glioma patients, we took advantage of The Cancer Genome Atlas (TCGA) database. The TCGA project started in 2006 with the aim to provide with large-scale multidimensional analysis of genetic mutations of human cancers, using genome sequencing and bioinformatics. Today, it comprises over 20,000 primary cancer and matched normal samples spanning from 33 cancer types (Cancer Genome Atlas Research, 2008). In our study, we took advantage of two publicly available TCGA-databases (TCGA-HGG: high-grade glioma and TCGA-LGG: low-grade glioma). Notably, our results demonstrate macrophage-like-enriched signature correlates with a worse patient survival compared to a microglia-like-enhanced program, supporting the notion that TAMs differently contribute to glioma patient survival. In line with our findings, higher ratio of microglia to macrophage-like cells correlates with increased GBM patient survival (Woolf et al., 2021). Moreover, macrophage-like cells from GBM biopsies exhibited higher levels of immunosuppression compared to microglial cells, when assessed their ability to interfere with the proliferation of activated T cells (Pinton et al., 2019). Also, microglial cells from grade 2 and 3 gliomas showed reduced immunosuppressive activity, indicating differential myeloid immune tolerogenic features in gliomas (Pinton et al., 2019). These results are of relevance as therapeutic strategies targeting TAMs indiscriminately have not shown significant improvement in the clinic. Taken together, these findings suggest that the presence of microglia within the TME may be beneficial and highlight the importance of cell-type specific therapies, such as targeting macrophage-like cells whilst sparing resident microglia-like cells.

5.2. Resident microglia and peripheral monocytic-derived macrophages display distinct transcriptional adaptation along Glioblastoma progression

Recent literature has pointed out the role of the brain microenvironment in shaping the microglial phenotype in a time- and region-dependent manner (Gosselin et al., 2014; Lavin et al., 2014; Masuda et al., 2019). Much of the knowledge regarding TAMs adaptation in GBM derives from studies at late

stages of the disease. This is due to the already advanced stage of the disease when GBM patients are diagnosed. In addition, there are currently no standard diagnostic or prognostic strategies for early stages GBM, which further limit our knowledge regarding TAMs adaptation along GBM progression.

In order to understand TAMs functional adaptation along GBM development, we investigated microglia and macrophage-like transcriptional signatures at early and late stage of GBM progression taking advantage of the syngeneic GL261 GBM mouse model. Briefly, tumour progresses through four main stages over a four-week period following implantation: perivascular organization, proliferation near vasculature, hypoxia through blood vessel degeneration and neovascularization towards necrotic regions (Oh et al, 2014). Thus, the orthotopic syngeneic GL261 GBM mouse model recapitulates several characteristics of GBM in patients (Ausman et al., 1970).

In our dataset, we detected microglia and macrophage-like cell subsets across all the analysed tumour stages (i.e. early, intermediate and late time points), thus indicating that, in agreement with previous studies, the infiltration of monocyte-derived macrophages occurs early during tumour development in GL261 model (Bowman et al., 2016). Notably, we detected a gradual decrease in the number of up-regulated differentially expressed genes between microglia and macrophage-like cells along tumour stages, indicating that the transcriptional programs of microglia-like and macrophage-like cells converge over time. Recently, in human GBM recurrent tumours, it has been uncovered that a subset of macrophage-like cells (SEPP1^{low}) express microglial signature genes (e.g. *CX3CR1, BIN1*, *SCIN*) suggesting macrophage-like cells transcriptionally adopt a resident-like signature (Pombo Antunes et al., 2021).

Along GBM progression, the ratio between microglia and macrophage-like populations did not significantly change across early and late stages. The analysis of up-regulated genes characterizing microglia and macrophage-like cells at early and late tumour stages versus naïve microglia uncovered a core transcriptional programme maintained along GBM progression. Particularly, both microglia and macrophage-like cells displayed a down-regulation of genes associated with antigen processing and presentation (e.g., *Cd74, H2-Ab1, H2-Aa*) and regulation of T-helper cells (e.g., *H2-Q7, H2-T23*) at late stage. In line with our scRNA-seq dataset, we observed a significant decrease of the antigen presenting cell markers MHC-II and CD74 at the protein level in both microglia and macrophage-like cells at later stage. The reduced antigen cross-presentation ability of both microglia- and macrophage-like cells at late stage may add to the recognised poor recruitment of T cells to the tumour site in GBM (Woroniecka et al., 2018), thus dampening potential T-cell-mediated anti-tumour responses in GBM. Precisely, e*x vivo* functional profiling of microglia- and macrophage-like cells from GL261 syngeneic model, revealed that both TAM populations were unable to induce

allogeneic CD4+ or CD8+ T-cell proliferation, thus demonstrating their poor T-cell stimulatory potential to induce adaptive anti-tumour immunity in GBM (Pombo Antunes et al., 2021). Notably, we measured higher percentage of IBA1 cells expressing MHC-II at the tumour margin compared to tumour core both at early and late stages. These results highlight microglia-like cells display higher immune reactive profiles compared to macrophage-like cells in the syngeneic GL261 model. In this context, although macrophage-like cells have been shown to possess higher immunosuppressive features compared to microglial cells (Pinton et al., 2019), recent results have shown that microglia-like cells show higher capacity to suppress T-cell proliferation compared to macrophage-like cells from GL261 syngeneic model (Pombo Antunes et al., 2021). These contradictory results might be explained due to species differences, thus more functional validations are needed to appreciate their respective contribution in GBM.

Focusing on tumour-associated microglia transcriptional adaptation along GBM development, we identified genes associated with chromatin remodelling (e.g. *Cbx5, Ezh2, Nasp*) at later stages. In particular, we found a subset of microglia-like cells up-regulating enhancer of zeste homolog 2 (*Ezh2)* expression. *EZH2* is a histone methyltransferase and together with the catalytic subunit of the polycomb repressive complex 2 leads to epigenetic silencing of target genes through the tri-methylation of the lysine 27 at the histone H3 (H3K27me3). In microglia, *Ezh2* expression is increased upon a pro-inflammatory stimuli mediated through TLR4 stimulation (Zhang et al., 2018) and has been proposed to promote a M1-like state by repressing the expression of suppressor of cytokine signalling 3 (SOCS3) gene (Cheray and Joseph, 2018). Inhibition of EZH2 with the selective small molecule inhibitor EPZ-6438 suppressed the expression of the transcription factors IRF1, IRF8 and STAT1, which regulate inflammatory responses (Arifuzzaman et al., 2017). Here, we hypothesize that a subset of microglia-like cells might upregulate *EZH2* histone methyltransferase as a timely inflammatory-associated response in the local microenvironment, which may be exploited to enhance anti-tumour immunity at later GBM stages. Moreover, these results indicate the importance of epigenetic mechanisms in the control of microglia polarization toward a specific phenotype or activation state that could differentially affect the TME.

Another level of plasticity comes from the intrinsic capacity of TAMs to rapidly reorganizing their actin network to fulfil specific *on-site* demands. In this context, microglia-like cells exhibited an actin nucleation/polymerization enriched gene signature (e.g. *Arpc1a, Arpc1b, Arpc2, Arpc3, Arpc5*) at later stages. Dynamic remodelling of the Arp2/3 complex is known to partially regulate various cellular processes such as division, phagocytosis and migration (Jimenez et al., 2000). In DCs, Cdc42- and Arp2/3-mediated accumulation of F-actin at the cell front slows motility, while this process is required for micropinocytosis and antigen uptake in immature dendritic cells (Vargas et

al., 2016). Interestingly, at later stages, we also identified enrichment of GO terms associated with pinocytosis and ATP synthesis. ATP efficiently triggers pinocytosis in microglia (Li et al., 2013a) and it has been described that resting microglia employs pinocytosis to monitor their microenvironment as a mechanism of immune surveillance (Nimmerjahn et al., 2005). Specifically, pinocytosis is described as a type of endocytosis process employed by the cells to engulf external fluids and mechanisms underlying the regulation of pinocytosis by microglia in the context of GBM have not been elucidated yet. Autocrine ATP signalling triggered microglial pinocytosis of amyloid-beta uptake through the activation of P2Y4 purinergic receptors (Li et al., 2013a). Different purinergic receptors have been shown to modulate the microglial phenotype associated with distinct microglial functions (Illes et al., 2020). In this context, the A2RA and P2RX4 purinergic receptors are upregulated in microglia leading to processes retraction allowing their migration to the injury site where they adopt an amoeboid morphology. In this morphological state, activation of P2RY6 mediates phagocytosis, while activation of P2RY4 promotes pinocytosis in spinal cord microglia (Illes et al., 2020). No specific studies have addressed the role of pinocytosis as an immune surveillance or anti-tumour mechanism employed by the innate immune cells in GBM. Whether this mechanism is employed by GBM-educated microglia also awaits further investigations.

Next, focusing on macrophage-like cells transcriptional adaptation during GBM progression, we detected a drastic reduction of type I interferon genes (e.g. *Irf1* and *Stat1*) together with an over-representation of GO terms associated with positive regulation of oxidative phosphorylation, angiogenesis and wound healing, suggesting macrophage-like cells display a characteristic M2-like signature at later stages. Anti-inflammatory TAMs have a proangiogenic role and increased numbers of macrophages around blood vessels is observed in GBM compared to healthy tissue (Hughes et al., 2015). In this context, CD163+ TAMs have been identified in proximity of CD31+ vascular structures (Klemm et al., 2020). An anti-inflammatory signature is characterized by a decreased glycolytic profile and enhanced oxidative phosphorylation (Mills et al., 2017). In line with this notion, it has been shown that blood-derived TAMs exhibit decreased glycolytic metabolism compared to microglia TAMs in human gliomas. Moreover, this metabolic reprogramming has been described to potentiate immunosuppression in the TME and being associated with poor patient survival in glioma (Muller et al., 2017).

In line with potential repolarization towards an M1-like phenotype, we observed enrichment of “activation of phospholipase D (PLD)” at later stages. PLD is a widely expressed enzyme that catalyses the hydrolysis of phosphatidylcholine, the major phospholipid in the membrane, to produce the water-soluble choline and phosphatidic acid (Zhu et al., 2018). PLD is rapidly activated in response to extracellular stimuli and its activity is regulated by many factors including small

GTPases, kinases or phosphoinositides (Brandenburg et al., 2014). Its precise role in the TME nor the link between PLD-mediated immune responses in GBM have been elucidated. Recent work has demonstrated that ablation of *Pld2* significantly promotes tumour growth associated with reduced CD8 T cell numbers in B16 melanoma and Lewis lung carcinoma mouse models. Moreover, engraftment of bone marrow cells into *Pld2*$^{-/-}$ mice significantly reduced B16 melanoma tumour growth (Ngo Thai Bich et al., 2018) suggesting its potential role in anti-tumour immunity. Macrophages lacking either PLD1 or PLD2 exhibit impaired phagocytosis and cell migration due to abnormal cytoskeletal organization (Ali et al., 2013). Additionally, it has been shown that PLD2 is critical for the proliferation and survival of CD8 T cells through activation of the Ras/Erk signalling pathway (Zhu et al., 2018). Therefore, PLD activity might represent a signalling mechanism with the potential to recruit the adaptive immune system to the TME. Here, it might be interesting to investigate whether macrophage-like cells up-regulate PLD activity as an intrinsic response mechanism to enhance anti-tumour immunity at later stages.

Collectively, our analyses across different stages of GBM development evidenced TAM distinct transcriptional programmes and their potential role as functional unit to shape the local anti-tumour immune response. Therefore, a new concept may emerge in which by boosting their anti-tumour functions across different phases of the disease, TAMs may be exploited for the development of innovative therapies in GBM.

5.3. Tumour-associated microglia/macrophages display higher immunological reactivity under aconitate decarboxylase 1 deficiency affecting T cell recruitment

Immune cells flexibly adapt their metabolic profile to sustain their polarization and function in specific environments (Gosselin et al., 2014). Under inflammatory conditions, the IRG1/ACOD1 gene is highly induced in myeloid cells and its encoded enzyme catalyses the decarboxylation of cis-aconitate, an intermediate metabolite of the TCA cycle to produce itaconate (Michelucci et al., 2013). Importantly, ACOD1-mediated itaconate production has been shown to inhibit LPS-induced cytokines, such as IL-6, IL-12, IL-1β, and type I IFN production in bone marrow derived macrophages, contributing to the resolution of inflammation (Hooftman and O'Neill, 2019; Mills et al., 2018). In the tumour context, itaconate has been measured in GBM patients (Wibom et al., 2010) or with lung cancer (Fan et al., 2016). In glioma patients, up-regulation of ACOD1/IRG1 expression levels was higher in CD49D^{high} macrophages compared to CD49D^{low} microglial cells (Klemm et al., 2020). These observations are in agreement with our results, where we identified a major

transcriptional effect of *Acod1*-deficiency in macrophage-like cells compared to microglial cells. To our knowledge, no studies have yet addressed the potential role of the ACOD1-itaconate axis in the myeloid compartment along GBM progression. In our analyses, we mainly detected *Acod1* induction in a subset of myeloid cells at early stages, while its expression was reduced at later tumour stages, indicating a time-dependent expression of *Acod1* in myeloid cells in GBM. Similarly, early induction of *Acod1* mRNA levels has been also observed upon LPS stimulation (Dominguez-Andres et al., 2019; Michelucci et al., 2013).

Focusing on the early stages, increased transcripts associated with TAM recruitment, such as *Ccr2, Mif, Ldha and Tspo*, were up-regulated in *Acod1* KO mice at early stages when compared to WT tumour-bearing mice. In line with these results, increased numbers of IBA1 cells were detected at early stages by immunofluorescence supporting myeloid recruitment to the tumour site. Previous reports have shown the crucial role of CCL2/CCR2 axis for monocyte migration into the inflamed CNS (Chen et al., 2017; Zhang et al., 2012). Precisely, a decreased number of infiltrative peripheral monocytes has been observed in *Ccr2*-KO mice at single cell resolution, supporting its origin in GBM (Pombo Antunes et al., 2021). Additionally, macrophage migration inhibitory factor (MIF) possesses chemokine-like functions and, functioning as a ligand for CXCR2 and CXCR4 chemokine receptors, it enhances monocyte recruitment and leukocyte chemotaxis in cancer (Guda et al., 2019). To date, a variety of MIF biological functions have been identified. For example, its ability to enhance the capacity of macrophages to kill intracellular parasites and tumour cells, its role to increase TNF, IL-1β and IFN-γ pro-inflammatory cytokines (Mitchell et al., 2002). In this context, we might speculate that increased *Mif* expression levels are employed in an autocrine fashion by TAMs to support their infiltration to the tumour site under *Acod1* deficiency.

At later stages, in comparison with WT mice, TAMs in *Acod1* KO mice displayed an enhanced immune activation profile characterized by the overexpression of markers associated to antigen processing and presentation via MHC class II (e.g. *Cd74, H2-Ab1, H2-Aa*) and inflammation (e.g. *Irf1*). We previously showed that macrophage-like cells in WT mice at later stages, exhibit a drastic reduction of type I interferon genes (e.g. *Irf1* and *Stat1*) associated with decreased antigen presentation features. Gene regulatory network analyses identified IRF1 among the main transcription factors regulating ACOD1 expression in mouse and human macrophages. In this context, siRNA targeting IRF1 correspondingly reduced *Acod1/Irg1* expression in macrophages (Tallam et al., 2016). It has been shown that IRF1 induction is mediated by type I and not type III interferons (Forero et al., 2019). Taken together, we hypothesise that type I IFN signalling might be responsible for the temporal regulation of *Acod1* in TAMs, thus, affecting their immunogenicity in GBM. In line with an increased TAM immunogenic signature in the *Acod1* KO mice, we detected

increased lymphocytic tumour infiltration compared to WT mice, suggesting an effective crosstalk between TAMs and the adaptive immune cell compartment in the TME. Applying single cell trajectory inference analysis, we observed that *Acod1* deficiency supports macrophage-like cellular diversity in GBM, independent of the tumour stage. Furthermore, we detected a subset of macrophage-like cells in *Acod1* KO mice that might support leukocyte migration to the tumour site (e.g., *Ccl17, Ccl22, Ccr7, Il12b* and *Cd1d1*). These results support the notion that A*cod1* deficiency enhances TAMs immunogenicity and diversity in the TME, with the potential to mediate T cell recruitment to the tumour site. As IDH-wildtype gliomas are characterized as "lymphocyte-depleted" subtype (Thorsson et al., 2018), these results demonstrate the potential role of the ACOD1-itaconate axis as a key immunometabolic component regulating innate and adaptive immune responses in GBM.

Lastly, despite enhanced TAM immunogenic phenotype with subsequent increased T cell infiltrates, we did not observe differences regarding the tumour growth neither we detected differences in the mouse survival between WT and *Acod1* KO GL261 tumour-bearing mice. However, it is important to notice that increased numbers of macrophage-like cells in *Acod1* KO mice did not correlate with decreased mouse survival rate, as we would expect according to our survival curves obtained from LGG and HGG patients. These results suggest that the TAM immune signature, rather than the TAM numbers at the tumour site, might be a better prognostic feature to take into consideration.

From a therapeutic point of view, although immune checkpoint blockade therapy has markedly improved survival in several immunogenic cancers, such as melanoma, its efficacy has not been extended to GBM patients, as observed in a randomized phase III clinical trial for recurrent GBM (CheckMate 143; Identifier NCT 02017717) (Reardon et al., 2020). As it is becoming increasingly evident that a mono-therapeutic approach is unlikely to provide anti-tumour efficacy, the combination of ACOD1 suppression in TAMs, which enables to harness both the innate and adaptive immune systems, together with immune checkpoints inhibitors , may advance therapeutic successes against GBM and other solid tumours.

II. Revealing tumour-associated microglia/macrophage heterogeneity across distinct Glioblastoma landscapes

5.4. Tumour-educated microglia/macrophages display distinct transcriptional adaptation across Glioblastoma landscapes

Loss of immunosuppressive signatures and acquisition of TAM pro-inflammatory phenotypes correlate with increased survival in mice and patients with diverse forms of cancer (Kaneda et al., 2016). Recent work elucidated differential TAM compositions dependent on tumour grade and genotype. In this context, IDH-mutant or LGG exhibited a predominance of microglial cells, while IDH-wildtype or HGG showed an increased invasion of monocyte-derived infiltrative cells (Friebel et al., 2020; Klemm et al., 2020).

TAMs spatial characterization is starting to shed light on their distinct functional adaptation within particular tumour niches. PDOX mouse models represent unique pre-clinical avatars to study specific features recapitulated in GBM patients (Golebiewska et al., 2020). In our study, we took advantage of two distinct paradigms of the disease displaying different tumour intrinsic architectures, including an invasive and an angiogenic tumour pattern. Previous work from the NORLUX Neuro-Oncology Laboratory has shown the presence of a disrupted BBB in the angiogenic compared to the invasive landscape by MRI contrast imaging (Bougnaud et al., 2016). In line with its angiogenic feature, by scRNA-seq, we detected higher percentage of endothelial cells composing the TME (20.42%) in comparison to the naïve brain (2.48%) and the invasive landscape (7.06%). Moreover, peripheral blood analysis showed significant reduction of platelet and red blood cell counts in the angiogenic landscape compared to naïve mice and the invasive tumour phenotype. It was shown that platelets carrying immune molecules (e.g., TGF-β, β-2 microglobulin) can contribute to the maintenance of brain homeostasis (Leiter and Walker, 2019). Whether platelet and red blood cells have the potential to migrate to the brain to exert wound healing roles or participate in the angiogenic cascade requires further investigation. Additionally, local endothelial proliferation may occur and the recruitment of platelets and red blood cells from the peripheral blood could ultimately contribute to the local endothelial pool in the angiogenic landscape.

Similarly to the GL261 syngeneic model, we were able to discriminate at the transcriptional level microglia-like from macrophage-like cells in the PDOX models. By scRNA-seq, we detected a higher percentage of macrophage-like cells in the angiogenic tumour phenotype compared to the corresponding invasive phenotype. In line with these findings, previous work in the laboratory showed increased inflammatory monocytes in the angiogenic landscape. Taken together, these results demonstrate enhanced peripheral monocytic infiltration in the angiogenic tumour phenotype, while the invasive phenotype is mainly characterized by a microglia enriched microenvironment. Notably, the angiogenic tumour phenotype associated with peripheral infiltration displayed shorter mouse survival compared to the invasive tumour phenotype (Bougnaud et al., 2016).

Under homeostatic conditions, microglia exhibit highly branched processes allowing the constant surveying of the local environment. When microglia encounter tissue damage, they become

active and dynamically modify their morphology by reducing their branches (Tremblay et al., 2011). This phenomenon has been reported in various diseases, including Alzheimer's disease (AD), amyotrophic lateral sclerosis (ALS) and demyelinating diseases (Holtman et al., 2015; Kamphuis et al., 2016; Remington et al., 2007). Similar results have been described in both murine and human GBM samples (Chen et al., 2017; Kvisten et al., 2019). Independently of the tumour phenotype, we detected increased numbers of IBA1+ cells in tumour sections compared to naïve brain, supporting TAMs recruitment to the tumour site in our PDOX models. As previously described by others, tumour-associated microglia showed remarkable morphological alterations as assessed by IBA1 surface area measurements. Specifically, microglia-like cells exhibited reduced branching compared with distal ramified microglia in the angiogenic landscape, supporting morphological regional heterogeneity of microglia-like cells in GBM tumour sections.

Investigation of the exclusive up-regulated genes in both microglia and macrophage-like cells uncovered a major transcriptional adaptation of these cells in the angiogenic landscape, supporting TAMs niche-specific transcriptional education in GBM. Moreover, despite exhibiting an immune reactive profile across the two analysed GBM landscapes, our work demonstrates that distinct tumour-intrinsic properties differentially affected microglia-like transcriptional programmes in the TME. The analysis of the relevant markers across our scRNA-seq datasets showed that microglia-like cells exhibit an immunologically reactive signature associated with overexpression of antigen presenting cell markers (e.g. *Itgax*, *Igf1* and *Cd74*) at later stages. In the healthy brain, only about 2–3% of microglial cells express CD11c (coded by *Itgax*). In response to CNS damage, CD11c expressing microglia was found in neuroinflammatory and neurodegenerative conditions (Butovsky et al., 2006; Remington et al., 2007). Approximately 60% of CD11c+ microglia was detected in the experimental autoimmune encephalomyelitis (EAE). In this context, it was reported that CD11c-microglia expressed low levels of MHC II and co-stimulatory molecules and were poor inducers of T cell proliferation (Wlodarczyk et al., 2014). Lastly, in the context of AD, CD11c+ microglia counteract amyloid deposition via increased Aβ-uptake and degradation, suggesting their enhanced phagocytic capacity (Kamphuis et al., 2016; Keren-Shaul et al., 2017). In the invasive tumour phenotype, 50% of the total activated microglia cell population co-expressed MHC-II and CD11c. Independently of MHC-II expression, we also observed that 15% of the cells expressed CD11c. These results show that GBM-educated microglia cells exhibited heterogeneous antigen-presenting cell subsets characterized by differential surface expression of MHC-II and CD11c.

5.5. Glioblastoma-educated microglia exhibit higher immune reactive profile

Increased phagocytic ability within the brain along with increased MHC-II molecules are characteristics of immune reactive microglia (Vilhardt, 2005). It has been described that phagocytosis favours M1-like phenotype promoting antigen presentation via MHC-I and MHC-II expression (Lecoultre et al., 2020). In cancer, TAMs phagocytic activity is emerging as a new mechanism to mediate tumour immunity in the TME with the potential to induce long-lasting and efficient anti-tumoral immune responses in GBM (von Roemeling et al., 2020). Cell–cell interactions between SIRPα on microglia and CD47 on tumour cells have been shown to suppress microglia phagocytosis in GBM (Hutter et al., 2019). We have shown that associated with increased antigen-presenting cell signatures, GBM-educated microglia cells exhibit increased phagocytic capacity in the invasive tumour phenotype compared to the counterparts in the angiogenic landscape. Some reports have highlighted the reciprocal signalling between microglia and macrophages, which differently contributes to their divergent functions in the CNS. For example, in the context of spinal cord injury, increasing numbers of infiltrative macrophages correlate with the suppression of the microglial inflammatory profile with subsequent reduced phagocytic ability (Greenhalgh et al., 2018).

As previously mentioned, actin remodelling is essential for cellular migration and purinergic receptors have been described to mediate chemotaxis of multiple cell types (Di Virgilio and Vuerich, 2015). ATP, the primary nucleotide in the CNS, regulates various physiological functions of microglia (Kettenmann et al., 2011; Koizumi et al., 2013) and microglial cells express several receptors for extracellular nucleotides named P2 receptors. Specifically, the expression levels of these receptors are largely dependent on their environment and respective set of purinergic receptors varies according to microglia phenotypes (Koizumi et al., 2013). On the basis of their signalling properties, P2 receptors can be further subdivided into metabotropic P2Y receptors (P2YRs) that are G-protein-coupled, and ionotropic P2X receptors (P2XRs) that are nucleotide-gated ion channels (Domercq et al., 2013). Activated microglia upregulates P2X4 receptor, which promotes P2Y12 receptor-mediated microglial migration to the injured sites (Koizumi et al., 2013). Under pathological conditions, the expression of the P2X4 receptor is increased (Inoue et al., 2005; Tsuda et al., 2003). By scRNA-seq, we identified *P2x4* receptor at later stage in GBM-educated microglia cells from the invasive tumour phenotype. Precisely, P2X4 receptor has been shown to mediate microglial chemotaxis towards regions of cell damage (Kurpius et al., 2007), while its pharmacological blockade suppressed microglia chemotaxis (Ohsawa et al., 2007). Additionally, microglia P2X4R activation drives phagocytic activity as a neuronal repair mechanism in the EAE model (Zabala et al., 2018). Phagocytic microglia are characterized by increased levels of P2Y6 receptors while migratory microglia by decreased levels of P2Y12 receptors, which might suggest a functional shift

from migratory to a phagocytic phenotype (Koizumi et al., 2007). In fact, P2X4 receptor can be localized both at the plasma membrane and at the lysosomal membrane, therefore its expression and downstream signalling activation might also depend on the local environment. In GBM, P2X4R protein expression was found to be expressed by TAMs in the C6 rat experimental GBM model (Guo et al., 2004). Hence, microglial purinergic receptors may be important in regulating microglia functions in GBM, including chemotaxis and phagocytosis, in a mutually exclusive but coordinated fashion. Hence, future perspectives might focus on the rationale of increasing TAM phagocytic activity and antigen presentation for an orchestrated anti-tumour immune response, as a mechanism to promote T-cell mediated adaptive immune responses.

A summary of the major findings is shown in **Figure 52**.

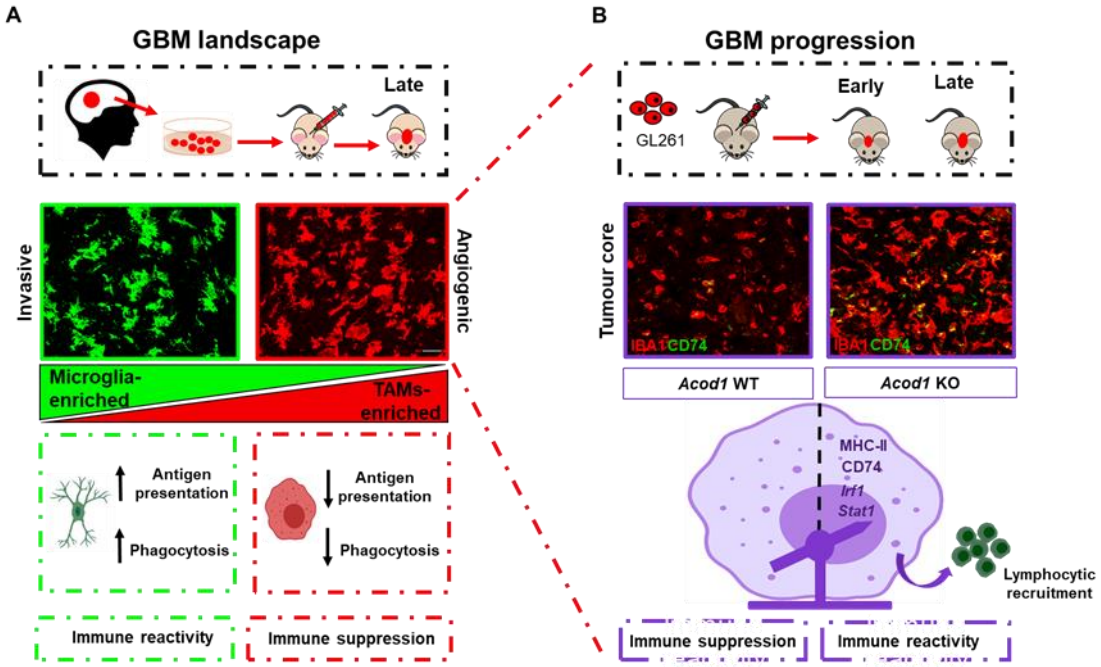

Figure 52. Schematic representation of TAMs functional adaptation across distinct GBM landscapes at late stage of the disease. (A) Human glioma biopsies from P8 (invasive tumour phenotype) and P13 (angiogenic tumour phenotype) patients were intracranially implanted into the frontal cortex of immunocompromised nude mice. We observed an enrichment of microglia-like cells in the invasive landscape, while both resident microglia and monocyte-derived macrophages were present in the angiogenic landscape. Microglia-like cells from the invasive landscape exhibited higher immune reactive profiles characterized by higher antigen presentation and phagocytic potential compared to immune suppressive counterparts in the angiogenic landscape. **(B)** The GL261 murine glioma model was chosen to investigate TAMs adaptation along GBM progression as well as the effect of ACOD1/IRG1 deficiency. This model is characterized by high peripheral monocytic-derived macrophages infiltration to the tumour site. Temporal analysis uncovered that TAMs exhibited decreased antigen-presenting cell signature at later stages of the disease, supporting the notion that these cells display an immune suppressive status at the tumour site.

Moreover, TAMs exhibited increased immunogenicity, including enhanced type I interferon response and antigen presentation correlating with increased lymphocytic recruitment to the tumour site.

CHAPTER 6

CONCLUSIONS & PERSPECTIVES

The main goal of the present PhD project was to elucidate the heterogeneity of TAMs under defined temporal and spatial settings in GBM. Taking advantage of the GBM GL261 syngeneic and PDOX mouse models and by combining single-cell RNA-sequencing, multicolour flow cytometry, immunohistological and functional immunological analyses we characterized TAM high plasticity and adaptive features, highlighting the importance to consider these aspects when designing novel therapeutic strategies targeting TAMs in GBM.

In chapter 4-I, we uncovered that myeloid cells display a prominent transcriptional adaptation in the TME of GBM GL261 syngeneic model in comparison to the other cell types in the TME. In GBM, resident parenchymal microglia are difficult to segregate from monocyte-derived macrophages. Taking advantage of the scRNA-seq dataset generated, we were able to distinguish at transcriptional level microglia- and macrophage-like cells in the TME. Dissecting their transcriptome, although we uncovered that both TAM subsets share an immunological transcriptional signature, we also identified exclusive transcriptional programme associated to microglia-like cells (e.g. positive regulation of phagocytosis and T cell mediated cytotoxicity) and to macrophage-like cells (e.g. positive regulation of cell migration and oxidation-reduction process), suggesting distinct ontogeny-based functional adaptations in our model. Analysing TAMs temporal adaptation in GBM, we uncovered a gradual transcriptional symbiotic adaptive mechanism along GBM progression. Differential TAMs transcriptional adaptation along GBM progression was observed but both TAM subsets exhibit decreased antigen-presenting cell signature at later stages of GBM, supporting the notion that these cell subsets display an immune suppressive status in the TME. Considering these evolutionary adaptive functions in the TME, future work should focus on the identification of regulatory factors controlling this phenotype switching or predictive of differential cell fate transitions among TAM subsets. In line with this notion and taking advantage of the temporal dataset generated, preliminary gene-regulatory network analyses uncovered common and exclusive key transcription factors involved in microglia- and macrophage-like cells differential education in the TME. Pharmacological or genetic modulation of the putative identified genetic targets might uncover targets with the capacity to re-educate TAMs towards anti-tumour phenotypes.

TAMs are being recognized as having a significant degree of plasticity and it has been shown that differential TAM education in the TME is regulated by epigenetic events, suggesting that TAMs might be poised to engage in distinct transcriptional programs based on initial enhancer selection (Bowman et al., 2016). We identified a subset of microglia-like cells up-regulating *Ezh2* histone methyltransferase as a timely inflammatory-associated response to the local environment. It has been described that IFN-γ induces EZH2 recruitment in human macrophages and selectively contributes to gene silencing of anti-inflammatory genes, such as MERTK (Qiao et al., 2016).

MERTK is a member of the Tyro-Axl-MerTK family of receptor tyrosine kinases present on macrophages. It has been described to be important for phagocytosis of apoptotic cells, a process known as efferocytosis, which ultimately promotes inflammation resolution (Cai et al., 2018). Contrary to phagocytosis, efferocytosis is associated with the decrease of pro-inflammatory cytokine secretion through STAT1 inhibition, while promoting IL-10 and TGFβ secretion. Additionally, it has the potential to rapidly degrade antigens by increasing acidic environment and thus limiting the cross-presentation capacity of the cells (Lecoultre et al., 2020). In tumour, usage of potent immunosuppressors for patient care, such as corticoids, have been reported to increase MERTK expression in macrophages (Zagorska et al., 2014). Binding of an apoptotic cell to MERTK counterbalances the secretion of type I IFNs while it upregulates the expression of toll-like receptors suppressors SOCS1 and SOCS3 (Elliott et al., 2017; Rothlin et al., 2007). As a future perspective it would be interesting to evaluate whether TAMs exhibit higher phagocytic or cytotoxic potential towards GBM cells via a mechanism involving EZH2, as well as whether epigenetic modifications can dictate TAMs plasticity in the TME.

Metabolic reprogramming of macrophages is emerging as an alternative to enhance anti-tumour immune response. In mammals, IRG1 encoded by *Acod1/Irg1* catalyses the production of itaconate from the decarboxylation of cis-aconitate, an intermediate metabolite of the TCA cycle (Michelucci et al., 2013). *Acod1/Irg1* is a key gene involved in the metabolic reprogramming of macrophages towards an anti-inflammatory phenotype. In our study, we detected an increased immunogenic profile of TAMs in *Acod1*-deficient compared to WT tumour bearing mice. The mechanistic link between ACOD1 deficiency and the increase of antigen presenting cell features in TAMs remains unclear. It has been shown that the transcriptional induction of the IRF1-responsive gene class II transactivator (CIITA) is impaired in IRF1-/- organoids (Forero et al., 2019). At later stages, isolated TAMs exhibited higher mRNA *Irf1* levels, and it should be evaluated CIITA is responsible for enhancing TAMs immunogenicity in GBM. In agreement with TAM increased immunogenicity, we detected higher T cell infiltrates in the TME at late stages, indicating an effective crosstalk between the innate and the adaptive immune system. By performing single cell trajectory inference analysis to investigate TAMs cellular diversity in the TME, we found a subset of macrophage-like cells enriched in genes associated with T cell migration and activation. In this context, further work should focus on assessing the cross-presentation capacity of this identified TAM subset arising under ACOD1 deficiency in modulating T cell activation and recruitment to the tumour site. Taking advantage of our scRNA-seq dataset, bioinformatics analyses should focus on the identification of ligand-receptor pairs that might contribute for the crosstalk between TAMs and the lymphocytic compartment in the TME, as previously addressed (Browaeys et al., 2020).

Additionally, GO analysis of exclusively up-regulated genes on macrophage-like cells at late GBM stage in *Acod1* KO compared to WT mice uncovered the enrichment of terms associated with antigen processing and presentation via MHC class I and T cell mediated cytotoxicity. In line with these results, the investigation of recruited CD8 T cells and the assessment of their respective immune status, such as cytotoxic activity and granular contents for an effective tumour killing activity should be further investigated. Moreover, the analysis of the tumour growth and mouse survival in GL261 tumour-bearing mice did not show significant differences between WT and *Acod1* KO mice. However, we identified a subset of T cells expressing high levels of the immune checkpoint CTLA-4. Thus, it would be interesting to evaluate whether anti-CTLA4 blockade in *Acod1* KO tumour-bearing mice might improve their survival rate. Finally, future studies should look for the comparison of potential secreted metabolites between WT and *Acod1*-deficient TAMs, which could improve T-cell-mediated long-term activation and response in the TME.

In chapter 4-II, we demonstrated that tumour-intrinsic phenotypes mediate specific transcriptional adaptations of microglia and macrophage-like cells in the TME. Taking advantage of PDOX models from the NORLUX Neuro-Oncology Laboratory, we observed that TAMs exhibit distinct transcriptional adaptations across GBM landscapes. Additionally, we showed the presence of inflammatory monocytes in the angiogenic tumour phenotype, while this population was largely absent in the invasive tumour phenotype. GBM-educated microglia cells in the invasive landscape exhibit an immune reactive profile, characterized by heterogeneous antigen-presenting cell signatures as observed by a differential expression of CD11c and MHC-II surface markers at late stages of the disease. Associated with an immunogenic profile, microglia-like cells also showed higher phagocytic index in comparison to CD11b+isolated cells from the angiogenic tumour phenotype. Here, future work should investigate the potential role of phagocytosis and antigen presentation, as an orchestrated mechanism to enhance local anti-tumour response in the TME. In line with the decreased phagocytic index of myeloid cells from the angiogenic landscape, the investigation of phagosome maturation and/or its dysfunction might contribute to immune escape mechanism and thus mediating tumour progression. Some reports have highlighted the reciprocal signaling between microglia and macrophages, which contributes to their divergent functions in the CNS. For example, in the context of spinal cord injury, increasing numbers of infiltrative macrophages correlate with the suppression of the microglial inflammatory profile with subsequent reduced phagocytic ability (Greenhalgh et al., 2018). Similar correlations remain poorly understood in the context of GBM and our work provide the first evidence into this paradigm using distinct GBM landscapes characterized by differential TAM composition in the TME. Among all malignant gliomas,

the proneural (32.73%) and mesenchymal (32.4%) subtypes are the most prevalent (Lin et al., 2014). Immune landscape analysis showed reduced immune infiltration in the proneural subtype associated with a better prognosis (Martinez-Lage et al., 2019), compared to higher tumour aggressiveness, associated with myeloid recruitment in the mesenchymal subtype (Brennan et al., 2013; Wang et al., 2017). The exact implication of immune infiltrates in distinct GBM subtypes are starting to emerge and thus, the identification of exclusive TAMs functional adaptation across distinct GBM landscapes might help the community to find evidence indicative of subtype-specific treatment for personalized therapy.

Lastly, we generated datasets describing the transcriptional adaptation programmes of microglia and macrophage-like cells across the GL261 syngeneic and PDOX, such as the identification of common and/or exclusive TAM mechanisms involved in biological functions, such as migration/invasion, antigen presentation and cross-presentation abilities by TAM and phagocytic potential. Particularly, the identification of common modules across the invasive and angiogenic GBM landscapes might be relevant for patient stratification and/or prediction of potential immune therapy strategies benefiting a specific cluster of patients. Additionally, taking advantage of these datasets, it would be important to identify and validate key genes responsible for the crosstalk between the innate and adaptive immune system using in the syngeneic versus the PDOX models.

CHAPTER 7

REFERENCES

REFERENCES

Ajami, B., Bennett, J.L., Krieger, C., McNagny, K.M., and Rossi, F.M. (2011). Infiltrating monocytes trigger EAE progression, but do not contribute to the resident microglia pool. Nat Neurosci *14*, 1142-1149.

Alban, T.J., Alvarado, A.G., Sorensen, M.D., Bayik, D., Volovetz, J., Serbinowski, E., Mulkearns-Hubert, E.E., Sinyuk, M., Hale, J.S., Onzi, G.R., *et al.* (2018). Global immune fingerprinting in glioblastoma patient peripheral blood reveals immune-suppression signatures associated with prognosis. JCI Insight *3*.

Alsamman, K., and El-Masry, O.S. (2018). Interferon regulatory factor 1 inactivation in human cancer. Biosci Rep *38*.

Arifuzzaman, S., Das, A., Kim, S.H., Yoon, T., Lee, Y.S., Jung, K.H., and Chai, Y.G. (2017). Selective inhibition of EZH2 by a small molecule inhibitor regulates microglial gene expression essential for inflammation. Biochem Pharmacol *137*, 61-80.

Ashton-Rickardt, P.G. (2013). An emerging role for Serine Protease Inhibitors in T lymphocyte immunity and beyond. Immunol Lett *152*, 65-76.

Aslan, K., Turco, V., Blobner, J., Sonner, J.K., Liuzzi, A.R., Nunez, N.G., De Feo, D., Kickingereder, P., Fischer, M., Green, E., *et al.* (2020). Heterogeneity of response to immune checkpoint blockade in hypermutated experimental gliomas. Nat Commun *11*, 931.

Ausman, J.I., Shapiro, W.R., and Rall, D.P. (1970). Studies on the chemotherapy of experimental brain tumors: development of an experimental model. Cancer Res *30*, 2394-2400.

Barrow, A.D., Edeling, M.A., Trifonov, V., Luo, J., Goyal, P., Bohl, B., Bando, J.K., Kim, A.H., Walker, J., Andahazy, M., *et al.* (2018). Natural Killer Cells Control Tumor Growth by Sensing a Growth Factor. Cell *172*, 534-548 e519.

Bernier, L.P., York, E.M., and MacVicar, B.A. (2020). Immunometabolism in the Brain: How Metabolism Shapes Microglial Function. Trends Neurosci *43*, 854-869.

Bhat, K.P.L., Balasubramaniyan, V., Vaillant, B., Ezhilarasan, R., Hummelink, K., Hollingsworth, F., Wani, K., Heathcock, L., James, J.D., Goodman, L.D., *et al.* (2013). Mesenchymal differentiation mediated by NF-kappaB promotes radiation resistance in glioblastoma. Cancer Cell *24*, 331-346.

Bloch, O., Crane, C.A., Kaur, R., Safaee, M., Rutkowski, M.J., and Parsa, A.T. (2013). Gliomas promote immunosuppression through induction of B7-H1 expression in tumor-associated macrophages. Clin Cancer Res *19*, 3165-3175.

Borden, E.C., Sen, G.C., Uze, G., Silverman, R.H., Ransohoff, R.M., Foster, G.R., and Stark, G.R. (2007). Interferons at age 50: past, current and future impact on biomedicine. Nat Rev Drug Discov *6*, 975-990.

Bougnaud, S., Golebiewska, A., Oudin, A., Keunen, O., Harter, P.N., Mader, L., Azuaje, F., Fritah, S., Stieber, D., Kaoma, T., *et al.* (2016). Molecular crosstalk between tumour and brain parenchyma instructs histopathological features in glioblastoma. Oncotarget *7*, 31955-31971.

Bowman, R.L., Klemm, F., Akkari, L., Pyonteck, S.M., Sevenich, L., Quail, D.F., Dhara, S., Simpson, K., Gardner, E.E., Iacobuzio-Donahue, C.A., *et al.* (2016). Macrophage Ontogeny Underlies Differences in Tumor-Specific Education in Brain Malignancies. Cell Rep *17*, 2445-2459.

Brandenburg, L.O., Pufe, T., and Koch, T. (2014). Role of phospholipase d in g-protein coupled receptor function. Membranes (Basel) *4*, 302-318.

Brat, D.J., Aldape, K., Colman, H., Figrarella-Branger, D., Fuller, G.N., Giannini, C., Holland, E.C., Jenkins, R.B., Kleinschmidt-DeMasters, B., Komori, T., *et al.* (2020). cIMPACT-NOW update 5: recommended grading criteria and terminologies for IDH-mutant astrocytomas. Acta Neuropathol *139*, 603-608.

Brat, D.J., Aldape, K., Colman, H., Holland, E.C., Louis, D.N., Jenkins, R.B., Kleinschmidt-DeMasters, B.K., Perry, A., Reifenberger, G., Stupp, R., *et al.* (2018). cIMPACT-NOW update 3: recommended diagnostic criteria for "Diffuse astrocytic glioma, IDH-wildtype, with molecular features of glioblastoma, WHO grade IV". Acta Neuropathol *136*, 805-810.

Bray, F., Ferlay, J., Soerjomataram, I., Siegel, R.L., Torre, L.A., and Jemal, A. (2018). Global cancer statistics 2018: GLOBOCAN estimates of incidence and mortality worldwide for 36 cancers in 185 countries. CA Cancer J Clin *68*, 394-424.

Brennan, C.W., Verhaak, R.G., McKenna, A., Campos, B., Noushmehr, H., Salama, S.R., Zheng, S., Chakravarty, D., Sanborn, J.Z., Berman, S.H., *et al.* (2013). The somatic genomic landscape of glioblastoma. Cell *155*, 462-477.

Browaeys, R., Saelens, W., and Saeys, Y. (2020). NicheNet: modeling intercellular communication by linking ligands to target genes. Nat Methods *17*, 159-162.

Buonfiglioli, A., Efe, I.E., Guneykaya, D., Ivanov, A., Huang, Y., Orlowski, E., Kruger, C., Deisz, R.A., Markovic, D., Fluh, C., *et al.* (2019). let-7 MicroRNAs Regulate Microglial Function and Suppress Glioma Growth through Toll-Like Receptor 7. Cell Rep *29*, 3460-3471 e3467.

Buonfiglioli, A., and Hambardzumyan, D. (2021). Macrophages and microglia: the cerberus of glioblastoma. Acta Neuropathol Commun *9*, 54.

Butovsky, O., Koronyo-Hamaoui, M., Kunis, G., Ophir, E., Landa, G., Cohen, H., and Schwartz, M. (2006). Glatiramer acetate fights against Alzheimer's disease by inducing dendritic-like microglia expressing insulin-like growth factor 1. Proc Natl Acad Sci U S A *103*, 11784-11789.

Butowski, N., Colman, H., De Groot, J.F., Omuro, A.M., Nayak, L., Wen, P.Y., Cloughesy, T.F., Marimuthu, A., Haidar, S., Perry, A., *et al.* (2016). Orally administered colony stimulating factor 1 receptor inhibitor PLX3397 in recurrent glioblastoma: an Ivy Foundation Early Phase Clinical Trials Consortium phase II study. Neuro Oncol *18*, 557-564.

Buttini, M., Orth, M., Bellosta, S., Akeefe, H., Pitas, R.E., Wyss-Coray, T., Mucke, L., and Mahley, R.W. (1999). Expression of human apolipoprotein E3 or E4 in the brains of Apoe-/- mice: isoform-specific effects on neurodegeneration. J Neurosci *19*, 4867-4880.

Cahoy, J.D., Emery, B., Kaushal, A., Foo, L.C., Zamanian, J.L., Christopherson, K.S., Xing, Y., Lubischer, J.L., Krieg, P.A., Krupenko, S.A., *et al.* (2008). A transcriptome database for astrocytes, neurons, and oligodendrocytes: a new resource for understanding brain development and function. J Neurosci *28*, 264-278.

Cai, B., Kasikara, C., Doran, A.C., Ramakrishnan, R., Birge, R.B., and Tabas, I. (2018). MerTK signaling in macrophages promotes the synthesis of inflammation resolution mediators by suppressing CaMKII activity. Sci Signal *11*.

Cancer Genome Atlas Research, N. (2008). Comprehensive genomic characterization defines human glioblastoma genes and core pathways. Nature *455*, 1061-1068.

Capper, D., Jones, D.T.W., Sill, M., Hovestadt, V., Schrimpf, D., Sturm, D., Koelsche, C., Sahm, F., Chavez, L., Reuss, D.E., *et al.* (2018). DNA methylation-based classification of central nervous system tumours. Nature *555*, 469-474.

Ceccarelli, M., Barthel, F.P., Malta, T.M., Sabedot, T.S., Salama, S.R., Murray, B.A., Morozova, O., Newton, Y., Radenbaugh, A., Pagnotta, S.M., *et al.* (2016). Molecular Profiling Reveals Biologically Discrete Subsets and Pathways of Progression in Diffuse Glioma. Cell *164*, 550-563.

Chen, Z., Feng, X., Herting, C.J., Garcia, V.A., Nie, K., Pong, W.W., Rasmussen, R., Dwivedi, B., Seby, S., Wolf, S.A., *et al.* (2017). Cellular and Molecular Identity of Tumor-Associated Macrophages in Glioblastoma. Cancer Res *77*, 2266-2278.

Chen, Z., and Hambardzumyan, D. (2018). Immune Microenvironment in Glioblastoma Subtypes. Front Immunol *9*, 1004.

Chen, Z., Ross, J.L., and Hambardzumyan, D. (2019). Intravital 2-photon imaging reveals distinct morphology and infiltrative properties of glioblastoma-associated macrophages. Proc Natl Acad Sci U S A *116*, 14254-14259.

Cheray, M., and Joseph, B. (2018). Epigenetics Control Microglia Plasticity. Front Cell Neurosci *12*, 243.

Cohen, A.L., Holmen, S.L., and Colman, H. (2013). IDH1 and IDH2 mutations in gliomas. Curr Neurol Neurosci Rep *13*, 345.

Cordes, T., Wallace, M., Michelucci, A., Divakaruni, A.S., Sapcariu, S.C., Sousa, C., Koseki, H., Cabrales, P., Murphy, A.N., Hiller, K., *et al.* (2016). Immunoresponsive Gene 1 and Itaconate Inhibit Succinate Dehydrogenase to Modulate Intracellular Succinate Levels. J Biol Chem *291*, 14274-14284.

Corse, E., and Allison, J.P. (2012). Cutting edge: CTLA-4 on effector T cells inhibits in trans. J Immunol *189*, 1123-1127.

Crane, C.A., Han, S.J., Barry, J.J., Ahn, B.J., Lanier, L.L., and Parsa, A.T. (2010). TGF-beta downregulates the activating receptor NKG2D on NK cells and CD8+ T cells in glioma patients. Neuro Oncol *12*, 7-13.

Daniels, B.P., Kofman, S.B., Smith, J.R., Norris, G.T., Snyder, A.G., Kolb, J.P., Gao, X., Locasale, J.W., Martinez, J., Gale, M., Jr., *et al.* (2019). The Nucleotide Sensor ZBP1 and Kinase RIPK3 Induce the Enzyme IRG1 to Promote an Antiviral Metabolic State in Neurons. Immunity *50*, 64-76 e64.

Darmanis, S., Sloan, S.A., Croote, D., Mignardi, M., Chernikova, S., Samghababi, P., Zhang, Y., Neff, N., Kowarsky, M., Caneda, C., *et al.* (2017). Single-Cell RNA-Seq Analysis of Infiltrating Neoplastic Cells at the Migrating Front of Human Glioblastoma. Cell Rep *21*, 1399-1410.

Davis, M.E. (2016). Glioblastoma: Overview of Disease and Treatment. Clin J Oncol Nurs *20*, S2-8.

De Leo, A., Ugolini, A., and Veglia, F. (2020). Myeloid Cells in Glioblastoma Microenvironment. Cells *10*.

Di Virgilio, F., and Vuerich, M. (2015). Purinergic signaling in the immune system. Auton Neurosci *191*, 117-123.

Dominguez-Andres, J., Novakovic, B., Li, Y., Scicluna, B.P., Gresnigt, M.S., Arts, R.J.W., Oosting, M., Moorlag, S., Groh, L.A., Zwaag, J., *et al.* (2019). The Itaconate Pathway Is a Central Regulatory Node Linking Innate Immune Tolerance and Trained Immunity. Cell Metab *29*, 211-220 e215.

Dubinski, D., Wolfer, J., Hasselblatt, M., Schneider-Hohendorf, T., Bogdahn, U., Stummer, W., Wiendl, H., and Grauer, O.M. (2016). CD4+ T effector memory cell dysfunction is associated with the accumulation of granulocytic myeloid-derived suppressor cells in glioblastoma patients. Neuro Oncol *18*, 807-818.

Dzaye, O., Hu, F., Derkow, K., Haage, V., Euskirchen, P., Harms, C., Lehnardt, S., Synowitz, M., Wolf, S.A., and Kettenmann, H. (2016). Glioma Stem Cells but Not Bulk Glioma Cells Upregulate IL-6 Secretion in Microglia/Brain Macrophages via Toll-like Receptor 4 Signaling. J Neuropathol Exp Neurol *75*, 429-440.

El Kasmi, K.C., and Stenmark, K.R. (2015). Contribution of metabolic reprogramming to macrophage plasticity and function. Semin Immunol *27*, 267-275.

Elliott, M.R., Koster, K.M., and Murphy, P.S. (2017). Efferocytosis Signaling in the Regulation of Macrophage Inflammatory Responses. J Immunol *198*, 1387-1394.

Ellison, D.W., Hawkins, C., Jones, D.T.W., Onar-Thomas, A., Pfister, S.M., Reifenberger, G., and Louis, D.N. (2019). cIMPACT-NOW update 4: diffuse gliomas characterized by MYB, MYBL1, or FGFR1 alterations or BRAF(V600E) mutation. Acta Neuropathol *137*, 683-687.

Fabbri, M., Paone, A., Calore, F., Galli, R., Gaudio, E., Santhanam, R., Lovat, F., Fadda, P., Mao, C., Nuovo, G.J., *et al.* (2012). MicroRNAs bind to Toll-like receptors to induce prometastatic inflammatory response. Proc Natl Acad Sci U S A *109*, E2110-2116.

Fan, T.W., Warmoes, M.O., Sun, Q., Song, H., Turchan-Cholewo, J., Martin, J.T., Mahan, A., Higashi, R.M., and Lane, A.N. (2016). Distinctly perturbed metabolic networks underlie differential tumor tissue damages induced by immune modulator beta-glucan in a two-case ex vivo non-small-cell lung cancer study. Cold Spring Harb Mol Case Stud *2*, a000893.

Fecci, P.E., Ochiai, H., Mitchell, D.A., Grossi, P.M., Sweeney, A.E., Archer, G.E., Cummings, T., Allison, J.P., Bigner, D.D., and Sampson, J.H. (2007). Systemic CTLA-4 blockade ameliorates glioma-induced changes to the CD4+ T cell compartment without affecting regulatory T-cell function. Clin Cancer Res *13*, 2158-2167.

Forero, A., Ozarkar, S., Li, H., Lee, C.H., Hemann, E.A., Nadjsombati, M.S., Hendricks, M.R., So, L., Green, R., Roy, C.N., *et al.* (2019). Differential Activation of the Transcription Factor IRF1 Underlies the Distinct Immune Responses Elicited by Type I and Type III Interferons. Immunity *51*, 451-464 e456.

Friebel, E., Kapolou, K., Unger, S., Nunez, N.G., Utz, S., Rushing, E.J., Regli, L., Weller, M., Greter, M., Tugues, S., *et al.* (2020). Single-Cell Mapping of Human Brain Cancer Reveals Tumor-Specific Instruction of Tissue-Invading Leukocytes. Cell *181*, 1626-1642 e1620.

Fuger, P., Hefendehl, J.K., Veeraraghavalu, K., Wendeln, A.C., Schlosser, C., Obermuller, U., Wegenast-Braun, B.M., Neher, J.J., Martus, P., Kohsaka, S., *et al.* (2017). Microglia turnover with aging and in an Alzheimer's model via long-term in vivo single-cell imaging. Nat Neurosci *20*, 1371-1376.

Furnari, F.B., Fenton, T., Bachoo, R.M., Mukasa, A., Stommel, J.M., Stegh, A., Hahn, W.C., Ligon, K.L., Louis, D.N., Brennan, C., *et al.* (2007). Malignant astrocytic glioma: genetics, biology, and paths to treatment. Genes Dev *21*, 2683-2710.

Gabrusiewicz, K., Rodriguez, B., Wei, J., Hashimoto, Y., Healy, L.M., Maiti, S.N., Thomas, G., Zhou, S., Wang, Q., Elakkad, A., *et al.* (2016). Glioblastoma-infiltrated innate immune cells resemble M0 macrophage phenotype. JCI Insight *1*.

Ginhoux, F., Greter, M., Leboeuf, M., Nandi, S., See, P., Gokhan, S., Mehler, M.F., Conway, S.J., Ng, L.G., Stanley, E.R., *et al.* (2010). Fate mapping analysis reveals that adult microglia derive from primitive macrophages. Science *330*, 841-845.

Goldmann, T., Wieghofer, P., Jordao, M.J., Prutek, F., Hagemeyer, N., Frenzel, K., Amann, L., Staszewski, O., Kierdorf, K., Krueger, M., *et al.* (2016). Origin, fate and dynamics of macrophages at central nervous system interfaces. Nat Immunol *17*, 797-805.

Golebiewska, A., Bougnaud, S., Stieber, D., Brons, N.H., Vallar, L., Hertel, F., Klink, B., Schrock, E., Bjerkvig, R., and Niclou, S.P. (2013). Side population in human glioblastoma is non-tumorigenic and characterizes brain endothelial cells. Brain *136*, 1462-1475.

Golebiewska, A., Hau, A.C., Oudin, A., Stieber, D., Yabo, Y.A., Baus, V., Barthelemy, V., Klein, E., Bougnaud, S., Keunen, O., *et al.* (2020). Patient-derived organoids and orthotopic xenografts of primary and recurrent gliomas represent relevant patient avatars for precision oncology. Acta Neuropathol *140*, 919-949.

Gomez Perdiguero, E., Klapproth, K., Schulz, C., Busch, K., Azzoni, E., Crozet, L., Garner, H., Trouillet, C., de Bruijn, M.F., Geissmann, F., *et al.* (2015). Tissue-resident macrophages originate from yolk-sac-derived erythro-myeloid progenitors. Nature *518*, 547-551.

Gosselin, D., Link, V.M., Romanoski, C.E., Fonseca, G.J., Eichenfield, D.Z., Spann, N.J., Stender, J.D., Chun, H.B., Garner, H., Geissmann, F., *et al.* (2014). Environment drives selection and function of enhancers controlling tissue-specific macrophage identities. Cell *159*, 1327-1340.

Grabowski, M.M., Sankey, E.W., Ryan, K.J., Chongsathidkiet, P., Lorrey, S.J., Wilkinson, D.S., and Fecci, P.E. (2020). Immune suppression in gliomas. J Neurooncol.

Greenhalgh, A.D., Zarruk, J.G., Healy, L.M., Baskar Jesudasan, S.J., Jhelum, P., Salmon, C.K., Formanek, A., Russo, M.V., Antel, J.P., McGavern, D.B., *et al.* (2018). Peripherally derived macrophages modulate microglial function to reduce inflammation after CNS injury. PLoS Biol *16*, e2005264.

Gschwandtner, M., Derler, R., and Midwood, K.S. (2019). More Than Just Attractive: How CCL2 Influences Myeloid Cell Behavior Beyond Chemotaxis. Front Immunol *10*, 2759.

Guda, M.R., Rashid, M.A., Asuthkar, S., Jalasutram, A., Caniglia, J.L., Tsung, A.J., and Velpula, K.K. (2019). Pleiotropic role of macrophage migration inhibitory factor in cancer. Am J Cancer Res *9*, 2760-2773.

Haage, V., Semtner, M., Vidal, R.O., Hernandez, D.P., Pong, W.W., Chen, Z., Hambardzumyan, D., Magrini, V., Ly, A., Walker, J., *et al.* (2019). Comprehensive gene expression meta-analysis identifies signature genes that distinguish microglia from peripheral monocytes/macrophages in health and glioma. Acta Neuropathol Commun *7*, 20.

Hambardzumyan, D., Gutmann, D.H., and Kettenmann, H. (2016). The role of microglia and macrophages in glioma maintenance and progression. Nat Neurosci *19*, 20-27.

Heimberger, A.B., Abou-Ghazal, M., Reina-Ortiz, C., Yang, D.S., Sun, W., Qiao, W., Hiraoka, N., and Fuller, G.N. (2008). Incidence and prognostic impact of FoxP3+ regulatory T cells in human gliomas. Clin Cancer Res *14*, 5166-5172.

Hodges, T.R., Ott, M., Xiu, J., Gatalica, Z., Swensen, J., Zhou, S., Huse, J.T., de Groot, J., Li, S., Overwijk, W.W., *et al.* (2017). Mutational burden, immune checkpoint expression, and mismatch repair in glioma: implications for immune checkpoint immunotherapy. Neuro Oncol *19*, 1047-1057.

Holtman, I.R., Raj, D.D., Miller, J.A., Schaafsma, W., Yin, Z., Brouwer, N., Wes, P.D., Moller, T., Orre, M., Kamphuis, W., *et al.* (2015). Induction of a common microglia gene expression signature by aging and neurodegenerative conditions: a co-expression meta-analysis. Acta Neuropathol Commun *3*, 31.

Hooftman, A., and O'Neill, L.A.J. (2019). The Immunomodulatory Potential of the Metabolite Itaconate. Trends Immunol *40*, 687-698.

Hu, F., Ku, M.C., Markovic, D., Dzaye, O., Lehnardt, S., Synowitz, M., Wolf, S.A., and Kettenmann, H. (2014). Glioma-associated microglial MMP9 expression is upregulated by TLR2 signaling and sensitive to minocycline. Int J Cancer *135*, 2569-2578.

Huang, J., Yu, J., Tu, L., Huang, N., Li, H., and Luo, Y. (2019). Isocitrate Dehydrogenase Mutations in Glioma: From Basic Discovery to Therapeutics Development. Front Oncol *9*, 506.

Hughes, R., Qian, B.Z., Rowan, C., Muthana, M., Keklikoglou, I., Olson, O.C., Tazzyman, S., Danson, S., Addison, C., Clemons, M., *et al.* (2015). Perivascular M2 Macrophages Stimulate Tumor Relapse after Chemotherapy. Cancer Res *75*, 3479-3491.

Hutter, G., Theruvath, J., Graef, C.M., Zhang, M., Schoen, M.K., Manz, E.M., Bennett, M.L., Olson, A., Azad, T.D., Sinha, R., *et al.* (2019). Microglia are effector cells of CD47-SIRPalpha antiphagocytic axis disruption against glioblastoma. Proc Natl Acad Sci U S A *116*, 997-1006.

Illes, P., Rubini, P., Ulrich, H., Zhao, Y., and Tang, Y. (2020). Regulation of Microglial Functions by Purinergic Mechanisms in the Healthy and Diseased CNS. Cells *9*.

Inoue, K., Tsuda, M., and Koizumi, S. (2005). ATP receptors in pain sensation: Involvement of spinal microglia and P2X(4) receptors. Purinergic Signal *1*, 95-100.

Jimenez, C., Portela, R.A., Mellado, M., Rodriguez-Frade, J.M., Collard, J., Serrano, A., Martinez, A.C., Avila, J., and Carrera, A.C. (2000). Role of the PI3K regulatory subunit in the control of actin organization and cell migration. J Cell Biol *151*, 249-262.

Kaffes, I., Szulzewsky, F., Chen, Z., Herting, C.J., Gabanic, B., Velazquez Vega, J.E., Shelton, J., Switchenko, J.M., Ross, J.L., McSwain, L.F., *et al.* (2019). Human Mesenchymal glioblastomas are characterized by an increased immune cell presence compared to Proneural and Classical tumors. Oncoimmunology *8*, e1655360.

Kaminska, B., Kocyk, M., and Kijewska, M. (2013). TGF beta signaling and its role in glioma pathogenesis. Adv Exp Med Biol *986*, 171-187.

Kamphuis, W., Kooijman, L., Schetters, S., Orre, M., and Hol, E.M. (2016). Transcriptional profiling of CD11c-positive microglia accumulating around amyloid plaques in a mouse model for Alzheimer's disease. Biochim Biophys Acta *1862*, 1847-1860.

Kaneda, M.M., Messer, K.S., Ralainirina, N., Li, H., Leem, C.J., Gorjestani, S., Woo, G., Nguyen, A.V., Figueiredo, C.C., Foubert, P., *et al.* (2016). PI3Kgamma is a molecular switch that controls immune suppression. Nature *539*, 437-442.

Keren-Shaul, H., Spinrad, A., Weiner, A., Matcovitch-Natan, O., Dvir-Szternfeld, R., Ulland, T.K., David, E., Baruch, K., Lara-Astaiso, D., Toth, B., *et al.* (2017). A Unique Microglia Type Associated with Restricting Development of Alzheimer's Disease. Cell *169*, 1276-1290 e1217.

Kettenmann, H., Hanisch, U.K., Noda, M., and Verkhratsky, A. (2011). Physiology of microglia. Physiol Rev *91*, 461-553.

Khalsa, J.K., Cheng, N., Keegan, J., Chaudry, A., Driver, J., Bi, W.L., Lederer, J., and Shah, K. (2020). Immune phenotyping of diverse syngeneic murine brain tumors identifies immunologically distinct types. Nat Commun *11*, 3912.

Kim, C.C., Nakamura, M.C., and Hsieh, C.L. (2016). Brain trauma elicits non-canonical macrophage activation states. J Neuroinflammation *13*, 117.

Klemm, F., Maas, R.R., Bowman, R.L., Kornete, M., Soukup, K., Nassiri, S., Brouland, J.P., Iacobuzio-Donahue, C.A., Brennan, C., Tabar, V., *et al.* (2020). Interrogation of the Microenvironmental Landscape in Brain Tumors Reveals Disease-Specific Alterations of Immune Cells. Cell *181*, 1643-1660 e1617.

Koizumi, S., Ohsawa, K., Inoue, K., and Kohsaka, S. (2013). Purinergic receptors in microglia: functional modal shifts of microglia mediated by P2 and P1 receptors. Glia *61*, 47-54.

Koizumi, S., Shigemoto-Mogami, Y., Nasu-Tada, K., Shinozaki, Y., Ohsawa, K., Tsuda, M., Joshi, B.V., Jacobson, K.A., Kohsaka, S., and Inoue, K. (2007). UDP acting at P2Y6 receptors is a mediator of microglial phagocytosis. Nature *446*, 1091-1095.

Kowal, J., Kornete, M., and Joyce, J.A. (2019). Re-education of macrophages as a therapeutic strategy in cancer. Immunotherapy *11*, 677-689.

Kurpius, D., Nolley, E.P., and Dailey, M.E. (2007). Purines induce directed migration and rapid homing of microglia to injured pyramidal neurons in developing hippocampus. Glia *55*, 873-884.

Kvisten, M., Mikkelsen, V.E., Stensjoen, A.L., Solheim, O., Van Der Want, J., and Torp, S.H. (2019). Microglia and macrophages in human glioblastomas: A morphological and immunohistochemical study. Mol Clin Oncol *11*, 31-36.

Landry, A.P., Balas, M., Alli, S., Spears, J., and Zador, Z. (2020). Distinct regional ontogeny and activation of tumor associated macrophages in human glioblastoma. Sci Rep *10*, 19542.

Lang, F.F., Conrad, C., Gomez-Manzano, C., Yung, W.K.A., Sawaya, R., Weinberg, J.S., Prabhu, S.S., Rao, G., Fuller, G.N., Aldape, K.D., *et al.* (2018). Phase I Study of DNX-2401 (Delta-24-RGD) Oncolytic Adenovirus: Replication and Immunotherapeutic Effects in Recurrent Malignant Glioma. J Clin Oncol *36*, 1419-1427.

Lavin, Y., Winter, D., Blecher-Gonen, R., David, E., Keren-Shaul, H., Merad, M., Jung, S., and Amit, I. (2014). Tissue-resident macrophage enhancer landscapes are shaped by the local microenvironment. Cell *159*, 1312-1326.

Lecoultre, M., Dutoit, V., and Walker, P.R. (2020). Phagocytic function of tumor-associated macrophages as a key determinant of tumor progression control: a review. J Immunother Cancer *8*.

Lee, J.K., Wang, J., Sa, J.K., Ladewig, E., Lee, H.O., Lee, I.H., Kang, H.J., Rosenbloom, D.S., Camara, P.G., Liu, Z., *et al.* (2017). Spatiotemporal genomic architecture informs precision oncology in glioblastoma. Nat Genet *49*, 594-599.

Leiter, O., and Walker, T.L. (2019). Platelets: The missing link between the blood and brain? Prog Neurobiol *183*, 101695.

Li, H.Q., Chen, C., Dou, Y., Wu, H.J., Liu, Y.J., Lou, H.F., Zhang, J.M., Li, X.M., Wang, H., and Duan, S. (2013a). P2Y4 receptor-mediated pinocytosis contributes to amyloid beta-induced self-uptake by microglia. Mol Cell Biol *33*, 4282-4293.

Li, Y., Zhang, P., Wang, C., Han, C., Meng, J., Liu, X., Xu, S., Li, N., Wang, Q., Shi, X., *et al.* (2013b). Immune responsive gene 1 (IRG1) promotes endotoxin tolerance by increasing A20 expression in macrophages through reactive oxygen species. J Biol Chem *288*, 16225-16234.

Lin, N., Yan, W., Gao, K., Wang, Y., Zhang, J., and You, Y. (2014). Prevalence and clinicopathologic characteristics of the molecular subtypes in malignant glioma: a multi-institutional analysis of 941 cases. PLoS One *9*, e94871.

Liu, S.C., Alomran, R., Chernikova, S.B., Lartey, F., Stafford, J., Jang, T., Merchant, M., Zboralski, D., Zollner, S., Kruschinski, A., *et al.* (2014). Blockade of SDF-1 after irradiation inhibits tumor recurrences of autochthonous brain tumors in rats. Neuro Oncol *16*, 21-28.

Lohoff, M., Ferrick, D., Mittrucker, H.W., Duncan, G.S., Bischof, S., Rollinghoff, M., and Mak, T.W. (1997). Interferon regulatory factor-1 is required for a T helper 1 immune response in vivo. Immunity *6*, 681-689.

Louis, D.N., Perry, A., Reifenberger, G., von Deimling, A., Figarella-Branger, D., Cavenee, W.K., Ohgaki, H., Wiestler, O.D., Kleihues, P., and Ellison, D.W. (2016). The 2016 World Health Organization Classification of Tumors of the Central Nervous System: a summary. Acta Neuropathol *131*, 803-820.

Louis, D.N., Wesseling, P., Aldape, K., Brat, D.J., Capper, D., Cree, I.A., Eberhart, C., Figarella-Branger, D., Fouladi, M., Fuller, G.N., *et al.* (2020). cIMPACT-NOW update 6: new entity and diagnostic principle

recommendations of the cIMPACT-Utrecht meeting on future CNS tumor classification and grading. Brain Pathol *30*, 844-856.

Macosko, E.Z., Basu, A., Satija, R., Nemesh, J., Shekhar, K., Goldman, M., Tirosh, I., Bialas, A.R., Kamitaki, N., Martersteck, E.M., *et al.* (2015). Highly Parallel Genome-wide Expression Profiling of Individual Cells Using Nanoliter Droplets. Cell *161*, 1202-1214.

Malta, T.M., de Souza, C.F., Sabedot, T.S., Silva, T.C., Mosella, M.S., Kalkanis, S.N., Snyder, J., Castro, A.V.B., and Noushmehr, H. (2018). Glioma CpG island methylator phenotype (G-CIMP): biological and clinical implications. Neuro Oncol *20*, 608-620.

Mantegazza, A.R., Magalhaes, J.G., Amigorena, S., and Marks, M.S. (2013). Presentation of phagocytosed antigens by MHC class I and II. Traffic *14*, 135-152.

Martinez-Lage, M., Lynch, T.M., Bi, Y., Cocito, C., Way, G.P., Pal, S., Haller, J., Yan, R.E., Ziober, A., Nguyen, A., *et al.* (2019). Immune landscapes associated with different glioblastoma molecular subtypes. Acta Neuropathol Commun *7*, 203.

Martinez, F.O., Sica, A., Mantovani, A., and Locati, M. (2008). Macrophage activation and polarization. Front Biosci *13*, 453-461.

Masuda, T., Sankowski, R., Staszewski, O., Bottcher, C., Amann, L., Sagar, Scheiwe, C., Nessler, S., Kunz, P., van Loo, G., *et al.* (2019). Spatial and temporal heterogeneity of mouse and human microglia at single-cell resolution. Nature *566*, 388-392.

Mathis, D., and Shoelson, S.E. (2011). Immunometabolism: an emerging frontier. Nat Rev Immunol *11*, 81.

Mercurio, L., Ajmone-Cat, M.A., Cecchetti, S., Ricci, A., Bozzuto, G., Molinari, A., Manni, I., Pollo, B., Scala, S., Carpinelli, G., *et al.* (2016). Targeting CXCR4 by a selective peptide antagonist modulates tumor microenvironment and microglia reactivity in a human glioblastoma model. J Exp Clin Cancer Res *35*, 55.

Michelucci, A., Cordes, T., Ghelfi, J., Pailot, A., Reiling, N., Goldmann, O., Binz, T., Wegner, A., Tallam, A., and Rausell, A. (2013). Immune-responsive gene 1 protein links metabolism to immunity by catalyzing itaconic acid production. Proceedings of the National Academy of Sciences *110*, 7820-7825.

Mills, C.D., Kincaid, K., Alt, J.M., Heilman, M.J., and Hill, A.M. (2000). M-1/M-2 macrophages and the Th1/Th2 paradigm. J Immunol *164*, 6166-6173.

Mills, E.L., Kelly, B., and O'Neill, L.A.J. (2017). Mitochondria are the powerhouses of immunity. Nat Immunol *18*, 488-498.

Mills, E.L., Ryan, D.G., Prag, H.A., Dikovskaya, D., Menon, D., Zaslona, Z., Jedrychowski, M.P., Costa, A.S.H., Higgins, M., Hams, E., *et al.* (2018). Itaconate is an anti-inflammatory metabolite that activates Nrf2 via alkylation of KEAP1. Nature *556*, 113-117.

Mitchell, R.A., Liao, H., Chesney, J., Fingerle-Rowson, G., Baugh, J., David, J., and Bucala, R. (2002). Macrophage migration inhibitory factor (MIF) sustains macrophage proinflammatory function by inhibiting p53: regulatory role in the innate immune response. Proc Natl Acad Sci U S A *99*, 345-350.

Molinaro, A.M., Hervey-Jumper, S., Morshed, R.A., Young, J., Han, S.J., Chunduru, P., Zhang, Y., Phillips, J.J., Shai, A., Lafontaine, M., *et al.* (2020). Association of Maximal Extent of Resection of Contrast-Enhanced and Non-Contrast-Enhanced Tumor With Survival Within Molecular Subgroups of Patients With Newly Diagnosed Glioblastoma. JAMA Oncol *6*, 495-503.

Molinaro, A.M., Taylor, J.W., Wiencke, J.K., and Wrensch, M.R. (2019). Genetic and molecular epidemiology of adult diffuse glioma. Nat Rev Neurol *15*, 405-417.

Motzer, R.J., Escudier, B., McDermott, D.F., George, S., Hammers, H.J., Srinivas, S., Tykodi, S.S., Sosman, J.A., Procopio, G., Plimack, E.R., *et al.* (2015). Nivolumab versus Everolimus in Advanced Renal-Cell Carcinoma. N Engl J Med *373*, 1803-1813.

Muller, A., Brandenburg, S., Turkowski, K., Muller, S., and Vajkoczy, P. (2015). Resident microglia, and not peripheral macrophages, are the main source of brain tumor mononuclear cells. Int J Cancer *137*, 278-288.

Muller, S., Kohanbash, G., Liu, S.J., Alvarado, B., Carrera, D., Bhaduri, A., Watchmaker, P.B., Yagnik, G., Di Lullo, E., Malatesta, M., *et al.* (2017). Single-cell profiling of human gliomas reveals macrophage ontogeny as a basis for regional differences in macrophage activation in the tumor microenvironment. Genome Biol *18*, 234.

Muri, J., Wolleb, H., Broz, P., Carreira, E.M., and Kopf, M. (2020). Electrophilic Nrf2 activators and itaconate inhibit inflammation at low dose and promote IL-1beta production and inflammatory apoptosis at high dose. Redox Biol *36*, 101647.

Nagaraj, S., and Gabrilovich, D.I. (2007). Myeloid-derived suppressor cells. Adv Exp Med Biol *601*, 213-223.

Nair, S., Sobotka, K.S., Joshi, P., Gressens, P., Fleiss, B., Thornton, C., Mallard, C., and Hagberg, H. (2019). Lipopolysaccharide-induced alteration of mitochondrial morphology induces a metabolic shift in microglia modulating the inflammatory response in vitro and in vivo. Glia *67*, 1047-1061.

Neftel, C., Laffy, J., Filbin, M.G., Hara, T., Shore, M.E., Rahme, G.J., Richman, A.R., Silverbush, D., Shaw, M.L., Hebert, C.M., *et al.* (2019). An Integrative Model of Cellular States, Plasticity, and Genetics for Glioblastoma. Cell *178*, 835-849 e821.

Netea, M.G., Quintin, J., and van der Meer, J.W. (2011). Trained immunity: a memory for innate host defense. Cell Host Microbe *9*, 355-361.

Ngo Thai Bich, V., Hongu, T., Miura, Y., Katagiri, N., Ohbayashi, N., Yamashita-Kanemaru, Y., Shibuya, A., Funakoshi, Y., and Kanaho, Y. (2018). Physiological function of phospholipase D2 in anti-tumor immunity: regulation of CD8(+) T lymphocyte proliferation. Sci Rep *8*, 6283.

Nimmerjahn, A., Kirchhoff, F., and Helmchen, F. (2005). Resting microglial cells are highly dynamic surveillants of brain parenchyma in vivo. Science *308*, 1314-1318.

Noushmehr, H., Weisenberger, D.J., Diefes, K., Phillips, H.S., Pujara, K., Berman, B.P., Pan, F., Pelloski, C.E., Sulman, E.P., Bhat, K.P., *et al.* (2010). Identification of a CpG island methylator phenotype that defines a distinct subgroup of glioma. Cancer Cell *17*, 510-522.

O'Neill, L.A., Kishton, R.J., and Rathmell, J. (2016). A guide to immunometabolism for immunologists. Nat Rev Immunol *16*, 553-565.

O'Neill, L.A.J., and Artyomov, M.N. (2019). Itaconate: the poster child of metabolic reprogramming in macrophage function. Nat Rev Immunol *19*, 273-281.

Ochocka, N., Segit, P., Walentynowicz, K.A., Wojnicki, K., Cyranowski, S., Swatler, J., Mieczkowski, J., and Kaminska, B. (2021). Single-cell RNA sequencing reveals functional heterogeneity of glioma-associated brain macrophages. Nat Commun *12*, 1151.

Ogasawara, K., Hida, S., Azimi, N., Tagaya, Y., Sato, T., Yokochi-Fukuda, T., Waldmann, T.A., Taniguchi, T., and Taki, S. (1998). Requirement for IRF-1 in the microenvironment supporting development of natural killer cells. Nature *391*, 700-703.

Oh, T., Fakurnejad, S., Sayegh, E.T., Clark, A.J., Ivan, M.E., Sun, M.Z., Safaee, M., Bloch, O., James, C.D., and Parsa, A.T. (2014). Immunocompetent murine models for the study of glioblastoma immunotherapy. J Transl Med *12*, 107.

Ohgaki, H., and Kleihues, P. (2013). The definition of primary and secondary glioblastoma. Clin Cancer Res *19*, 764-772.

Ohkuri, T., Ghosh, A., Kosaka, A., Zhu, J., Ikeura, M., David, M., Watkins, S.C., Sarkar, S.N., and Okada, H. (2014). STING contributes to antiglioma immunity via triggering type I IFN signals in the tumor microenvironment. Cancer Immunol Res *2*, 1199-1208.

Ohsawa, K., Irino, Y., Nakamura, Y., Akazawa, C., Inoue, K., and Kohsaka, S. (2007). Involvement of P2X4 and P2Y12 receptors in ATP-induced microglial chemotaxis. Glia *55*, 604-616.

Patel, A.P., Tirosh, I., Trombetta, J.J., Shalek, A.K., Gillespie, S.M., Wakimoto, H., Cahill, D.P., Nahed, B.V., Curry, W.T., Martuza, R.L., *et al.* (2014). Single-cell RNA-seq highlights intratumoral heterogeneity in primary glioblastoma. Science *344*, 1396-1401.

Paz-Ares, L., Luft, A., Vicente, D., Tafreshi, A., Gumus, M., Mazieres, J., Hermes, B., Cay Senler, F., Csoszi, T., Fulop, A., *et al.* (2018). Pembrolizumab plus Chemotherapy for Squamous Non-Small-Cell Lung Cancer. N Engl J Med *379*, 2040-2051.

Peng, S.B., Zhang, X., Paul, D., Kays, L.M., Gough, W., Stewart, J., Uhlik, M.T., Chen, Q., Hui, Y.H., Zamek-Gliszczynski, M.J., *et al.* (2015). Identification of LY2510924, a novel cyclic peptide CXCR4 antagonist that exhibits antitumor activities in solid tumor and breast cancer metastatic models. Mol Cancer Ther *14*, 480-490.

Pinton, L., Masetto, E., Vettore, M., Solito, S., Magri, S., D'Andolfi, M., Del Bianco, P., Lollo, G., Benoit, J.P., Okada, H., *et al.* (2019). The immune suppressive microenvironment of human gliomas depends on the accumulation of bone marrow-derived macrophages in the center of the lesion. J Immunother Cancer *7*, 58.

Piperi, C., Papavassiliou, K.A., and Papavassiliou, A.G. (2019). Pivotal Role of STAT3 in Shaping Glioblastoma Immune Microenvironment. Cells *8*.

Pires-Afonso, Y., Niclou, S.P., and Michelucci, A. (2020). Revealing and Harnessing Tumour-Associated Microglia/Macrophage Heterogeneity in Glioblastoma. Int J Mol Sci *21*.

Pombo Antunes, A.R., Scheyltjens, I., Lodi, F., Messiaen, J., Antoranz, A., Duerinck, J., Kancheva, D., Martens, L., De Vlaminck, K., Van Hove, H., *et al.* (2021). Single-cell profiling of myeloid cells in glioblastoma across species and disease stage reveals macrophage competition and specialization. Nat Neurosci *24*, 595-610.

Preusse, M., Tantawy, M.A., Klawonn, F., Schughart, K., and Pessler, F. (2013). Infection- and procedure-dependent effects on pulmonary gene expression in the early phase of influenza A virus infection in mice. BMC Microbiol *13*, 293.

Puchalski, R.B., Shah, N., Miller, J., Dalley, R., Nomura, S.R., Yoon, J.G., Smith, K.A., Lankerovich, M., Bertagnolli, D., Bickley, K., *et al.* (2018). An anatomic transcriptional atlas of human glioblastoma. Science *360*, 660-663.

Pyonteck, S.M., Akkari, L., Schuhmacher, A.J., Bowman, R.L., Sevenich, L., Quail, D.F., Olson, O.C., Quick, M.L., Huse, J.T., Teijeiro, V., *et al.* (2013). CSF-1R inhibition alters macrophage polarization and blocks glioma progression. Nat Med *19*, 1264-1272.

Qian, J., Luo, F., Yang, J., Liu, J., Liu, R., Wang, L., Wang, C., Deng, Y., Lu, Z., Wang, Y., *et al.* (2018). TLR2 Promotes Glioma Immune Evasion by Downregulating MHC Class II Molecules in Microglia. Cancer Immunol Res *6*, 1220-1233.

Qiao, Y., Kang, K., Giannopoulou, E., Fang, C., and Ivashkiv, L.B. (2016). IFN-gamma Induces Histone 3 Lysine 27 Trimethylation in a Small Subset of Promoters to Stably Silence Gene Expression in Human Macrophages. Cell Rep *16*, 3121-3129.

Quail, D.F., Bowman, R.L., Akkari, L., Quick, M.L., Schuhmacher, A.J., Huse, J.T., Holland, E.C., Sutton, J.C., and Joyce, J.A. (2016). The tumor microenvironment underlies acquired resistance to CSF-1R inhibition in gliomas. Science *352*, aad3018.

Quail, D.F., and Joyce, J.A. (2017). The Microenvironmental Landscape of Brain Tumors. Cancer Cell *31*, 326-341.

Raychaudhuri, B., Rayman, P., Huang, P., Grabowski, M., Hambardzumyan, D., Finke, J.H., and Vogelbaum, M.A. (2015). Myeloid derived suppressor cell infiltration of murine and human gliomas is associated with reduction of tumor infiltrating lymphocytes. J Neurooncol *122*, 293-301.

Razavi, S.M., Lee, K.E., Jin, B.E., Aujla, P.S., Gholamin, S., and Li, G. (2016). Immune Evasion Strategies of Glioblastoma. Front Surg *3*, 11.

Reardon, D.A., Brandes, A.A., Omuro, A., Mulholland, P., Lim, M., Wick, A., Baehring, J., Ahluwalia, M.S., Roth, P., Bahr, O.*, et al.* (2020). Effect of Nivolumab vs Bevacizumab in Patients With Recurrent Glioblastoma: The CheckMate 143 Phase 3 Randomized Clinical Trial. JAMA Oncol *6*, 1003-1010.

Remington, L.T., Babcock, A.A., Zehntner, S.P., and Owens, T. (2007). Microglial recruitment, activation, and proliferation in response to primary demyelination. Am J Pathol *170*, 1713-1724.

Ribas, A., Puzanov, I., Dummer, R., Schadendorf, D., Hamid, O., Robert, C., Hodi, F.S., Schachter, J., Pavlick, A.C., Lewis, K.D.*, et al.* (2015). Pembrolizumab versus investigator-choice chemotherapy for ipilimumab-refractory melanoma (KEYNOTE-002): a randomised, controlled, phase 2 trial. Lancet Oncol *16*, 908-918.

Ricard, C., Tchoghandjian, A., Luche, H., Grenot, P., Figarella-Branger, D., Rougon, G., Malissen, M., and Debarbieux, F. (2016). Phenotypic dynamics of microglial and monocyte-derived cells in glioblastoma-bearing mice. Sci Rep *6*, 26381.

Roesch, S., Rapp, C., Dettling, S., and Herold-Mende, C. (2018). When Immune Cells Turn Bad-Tumor-Associated Microglia/Macrophages in Glioma. Int J Mol Sci *19*.

Rothlin, C.V., Ghosh, S., Zuniga, E.I., Oldstone, M.B., and Lemke, G. (2007). TAM receptors are pleiotropic inhibitors of the innate immune response. Cell *131*, 1124-1136.

Sankowski, R., Bottcher, C., Masuda, T., Geirsdottir, L., Sagar, Sindram, E., Seredenina, T., Muhs, A., Scheiwe, C., Shah, M.J.*, et al.* (2019). Mapping microglia states in the human brain through the integration of high-dimensional techniques. Nat Neurosci *22*, 2098-2110.

Sasmita, A.O., Wong, Y.P., and Ling, A.P.K. (2018). Biomarkers and therapeutic advances in glioblastoma multiforme. Asia Pac J Clin Oncol *14*, 40-51.

Sayour, E.J., McLendon, P., McLendon, R., De Leon, G., Reynolds, R., Kresak, J., Sampson, J.H., and Mitchell, D.A. (2015). Increased proportion of FoxP3+ regulatory T cells in tumor infiltrating lymphocytes is associated with tumor recurrence and reduced survival in patients with glioblastoma. Cancer Immunol Immunother *64*, 419-427.

Sedgwick, A.J., Ghazanfari, N., Constantinescu, P., Mantamadiotis, T., and Barrow, A.D. (2020). The Role of NK Cells and Innate Lymphoid Cells in Brain Cancer. Front Immunol *11*, 1549.

Segerman, A., Niklasson, M., Haglund, C., Bergstrom, T., Jarvius, M., Xie, Y., Westermark, A., Sonmez, D., Hermansson, A., Kastemar, M.*, et al.* (2016). Clonal Variation in Drug and Radiation Response among Glioma-Initiating Cells Is Linked to Proneural-Mesenchymal Transition. Cell Rep *17*, 2994-3009.

Shemer, A., and Jung, S. (2015). Differential roles of resident microglia and infiltrating monocytes in murine CNS autoimmunity. Semin Immunopathol *37*, 613-623.

Silvin, A., and Ginhoux, F. (2018). Microglia heterogeneity along a spatio-temporal axis: More questions than answers. Glia *66*, 2045-2057.

Sottoriva, A., Spiteri, I., Piccirillo, S.G., Touloumis, A., Collins, V.P., Marioni, J.C., Curtis, C., Watts, C., and Tavare, S. (2013). Intratumor heterogeneity in human glioblastoma reflects cancer evolutionary dynamics. Proc Natl Acad Sci U S A *110*, 4009-4014.

Sousa, C., Biber, K., and Michelucci, A. (2017). Cellular and Molecular Characterization of Microglia: A Unique Immune Cell Population. Front Immunol *8*, 198.

Sousa, C., Golebiewska, A., Poovathingal, S.K., Kaoma, T., Pires-Afonso, Y., Martina, S., Coowar, D., Azuaje, F., Skupin, A., Balling, R.*, et al.* (2018). Single-cell transcriptomics reveals distinct inflammation-induced microglia signatures. EMBO Rep *19*.

Stratoulias, V., Venero, J.L., Tremblay, M.E., and Joseph, B. (2019). Microglial subtypes: diversity within the microglial community. EMBO J *38*, e101997.

Strelko, C.L., Lu, W., Dufort, F.J., Seyfried, T.N., Chiles, T.C., Rabinowitz, J.D., and Roberts, M.F. (2011). Itaconic acid is a mammalian metabolite induced during macrophage activation. J Am Chem Soc *133*, 16386-16389.

Stupp, R., Mason, W.P., van den Bent, M.J., Weller, M., Fisher, B., Taphoorn, M.J., Belanger, K., Brandes, A.A., Marosi, C., Bogdahn, U.*, et al.* (2005). Radiotherapy plus concomitant and adjuvant temozolomide for glioblastoma. N Engl J Med *352*, 987-996.

Szatmari, T., Lumniczky, K., Desaknai, S., Trajcevski, S., Hidvegi, E.J., Hamada, H., and Safrany, G. (2006). Detailed characterization of the mouse glioma 261 tumor model for experimental glioblastoma therapy. Cancer Sci *97*, 546-553.

Szulzewsky, F., Pelz, A., Feng, X., Synowitz, M., Markovic, D., Langmann, T., Holtman, I.R., Wang, X., Eggen, B.J., Boddeke, H.W.*, et al.* (2015). Glioma-associated microglia/macrophages display an expression profile different from M1 and M2 polarization and highly express Gpnmb and Spp1. PLoS One *10*, e0116644.

Tallam, A., Perumal, T.M., Antony, P.M., Jager, C., Fritz, J.V., Vallar, L., Balling, R., Del Sol, A., and Michelucci, A. (2016). Gene Regulatory Network Inference of Immunoresponsive Gene 1 (IRG1) Identifies Interferon Regulatory Factor 1 (IRF1) as Its Transcriptional Regulator in Mammalian Macrophages. PLoS One *11*, e0149050.

Tamimi, A.F., and Juweid, M. (2017). Epidemiology and Outcome of Glioblastoma. In Glioblastoma, S. De Vleeschouwer, ed. (Brisbane (AU)).

Tan, M.S.Y., Sandanaraj, E., Chong, Y.K., Lim, S.W., Koh, L.W.H., Ng, W.H., Tan, N.S., Tan, P., Ang, B.T., and Tang, C. (2019). A STAT3-based gene signature stratifies glioma patients for targeted therapy. Nat Commun *10*, 3601.

Taniguchi, T., Ogasawara, K., Takaoka, A., and Tanaka, N. (2001). IRF family of transcription factors as regulators of host defense. Annu Rev Immunol *19*, 623-655.

Tannahill, G.M., Curtis, A.M., Adamik, J., Palsson-McDermott, E.M., McGettrick, A.F., Goel, G., Frezza, C., Bernard, N.J., Kelly, B., Foley, N.H.*, et al.* (2013). Succinate is an inflammatory signal that induces IL-1beta through HIF-1alpha. Nature *496*, 238-242.

Tasic, B., Menon, V., Nguyen, T.N., Kim, T.K., Jarsky, T., Yao, Z., Levi, B., Gray, L.T., Sorensen, S.A., Dolbeare, T.*, et al.* (2016). Adult mouse cortical cell taxonomy revealed by single cell transcriptomics. Nat Neurosci *19*, 335-346.

Thomas, R.P., Nagpal, S., Iv, M., Soltys, S.G., Bertrand, S., Pelpola, J.S., Ball, R., Yang, J., Sundaram, V., Lavezo, J.*, et al.* (2019). Macrophage Exclusion after Radiation Therapy (MERT): A First in Human Phase I/II Trial using a CXCR4 Inhibitor in Glioblastoma. Clin Cancer Res *25*, 6948-6957.

Thorsson, V., Gibbs, D.L., Brown, S.D., Wolf, D., Bortone, D.S., Ou Yang, T.H., Porta-Pardo, E., Gao, G.F., Plaisier, C.L., Eddy, J.A.*, et al.* (2018). The Immune Landscape of Cancer. Immunity *48*, 812-830 e814.

Tremblay, M.E., Stevens, B., Sierra, A., Wake, H., Bessis, A., and Nimmerjahn, A. (2011). The role of microglia in the healthy brain. J Neurosci *31*, 16064-16069.

Tsuda, M., Shigemoto-Mogami, Y., Koizumi, S., Mizokoshi, A., Kohsaka, S., Salter, M.W., and Inoue, K. (2003). P2X4 receptors induced in spinal microglia gate tactile allodynia after nerve injury. Nature *424*, 778-783.

Uriarte Huarte, O., Kyriakis, D., Heurtaux, T., Pires-Afonso, Y., Grzyb, K., Halder, R., Buttini, M., Skupin, A., Mittelbronn, M., and Michelucci, A. (2021). Single-Cell Transcriptomics and In Situ Morphological Analyses Reveal Microglia Heterogeneity Across the Nigrostriatal Pathway. Front Immunol *12*, 639613.

Utz, S.G., See, P., Mildenberger, W., Thion, M.S., Silvin, A., Lutz, M., Ingelfinger, F., Rayan, N.A., Lelios, I., Buttgereit, A.*, et al.* (2020). Early Fate Defines Microglia and Non-parenchymal Brain Macrophage Development. Cell *181*, 557-573 e518.

van den Bossche, W.B.L., Kleijn, A., Teunissen, C.E., Voerman, J.S.A., Teodosio, C., Noske, D.P., van Dongen, J.J.M., Dirven, C.M.F., and Lamfers, M.L.M. (2018). Oncolytic virotherapy in glioblastoma patients induces a tumor macrophage phenotypic shift leading to an altered glioblastoma microenvironment. Neuro Oncol *20*, 1494-1504.

Vargas, P., Maiuri, P., Bretou, M., Saez, P.J., Pierobon, P., Maurin, M., Chabaud, M., Lankar, D., Obino, D., Terriac, E.*, et al.* (2016). Innate control of actin nucleation determines two distinct migration behaviours in dendritic cells. Nat Cell Biol *18*, 43-53.

Venteicher, A.S., Tirosh, I., Hebert, C., Yizhak, K., Neftel, C., Filbin, M.G., Hovestadt, V., Escalante, L.E., Shaw, M.L., Rodman, C.*, et al.* (2017). Decoupling genetics, lineages, and microenvironment in IDH-mutant gliomas by single-cell RNA-seq. Science *355*.

Verhaak, R.G., Hoadley, K.A., Purdom, E., Wang, V., Qi, Y., Wilkerson, M.D., Miller, C.R., Ding, L., Golub, T., Mesirov, J.P.*, et al.* (2010). Integrated genomic analysis identifies clinically relevant subtypes of glioblastoma characterized by abnormalities in PDGFRA, IDH1, EGFR, and NF1. Cancer Cell *17*, 98-110.

Vilhardt, F. (2005). Microglia: phagocyte and glia cell. Int J Biochem Cell Biol *37*, 17-21.

von Roemeling, C.A., Wang, Y., Qie, Y., Yuan, H., Zhao, H., Liu, X., Yang, Z., Yang, M., Deng, W., Bruno, K.A.*, et al.* (2020). Therapeutic modulation of phagocytosis in glioblastoma can activate both innate and adaptive antitumour immunity. Nat Commun *11*, 1508.

Wainwright, D.A., Balyasnikova, I.V., Chang, A.L., Ahmed, A.U., Moon, K.S., Auffinger, B., Tobias, A.L., Han, Y., and Lesniak, M.S. (2012). IDO expression in brain tumors increases the recruitment of regulatory T cells and negatively impacts survival. Clin Cancer Res *18*, 6110-6121.

Walters, M.J., Ebsworth, K., Berahovich, R.D., Penfold, M.E., Liu, S.C., Al Omran, R., Kioi, M., Chernikova, S.B., Tseng, D., Mulkearns-Hubert, E.E.*, et al.* (2014). Inhibition of CXCR7 extends survival following irradiation of brain tumours in mice and rats. Br J Cancer *110*, 1179-1188.

Wang, Q., Hu, B., Hu, X., Kim, H., Squatrito, M., Scarpace, L., deCarvalho, A.C., Lyu, S., Li, P., Li, Y.*, et al.* (2017). Tumor Evolution of Glioma-Intrinsic Gene Expression Subtypes Associates with Immunological Changes in the Microenvironment. Cancer Cell *32*, 42-56 e46.

Wang, T., Niu, G., Kortylewski, M., Burdelya, L., Shain, K., Zhang, S., Bhattacharya, R., Gabrilovich, D., Heller, R., Coppola, D., *et al.* (2004). Regulation of the innate and adaptive immune responses by Stat-3 signaling in tumor cells. Nat Med *10*, 48-54.

Warburg, O., Wind, F., and Negelein, E. (1927). The Metabolism of Tumors in the Body. J Gen Physiol *8*, 519-530.

Weiss, J.M., Davies, L.C., Karwan, M., Ileva, L., Ozaki, M.K., Cheng, R.Y., Ridnour, L.A., Annunziata, C.M., Wink, D.A., and McVicar, D.W. (2018). Itaconic acid mediates crosstalk between macrophage metabolism and peritoneal tumors. J Clin Invest *128*, 3794-3805.

Weller, M., van den Bent, M., Preusser, M., Le Rhun, E., Tonn, J.C., Minniti, G., Bendszus, M., Balana, C., Chinot, O., Dirven, L., *et al.* (2021). EANO guidelines on the diagnosis and treatment of diffuse gliomas of adulthood. Nat Rev Clin Oncol *18*, 170-186.

Wesolowska, A., Kwiatkowska, A., Slomnicki, L., Dembinski, M., Master, A., Sliwa, M., Franciszkiewicz, K., Chouaib, S., and Kaminska, B. (2008). Microglia-derived TGF-beta as an important regulator of glioblastoma invasion--an inhibition of TGF-beta-dependent effects by shRNA against human TGF-beta type II receptor. Oncogene *27*, 918-930.

Wibom, C., Surowiec, I., Moren, L., Bergstrom, P., Johansson, M., Antti, H., and Bergenheim, A.T. (2010). Metabolomic patterns in glioblastoma and changes during radiotherapy: a clinical microdialysis study. J Proteome Res *9*, 2909-2919.

Williams, J.O., Roche, T.E., and McFadden, B.A. (1971). Mechanism of action of isocitrate lyase from Pseudomonas indigofera. Biochemistry *10*, 1384-1390.

Wlodarczyk, A., Benmamar-Badel, A., Cedile, O., Jensen, K.N., Kramer, I., Elsborg, N.B., and Owens, T. (2018). CSF1R Stimulation Promotes Increased Neuroprotection by CD11c+ Microglia in EAE. Front Cell Neurosci *12*, 523.

Wlodarczyk, A., Lobner, M., Cedile, O., and Owens, T. (2014). Comparison of microglia and infiltrating CD11c(+) cells as antigen presenting cells for T cell proliferation and cytokine response. J Neuroinflammation *11*, 57.

Woolf, Z., Swanson, M.E.V., Smyth, L.C., Mee, E.W., Schweder, P., Heppner, P., Kim, B.J.H., Turner, C., Oldfield, R.L., Curtis, M.A., *et al.* (2021). Single-cell image analysis reveals a protective role for microglia in glioblastoma. Neuro-Oncology Advances.

Woroniecka, K.I., Rhodin, K.E., Chongsathidkiet, P., Keith, K.A., and Fecci, P.E. (2018). T-cell Dysfunction in Glioblastoma: Applying a New Framework. Clin Cancer Res *24*, 3792-3802.

Wu, S.Y., and Watabe, K. (2017). The roles of microglia/macrophages in tumor progression of brain cancer and metastatic disease. Front Biosci (Landmark Ed) *22*, 1805-1829.

Xu, S., Tang, L., Li, X., Fan, F., and Liu, Z. (2020). Immunotherapy for glioma: Current management and future application. Cancer Lett *476*, 1-12.

Ye, X.Z., Xu, S.L., Xin, Y.H., Yu, S.C., Ping, Y.F., Chen, L., Xiao, H.L., Wang, B., Yi, L., Wang, Q.L., *et al.* (2012). Tumor-associated microglia/macrophages enhance the invasion of glioma stem-like cells via TGF-beta1 signaling pathway. J Immunol *189*, 444-453.

Zagorska, A., Traves, P.G., Lew, E.D., Dransfield, I., and Lemke, G. (2014). Diversification of TAM receptor tyrosine kinase function. Nat Immunol *15*, 920-928.

Zhang, F., Parayath, N.N., Ene, C.I., Stephan, S.B., Koehne, A.L., Coon, M.E., Holland, E.C., and Stephan, M.T. (2019). Genetic programming of macrophages to perform anti-tumor functions using targeted mRNA nanocarriers. Nat Commun *10*, 3974.

Zhang, J., Sarkar, S., Cua, R., Zhou, Y., Hader, W., and Yong, V.W. (2012). A dialog between glioma and microglia that promotes tumor invasiveness through the CCL2/CCR2/interleukin-6 axis. Carcinogenesis *33*, 312-319.

Zhang, X., Wang, Y., Yuan, J., Li, N., Pei, S., Xu, J., Luo, X., Mao, C., Liu, J., Yu, T.*, et al.* (2018). Macrophage/microglial Ezh2 facilitates autoimmune inflammation through inhibition of Socs3. J Exp Med *215*, 1365-1382.

Zhou, W., Ke, S.Q., Huang, Z., Flavahan, W., Fang, X., Paul, J., Wu, L., Sloan, A.E., McLendon, R.E., Li, X.*, et al.* (2015). Periostin secreted by glioblastoma stem cells recruits M2 tumour-associated macrophages and promotes malignant growth. Nat Cell Biol *17*, 170-182.

Zhu, C., Kros, J.M., Cheng, C., and Mustafa, D. (2017). The contribution of tumor-associated macrophages in glioma neo-angiogenesis and implications for anti-angiogenic strategies. Neuro Oncol *19*, 1435-1446.

Zhu, M., Foreman, D.P., O'Brien, S.A., Jin, Y., and Zhang, W. (2018). Phospholipase D in TCR-Mediated Signaling and T Cell Activation. J Immunol *200*, 2165-2173.

APPENDIX

PAPER 1: Review article

International Journal of
Molecular Sciences

MDPI

Review

Revealing and Harnessing Tumour-Associated Microglia/Macrophage Heterogeneity in Glioblastoma

Yolanda Pires-Afonso [1,2], Simone P. Niclou [3,4] and Alessandro Michelucci [1,5,*]

1 Neuro-Immunology Group, Department of Oncology, Luxembourg Institute of Health, L-1526 Luxembourg, Luxembourg; yolanda.piresafonso@lih.lu
2 Doctoral School of Science and Technology, University of Luxembourg, L-4365 Esch-sur-Alzette, Luxembourg
3 NORLUX Neuro-Oncology Laboratory, Department of Oncology, Luxembourg Institute of Health, L-1526 Luxembourg, Luxembourg; simone.niclou@lih.lu
4 Department of Biomedicine, University of Bergen, N-5007 Bergen, Norway
5 Luxembourg Centre for Systems Biomedicine, University of Luxembourg, L-4365 Esch-sur-Alzette, Luxembourg
* Correspondence: alessandro.michelucci@lih.lu; Tel.: +352-26970-263; Fax: +352-26970-390

Received: 20 December 2019; Accepted: 20 January 2020; Published: 21 January 2020

check for updates

Abstract: Cancer heterogeneity and progression are subject to complex interactions between neoplastic cells and their microenvironment, including the immune system. Although glioblastomas (GBMs) are classified as 'cold tumours' with very little lymphocyte infiltration, they can contain up to 30–40% of tumour-associated macrophages, reported to contribute to a supportive microenvironment that facilitates tumour proliferation, survival and migration. In GBM, tumour-associated macrophages comprise either resident parenchymal microglia, perivascular macrophages or peripheral monocyte-derived cells. They are recruited by GBMs and in turn release growth factors and cytokines that affect the tumour. Notably, tumour-associated microglia/macrophages (TAMs) acquire different expression programs, which shape the tumour microenvironment and contribute to GBM molecular subtyping. Further, emerging evidence highlights that TAM programs may adapt to specific tumour features and landscapes. Here, we review key evidence describing TAM transcriptional and functional heterogeneity in GBM. We propose that unravelling the intricate complexity and diversity of the myeloid compartment as well as understanding how different TAM subsets may affect tumour progression will possibly pave the way to new immune therapeutic avenues for GBM patients.

Keywords: glioblastoma; tumour-associated microglia/macrophages; cellular heterogeneity; immunotherapy; precision medicine

1. Introduction

Gliomas represent approximately 80% of all malignant tumours of the central nervous system (CNS) [1]. Among them, glioblastoma (GBM) is the highest-grade glioma (grade IV) and the most common malignant brain tumour in adults. The standard care of treatment for GBM relies on maximal surgical resection followed by radiation therapy and concomitant chemotherapy with the alkylating agent temozolomide as established in 2005 [2]. However, recurrence is inevitable, and prognosis remains poor with a median survival of 15 months after diagnosis. Hence, the development of novel therapeutic options, including immunotherapies, are needed.

The immune landscape of brain tumours is intensely investigated, unveiling new insight in the interactions between neoplastic cells and the immune system [3]. GBM is a highly immunosuppressive cancer, where resident microglia and peripheral infiltrated macrophages play a key role in immune escape mechanisms [4]. Tumour-associated microglia/macrophages (TAMs), which can constitute up

to 30–40% of the bulk tumour mass, outnumber by far infiltrating lymphocytes in these tumours [3]. This scarcity of lymphocytes in the tumour microenvironment contrasts with other tumour types, e.g., melanoma or lung cancer, therefore classifying GBM as immunologically 'cold tumours'. Whether or not these tumours are intrinsically non-immunogenic or whether lymphocytes, including T cells, are actively excluded, remains to be determined [5]. In this context, an extensive immunogenomic analysis of more than 10,000 tumours comprising data from 33 diverse cancer types compiled by The Cancer Genome Atlas (TCGA) allowed to identify six different immune subtypes: wound healing, IFN-γ dominant, inflammatory, lymphocyte depleted, immunologically quiet and TGF-β dominant [6]. Their characterization was based on differences in macrophage or lymphocyte signatures, Th1:Th2 cell ratio, extent of intra-tumour heterogeneity, aneuploidy, extent of neoantigen load, overall cell proliferation, expression of immunomodulatory genes and prognosis. Notably, specific driver mutations correlated with lower (CTNNB1, NRAS, or IDH1) or higher (BRAF, TP53, or CASP8) leukocyte levels across all cancers. Future studies should investigate the link between specific genomic alterations and their contribution to the adaptation of the tumour microenvironment. As expected, in this classification GBMs were among the "lymphocyte depleted" subtype displaying a prominent macrophage signature, with Th1 suppressed and high M2 response [6].

Due to their large number in the tumour microenvironment, TAMs represent a key target for GBM immunotherapy and a range of immunomodulatory agents are currently being trialled in patients. For example, as TAMs critically depend on colony-stimulating factor-1 (CSF-1) for their survival, differentiation and proliferation, strategies to target TAMs in the clinic include CSF-1 receptor (CSF-1R) blockade [7,8]. However, despite having shown an effect on tumour growth in mouse models, this approach failed to improve overall survival in patients [9], suggesting that putative TAM subpopulations may be resistant to CSF-1R inhibition [10].

Despite extensive efforts in this direction, the precise role of TAMs in GBM onset and progression as well as how TAMs may affect current immunotherapeutic approaches, including vaccines, oncolytic viruses and immune-checkpoint inhibitors, remains unclear. Therefore, a deeper understanding of the complexity and diversity of TAM adaptive features is critical to develop novel personalized immune therapeutic strategies for GBM patients.

In this review, we will describe different features underlying TAMs heterogeneity and adaptation in GBM. Further, we will pinpoint the aspects linked to their diversity that warrant further investigations and how this heterogeneity may ultimately be harnessed for the development of novel personalized immune therapeutic strategies.

2. Tumour-Associated Microglia/Macrophages in Glioblastoma

2.1. M1 and M2 Polarization States: The Basic School of Thought

Macrophages are highly dynamic cells whose molecular profiles are substantially influenced by specific environmental cues. In vitro studies enabled classification of activated macrophages according to a binary system, with pro-inflammatory cytokines (e.g., IFNγ) skewing them towards a classical (M1-like) activation state, while anti-inflammatory cytokines (e.g., IL4) polarizing macrophages into an alternative (M2-like) phenotype [11]. A similar dual classification has been described in cultivated microglia exposed either to LPS/IFNγ or IL10/IL4 [12]. In cancer, this nomenclature has been used for decades to discriminate M1-like anti-tumour versus M2-like pro-tumour macrophages, with the latter assumed to constitute the majority of macrophages in the tumour according to their immune-suppressive properties [13]. However, this simplistic classification described in vitro does not apply to the in vivo situation as it only represents the two extremes of a continuum of activated states. Over time, further intermediate states describing M2-like macrophages have been introduced, with a putative M2c state associated to immune regulation, matrix deposition and tissue remodelling mostly observed in brain malignancies [14]. However, despite these efforts, little exclusivity was observed between these different categories of TAMs in GBM [15]. This is supported by studies conducted

in GBM murine models where TAMs display an expression profile different from the predefined M1 and M2 polarization states, including a mixture of M1- and M2-specific genes [16] or analyses in GBM patients showing that TAMs exhibit a non-polarized M0 phenotype [17] (Figure 1). More recently, another attempt to distinguish between pro- and anti-tumour macrophages has been based on surface markers, where M1-like macrophages have been associated with the expression of CD40, CD74, MHC-II and phosphorylated STAT1, whereas M2-like cells express CD163, CD204, arginase-1 (ARG1) and phosphorylated STAT3 [14]. However, these markers have also failed to provide a robust separation and the subsequent understanding of their relative contribution to disease pathogenesis is still unclear.

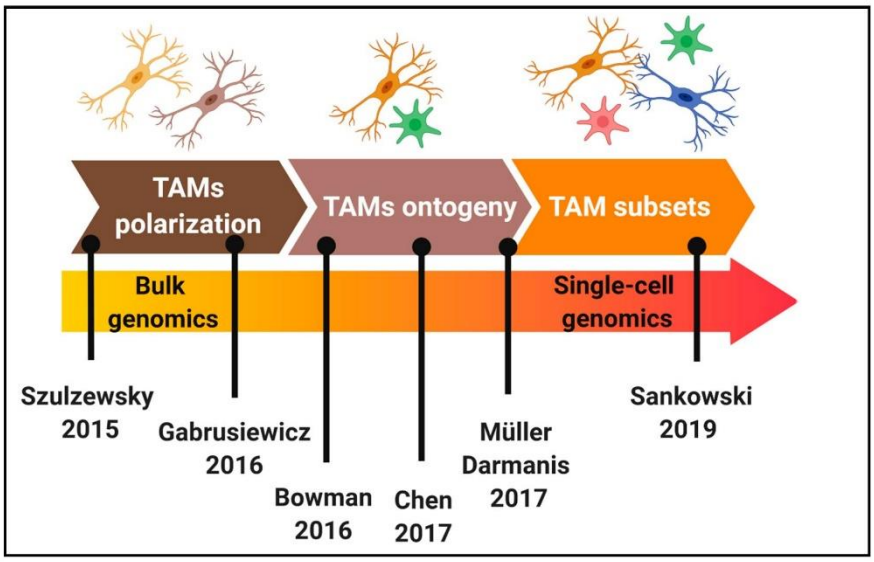

Figure 1. Chronology of the characterization of tumour-associated microglia/macrophages (TAMs) heterogeneity in glioblastoma (GBM). Key studies that have contributed to elucidate TAMs polarization, ontogeny and subsets in GBM mouse models and patients.

2.2. *Impact of Ontogeny on Tumour-Associated Microglia/Macrophage Functionality*

The healthy brain harbours specific populations of tissue-resident macrophages effectively located in the parenchyma, perivascular spaces, meninges and choroid plexus where they maintain tissue homeostasis and ensure immune functions [18]. Within the parenchyma of the central nervous system (CNS), microglia are unique specialized immune effector cells that populate the brain early during embryogenesis [19]. In the adult brain, microglia continuously scan the environment and carry out several tasks, including neuronal support, phagocytosis of apoptotic cells and immune surveillance [20,21]. Their pool is maintained by self-renewal without contribution from bone marrow-derived progenitors, thus making microglia the only resident immune cell population in the healthy brain [22,23]. However, under certain pathological conditions, such as in GBM, the local inflammatory environment can compromise the integrity of the blood brain barrier leading to the infiltration of inflammatory monocytes from the circulation, which subsequently differentiate into monocyte-derived macrophages once they enter the brain tissue [24]. Therefore, in GBM, tumour-associated macrophages encompass resident parenchymal microglia, perivascular macrophages and peripheral monocyte-derived cells [25]. As a general observation, although tumour-associated macrophage proportions may vary in an organ-dependent manner, they have emerged as one of the most critical cell types contributing to worse prognosis across the vast majority of cancers [26].

In GBM, TAMs are recruited to the tumour site through various mediators, including CCL2, CX3CL1, CSF-1, GM-CSF and osteopontin released by neoplastic cells [24,27–29]. Upon accumulation at the tumour site, the functions of TAMs are supposed to be progressively overturned towards a pro-tumorigenic phenotype. For example, TAMs promote immune suppression and angiogenesis through the release of specific anti-inflammatory cytokines (e.g., TGFβ or IL10) and angiogenic factors (e.g., VEGFα) (see reviews [14,30]. Functionally, microglia and monocyte-derived macrophages react differently to various types of CNS insults [31] and the specific roles for these distinct cell populations are now starting to emerge in GBM. For example, it has been recently shown that the immune suppressive microenvironment in GBM patients depends on the accumulation of monocyte-derived macrophages [32].

Experimentally, approaches to distinguish resident microglia from other inflammatory immune cells entering the CNS have traditionally relied on CD45 expression to discriminate resident microglia ($CD11b^{+}CD45^{low}$ cells) from peripheral monocyte-derived macrophages ($CD11b^{+}CD45^{high}$ cells) [33]. However, this strategy has been recently challenged showing that glioma-associated microglia upregulate CD45 expression, thus limiting the effective discrimination of both populations in this disease [34]. Recently, using multiple genetic lineage tracing in transgenic (GEMM-shP53) and syngeneic GL261 mouse models, Bowman and collaborators have demonstrated that microglia specifically repress *Itga4* (CD49D), enabling the distinction between microglia and monocyte-derived macrophages in murine tumours [35] (Figure 1). Gene expression profiling demonstrated that both populations exhibit distinct activation states despite common traits of tumour education [35]. An unbiased meta-analysis of five published murine transcriptional datasets identified discriminatory marker sets distinguishing microglia versus peripheral monocytes/macrophages in health and gliomas [36]. These findings were validated at the protein level using syngeneic GL261 and RCAS-PDGFB driven GBM mouse models, where microglia-enriched genes included *P2ry12*, *Tmem119*, *Slc2a5* and *Fcrls*, whereas *Emilin2*, *Gda*, *Hp* and *Sell* were mainly expressed by peripheral monocytes/macrophages [36].

Further investigations will be critical to study how monocyte-derived macrophages in GBM influence the immunological functions of resident microglia. For example, during CNS injuries, peripheral macrophages affect nuclear factor kappa B (NFκB) signalling pathways in microglia reducing their phagocytic and inflammatory responses [37]. In cancer, targeting NFκB prompts TAMs towards a more cytotoxic anti-tumorigenic phenotype with a more activated state characterized by higher IL12 and MHC-II expression together with reduced levels of IL10 and ARG1 [38].

3. Tumour-Associated Microglia/Macrophages as Therapeutic Targets in Glioblastoma

3.1. Effect of Chemotherapy and Radiotherapy on Tumour-Associated Microglia/Macrophages

To date, the combination of radio-chemotherapy with immunotherapeutic agents has not been effective in GBM and drugs driving anti-tumour immune responses are currently evaluated in clinical trials. In principle, radiation can increase in situ immunogenicity of malignant cells, thus improving tumour immune recognition and T-cell mediated anti-tumour responses [39]. In these regimens, it remains to be determined what is the optimal radiation dose and schedule to harness the best immune effect. Moreover, it has to be considered that systemic administration of chemotherapeutic agents has immunosuppressive effects, thus representing a major challenge for effective anti-cancer immunotherapy-based strategies. In addition, high doses of glucocorticoids, such as dexamethasone, are usually administered to GBM patients to reduce inflammation and radiotherapy-induced cerebral oedema [40], thus dampening the inflammatory response by exerting profound effects on T cell subsets and NK cells [41]. Regarding TAMs, they are supposed to have a bimodal response to chemotherapy and radiotherapy, which can either reduce or amplify the magnitude of the anti-tumour responses [15]. These can be induced upon irradiation where targeted cancer cells generate damage-associated molecular patterns (DAMPs), such as high mobility group box 1 (HMGB1), that are recognized by pattern-recognition receptors (PRRs), including TLR2 and TLR4 in myeloid cells, that in turn trigger a

pro-inflammatory phenotype [42]. Another route how radiation can induce anti-tumour immunity in immunogenic tumours is via STING and type I IFN-dependent signalling in dendritic cells [43]. It remains to be seen whether such mechanisms are active in immunologically 'cold tumours' such as GBM. Overall, it is evident that a thorough understanding of the complex interplay between tumour immunogenicity, the immune system and the adjuvant therapy will be critical to optimize and fine-tune the efficacy of immunotherapeutic approaches in GBM.

3.2. Depletion of Tumour-Associated Microglia/Macrophages in Glioblastoma

Upon accumulation to the tumour site, TAMs are thought to drive immune-suppression and promote tumour progression. Due to their high numbers in GBM, their genomic stability and adaptability to the microenvironment, several strategies to deplete TAMs have been developed. For example, liposome-encapsulated clodronate, which has been commonly used to deplete macrophage populations by inducing their apoptosis once phagocytosed by the cells, reduced tumour invasion in GL261 cultured brain slices, which was restored after addition of TAMs [44]. However, it has been recently demonstrated that intracerebral administration of clodronate liposomes into brain parenchyma can deplete microglia, but can also damage other brain cells and blood vessel integrity [45], therefore lacking specificity for TAMs. Further, attempts to specifically target peripheral macrophages, for example limiting monocyte infiltration via *Ccl2* genetic ablation, prolonged the survival of tumour-bearing mice [46], but these approaches have not been applied to patients yet. On the contrary, administration of ganciclovir to transgenic mice expressing thymidine kinase under the CD11b promoter reduced the $CD11b^+$ population and contributed to 30% of tumour increase in the GBM syngeneic GL261 mouse model [47]. A major drawback of these studies is that these results were obtained in highly immunogenic GBM mouse models, while GBMs in patients are poorly immunogenic and display low T cell infiltration [48]. Further, TAMs depletion occurred prior to glioma cells implantation, therefore gliomagenesis may be substantially affected in the absence of TAMs. In silico studies have shown that TAM depletion therapy may be beneficial only for patients treated at early stages with a concomitant cytokine therapy [49].

These results highlight that depleting TAMs indiscriminately is probably not the optimal approach, as TAMs might play different roles depending on GBM features, including immunogenicity.

3.3. Immune Checkpoint Inhibitors and Reprogramming of Tumour-Associated Microglia/Macrophages in Glioblastoma

Immunotherapy is emerging as a promising approach holding great potential to foster tumour elimination by unleashing the immune system. The intense crosstalk between tumour cells, antigen presenting cells (APCs) and T cells is intricately controlled by multiple ligand-receptor interactions, known as checkpoints, which generally inhibit T-cell activation, ultimately affecting T cell cytotoxicity against tumour cells [50]. For example, the binding of PD-L1 expressed by tumour cells to its receptor PD-1 on T cells keeps the immune response in check. Hence, blocking this binding with an immune checkpoint inhibitor (e.g., anti-PD-L1 or anti-PD-1) enables T cells to attack the tumour cells. Similarly, the binding of APC-derived CD80/CD86 to CTLA-4 on T cells maintains the T cells in an inactive state and interfering with this binding allows T cells to be reactive. Evidently, the efficacy of T cell-based therapies is based on the amounts of tumour infiltrating lymphocytes (TILs), which are remarkably low in GBM [51]. Preclinical studies in the immunogenic GL261 syngeneic GBM mouse model have demonstrated the efficacy of targeting T cell immune-checkpoints, including CTLA-4, PD-1, PD-L1 and PD-L2 as monotherapies or in combination with radiotherapy [52]. However, as indicated above, this model poorly reflects human disease, since GBM patients typically show low mutational load and weak tumour immunogenicity, which correlates with poor response to immune checkpoint inhibitors [53]. The anti-PD-1 antibody advanced furthest in patients with GBM, however, in the phase III clinical trial, despite showing drug safety, it did not meet the primary endpoint of the study [5].

Due to TAMs abundance within GBM and their fast response to external stimuli, strategies to re-educate TAMs in mouse glioma models may be more efficient than their depletion or the use of immune checkpoint inhibitors. In this context, a promising target is signal-regulatory protein (SIRP) α, an inhibitory receptor expressed on myeloid cells that recognizes the CD47 ligand on tumour cells and contributes to immune evasion. The targeting of this axis with humanized anti-CD47 antibodies enhanced tumour phagocytosis and reduced tumour burden in patient-derived orthotopic xenografts of paediatric brain tumours [54]. Interesting results were also obtained using orthotopic xenografts and a syngeneic mouse model with genetically color-coded macrophages (*Ccr2*^{RFP}) and microglia (*Cx3cr1*^{GFP}), in which microglia were found to effectively phagocytose tumour cells in response to anti-CD47 blockade with a reduced inflammatory signature, making them a promising target for clinical applications [55]. Another example highlighting TAM subset-specific facets is the response to the VEGF neutralizing antibody bevacizumab, where blood-derived TAMs, instead of resident microglia, preferentially contributed to therapy resistance [56].

Combinatorial approaches targeting immune-suppressive populations concomitantly with promoting endogenous anti-tumour immune responses successfully impaired tumour progression in various subcutaneous tumour models. For example, dual targeting of suppressive myeloid populations by inhibiting CSF-1/CSF-1R signalling and activation of APCs with CD40 agonists conferred superior anti-tumour efficacy and increased survival compared with monotherapy. This effect was attributed to the decrease of immunosuppressive TAMs and Foxp3^{+} regulatory T cells as well as accumulation of tumour-infiltrating effector T cells exhibiting anti-tumorigenic features [57]. Further, the combination of an oncolytic virus expressing IL-12 together with the two immune checkpoint inhibitors anti-CTLA-4 and anti-PD1 was able to significantly reduce tumour growth in GBM intracranial mouse models [58]. Lastly, monotherapies or combinatorial approaches targeting TAMs are currently being undertaken in GBM clinical trials (Table 1).

Table 1. Examples of current clinical trials targeting TAMs in GBM. RT: radiotherapy; TMZ: temozolomide; MRI: magnetic resonance imaging; LITT: laser interstitial thermal therapy; rGBM: relapsed/recurrent glioblastoma.

Myeloid Target	Drug Name	Additional Treatment	Study Phase	Tumour Type	Study Identifier
CSF-1R inhibitor	Cabiralizumab	Nivolumab (anti-PD-1)	I	GBM	NCT02526017
CSF-1R inhibitor	BLZ945	PDR001 (anti-PD-1)	I/II	GBM/rGBM	NCT02829723
CSF-1R inhibitor	Pexidartinib	RT + TMZ	I/II	GBM	NCT01790503
CXCR4 inhibitor	USL311	Lomustine	II	rGBM	NCT02765165
PD-L1 inhibitor	Avelumab	MRI-guided LITT therapy	I	rGBM	NCT03341806
STAT3 inhibitor	WP1066	-	I	rGBM	NCT01904123
GM-CSF	VBI-1901	-	I/II	rGBM	NCT03382977
MIF inhibitor	Ibudilast	TMZ	I/II	GBM/rGBM	NCT03782415

Taken together, strategies aiming at reprogramming immunosuppressive myeloid cell populations and/or fostering anti-tumour immune responses in the tumour microenvironment may be necessary to empower checkpoint-based immune therapeutics in GBM. However, TAMs heterogeneity may represent a barrier to non-selective immunotherapies, which seek to target TAMs indiscriminately.

4. Dissecting Tumour-Associated Microglia/Macrophages Diversity at Single-Cell Resolution

4.1. Glioblastoma Subtyping and Single-Cell Analyses

In the last 10 years, multiple attempts have used transcriptional profiling to sub-classify GBMs into clinically meaningful tumour subtypes [59–61]. Although three common molecular subtypes (mesenchymal, classical and proneural) have been proposed in various studies, they poorly correlate with clinically relevant parameters, such as patient survival, except in a subgroup of patients [62]. Of note, the mesenchymal subtype was found to be characterized by a low tumour purity score along with an enrichment of TAMs, highlighting the contribution of the microenvironment in transcriptional

profiling based on bulk tissue analysis. Furthermore, surgical multisampling has revealed that molecular subtypes can be present within the same patient tumour, suggesting that they do not represent bonafide subtypes, but rather reflect heterogeneous cellular expression programs [63]. More recently, this has been confirmed by single-cell RNA-sequencing (scRNA-seq) revealing the dynamic plasticity of GBM cells [64,65]. Hence, these studies highlight that tumour cells from a distinct GBM biopsy can display molecular traits reflecting different cellular states, a concept that is reminiscent of the M1 and M2 states in TAMs. Thus, at present the most promising classification strategies for gliomas are based on DNA methylation, allowing to discriminate IDH-mutant gliomas and IDH-wildtype gliomas [61,66].

4.2. Single-Cell Analyses of Microglia and Macrophages in Glioblastoma: Heterogeneity beyond Polarization States and Ontogeny?

Recent scRNA-seq studies also highlighted tissue-specific myeloid cell heterogeneity associated with distinct brain region-dependent transcriptional identities in health and disease [18,67,68]. For example, a specific disease-associated microglia subset localized around beta amyloid plaques has been described in Alzheimer's disease [69]. The existence of distinct subpopulations of microglia, recently described under acute inflammatory conditions [70], suggests that different pools of microglia readjust their phenotype in response to environmental stimuli. Supporting this concept, studies conducted in neuroinflammatory diseases, including multiple sclerosis, have revealed the intricate heterogeneity of the myeloid compartment of the central nervous system along disease progression [71].

Likewise, the heterogeneity of TAMs in GBM is also starting to emerge. For example, scRNA-seq analyses of GBM biopsies demonstrated that TAMs frequently co-express canonical pro-inflammatory (M1) and alternatively activated (M2) genes in individual cells [72] (Figure 1). Further, in low grade gliomas, a gene signature of blood monocyte-derived TAMs, but not that of resident microglial TAMs, correlated with poor survival [72]. Similar studies provided insights about the spatial localization of TAMs. Correlation studies from a panel of established macrophage- and microglia-specific marker genes [73] enabled identification of a macrophage core signature highly present within the tumour core, while cells from the periphery expressed an evident microglia signature [74]. Additionally, pro-inflammatory markers (e.g., *IL1α* and *IL1β*) were highly expressed at the tumour periphery, while a more anti-inflammatory phenotype (e.g., *IL1RN*) was observed in the tumour core (Figure 2). Lastly, subpopulations within the tumour core seemed to promote vascular permeability and endothelial growth via the expression of *VEGFα* and an extracellular matrix remodelling gene signature [74].

The cellular composition of IDH-mutant gliomas was also unveiled by scRNA-seq, suggesting that astrocytomas (IDH-A) and oligodendrogliomas (IDH-O) share common lineages of glial differentiation with distinct tumour microenvironment signatures [75]. Specifically, a higher fraction of undifferentiated and cycling tumour cells was associated with enriched microglia/macrophage signatures in IDH-A, which correlated with tumour grade, thus providing a molecular fingerprint of tumour progression [76]. The authors propose that the composition of the tumour microenvironment may be driven by genetic influences, such as TP53, which is mutated in IDH-A, but not IDH-O gliomas, and TP53 has been shown to influence several immune pathways, including NF-kB [77].

In IDH-wildtype gliomas, it has been very recently shown that TAMs acquire a disease-associated signature related to aging microglia programs, including downregulation of the microglia homeostatic genes and upregulation of inflammatory, metabolic and interferon-associated genes. Various TAM clusters, including subsets enriched for positive regulation of vasculature development or antigen processing via MHC class I, have been identified [78] (Figure 1). Taken together, TAMs heterogeneity in glioma is currently emerging and should be taken into account when designing therapeutic approaches based on specific GBM features.

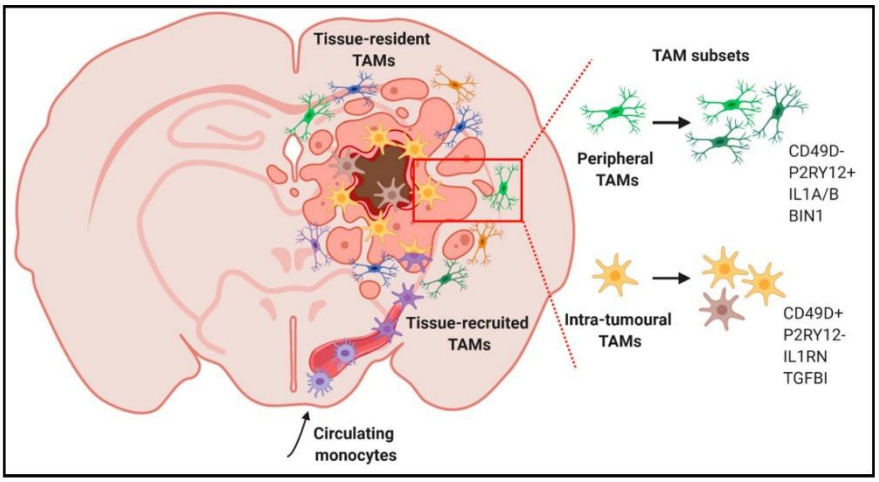

Figure 2. Discrimination of specific TAM subpopulations in GBM patients. TAMs present distinct features according to their ontogeny and spatial localization in specific tumour areas.

5. Conclusions and Perspectives

Microglia and macrophages in GBM are educated by the tumour and display unique molecular programs, which largely drive tumour-supportive phenotypes. However, the available subpopulations and functions of these cells along GBM development and progression are only partially understood. TAMs have been classified based on their activation state, their function and their morphology. With the advent of single cell analyses, it has become increasingly clear that the classification is complex and does not fully capture the heterogeneity of these cells in the context of GBM. Immunotherapeutic approaches in GBM will need to take into account the role of TAMs and their functional, spatial and temporal heterogeneity.

The local GBM microenvironment actively reprograms TAMs to establish new functional states with distinct gene expression profiles. If so, which TAM subsets arise during GBM development? Which subset of TAMs are more prone to be re-educated? Are their dynamic molecular states associated to TAM specific functions along GBM development and progression? Will their dissection help to improve TAM targeted therapies in combination with current treatment regimens? Taken together, it will be critical to address these questions to determine the most appropriate combinatorial approaches and to identify patient subgroups that may benefit most.

As perspectives, it will be fundamental to combine single-cell approaches, such as scRNA-seq and imaging mass cytometry, with functional screening of inferred cellular diversity, which will be critical to identify TAM subsets across GBM subtypes, landscapes and tumour stages, thus enabling targeting of putative pro-tumorigenic TAM subpopulations and/or to empower the anti-tumorigenic ones. Further, shedding light on the functional crosstalk between neoplastic cells and the tumour microenvironment at single-cell resolution will enable to dissect complex cell–cell interactions and how these may affect patient outcomes. Using a combination of scRNA-seq and flow cytometry in syngeneic mouse models of solid tumours allowed to profile potential cell-cell interactions between neoplastic and non-neoplastic cells [79]. Building precise cellular and molecular networks, which accurately reflect the complex and heterogeneous interactions between the tumour and immune elements, will open up avenues for novel combinatorial immunotherapies aiming at restoring an efficient immune response ultimately supporting the eradication of GBM.

Author Contributions: Manuscript design and writing, Y.P.-A. and A.M.; Picture conception and creation, Y.P.-A. and A.M.; Manuscript writing and editing, S.P.N.; Critical revision and approval of the final version of the manuscript, S.P.N. and A.M. All authors have read and agreed to the published version of the manuscript.

Funding: Y.P.-A. was supported by the CANBIO Program of the Luxembourg National Research Fund (PRIDE15/10675146/CANBIO) and by the Fondation du Pélican de Mie et Pierre Hippert-Faber (Fondation de Luxembourg). We acknowledge financial support by the Luxembourg Institute of Health and the Luxembourg Centre for Systems Biomedicine (MIGLISYS).

Conflicts of Interest: The authors declare no competing interests.

References

1. Goodenberger, M.L.; Jenkins, R.B. Genetics of adult glioma. *Cancer Genet.* **2012**, *205*, 613–621. [CrossRef]
2. Stupp, R.; Mason, W.P.; van den Bent, M.J.; Weller, M.; Fisher, B.; Taphoorn, M.J.; Belanger, K.; Brandes, A.A.; Marosi, C.; Bogdahn, U.; et al. Radiotherapy plus concomitant and adjuvant temozolomide for glioblastoma. *N. Engl. J. Med.* **2005**, *352*, 987–996. [CrossRef]
3. Quail, D.F.; Joyce, J.A. The Microenvironmental Landscape of Brain Tumors. *Cancer Cell* **2017**, *31*, 326–341. [CrossRef] [PubMed]
4. Glass, R.; Synowitz, M. CNS macrophages and peripheral myeloid cells in brain tumours. *Acta Neuropathol.* **2014**, *128*, 347–362. [CrossRef] [PubMed]
5. Lim, M.; Xia, Y.; Bettegowda, C.; Weller, M. Current state of immunotherapy for glioblastoma. *Nat. Rev. Clin. Oncol.* **2018**, *15*, 422–442. [CrossRef] [PubMed]
6. Thorsson, V.; Gibbs, D.L.; Brown, S.D.; Wolf, D.; Bortone, D.S.; Ou Yang, T.H.; Porta-Pardo, E.; Gao, G.F.; Plaisier, C.L.; Eddy, J.A.; et al. The Immune Landscape of Cancer. *Immunity* **2018**, *48*, 812–830.e14. [CrossRef] [PubMed]
7. Coniglio, S.J.; Eugenin, E.; Dobrenis, K.; Stanley, E.R.; West, B.L.; Symons, M.H.; Segall, J.E. Microglial stimulation of glioblastoma invasion involves epidermal growth factor receptor (EGFR) and colony stimulating factor 1 receptor (CSF-1R) signaling. *Mol. Med.* **2012**, *18*, 519–527. [CrossRef] [PubMed]
8. Patel, S.; Player, M.R. Colony-stimulating factor-1 receptor inhibitors for the treatment of cancer and inflammatory disease. *Curr. Top. Med. Chem.* **2009**, *9*, 599–610. [CrossRef] [PubMed]
9. Pyonteck, S.M.; Akkari, L.; Schuhmacher, A.J.; Bowman, R.L.; Sevenich, L.; Quail, D.F.; Olson, O.C.; Quick, M.L.; Huse, J.T.; Teijeiro, V.; et al. CSF-1R inhibition alters macrophage polarization and blocks glioma progression. *Nat. Med.* **2013**, *19*, 1264–1272. [CrossRef]
10. Quail, D.F.; Joyce, J.A. Molecular Pathways: Deciphering Mechanisms of Resistance to Macrophage-Targeted Therapies. *Clin. Cancer Res.* **2017**, *23*, 876–884. [CrossRef]
11. Mills, C.D.; Kincaid, K.; Alt, J.M.; Heilman, M.J.; Hill, A.M. Pillars Article: M-1/M-2 Macrophages and the Th1/Th2 Paradigm. *J. Immunol.* **2017**, *164*, 6166–6173; Erratum in **2017**, *199*, 2194–2201. [CrossRef] [PubMed]
12. Michelucci, A.; Heurtaux, T.; Grandbarbe, L.; Morga, E.; Heuschling, P. Characterization of the microglial phenotype under specific pro-inflammatory and anti-inflammatory conditions: Effects of oligomeric and fibrillar amyloid-beta. *J. Neuroimmunol.* **2009**, *210*, 3–12. [CrossRef]
13. Mantovani, A.; Sozzani, S.; Locati, M.; Allavena, P.; Sica, A. Macrophage polarization: Tumor-associated macrophages as a paradigm for polarized M2 mononuclear phagocytes. *Trends Immunol.* **2002**, *23*, 549–555. [CrossRef]
14. Roesch, S.; Rapp, C.; Dettling, S.; Herold-Mende, C. When Immune Cells Turn Bad-Tumor-Associated Microglia/Macrophages in Glioma. *Int. J. Mol. Sci.* **2018**, *19*, 436. [CrossRef]
15. Mantovani, A.; Marchesi, F.; Malesci, A.; Laghi, L.; Allavena, P. Tumour-associated macrophages as treatment targets in oncology. *Nat. Rev. Clin. Oncol.* **2017**, *14*, 399–416. [CrossRef] [PubMed]
16. Szulzewsky, F.; Pelz, A.; Feng, X.; Synowitz, M.; Markovic, D.; Langmann, T.; Holtman, I.R.; Wang, X.; Eggen, B.J.; Boddeke, H.W.; et al. Glioma-associated microglia/macrophages display an expression profile different from M1 and M2 polarization and highly express Gpnmb and Spp1. *PLoS ONE* **2015**, *10*, e0116644. [CrossRef] [PubMed]
17. Gabrusiewicz, K.; Rodriguez, B.; Wei, J.; Hashimoto, Y.; Healy, L.M.; Maiti, S.N.; Thomas, G.; Zhou, S.; Wang, Q.; Elakkad, A.; et al. Glioblastoma-infiltrated innate immune cells resemble M0 macrophage phenotype. *JCI Insight* **2016**, *1*, e85841. [CrossRef]

18. Goldmann, T.; Wieghofer, P.; Jordao, M.J.; Prutek, F.; Hagemeyer, N.; Frenzel, K.; Amann, L.; Staszewski, O.; Kierdorf, K.; Krueger, M.; et al. Origin, fate and dynamics of macrophages at central nervous system interfaces. *Nat. Immunol.* **2016**, *17*, 797–805. [CrossRef]
19. Ginhoux, F.; Greter, M.; Leboeuf, M.; Nandi, S.; See, P.; Gokhan, S.; Mehler, M.F.; Conway, S.J.; Ng, L.G.; Stanley, E.R.; et al. Fate mapping analysis reveals that adult microglia derive from primitive macrophages. *Science* **2010**, *330*, 841–845. [CrossRef]
20. Colonna, M.; Butovsky, O. Microglia Function in the Central Nervous System During Health and Neurodegeneration. *Annu. Rev. Immunol.* **2017**, *35*, 441–468. [CrossRef]
21. Salter, M.W.; Stevens, B. Microglia emerge as central players in brain disease. *Nat. Med.* **2017**, *23*, 1018–1027. [CrossRef] [PubMed]
22. Crotti, A.; Ransohoff, R.M. Microglial Physiology and Pathophysiology: Insights from Genome-wide Transcriptional Profiling. *Immunity* **2016**, *44*, 505–515. [CrossRef] [PubMed]
23. Sousa, C.; Biber, K.; Michelucci, A. Cellular and Molecular Characterization of Microglia: A Unique Immune Cell Population. *Front. Immunol.* **2017**, *8*, 198. [CrossRef] [PubMed]
24. Hambardzumyan, D.; Gutmann, D.H.; Kettenmann, H. The role of microglia and macrophages in glioma maintenance and progression. *Nat. Neurosci.* **2016**, *19*, 20–27. [CrossRef]
25. Ricard, C.; Tchoghandjian, A.; Luche, H.; Grenot, P.; Figarella-Branger, D.; Rougon, G.; Malissen, M.; Debarbieux, F. Phenotypic dynamics of microglial and monocyte-derived cells in glioblastoma-bearing mice. *Sci. Rep.* **2016**, *6*, 26381. [CrossRef]
26. Cassetta, L.; Pollard, J.W. Targeting macrophages: Therapeutic approaches in cancer. *Nat. Rev. Drug Discov.* **2018**, *17*, 887–904. [CrossRef]
27. Li, W.; Graeber, M.B. The molecular profile of microglia under the influence of glioma. *Neuro-Oncol.* **2012**, *14*, 958–978. [CrossRef]
28. Wei, J.; Marisetty, A.; Schrand, B.; Gabrusiewicz, K.; Hashimoto, Y.; Ott, M.; Grami, Z.; Kong, L.Y.; Ling, X.; Caruso, H.; et al. Osteopontin mediates glioblastoma-associated macrophage infiltration and is a potential therapeutic target. *J. Clin. Investig.* **2019**, *129*, 137–149. [CrossRef]
29. Zhang, J.; Sarkar, S.; Cua, R.; Zhou, Y.; Hader, W.; Yong, V.W. A dialog between glioma and microglia that promotes tumor invasiveness through the CCL2/CCR2/interleukin-6 axis. *Carcinogenesis* **2012**, *33*, 312–319. [CrossRef]
30. Graeber, M.B.; Scheithauer, B.W.; Kreutzberg, G.W. Microglia in brain tumors. *Glia* **2002**, *40*, 252–259. [CrossRef]
31. London, A.; Cohen, M.; Schwartz, M. Microglia and monocyte-derived macrophages: Functionally distinct populations that act in concert in CNS plasticity and repair. *Front. Cell. Neurosci.* **2013**, *7*, 34. [CrossRef]
32. Pinton, L.; Masetto, E.; Vettore, M.; Solito, S.; Magri, S.; D'Andolfi, M.; Del Bianco, P.; Lollo, G.; Benoit, J.P.; Okada, H.; et al. The immune suppressive microenvironment of human gliomas depends on the accumulation of bone marrow-derived macrophages in the center of the lesion. *J. Immunother. Cancer* **2019**, *7*, 58. [CrossRef] [PubMed]
33. Sedgwick, J.D.; Schwender, S.; Imrich, H.; Dorries, R.; Butcher, G.W.; ter Meulen, V. Isolation and direct characterization of resident microglial cells from the normal and inflamed central nervous system. *Proc. Natl. Acad. Sci. USA* **1991**, *88*, 7438–7442. [CrossRef] [PubMed]
34. Muller, A.; Brandenburg, S.; Turkowski, K.; Muller, S.; Vajkoczy, P. Resident microglia, and not peripheral macrophages, are the main source of brain tumor mononuclear cells. *Int. J. Cancer* **2015**, *137*, 278–288. [CrossRef]
35. Bowman, R.L.; Klemm, F.; Akkari, L.; Pyonteck, S.M.; Sevenich, L.; Quail, D.F.; Dhara, S.; Simpson, K.; Gardner, E.E.; Iacobuzio-Donahue, C.A.; et al. Macrophage Ontogeny Underlies Differences in Tumor-Specific Education in Brain Malignancies. *Cell Rep.* **2016**, *17*, 2445–2459. [CrossRef] [PubMed]
36. Haage, V.; Semtner, M.; Vidal, R.O.; Hernandez, D.P.; Pong, W.W.; Chen, Z.; Hambardzumyan, D.; Magrini, V.; Ly, A.; Walker, J.; et al. Comprehensive gene expression meta-analysis identifies signature genes that distinguish microglia from peripheral monocytes/macrophages in health and glioma. *Acta Neuropathol. Commun.* **2019**, *7*, 20. [CrossRef]
37. Greenhalgh, A.D.; Zarruk, J.G.; Healy, L.M.; Baskar Jesudasan, S.J.; Jhelum, P.; Salmon, C.K.; Formanek, A.; Russo, M.V.; Antel, J.P.; McGavern, D.B.; et al. Peripherally derived macrophages modulate microglial function to reduce inflammation after CNS injury. *PLoS Biol.* **2018**, *16*, e2005264. [CrossRef]

38. Hagemann, T.; Lawrence, T.; McNeish, I.; Charles, K.A.; Kulbe, H.; Thompson, R.G.; Robinson, S.C.; Balkwill, F.R. "Re-educating" tumor-associated macrophages by targeting NF-kappaB. *J. Exp. Med.* **2008**, *205*, 1261–1268. [CrossRef]
39. Nesseler, J.P.; Schaue, D.; McBride, W.H.; Lee, M.H.; Kaprealian, T.; Niclou, S.P.; Nickers, P. Irradiation to Improve the Response to Immunotherapeutic Agents in Glioblastomas. *Adv. Radiat. Oncol.* **2019**, *4*, 268–282. [CrossRef]
40. Brown, N.F.; Carter, T.J.; Ottaviani, D.; Mulholland, P. Harnessing the immune system in glioblastoma. *Br. J. Cancer* **2018**, *119*, 1171–1181. [CrossRef]
41. Olnes, M.J.; Kotliarov, Y.; Biancotto, A.; Cheung, F.; Chen, J.; Shi, R.; Zhou, H.; Wang, E.; Tsang, J.S.; Nussenblatt, R.; et al. Effects of Systemically Administered Hydrocortisone on the Human Immunome. *Sci. Rep.* **2016**, *6*, 23002. [CrossRef]
42. Kalbasi, A.; June, C.H.; Haas, N.; Vapiwala, N. Radiation and immunotherapy: A synergistic combination. *J. Clin. Investig.* **2013**, *123*, 2756–2763. [CrossRef]
43. Deng, L.; Liang, H.; Xu, M.; Yang, X.; Burnette, B.; Arina, A.; Li, X.D.; Mauceri, H.; Beckett, M.; Darga, T.; et al. STING-Dependent Cytosolic DNA Sensing Promotes Radiation-Induced Type I Interferon-Dependent Antitumor Immunity in Immunogenic Tumors. *Immunity* **2014**, *41*, 843–852. [CrossRef]
44. Markovic, D.S.; Glass, R.; Synowitz, M.; Rooijen, N.; Kettenmann, H. Microglia stimulate the invasiveness of glioma cells by increasing the activity of metalloprotease-2. *J. Neuropathol. Exp. Neurol.* **2005**, *64*, 754–762. [CrossRef]
45. Han, X.; Li, Q.; Lan, X.; El-Mufti, L.; Ren, H.; Wang, J. Microglial Depletion with Clodronate Liposomes Increases Proinflammatory Cytokine Levels, Induces Astrocyte Activation, and Damages Blood Vessel Integrity. *Mol. Neurobiol.* **2019**, *56*, 6184–6196. [CrossRef]
46. Chen, Z.; Feng, X.; Herting, C.J.; Garcia, V.A.; Nie, K.; Pong, W.W.; Rasmussen, R.; Dwivedi, B.; Seby, S.; Wolf, S.A.; et al. Cellular and Molecular Identity of Tumor-Associated Macrophages in Glioblastoma. *Cancer Res.* **2017**, *77*, 2266–2278. [CrossRef]
47. Galarneau, H.; Villeneuve, J.; Gowing, G.; Julien, J.P.; Vallieres, L. Increased glioma growth in mice depleted of macrophages. *Cancer Res.* **2007**, *67*, 8874–8881. [CrossRef]
48. Alban, T.J.; Alvarado, A.G.; Sorensen, M.D.; Bayik, D.; Volovetz, J.; Serbinowski, E.; Mulkearns-Hubert, E.E.; Sinyuk, M.; Hale, J.S.; Onzi, G.R.; et al. Global immune fingerprinting in glioblastoma patient peripheral blood reveals immune-suppression signatures associated with prognosis. *JCI Insight* **2018**, *3*, e122264. [CrossRef] [PubMed]
49. Wu, Y.; Lu, Y.; Chen, W.; Fu, J.; Fan, R. In silico experimentation of glioma microenvironment development and anti-tumor therapy. *PLoS Comput. Biol.* **2012**, *8*, e1002355. [CrossRef] [PubMed]
50. Boussiotis, V.A.; Charest, A. Immunotherapies for malignant glioma. *Oncogene* **2018**, *37*, 1121–1141. [CrossRef] [PubMed]
51. Tomaszewski, W.; Sanchez-Perez, L.; Gajewski, T.F.; Sampson, J.H. Brain Tumor Microenvironment and Host State: Implications for Immunotherapy. *Clin. Cancer Res.* **2019**, *25*, 4202–4210. [CrossRef] [PubMed]
52. Reardon, D.A.; Gokhale, P.C.; Klein, S.R.; Ligon, K.L.; Rodig, S.J.; Ramkissoon, S.H.; Jones, K.L.; Conway, A.S.; Liao, X.; Zhou, J.; et al. Glioblastoma Eradication Following Immune Checkpoint Blockade in an Orthotopic, Immunocompetent Model. *Cancer Immunol. Res.* **2016**, *4*, 124–135. [CrossRef] [PubMed]
53. Yarchoan, M.; Hopkins, A.; Jaffee, E.M. Tumor Mutational Burden and Response Rate to PD-1 Inhibition. *N. Engl. J. Med.* **2017**, *377*, 2500–2501. [CrossRef] [PubMed]
54. Gholamin, S.; Mitra, S.S.; Feroze, A.H.; Liu, J.; Kahn, S.A.; Zhang, M.; Esparza, R.; Richard, C.; Ramaswamy, V.; Remke, M.; et al. Disrupting the CD47-SIRPalpha anti-phagocytic axis by a humanized anti-CD47 antibody is an efficacious treatment for malignant pediatric brain tumors. *Sci. Transl. Med.* **2017**, *9*, eaaf2968. [CrossRef]
55. Hutter, G.; Theruvath, J.; Graef, C.M.; Zhang, M.; Schoen, M.K.; Manz, E.M.; Bennett, M.L.; Olson, A.; Azad, T.D.; Sinha, R.; et al. Microglia are effector cells of CD47-SIRPalpha antiphagocytic axis disruption against glioblastoma. *Proc. Natl. Acad. Sci. USA* **2019**, *116*, 997–1006. [CrossRef]
56. Castro, B.A.; Flanigan, P.; Jahangiri, A.; Hoffman, D.; Chen, W.; Kuang, R.; De Lay, M.; Yagnik, G.; Wagner, J.R.; Mascharak, S.; et al. Macrophage migration inhibitory factor downregulation: A novel mechanism of resistance to anti-angiogenic therapy. *Oncogene* **2017**, *36*, 3749–3759. [CrossRef]

57. Wiehagen, K.R.; Girgis, N.M.; Yamada, D.H.; Smith, A.A.; Chan, S.R.; Grewal, I.S.; Quigley, M.; Verona, R.I. Combination of CD40 Agonism and CSF-1R Blockade Reconditions Tumor-Associated Macrophages and Drives Potent Antitumor Immunity. *Cancer Immunol. Res.* **2017**, *5*, 1109–1121. [CrossRef]
58. Saha, D.; Martuza, R.L.; Rabkin, S.D. Macrophage Polarization Contributes to Glioblastoma Eradication by Combination Immunovirotherapy and Immune Checkpoint Blockade. *Cancer Cell* **2017**, *32*, 253–267.e5. [CrossRef]
59. Phillips, H.S.; Kharbanda, S.; Chen, R.; Forrest, W.F.; Soriano, R.H.; Wu, T.D.; Misra, A.; Nigro, J.M.; Colman, H.; Soroceanu, L.; et al. Molecular subclasses of high-grade glioma predict prognosis, delineate a pattern of disease progression, and resemble stages in neurogenesis. *Cancer Cell* **2006**, *9*, 157–173. [CrossRef]
60. Verhaak, R.G.; Hoadley, K.A.; Purdom, E.; Wang, V.; Qi, Y.; Wilkerson, M.D.; Miller, C.R.; Ding, L.; Golub, T.; Mesirov, J.P.; et al. Integrated genomic analysis identifies clinically relevant subtypes of glioblastoma characterized by abnormalities in PDGFRA, IDH1, EGFR, and NF1. *Cancer Cell* **2010**, *17*, 98–110. [CrossRef]
61. Ceccarelli, M.; Barthel, F.P.; Malta, T.M.; Sabedot, T.S.; Salama, S.R.; Murray, B.A.; Morozova, O.; Newton, Y.; Radenbaugh, A.; Pagnotta, S.M.; et al. Molecular Profiling Reveals Biologically Discrete Subsets and Pathways of Progression in Diffuse Glioma. *Cell* **2016**, *164*, 550–563. [CrossRef] [PubMed]
62. Wang, Q.; Hu, B.; Hu, X.; Kim, H.; Squatrito, M.; Scarpace, L.; de Carvalho, A.C.; Lyu, S.; Li, P.; Li, Y.; et al. Tumor Evolution of Glioma-Intrinsic Gene Expression Subtypes Associates with Immunological Changes in the Microenvironment. *Cancer Cell* **2017**, *32*, 42–56.e6. [CrossRef] [PubMed]
63. Sottoriva, A.; Spiteri, I.; Piccirillo, S.G.; Touloumis, A.; Collins, V.P.; Marioni, J.C.; Curtis, C.; Watts, C.; Tavare, S. Intratumor heterogeneity in human glioblastoma reflects cancer evolutionary dynamics. *Proc. Natl. Acad. Sci. USA* **2013**, *110*, 4009–4014. [CrossRef] [PubMed]
64. Neftel, C.; Laffy, J.; Filbin, M.G.; Hara, T.; Shore, M.E.; Rahme, G.J.; Richman, A.R.; Silverbush, D.; Shaw, M.L.; Hebert, C.M.; et al. An Integrative Model of Cellular States, Plasticity, and Genetics for Glioblastoma. *Cell* **2019**, *178*, 835–849.e21. [CrossRef] [PubMed]
65. Patel, A.P.; Tirosh, I.; Trombetta, J.J.; Shalek, A.K.; Gillespie, S.M.; Wakimoto, H.; Cahill, D.P.; Nahed, B.V.; Curry, W.T.; Martuza, R.L.; et al. Single-cell RNA-seq highlights intratumoral heterogeneity in primary glioblastoma. *Science* **2014**, *344*, 1396–1401. [CrossRef] [PubMed]
66. Capper, D.; Jones, D.T.W.; Sill, M.; Hovestadt, V.; Schrimpf, D.; Sturm, D.; Koelsche, C.; Sahm, F.; Chavez, L.; Reuss, D.E.; et al. DNA methylation-based classification of central nervous system tumours. *Nature* **2018**, *555*, 469–474. [CrossRef]
67. Van Hove, H.; Martens, L.; Scheyltjens, I.; De Vlaminck, K.; Pombo Antunes, A.R.; De Prijck, S.; Vandamme, N.; De Schepper, S.; Van Isterdael, G.; Scott, C.L.; et al. A single-cell atlas of mouse brain macrophages reveals unique transcriptional identities shaped by ontogeny and tissue environment. *Nat. Neurosci.* **2019**, *22*, 1021–1035. [CrossRef]
68. Mrdjen, D.; Pavlovic, A.; Hartmann, F.J.; Schreiner, B.; Utz, S.G.; Leung, B.P.; Lelios, I.; Heppner, F.L.; Kipnis, J.; Merkler, D.; et al. High-Dimensional Single-Cell Mapping of Central Nervous System Immune Cells Reveals Distinct Myeloid Subsets in Health, Aging, and Disease. *Immunity* **2018**, *48*, 380–395.e6. [CrossRef]
69. Keren-Shaul, H.; Spinrad, A.; Weiner, A.; Matcovitch-Natan, O.; Dvir-Szternfeld, R.; Ulland, T.K.; David, E.; Baruch, K.; Lara-Astaiso, D.; Toth, B.; et al. A Unique Microglia Type Associated with Restricting Development of Alzheimer's Disease. *Cell* **2017**, *169*, 1276–1290.e17. [CrossRef]
70. Sousa, C.; Golebiewska, A.; Poovathingal, S.K.; Kaoma, T.; Pires-Afonso, Y.; Martina, S.; Coowar, D.; Azuaje, F.; Skupin, A.; Balling, R.; et al. Single-cell transcriptomics reveals distinct inflammation-induced microglia signatures. *EMBO Rep.* **2018**, *19*, e46171. [CrossRef]
71. Jordao, M.J.C.; Sankowski, R.; Brendecke, S.M.; Locatelli, G.; Tai, Y.H.; Tay, T.L.; Schramm, E.; Armbruster, S.; Hagemeyer, N.; Gross, O.; et al. Single-cell profiling identifies myeloid cell subsets with distinct fates during neuroinflammation. *Science* **2019**, *363*, eaat7554. [CrossRef] [PubMed]
72. Muller, S.; Kohanbash, G.; Liu, S.J.; Alvarado, B.; Carrera, D.; Bhaduri, A.; Watchmaker, P.B.; Yagnik, G.; Di Lullo, E.; Malatesta, M.; et al. Single-cell profiling of human gliomas reveals macrophage ontogeny as a basis for regional differences in macrophage activation in the tumor microenvironment. *Genome Biol.* **2017**, *18*, 234. [CrossRef] [PubMed]
73. Bennett, M.L.; Bennett, F.C.; Liddelow, S.A.; Ajami, B.; Zamanian, J.L.; Fernhoff, N.B.; Mulinyawe, S.B.; Bohlen, C.J.; Adil, A.; Tucker, A.; et al. New tools for studying microglia in the mouse and human CNS. *Proc. Natl. Acad. Sci. USA* **2016**, *113*, E1738–E1746. [CrossRef] [PubMed]

74. Darmanis, S.; Sloan, S.A.; Croote, D.; Mignardi, M.; Chernikova, S.; Samghababi, P.; Zhang, Y.; Neff, N.; Kowarsky, M.; Caneda, C.; et al. Single-Cell RNA-Seq Analysis of Infiltrating Neoplastic Cells at the Migrating Front of Human Glioblastoma. *Cell Rep.* **2017**, *21*, 1399–1410. [CrossRef] [PubMed]
75. Lucas, C.G.; Solomon, D.A.; Perry, A. A review of recently described genetic alterations in central nervous system tumors. *Hum. Pathol.* **2019**. [CrossRef]
76. Venteicher, A.S.; Tirosh, I.; Hebert, C.; Yizhak, K.; Neftel, C.; Filbin, M.G.; Hovestadt, V.; Escalante, L.E.; Shaw, M.L.; Rodman, C.; et al. Decoupling genetics, lineages, and microenvironment in IDH-mutant gliomas by single-cell RNA-seq. *Science* **2017**, *355*, eaai8478. [CrossRef]
77. Munoz-Fontela, C.; Mandinova, A.; Aaronson, S.A.; Lee, S.W. Emerging roles of p53 and other tumour-suppressor genes in immune regulation. *Nat. Rev. Immunol.* **2016**, *16*, 741–750. [CrossRef]
78. Sankowski, R.; Bottcher, C.; Masuda, T.; Geirsdottir, L.; Sagar; Sindram, E.; Seredenina, T.; Muhs, A.; Scheiwe, C.; Shah, M.J.; et al. Mapping microglia states in the human brain through the integration of high-dimensional techniques. *Nat. Neurosci.* **2019**, *22*, 2098–2110. [CrossRef]
79. Kumar, M.P.; Du, J.; Lagoudas, G.; Jiao, Y.; Sawyer, A.; Drummond, D.C.; Lauffenburger, D.A.; Raue, A. Analysis of Single-Cell RNA-Seq Identifies Cell-Cell Communication Associated with Tumor Characteristics. *Cell Rep.* **2018**, *25*, 1458–1468.e4. [CrossRef]

PAPER 2: Research article

Elucidating tumour-associated microglia/macrophage diversity along Glioblastoma progression and under ACOD1 deficiency

Yolanda Pires-Afonso[1,2], Arnaud Muller[3], Kamil Grzyb[4], Anaïs Oudin[5], Carole Sousa[1,5,6], Antonio Cosma[4], Rashi Halder[7], Yahaya A Yabo[2,5], Djalil Coowar[7], Anna Golebiewska[5], Alexander Skupin[7,8], Simone P Niclou[5,9], Alessandro Michelucci[1*]

[1]Neuro-Immunology Group, Department of Oncology, Luxembourg Institute of Health, Luxembourg, Luxembourg

[2]Doctoral School of Science and Technology, University of Luxembourg, Esch-sur-Alzette, Luxembourg

[3]Quantitative Biology Unit, Bioinformatics Platform, Luxembourg Institute of Health, Luxembourg, Luxembourg

[4]Quantitative Biology Unit, National Cytometry Platform, Luxembourg Institute of Health, Luxembourg, Luxembourg

[5]NORLUX Neuro-Oncology Laboratory, Department of Oncology, Luxembourg Institute of Health, Luxembourg, Luxembourg

[6]Department of Neurology and Neurophysiology, University Medical Center Freiburg, Freiburg, Germany (current address)

[7]Luxembourg Centre for Systems Biomedicine, University of Luxembourg, Esch-Belval, Luxembourg

[8]National Centre for Microscopy and Imaging Research, University of California San Diego, La Jolla, USA

[9]KG Jebsen Brain Tumour Research Center, Department of Biomedicine, University of Bergen, Bergen, Norway

29 * Corresponding author
30 Alessandro Michelucci, PhD
31 Luxembourg Institute of Health
32 Department of Oncology
33 Neuro-Immunology Group
34 84, rue Val Fleuri, L-1526 Luxembourg
35 Tel. + 352-26970-263
36 alessandro.michelucci@lih.lu

37

38 **RUNNING TITLE**

39

40 **TAM diversity in GBM**

ABSTRACT

In Glioblastoma (GBM), tumour-associated microglia/macrophages (TAMs) represent the major cell type of the stromal compartment and contribute to tumour immune escape mechanisms. Thus, targeting TAMs is emerging as a promising strategy for immunotherapy. However, TAM heterogeneity and metabolic adaptation along GBM progression represent critical features for the design of effective TAM-targeted therapies. Here, we comprehensively study the cellular and molecular changes of TAMs in the GL261 GBM mouse model combining single-cell RNA-sequencing with flow cytometry and immunohistological analyses along GBM progression and in the absence of *Acod1/Irg1*, a key gene involved in the metabolic reprogramming of macrophages towards an anti-inflammatory phenotype. We identify distinct TAM profiles, mainly based on their ontogeny and recapitulated in patients, which reiterate microglia- versus macrophage-like features showing key transcriptional differences and dynamically adapting along GBM stages. Notably, we uncover a decreased antigen-presenting cell signature in TAMs along tumour progression that is instead maintained in *Acod1/Irg1*-deficient mice. Overall, our results provide insight into TAM heterogeneity and highlight a novel role for *Acod1/Irg1* in TAM adaptation during GBM progression.

KEYWORDS

Tumour-associated microglia/macrophages, Glioblastoma, Heterogeneity, ACOD1/IRG1, Metabolic reprogramming, Single-cell RNA-sequencing

62 **1. INTRODUCTION**

63

64 Complex interactions between neoplastic cells and their microenvironment sustain cancer heterogeneity
65 and evolution [1, 2]. In the brain, tumours develop within a network of resident central nervous system
66 (CNS) cells, including neurons, astrocytes, oligodendrocytes, endothelial cells and microglia, together
67 with peripheral infiltrating immune components. These cells, together with the extracellular matrix,
68 constitute the tumour microenvironment (TME), which drives disease progression by affecting tumour
69 growth, patient survival and response to therapy. In Glioblastoma (GBM), the most aggressive brain
70 tumour in adults, the TME is mainly composed of tumour-associated microglia/macrophages (TAMs),
71 which can represent up to 40% of the tumour mass, creating a supportive milieu that facilitates tumour
72 proliferation, survival and migration [3]. TAMs are either resident parenchymal microglia, whose
73 progenitors migrated to the CNS during early development [4, 5] or peripheral monocyte-derived cells
74 that have crossed the blood-brain barrier [6]. Once in the CNS, the latter differentiate into tumour-
75 associated macrophages becoming nearly indistinguishable from activated resident microglia [7]. Thus,
76 how ontogeny contributes to TAM education has only been started to be described in GBM transgenic
77 mouse models [8] or in patients [9, 10] as a result of recently discovered specific markers.
78 GBM recruits TAMs, which in turn release growth factors and cytokines that affect the tumour. TAMs
79 display specific immune properties that are different from classical pro-inflammatory activated
80 (immune-permissive) M1 or alternatively activated (immune-suppressive) M2 reactive profiles [11, 12]
81 or even exhibit non-polarized M0 features [13]. The complex interplay between pro- and anti-tumour
82 processes depending on the molecular signals within the TME, both within and across cell types,
83 contributes to the difficulty in interpreting tissue-resolution bulk signatures of GBM. In this context,
84 single-cell RNA-sequencing (scRNA-seq) provides a remarkable method to depict heterogeneous cell
85 populations and measure cell-to-cell expression variability of thousands of genes [14-17]. Specifically,
86 in GBM patients scRNA-seq has emerged as a critical tool to discriminate TAM heterogeneity and their
87 contribution to distinct glioma subtypes [10, 18]. Notably, scRNA-seq analyses enabled to discover that
88 TAMs frequently co-express canonical M1 and M2 genes in individual cells [9].

89 Here, we combine scRNA-seq analyses with flow cytometry and immunofluorescence studies to
90 elucidate the cellular and molecular properties of the TME, with a specific focus on TAMs. Following
91 the discrimination of microglia from monocyte-derived macrophages and the characterization of their
92 transcriptional programmes along tumour progression, we assess the role of aconitate decarboxylase
93 1/immunoresponsive gene 1 (*Acod1/Irg1*) in TAM polarization. The ACOD1/IRG1 enzyme catalyses
94 the production of the anti-microbial immunometabolite itaconate from *cis*-aconitate in the tricarboxylic
95 acid (TCA) cycle [19]. In macrophages, the induction of itaconate under inflammatory conditions
96 reprograms them into a more pronounced anti-inflammatory phenotype, participating to the resolution
97 of inflammation [20, 21]. Notably, the induction of the ACOD1/IRG1-itaconate axis in monocytes
98 contributes to the immune paralysis in sepsis [22], while its inhibition in macrophages reduces the
99 tumour burden in peritoneal tumours [23]. Here, we identify discrete TAM profiles, which reiterate
100 microglia- versus macrophage-like features showing key transcriptional differences and dynamically
101 adapting along GBM stages. Notably, we demonstrate that TAMs display a decreased antigen-
102 presenting cell signature along tumour progression, which is instead maintained in *Acod1/Irg1*-deficient
103 mice.
104 The understanding of TAM diversity, and more systematically of TME heterogeneity, which
105 significantly contributes to GBM growth, is of utmost relevance for the discovery of novel
106 immunotherapeutic opportunities [24]. Hence, our results point to important aspects to take into
107 consideration when targeting TAMs and highlight a novel role for *Acod1/Irg1* in TAM adaptation
108 during GBM progression.

109 **2. Materials and Methods**

110 **2.1. Animals**

111

112 *Acod1 KO* mice were generated by Dr. Haruhiko Koseki at the RIKEN Institute using embryonic stem
113 cells purchased from the Knockout Mouse Project Repository (KOMP, University of California,
114 DAVIS) under strain ID $Irg1^{tm1a(KOMP)Wtsi}$ containing an insertion cassette between exons 3 and 5.
115 Briefly, *Acod1 KO* C57BL/6N ESCs were injected into recipient female C57BL/6N mouse blastocysts
116 and selected females were subsequently bred with wild-type C57BL/6N mice. For the experiments,
117 heterozygotes animals were crossed to generate homozygote *Acod1 KO* mice and *WT* littermate
118 controls. We confirmed their genotype by PCR and we used a mix of male and female littermates for
119 the experiments. Mice were housed in 12 h light/dark cycle and had free access to sterile food and water.
120 All animal procedures were approved by the national authorities and the animal welfare structure of
121 LIH under the reference LUPA 2017/20. The animal work of the present study has been conducted and
122 reported in accordance to the ARRIVE (Animal Research: Reporting of In Vivo Experiments)
123 guidelines to improve the design, analysis and reporting of research using animals, maximizing
124 information published and minimizing unnecessary studies.

125

126 **2.2. Glioma cell line**

127

128 Mouse glioma 261 (GL261) cells were kindly provided by Dr. Poli and were maintained at 37ºC with
129 5% CO_2 in culture medium (Dulbecco's Modified Eagle's Medium (DMEM (Gibco/Life Technologies))
130 supplemented with 10% Fetal Bovine Serum (FBS; Gibco/Life Technologies) and pen-strep (100 U/ml/;
131 Gibco/Life Technologies). Cells at 80% confluence were dissociated with 0.05% Trypsin-EDTA
132 (Gibco/Life Technologies) and tested for mycoplasma (MycoAlert PLUS Mycoplasma Detection Kit,
133 Westburg, The Netherlands) before mice implantation. For mice orthotopic implantation, GL261 cells
134 were re-suspended in serum-free medium.

135 **2.3. Differentiation of murine bone marrow-derived macrophages and co-culture**
136 **experiments with GL261 cells**
137
138 Bone-marrow cells were obtained by flushing the tibia and femurs of WT and *Acod1* KO adult mice.
139 Briefly, mice were euthanized and their legs were removed. Bone marrow precursors were flushed out
140 and cell suspension was further incubated with red blood cells hypotonic lysis buffer. After washing,
141 cells were plated in DMEM media containing 10% FBS supplemented with 20% of L929 supernatant
142 for seven days for full differentiation of bone marrow-derived macrophages (BMDMs).
143 GL261 and BMDMs were co-cultured in 1:1 mix in DMEM medium containing 10% FBS. GL261 cells
144 were plated on top of 1 µm pore size Boyden chambers (Thincert, Greiner), whereas BMDMs were
145 plated on the bottom of the 6-well plates. The mRNA was isolated from BMDMs at 0, 24 and 48 hours
146 using the RNeasy mini kit according to the manufacturer' instructions (QIAGEN, Germantown, USA).
147
148 **2.4. GL261 orthotopic implantation and tumour volume measurement**
149
150 Before the implantation, mice were intraperitoneally anesthetized with a mixture of ketamine (100
151 mg/kg) and xylazine (10 mg/kg) and placed in a stereotactic frame. A local anaesthetic was administered
152 subcutaneously (Marcain 0.25% with Adrenalin) and 1 µl containing 500 GL261 cells were implanted
153 into the frontal cortex of the brain using a Hamilton syringe (Hamilton, Reno, NV, USA). Mice were
154 monitored weekly for the first 2 weeks and daily from day 15 post-implantation. Magnetic resonance
155 imaging (MRI) was performed weekly upon 15 post-implantation to assess tumour volume, using a 3T
156 preclinical horizontal bore scanner (MR Solutions, Guilford, UK), equipped with a quadrature volume
157 coil designed for mouse head imaging. Animals were placed prone in the cradle and maintained asleep
158 during the duration of the scans, using 2-3% isoflurane mixed with oxygen. The body temperature was
159 kept constant at 37°C and breathing was monitored throughout the scan sessions. Anatomical series
160 were used to screen the animals and calculate tumour volumes. The Fast Spin Echo T2-weighted MRI
161 sequence was acquired, with the following acquisition parameters: TE: 68 ms, TR: 3000 ms, echo train:
162 8, averages: 4, plane resolution: 256 µm, slice thickness: 1 mm, slices: 15, orientation: coronal. Tumour

163 volume was measured on ImageJ software (NIH, Bethesda, MD, USA) as the sum of area obtained by
164 delineating the tumour in each slice and multiplying by slice thickness. Tumour volume quantification
165 was normalized to the initial tumour take.
166
167 **2.5. Survival analysis**
168
169 Mice survival analyses were performed according to humane endpoints guidelines, including loss of
170 locomotor activity, weight loss (up to 20%) and central nervous system symptoms. The survival time
171 was measured from the day of tumour cell implantation to the day of euthanasia and median mouse
172 survival time was calculated for each group (WT and *Acod1* KO mice).
173
174 **2.6. Brain tissue processing and dissociation**
175
176 Animals were intraperitoneally anesthetized with a mixture of ketamine (100 mg/kg) with
177 medetomidine (0.5 mg/Kg) and buprenorphine (0.05 mg/kg) before intracardiac perfusion with ice-cold
178 phosphate-buffered saline (PBS). Brain samples were isolated and processed according to the different
179 applications. For immunofluorescence staining, brains were fixed in 4% PFA for 48 h at room
180 temperature, immersed in 30% sucrose (dissolved in PBS) for 48 h at 4ºC, embedded in optimal cutting
181 temperature (OCT, Tissue-Tek) solution, sectioned (12 µm), slide mounted and stored at -20C. For *ex*
182 *vivo* studies, naïve brains and tumour-bearing brains (demarcated taking the tumour core region based
183 on MRI scan) were dissociated using the Neural Dissociation Kit P (MACS Miltenyi Biotec)
184 accordingly to the manufacturer's instruction. The tissue was gently digested in order to yield a single-
185 cell suspension. All processing was performed at 4ºC, except for enzymatic digestion, accordingly to
186 the manufacturer's instructions The single-cell suspension was filtered through a 50 µm and centrifuged
187 at 300g, 4ºC for 10 min. The single-cell suspension was further used for flow cytometry phenotyping.
188 Flow cytometry acquisition was performed using a FACSAria IIu SORP cytometer (Becton Dickinson)
189 and data was further analysed using FlowJo version 10.6.1 (Becton Dickinson).
190

191 **2.7. Single-cell RNA-sequencing using Drop-sequencing**

192

193 Single-cell suspensions derived from both naïve and GL261-tumour bearing mice (**Table 1**) were
194 obtained using an adapted protocol from MACS Miltenyi.

195

196 ***Table 1.*** *Tumour volume measurement by MRI for biopsy collection at early, intermediate and late*
197 *stage in GL261 tumour-bearing WT and Acod1 KO mice used for scRNA-seq analyses.*

198

	Tumour volume (mm3)	
Time-point	**WT**	***Acod1* KO**
Early stage	6,11	9,61
Intermediate stage	22,63	20,48
Late stage	33,14	33,83

199

200 Specifically, tissue enzymatic dissociation was performed using the Neural Dissociation Kit P (MACS
201 Miltenyi Biotec) and the cell suspension was subsequently added into "C tubes" for the gentleMACS
202 Dissociator (gentleMACS™ Octo Dissociator with Heaters, Miltenyi Biotec). The 37C_ABDK_01
203 program was used to dissociate the brain tissue (>100 mg). We centrifuged the cellular suspension and
204 we removed the myelin following the Myelin removal beads kit (Myelin Removal Beads II, MACS
205 Miltenyi Biotec) accordingly to the manufacturer's instruction for 500 mg of tissue. Briefly, brain tissue
206 was suspended in 1800 µL of MACS buffer and incubated with 200 µl of myelin Microbeads (MACS
207 Miltenyi Biotec) at 4ºC for 15 min. Cells were washed, centrifuged for 10 min at 300g and suspended
208 in MACS buffer (3 x 1000 µl/mouse brain). The cell suspension was applied into the LS columns
209 (1000µl/each column) and the eluted fraction was collected in 2% BSA RNAse free solution. Cell
210 viability and counting was assessed prior injection into Drop-seq. A total of 5'659 single cells were
211 successfully sequenced and analysed. Cells handling, microfluidics fabrication, single cell droplet
212 encapsulation and next-generation sequencing preparation for Drop-seq libraries were done as
213 previously described (Sousa et al 2018).

214

215 **2.7.1. Single-cell RNA-sequencing bioinformatics processing, data and statistical analyses**

216

217 The FASTQ files were assembled from the raw BCL files using Illumina's bcl2fastq converter and ran
218 through the FASTQC codes [Babraham bioinformatics;
219 https://www.bioinformatics.babraham.ac.uk/projects/fastqc/] to check for the consistency in the library
220 qualities. The monitored quality assessment parameters were: a) quality per base sequence (especially
221 for the read 2 of the gene); b) per base N content; c) per base sequence content and d) over-represented
222 sequences. The libraries, which showed significant deviation, were re-sequenced. Then, the FASTQ
223 files were merged and converted to binaries using PICARD's fastqtosam algorithm. We have applied
224 the Drop-seq bioinformatics pipeline [14]. The sequencing reads were converted to digital gene
225 expression (DGE) matrix. To normalize for the transcript loading between the beads, the averaged
226 normalized expression levels (log2(TPM+1)) were calculated. To distinguish between cell-containing
227 and empty beads, a cumulative function of the total number of transcripts per barcode was plotted. Then,
228 a threshold was applied empirically on the resulting "knee plot" to estimate the beads exposed to the
229 cell content. For each experimental batch, we retained top 1'000 cell barcodes based on the cumulative
230 distribution, leading to 8'000 cells. We removed low-abundance genes and only genes that were
231 expressed in at least 30 cells were considered for further analysis. We additionally removed cells
232 expressing less than 1'000 genes. Lastly, we concatenated each batch in a single matrix of the following
233 dimensions: 5'659 cells x 18'338 genes. These pre-analytical filtering steps were processed using R
234 environment with the tidyverse package. The tSNE projection was processed with the Rtsne package
235 with a perplexity = 50, followed by a topological clustering with the library HDBSCAN (Hierarchical
236 DBSCAN with a minimum of 19 points - cells - for a cluster to be considered). We conducted statistical
237 analysis for significant expression between groups using pairwise Wilcoxon test, while p-values were
238 adjusted with Benjamini Hochberg (BH) method. Single cell trajectory inference analysis was done
239 with Monocle 2 in R (version 3.6.3) using default parameters [25, 26]. The branching method orders
240 cells along a trajectory based on gene expression similarities. Monocle 2 uses reversed graph embedding
241 to describe multiple fate decisions in a fully unsupervised manner. Branches in the trajectory represent
242 cell fate decisions through a developmental process.

243 Data visualization and downstream investigations were performed with Tableau Desktop software
244 (Seattle, USA). We used FlowSOM advanced analysis from Cytobank (Santa Clara, CA) for data
245 dimensionality reduction. Thus, the selected top 40 differentially expressed genes (p-value ≤ 0.01)
246 across distinct comparisons (see **Table S2**) were merged in n = 49 clusters and n = 10 metaclusters and
247 data visualization by two-way hierarchical clustering was obtained using the Glucore version 3.5 (Lund,
248 Sweden) software for heat-map representations.
249

250 **2.7.2. Single cell trajectory inference analysis**

251

252 Single cell trajectory inference analysis was done with Monocle 2 in R (version 3.6.3) using default
253 parameters [25, 26]. The branching method orders cells along a trajectory based on gene expression
254 similarities. Monocle 2 uses reversed graph embedding to describe multiple fate decisions in a fully
255 unsupervised manner. Branches in the trajectory represent cell fate decisions through a developmental
256 process.
257

258 **2.8. Gene Ontology analysis**

259

260 The DAVID (The Database for Annotation, Visualization and Integrated Discovery) gene functional
261 classification tool (http://david.abcc.ncifcrf.gov) was used to investigate and interpret the respective
262 functional biological terms from the large gene lists of differentially expressed genes. Representation
263 of GO terms enrichment was done on Cytoscape Software (National Institute of General Medical
264 Sciences, https://cytoscape.org/). Each node represents a GO term and the size of each node is
265 proportional to the number of nodes from the correspondent query set with that term. Only nodes with
266 p-value < 0.001 were chosen for network representation.
267

268 **2.9. Mouse brain CD11b+ cell isolation**

269

270 Murine brain CD11b+ isolated cells were enriched by magnetic separation using CD11b beads (MACS
271 Miltenyi Biotec) for RNA extraction or for flow cytometry phenotyping experiments. Briefly, 1×10^7
272 cells were resuspended in 90 µl of PBS supplemented with 0.5% BSA (Sigma-Aldrich) and 2 mM
273 EDTA (MACS buffer) and incubated with 10 µl of CD11b beads (MACS Miltenyi Biotec) at 4°C for
274 20 min. Cells were washed with MACS buffer, centrifuged for 10 min at 300g and resuspended in 500
275 µl of MACS buffer at a density of 1×10^8 cells. The cell suspension was applied into the LS columns
276 (MACS Miltenyi Biotec) and the CD11b+ fraction was eluted. Flow cytometry experiments to evaluate
277 the lymphocytic population were performed without prior CD11b+ beads isolation. Flow cytometry
278 acquisition was performed using an FACSAria IIu SORP cytometer (Becton Dickinson) and data was
279 further analysed using FlowJo version 10.6.1 (Becton Dickinson).
280

281 **2.10. Flow cytometry analyses**

282 Single-cell suspension was obtained as previously described. The cells were resuspended in ice-cold
283 HBSS with 2% FBS and 10 mM HEPES (FACS buffer) and filtered through a 70 µm nylon mesh
284 (CellTrics). For multicolour phenotyping, cells were blocked with Fc receptor binding inhibitor (anti-
285 mouse CD16/CD32 monoclonal antibody; 1:100; eBioscience) for 15 min at 4ºC to reduce binding of
286 non-specific Fc-gamma receptors, and then stained with fluorochrome-conjugated antibodies for 30 min
287 at 4°C in the dark. The following antibodies were used in the present study: rat anti-mouse CD45
288 monoclonal antibody (clone 30-F11), FITC; rat anti-mouse CD74 monoclonal antibody (clone In-1),
289 FITC; rat anti-mouse CD11b monoclonal antibody (clone M1/70), Percp-Cy5.5; rat anti-mouse
290 P2RY12 monoclonal antibody (clone S16007D) PE and mouse anti-mouse MHC-II (clone AF6-120,1)
291 APC. Unstained (control) and stained cells were washed and re-suspended in 100 µL of FACS buffer
292 prior acquisition. Before acquisition, the performance of the instrument was assessed using CS&T beads
293 according to the manufacturer's instructions. Single-stain controls were prepared with UltraComp
294 eBeads (eBioscience) following the manufacturer's instructions and thus used to calculate the
295 compensation matrix. Hoechst (0.1 µg/ml, Bisbenzimide, 33342; Sigma) or Zombie NIR (1:1000
296 dilution in PBS, Biolegend) was added for dead cell discrimination. Samples were run on FACSAria

297 IIu SORP cytometer (Becton Dickinson) and flow cytometry data was analysed using FlowJo software
298 (v. 10.6.1, Becton Dickinson).
299
300 **2.11. RNA extraction and qPCR analysis**
301
302 Total RNA was extracted from BMDMs and freshly isolated CD11b+ cells from tumour-bearing mice
303 at late stage using the RNeasy Mini Kit (Qiagen, Germantown, MD), according to the manufacturer's
304 instructions. RNA concentration was quantified by NanoDrop (NanoDrop Technologies) and RNA
305 quality was assessed by the quotient of the 28S to 18S ribosomal RNA electropherogram peak using a
306 bioanalyser (Agilent 2100; Agilent Technologies). For cDNA synthesis, RNA was reverse-transcribed
307 using SuperScript™ III reverse transcriptase (10,000 U; Invitrogen/Life Technologies) with 1 µl (50
308 µM)/reaction oligo(dT)20 (25 µM; Invitrogen/Life Technologies) as primer according to the
309 manufacturer's instructions. Reverse transcription was performed at 50°C for 60 min. Gene expression
310 reaction mixtures contained 2 µl of diluted cDNA, 10 µl of Fast SYBR Green Master Mix (Applied
311 Biosystems/Thermo Fisher Scientific) and 0.5 µl of each 10 µM forward and reverse primers. PCRs
312 were carried out in 384-well plates on a ViiA™ 7 real-time PCR system (Applied Biosystems/Thermo
313 Fisher Scientific) using the following programme: 95°C for 20 s, 40 cycles at 95°C for 1 s and 60°C for
314 20 s. Samples were run in triplicates, and the mean *C* t (threshold cycle) values were used to calculate
315 the relative amount of product by the Δ*C* t method using 60S ribosomal protein L27 (Rpl27) as
316 housekeeping gene. The specific primer sequences were as follows: Acod1 forward: 5' GCA ACA TGA
317 TGC TCA AGT CTG 3'; Acod1 reverse: 5' TGC TCC TCC GAA TGA TAC CA 3'; Cd74 forward: 5'
318 GAC CCA GGA CCA TGT GAT GC 3'; Cd74 reverse: 5' TTC CTG GCA CTT GGT CAG TAC TTT
319 A 3'; H2-Ab1 forward: 5' TCA CTG TGG AGT GGA GGG CA 3'; H2-Ab1 reverse: 5' GGC AGT
320 CAG GAA TTC GGA GC 3'; H2-Aa forward: 5' TCT GTG GAG GTG AAG ACG AC 3'; H2-Aa
321 reverse: 5' AGG AGC CTC ATT GGT AGC TGG 3'; Irf1 forward: 5' ACT CGA ATG CGG ATG
322 AGA CC 3'; Irf1 reverse: 5' GCT TTG TAT CGG CCT GTG TG 3'; RpL27 forward: 5' TGG AAT
323 TGA CCG CTA TCC CC 3'; Rpl27 reverse: 5' CCT GTC TTG TAT CGC TCC TCA A 3'.
324

325 **2.12. Immunofluorescence staining and microscopy imaging acquisition**

326

327 Coronal sections of 12 µm tickness were prepared adopting the standard protocol with minor
328 modifications [27]. Briefly, sections were washed (PBS with 0.1% Triton X-100), permeabilised (PBS
329 with 1.5% Triton X-100), blocked (PBS with 5% BSA) and incubated with the following primary
330 antibodies: rabbit anti-Iba1 (1:1000; Abcam), rat anti-MHC-II (1:100; Abcam), rat anti-CD74 FITC
331 (1:50; eBiocience) and mouse anti-IRF1 (1:100; Santa Cruz Biotechnology). Secondary antibodies
332 against the appropriate species were incubated for 2 h at room temperature. Cell nuclei were
333 counterstained with Hoechst (1 mg/ml; Sigma). Sections were mounted on glass slides cover slipped
334 using FluoromountTM Aqueous Mounting Medium (Sigma). For each brain section, at least 5 random
335 40X and 63X confocal images along the tumour margin and the tumour core were acquired with a Zeiss
336 LSM880 microscope (Jena, Germany). High-resolution XYZ stack images (1.024 x 1.024 pixels per Z
337 step) were taken with a step size of 0.50 µm. Cell quantifications were peformed using NIH ImageJ
338 software (NIH, Bethesda, MD, USA) and values for single mouse are represented with disticnt shape.
339 Hoechst staining was used as reference for tumour localization.

340

341 **2.13. Raw data files**

342

343 All relevant datasets are whithin the paper and its supporting information files (Fig. S1-S6 and Tables
344 S1-S4). We deposited the raw scRNA-seq data in Gene Expression Omnibus (GEO) database under the
345 accession number GSE158016.

346

347 **2.14. Statistical analysis**

348

349 Data were analyzed using the GraphPad Prism 8 software (GraphPad software, La Jolla, CA, USA) and
350 R environment (R Core Team, Vienna, Austria). Unless otherwise indicated, all data are presented as
351 mean ± standard error of the mean (SEM) of at least three independent biological experiments.
352 Statistical analysis was performed using Unpaired t test or Two-way ANOVA. All differences were

considered significantly different at p value <0.05 and were annotated as follows: *<0.05, **<0.01, ***<0.001, ns>0.05.

355 **3. RESULTS AND DISCUSSION**

356

357 **3.1. Single-cell transcriptomics reveals cellular diversity and cell type-specific differential**
358 **gene expression in naïve and GL261 tumour-bearing wild type and ACOD1/IRG1 knock-**
359 **out mice**

360

361 To investigate the heterogeneity of the TME in GBM, both at baseline and under ACOD1/IRG1
362 deficiency, we dissected brain tissue from naïve and GL261 tumour-bearing mice at early (5-10 mm^3),
363 intermediate (20-25 mm^3) and late (30-35 mm^3) stage of tumour progression, both from wild type (WT)
364 and age-matched ACOD1/IRG1 knock-out (KO) C57BL/6N mice. Briefly, we took advantage of the
365 GL261 (mouse glioma 261) syngeneic murine model as a widely used paradigm for immunotherapy
366 studies in GBM [28]. This model allows the engraftment of immortalized tumour cells from the same
367 strain with low immune rejection, thus enabling the investigation of an immunocompetent TME *in vivo*,
368 including functional T and B cells [29-31]. Recent studies aimed at comparing datasets obtained in
369 GBM patients with distinct GBM syngeneic mouse models identified high correlation levels with both
370 the 005 and GL261 models, thus serving as reliable preclinical models recapitulating several GBM
371 patient features [32]. For our aims, the tissue was digested to a single-cell suspension and analysed
372 using scRNA-seq to profile hundreds of cells isolated from the corresponding naïve and orthotopic
373 syngeneic GL261-implanted mice (**Fig. 1A**). Following pre-analytical filtering of the scRNA-seq
374 experiments, we obtained a matrix composed of 5'659 single cells (n = 18'338 genes). In order to reduce
375 the dimensionality of the matrix, we applied t-Distributed Stochastic Neighbourhood Embedding
376 followed by unsupervised topological clustering with DBSCAN on the 2D projection of the tSNE. We
377 identified 12 cell clusters with distinct gene expression signatures, irrespective of the tumour burden
378 and genotype (**Fig. 1B**). We annotated 11 of them (n > 30 cells) based on cell type-specific gene markers
379 [33, 34] and gene set enrichment analysis (GO) of up-regulated genes in the correspondent clusters.
380 Specifically, in addition to tumour cells (*Cd44*$^+$, n = 3'332 cells), we identified 10 stromal clusters that
381 we classified as pericytes (*Dbi*$^+$, n = 61 cells), lymphocytes (*Trac*$^+$, n = 178 cells), ependymal cells (*Ttr*$^+$,
382 n = 73 cells), endothelial cells (*Pecam1*$^+$, n = 328 cells), astrocytes (*Slc1a2*$^+$, n = 289 cells),

383 oligodendrocytes (*Plp1*$^+$, n = 365 cells), oligodendrocyte precursor cells (OPCs, *Pdgfra*$^+$, n = 60 cells),
384 neural stem cells (NSCs, *Meg3*$^+$, n = 36 cells) and myeloid cells 1 and 2 (*Itgam*$^+$, n = 836 cells) (**Fig.**
385 **1C, Fig. S1A**). Cells in the additional small subset (n = 20 cells) expressed myeloid markers (e.g. *Itgam,*
386 *Aif1*), but clustered independently from the annotated main myeloid clusters (**Fig. 1B**). The analysis of
387 additional specific markers provided robust molecular definitions of the major cell types present in the
388 brain of naïve and tumour-bearing mice (**Fig. S1**). Notably, identities, markers, and proportions of cell
389 types in naïve mice matched previous single-cell droplet-based sequencing data from mouse brain tissue
390 [35], indicating that our results were robust to the inclusion of tumour-affected brains. In addition, the
391 proportion of the cell types identified here were similar to the ones described in recent single-cell studies
392 conducted in GBM patients [18, 36, 37]. Lastly, as GBM is an archetypal heterogeneous tumour
393 characterized by a significant extent of common genetic alterations affecting tumour progression [38],
394 we verified the expression levels of specific oncogenes in the GL261-implanted mice. In line with
395 previous studies [39], *Myc* and *Trp53* were the main highly overexpressed genes in tumour cells
396 compared to non-malignant cells (**Fig. S2**).
397 Focusing on the TME, we first observed that lymphocytes, OPCs and a subset of myeloid cells were
398 solely present in tumour-bearing mice (**Fig. 1D**). Next, a direct comparison of tumour-associated cells
399 versus the corresponding cells in naïve mice enabled to identify differentially expressed genes (p value
400 < 0.01; log FC $> \pm 0.5$) (**Fig. 1E, Table S1**) according to the defined cell types. We observed a
401 prominent transcriptional adaptation in tumour-associated endothelial cells, oligodendrocytes as well
402 as in the myeloid subset (**Fig. 1D**). Among them, myeloid cells displayed the highest number of up-
403 regulated genes (n = 574) followed by endothelial cells (n = 178), oligodendrocytes (n = 18) and
404 astrocytes (n = 7) (**Fig. 1E**), thus indicating a prominent adaptation of the resident myeloid compartment
405 (myeloid cells 1) in the TME of GBM, which has been described also in patients [18, 37]. We detected
406 cell-type specific up-regulated genes across the four CNS resident cells (**Fig. 1F, Fig. S3A**). Notably,
407 all four cell types displayed a shared antigen processing and presentation gene signature (e.g. *H2-D1*,
408 *H2-K1* and *B2m*) (**Table S1**). Specifically, more than 90 genes (e.g. *Junb*, *Spp1*, *Cd74, B2m, H2-K1*
409 *and H2-Q7*) were up-regulated in both tumour-associated endothelial and myeloid cells compared to
410 the corresponding naïve cells, indicating that endothelial cells are also active immune modulators in the

411 TME of GBM. Indeed, the tumour vasculature is a key element of the TME, which largely contributes
412 to the immunosuppressive features of GBM [40]. In line with this notion, endothelial cells and
413 macrophages engage in tight interactions contributing to the modulation of the vascular function with
414 CD163+ TAMs enriched in parenchymal and perivascular areas [41].
415 Overall, these results show that, in analogy to GBM patients, the growing tumour in the analysed
416 syngeneic mouse model induces the emergence of cells in the TME that are normally absent in the
417 homeostatic CNS. Further, it specifically affects the transcriptional signature of the major resident CNS
418 cell types, with the myeloid compartment displaying high heterogeneity and major tumour-associated
419 education.
420

421 **3.2. Tumour-associated myeloid cells in Glioblastoma are heterogeneous and display distinct**
422 **transcriptional programmes**
423

424 Similar to GBM patients, the myeloid compartment constituted the biggest cluster in the TME of the
425 GL261 GBM mouse model (39.3% of the TME) (**Fig. S3B**) and displayed prominent transcriptional
426 adaptation and heterogeneity, thus representing a relevant paradigm to deepen and address its molecular
427 profile. Resident parenchymal microglia are difficult to segregate from peripheral monocyte-derived
428 cells, which prevalently constitute the myeloid compartment in GBM. Thus, we took advantage of our
429 scRNA-seq dataset obtained in WT mice to analyse the expression of known microglia and monocyte-
430 derived macrophage markers across naïve and the two TAM subsets identified by 2D-tSNE (**Fig. 2A**).
431 Naïve and TAM I clusters showed high expression levels of the microglia homeostatic genes (e.g.
432 *Gpr34, Hexb, P2ry12, Siglech, Sparc*), while these genes were almost undetectable (except *Hexb*) in
433 the TAM II cluster. Accordingly, the TAM II cluster exhibited high levels of peripheral monocytic-
434 derived macrophage markers (e.g. *Arg1, Ccr2, Ly6c2, Mrc1, Tgfbi*) (**Fig. 2B**). These observations were
435 supported by flow cytometry analyses of the macro-dissected tumour region to discriminate CD11b+
436 P2ry12+ from CD11b+ P2ry12-/low cells (**Fig. S4A**). Compared to naïve mice, where more than 95%
437 of CD11b+ cells were P2ry12+ resident microglial cells, the amount of CD11b+ P2ry12+ cells in
438 tumour-bearing mice was significantly reduced (mean 58.16 ± 5.6 %) (**Fig. 2C**). These analyses allowed

439 to discriminate microglia-like (TAM I) from macrophage-like (TAM II) cells in the GL261 syngeneic
440 model. Notably, our results are in line with recent single-cell profiling studies of myeloid cells
441 uncovering similar cellular distributions in the corresponding GBM mouse model and patients [42, 43].
442 Hierarchical clustering based on the top 40 differentially expressed genes with the lowest p-value
443 between naïve, microglia- and macrophage-like cells (**Table S2**) revealed, in agreement with their
444 different ontogeny, a less pronounced difference between naïve and tumour-associated microglia
445 compared to the monocyte/macrophage cluster (**Fig. 2D**). This observation was supported by the overall
446 higher number of differentially expressed genes between naïve microglia and tumour-associated
447 monocytes/macrophages (up = 943 genes, down = 111 genes) compared to tumour-associated microglia
448 (up = 574 genes, down = 17 genes) (**Fig. 2E**). In line with the decrease of homeostatic genes in microglia
449 under inflammatory conditions [44], the latter displayed a decreased expression of these genes (e.g.
450 *Siglech*, *P2ry12*, *Gpr34*) in the tumour when compared to the naïve group (**Fig. 2D**). Notably, we further
451 detected two subsets with distinct transcriptional profiles representing both TAM I and TAM II
452 populations that we latterly attributed to different tumour stages. Specifically, the main difference
453 between TAM I subsets relied on the differential expression of the microglia homeostatic genes, while
454 TAM II subpopulations differently up-regulated genes associated with antigen presentation (e.g. *H2-*
455 *Aa, Cd74*), positive regulation of angiogenesis (e.g. *Lgals3, Il1β, Cybb, Thbs1, Plek, Vim, Stat1*) and
456 metabolic redox metabolism (e.g. *Cybb, Msrb1*) (**Fig. 2D**). Overall, these results point towards the
457 heterogeneous composition of TAMs and their distinct adaptation profiles in the TME of GBM.
458 Gene set enrichment analysis of tumour-associated microglia or tumour-associated-
459 monocyte/macrophage transcriptional programmes revealed immunological terms shared by both cell
460 types (e.g. inflammatory response and innate immune response). We also identified terms specifically
461 associated with TAM I (e.g. positive regulation of phagocytosis and T cell mediated cytotoxicity) or
462 TAM II (e.g. positive regulation of cell migration and oxidation-reduction process), suggesting distinct
463 ontogeny-based functional adaptations to the tumour (**Fig. 2F**).
464 Next, to strengthen our findings obtained in the GL261 syngeneic mouse model, we compared
465 microglia-like (TAM I) and monocyte/macrophage-like (TAM II) transcriptional signatures with
466 putative corresponding cell types recently described in GBM patients at single-cell resolution [9].

467 Overall, 8.6% of up-regulated genes in TAM I ($p < 0.01$; Log FC > 0.5) were shared with tumour-
468 associated microglia-like cells in GBM patients. In addition, 7% of differentially expressed genes
469 characterizing TAM II ($p < 0.01$; Log FC > 0.5) were mutually up-regulated in blood monocyte-derived
470 macrophage-like cells in GBM patients (**Fig. S4B**). This comparison enabled to identify robust
471 transcriptional signatures maintained across the two species allowing discriminating tumour-associated
472 microglia (e.g. *CCL4, CCL3, P2RY12, CX3CR1, BIN1, SELPLG, CD83, SALL1*) and macrophages (e.g.
473 *TGFBI, THBS1, VIM, IL1B, IL1RN, F13A1, CYBB*) both in the GBM syngeneic murine model and in
474 patients. We used the characterized transcriptional signatures to verify their prognostic value in GBM
475 patients. For this, we took advantage of The Cancer Genome Atlas (TCGA) datasets allowing to link
476 patient survival with corresponding bulk transcriptional data from two publicly available TCGA-
477 databases (TCGA-GBM: high grade glioma and TCGA-LGG: low grade glioma). Notably, a
478 macrophage-like-enriched signature correlated with a worse patient survival compared to a microglia-
479 like-enhanced programme, supporting the notion that tumour-associated microglia may possess
480 effective immunological functionality, while tumour-associated macrophages display an immune-
481 suppressed pro-tumorigenic phenotype (**Fig. 2G**).
482 Taken together, our scRNA-seq analyses enabled a clear separation of microglia from peripheral
483 monocytic-derived macrophages displaying key transcriptional and functional differences along their
484 adaptation to the tumour, with microglia-like cells showing higher immune reactivity than macrophage-
485 like cells, both in the GBM syngeneic mouse model and patients. Our results are in agreement with
486 recent prognostic studies conducted in GBM patients showing that immunosuppressive immune cell
487 infiltrates increase from grade II to grade IV [45] and a reduced immune suppressive phenotype
488 correlates with extended survival, as observed in LGG patients [46]. Collectively, we demonstrate the
489 relevance of discriminating between microglia and monocyte-derived macrophages for prognostic
490 purposes in GBM patients. We take advantage of this critical distinction to separately characterizing
491 tumour-associated microglia and macrophage subsets along GBM progression.
492
493 **3.3. TAMs rapidly infiltrate the tumour and adapt along GBM progression**
494

495 By studying TAM heterogeneity along GBM progression in WT mice at single-cell resolution, we
496 detected microglia-like and macrophage-like cell subsets in all analysed tumour stages (i.e. early,
497 intermediate and late time points), indicating that, in agreement with prior observations [8], in this
498 model the infiltration of monocyte-derived macrophages occurs early during tumour growth (**Fig. 3A**).
499 Notably, we observed a gradual decrease in the number of up-regulated genes (early n = 372,
500 intermediate n = 291 and late n = 143) and a relatively constant number of down-regulated genes (early
501 n = 138; intermediate n = 110 and late n = 167) between macrophage-like and microglia-like cells along
502 tumour stages. These results indicate that the transcriptional programmes of microglia and peripheral
503 infiltrated macrophages converge over time (**Fig. 3B**). Overall, the ratios of microglia-like and
504 macrophage-like cells in the GBM TME did not significantly change across early (TAM I: 29,35%;
505 TAM II: 70,65%) and late (TAM I: 24,43%; TAM II: 75,57%) stages (**Fig. 3C**). Next, we sought to
506 investigate microglia-like and peripheral macrophage-like cell transcriptional programmes along
507 tumour progression separately, with a special focus at early and late stages.
508 Hierarchical clustering based on the top 40 differentially expressed genes with the lowest p value across
509 the tumour stages revealed three clusters mainly represented by naïve microglia, tumour-associated
510 microglia at early/intermediate time points and a late-enriched group (**Fig. S5A**). We analysed up-
511 regulated genes characterizing microglia-like cells at early and late tumour stages versus naïve
512 microglia (**Fig. 3D**). We found great overlap (34.1%) of genes expressed by microglia-like cells
513 between the two stages (e.g. *H2-D1, H2-K1, Cd83, Il1b, Ccl12, Ccl4, Lyz2, Fth1, Ctsb, Atf3, Cst7, B2m,*
514 *Cd52, Nfkbia*), indicating a core transcriptional programme maintained along GBM progression (**Table**
515 **S3**). When comparing the levels of specific differentially expressed genes between early (n = 112) and
516 late (n = 329) tumour stages, markers associated with antigen processing and presentation (e.g. *Cd74*,
517 *H2-Ab1*, *H2-Aa*) or T-cell activation and cytotoxicity (e.g. *H2-T23*, *H2-Q7*) and inflammatory response
518 (e.g. *Axl*, *Cybb*) were largely decreased at later tumour stages (**Fig. 3E, Fig. S5B**). In parallel, genes
519 associated with chromatin remodelling (e.g. *Cbx5*, *Ezh2, Nasp)* and actin nucleation/polymerization
520 (e.g. *Arpc1a, Arpc1b*) were enhanced at later stages (**Fig. 3E**). In particular, we found a subset of
521 microglia-like cells up-regulating *Ezh2* expression at late stage. Although studies have demonstrated
522 that *Ezh2* is frequently overexpressed in a wide variety of cancers, mechanistic links of *Ezh2* expression

523 in TAMs to cancer progression remains to be elucidated. In ovarian cancer, *Ezh2* has direct roles on T
524 cell response and inhibition of *Ezh2* in tumour-specific T cells increases the tumour burden *in vivo* [47].
525 We conducted similar analyses for the macrophage-like subset. Unsupervised clustering of the top 40
526 differentially expressed genes along the tumour stages revealed a less pronounced separation of the
527 clusters across tumour stages compared to microglia-like cells, probably due to the strong
528 transcriptional differences between naïve microglia and the overall TAM II subset (**Fig. S5C**, **Table**
529 **S3**). We found prominent overlap (54.3%) of genes up-regulated both at early and late tumour stages
530 expressed by macrophage-like cells compared to naïve microglia (e.g. *Lyz2, Apoe, Fth1, Il1β, H2-K1,*
531 *H2-D1, Vim, Cd14, Cybb, Tgfbi*) indicating, similarly to microglia-like cells, a main transcriptional
532 programme preserved along GBM progression (**Fig. 3F**).
533 The comparison of the levels of specific differentially expressed genes between early and late tumour
534 stages revealed the decrease of macrophage activation markers (e.g. *Ccl5, Ass1, Tlr2, Itgb2, Klf4*) as
535 well as, similarly to microglia-like cells, the down-regulation of genes associated with antigen
536 processing and presentation (e.g. *Cd74, H2-Ab1, H2-Aa*) and regulation of T-helper cells (e.g. *H2-Q7,*
537 *H2-T23*). In addition, type I interferon genes (e.g. *Irf1, Stat1*) were drastically reduced at late stage (**Fig.**
538 **3G, Fig. S5D**). Taken together, the reduced antigen cross-presentation ability of both microglia- and
539 macrophage-like cells at later time points may add to the recognised poor recruitment of T cells to the
540 tumour site in GBM [48], thus dampening potential T-cell-mediated tumour eradication along its
541 progression.
542 To corroborate these results at the protein level, we compared the expression levels of CD74 and MHC-
543 II (encoded by *H2-Ab1*) at early and late stages in corresponding tissue sections. To discriminate brain-
544 resident microglia and blood derived-monocytes/macrophages in immunohistological analyses, we took
545 advantage of the Ivy Glioblastoma Atlas Project to infer TAM spatial localization in laser-micro-
546 dissected regions of GBM patients [49]. Here, we observed an enrichment of microglia-like cells
547 (expressing *BIN1, CX3CR1, P2RY12*) at the leading edge of the tumour, while macrophage-like cells
548 (expressing *IL1RN, TGFBI, THBS1*) were mostly detected in the microvascular compartment (**Fig. 3H**).
549 Similar findings were described by spatial scRNA-seq of the myeloid compartment in GBM patients
550 where *TGFBI*, *VEGFA* and *IL1RN* were mainly expressed by macrophages in the tumour core, while

551 microglial cells enriched in the tumour periphery displayed a reduced expression of these genes [18].
552 Supporting these observations, 2-photon microscopy in murine GBM sections recently revealed two
553 distinct cell types with different morphological properties composing TAMs. Specifically, cells with
554 reduced branching and increased surface area compared to naïve resident parenchymal cells mainly
555 accumulated at the tumour margins and represented tumour-associated microglia, while monocyte-
556 derived macrophages displaying shrank surface area and increased migratory properties were mainly
557 located in the tumour core [50]. In agreement with this, we observed a significant reduction of the
558 surface area of macrophage-like infiltrative cells in the tumour core compared to larger and branched
559 microglia-like enriched cells in the tumour margin independent of tumour stage (**Fig. 3I-J** and **Fig.**
560 **S5E**). In line with our scRNA-seq data, we observed a significant decrease of the antigen presenting
561 cell markers MHC-II (**Fig. 3K**) and CD74 (**Fig. 3L**) at late GBM stage in both the tumour margin and
562 core. Notably, we observed a higher percentage of Iba1+ MHC-II+ cells in the tumour margin compared
563 to tumour core both at early and late stages (**Fig. 3K**), highlighting spatial heterogeneity of TAMs at
564 the protein level.
565 Collectively, these analyses show that TAMs display distinct transcriptional programmes along GBM
566 progression, with both microglia and monocytic-derived macrophages exhibiting decreased antigen
567 presenting cell features at later tumour stages compared to earlier phases.
568

569 **3.4. TAMs display higher immunological reactivity under aconitate decarboxylase 1**
570 **deficiency affecting T cell recruitment**

571

572 In mammals, immune-responsive gene 1 protein (IRG1), encoded by aconitate decarboxylase
573 1/immunoresponsive gene 1 (*Acod1/Irg1*), catalyses the production of itaconate from the
574 decarboxylation of cis-aconitate, an intermediate metabolite of the TCA cycle [19, 51]. Itaconate is one
575 of the most upregulated metabolites in activated macrophages [52] exhibiting anti-inflammatory
576 properties, thus contributing to the resolution of inflammation [20, 21]. Interestingly, it has been
577 recently shown that low doses of itaconate inhibits inflammation, while it promotes inflammation at

578 high doses [53]. Due to the emerging role of various immune metabolites in macrophage
579 reprogramming towards specific phenotypes, we sought to analyse the role of *Acod1/Irg1* in TAM
580 adaptation along GBM progression and characterize TAM subsets under ACOD1 deficiency at single
581 cell resolution.
582 In the GL261 model, we exclusively detected *Acod1/Irg1* induction across the myeloid compartment
583 and, at a larger extent, within the macrophage-like subset (**Fig. S6A**). We observed similar results in
584 the Brain Tumour Immune Micro Environment dataset acquired in GBM patients by RNA-seq [54].
585 Indeed, *ACOD1/IRG1* expression was up-regulated in both CD49D^{low} microglial cells and CD49D^{high}
586 macrophages, with higher expression levels in IDH-wildtype compared to IDH-mutant gliomas (**Fig.**
587 **S6B**). Microarrays analysis of RNA extracted from CD11b+ MACS-isolated cells from naïve and
588 GL261-implanted mouse brains showed also a significant increase of *Acod1/Irg1* expression in tumour-
589 bearing compared to naïve mice (**Fig. S6C**) [11]. In our hands, *Acod1/Irg1* was mainly induced by a
590 subset of myeloid cells at early stages, while its expression was reduced at later tumour stages (**Fig.**
591 **4A**), indicating a time-dependent expression of *Acod1/Irg1* in myeloid cells in GBM. Bone marrow-
592 derived macrophages (BMDMs) co-cultured with GL261 tumour cells *in vitro* showed time-dependent
593 expression of *Acod1,* while its expression was undetectable in BMDMs obtained from *Acod1* KO mice
594 (**Fig. 4B**). Similarly to LPS stimulation [19, 22], the expression of *Acod1/Irg1* was mainly induced at
595 earlier (24h) compared to later (48h) time points (**Fig. 4B**).
596 The analysis of TAM subsets by scRNA-seq suggested an over-representation of the macrophage-like
597 population in *Acod1* KO mice (81.15%) compared to age-matched WT mice (63.11%) (**Fig. 4C**). Albeit
598 we did not detect differences in the total number of bone-marrow precursors between naïve WT and
599 *Acod1* KO mice (**Fig. S6D**), we observed an increase in the number of CD11b+ cells in the brain of
600 *Acod1* KO compared to WT tumour-bearing mice (p value = 0.05) (**Fig. 4D**). Indeed,
601 immunofluorescence analyses revealed a significant increase in the number of Iba1+ cells at early stages
602 at both the tumour margin and core, thus confirming enhanced infiltration of myeloid cells in *Acod1*
603 KO mice (**Fig. 4E**). Investigation of the exclusively up-regulated genes in microglia-like and
604 macrophage-like cells at early stages in *Acod1* KO mice versus their corresponding counterparts in WT
605 mice identified a major transcriptional effect on macrophage-like (n = 41 genes) compared to microglia-

606 like (n = 3 genes) cells (**Fig. 4F**). Genes associated with TAM recruitment, such as *Ccr2, Mif, Ldha and*
607 *Tspo*, were uniquely overexpressed in macrophage-like cells from *Acod1* KO mice (**Fig. 4F**).
608 Specifically, the CCL2/CCR2 axis is essential for monocyte migration into the inflamed CNS [55, 56].
609 Further, macrophage migration inhibitory factor (MIF) plays an important role in regulating
610 inflammatory responses in innate immune cells [57] and can directly interact with CXCR2 and CXCR4
611 promoting inflammatory activity and leukocyte chemotaxis in cancer [58].
612 Similarly to early stages, the number of exclusively up-regulated genes was higher in macrophage-like
613 (n = 68 genes) compared to microglia-like (n = 9 genes) cells when comparing *Acod1* KO with WT
614 tumour-bearing mice at late stage (**Fig. 5A**, **Table S4**), confirming that the lack of *Acod1/Irg1* mainly
615 affected the transcriptional programme of peripheral infiltrating macrophages compared to microglia.
616 Gene set enrichment analysis of macrophage-like cell exclusively up-regulated genes at late GBM stage
617 in *Acod1 KO* compared to WT mice uncovered enrichment of terms associated with inflammation (e.g.
618 *Irf1*), antigen processing and presentation via MHC class I (e.g. *H2-K1*) and T cell mediated cytotoxicity
619 (e.g. *H2-T23*) (**Fig. 5A**, **Fig. S6E**). The common 15 microglia-like and macrophage-like cell up-
620 regulated genes in *Acod1* KO compared to WT mice were associated with antigen presenting cell (e.g.
621 *Cd74, H2-Ab1*) and inflammatory (*Stat1*) markers (**Fig. 5A**), reflecting an enhanced immune activation
622 at late stage in *Acod1* KO mice. In agreement with these results at single-cell resolution, we detected a
623 higher induction of antigen presentation (e.g. *Cd74*, *H2-Ab1*, *H2-Aa*) and inflammatory (e.g. *Irf1*)
624 transcripts in *ex vivo* CD11b+ isolated TAMs from *Acod1* KO compared to WT tumour-bearing mice
625 at late stages (**Fig. 5B**). IRF family members play essential roles in regulating immune responses [59,
626 60] and seminal work has shown that *Irf1* KO mice exhibit impaired NK cell maturation and defective
627 Th1 responses [61, 62]. Additionally, IRF1 operates as a tumour suppressor and its inactivation has
628 been shown to significantly increase risk of malignancy [63]. To investigate the expression of IRF1 at
629 the protein level, we conducted immunofluorescence analysis and detected higher numbers of
630 IBA1+IRF1+ positive cells in the tumour core in *Acod1* KO compared to WT mice (**Fig. 5C**). Amongst
631 the downstream targets of IRF1, we detected by flow cytometry an increased expression of MHC-II in
632 TAMs isolated at late stage from *Acod1* KO compared to WT mice (**Fig. 5D, Fig. S6F**). Additionally,
633 in brain sections from *Acod1* KO tumour-bearing mice, we detected a significant increase of CD74

634 expressed by macrophage-like cells, which were enriched in the tumour core, compared to WT mice
635 (**Fig. 5E**). As gliomas are characterized as "immunologically silent" in IDH-mutant or "lymphocyte-
636 depleted" in IDH-wildtype subtypes [64], we sought to investigate whether the ablation of *Acod1*, which
637 induces an enhanced TAM immunogenic phenotype, could influence the recruitment of T cells to the
638 tumour site. Indeed, we observed a considerable increase of the lymphocytic population in *Acod1 KO*
639 compared to WT mice, both in our scRNA-seq dataset (**Fig. S6G**) and by flow cytometry (**Fig. 5F, Fig.**
640 **S6F**), thus suggesting an effective crosstalk between TAMs and the adaptive immune cell compartment.
641 In order to elucidate if specific TAM subsets under ACOD1 deficiency display enhanced immunogenic
642 phenotypes, we conducted single cell trajectory inference analyses. We showed higher macrophage-
643 like cell heterogeneity in *Acod1 KO* compared to WT mice, thus suggesting that ACOD1 deficiency
644 also supports TAM diversity (**Fig. 5G**). Specifically, pseudo-time analyses uncovered four distinct
645 cellular states across the TAM II subset under *Acod1* deficiency (**Fig. S7A-B**). Further analysis of
646 exclusive genes driving the most prominent cellular state (cellular state four) revealed a TAM II subset
647 exclusively present in *Acod1* deficient tumour-bearing mice, which might support leukocyte migration
648 and T cell activation (e.g. *Ccl17, Ccl22, Ccr7, IL12b, Cd1d1*) to the tumour site (**Fig. S7C**). This subset
649 was also characterized by higher expression levels of genes encoding serine proteinase inhibitors (e.g.
650 *Serpinb6b* and *Serpinb9*) (**Fig. S7C**), which have been described to play a critical role in T lymphocyte
651 mediated immunity [65]. Although *Acod1/Irg1* silencing in macrophages has been shown to
652 significantly reduce the peritoneal tumour burden (Weiss et al., 2018), the analysis of tumour growth in
653 GL261 tumour-bearing mice did not show significant differences between WT and *Acod1* KO, neither
654 we detected differences in the mouse survival (data not shown), most probably due to the very high
655 aggressiveness of the tumour in the analysed model.
656

657 ## 4. CONCLUSION

658

659 In summary, we here elucidated the diversity of the myeloid compartment along GBM progression and
660 under ACOD1 deficiency. Specifically, we demonstrate that the myeloid compartment is the most
661 affected and heterogeneous stromal cell component in GBM, with microglia and macrophages acquiring

662 key transcriptional differences and rapidly adapting along GBM progression. Specifically, we show that
663 TAMs display a decreased antigen-presenting cell signature along GBM progression, which is retained
664 under ACOD1 deficiency. Collectively, these results are in line with the anti-inflammatory role of
665 ACOD1/itaconate [66], since their absence skewed TAMs in GBM towards a more reactive and
666 immunogenic phenotype. Mechanistically, itaconate modifies a range of proteins in macrophages,
667 including KEAP1, which leads to NRF2 activation and induction of NRF2-dependent genes encoding
668 anti-inflammatory and antioxidant factors. Similarly, itaconate might also modify GILT (IFI30), a
669 protein that regulates antigen presentation [66]. However, how itaconate and GILT might potentially
670 contribute to the decrease of antigen presentation marks warrants further investigation. From a
671 therapeutic point of view, although immune checkpoint blockade therapy has markedly improved
672 survival in several immunogenic cancers, such as melanoma, its efficacy has not been extended to GBM
673 patients, as observed in a randomized phase III clinical trial for recurrent GBM (CheckMate 143;
674 Identifier NCT 02017717) [67]. As it is becoming increasingly evident that a mono-therapeutic
675 approach is unlikely to provide anti-tumour efficacy, the combination of ACOD1 suppression in TAMs,
676 which enables to harness both the innate and adaptive immune systems, together with the inhibition of
677 immune checkpoints may advance therapeutic successes against GBM and other solid tumours.

678 **ACKNOWLEDGMENTS**

679

680 We thank Amandine Bernard for genotyping the mice, Virginie Baus for helping with the MRI as well
681 as Thomas Cerutti for the support with flow cytometry experiments. We are grateful to Oihane Uriarte
682 and Dr Tony Heurtaux for aiding with gentleMACS™ Dissociator. Y.P.A. and C.S. were supported by
683 the Luxembourg National Research Fund (PRIDE15/10675146/CANBIO and AFR6916713,
684 respectively) and the Fondation du Pélican de Mie et Pierre Hippert-Faber under the aegis of Fondation
685 de Luxembourg. Y.A.Y. was supported by GLIOTRAIN ITN funded by the European Union's Horizon
686 2020 research and innovation programme under the Marie Skłodowska-Curie grant agreement No
687 766069 (The material presented and views expressed here are the responsibility of the author(s) only.
688 The EU Commission takes no responsibility for any use made of the information set out). A.S. was
689 supported by the C14/BM/7975668/CaSCAD project as well as by the National Biomedical
690 Computation Resource (NBCR) through the NIH P41 GM103426 grant from the National Institutes of
691 Health. A.M. was supported by Action Lions "Vaincre le Cancer" Luxembourg. We acknowledge
692 financial support by the Luxembourg Institute of Health (MIGLISYS) and the Luxembourg Centre for
693 Systems Biomedicine.

694

695 **AUTHOR CONTRIBUTIONS**

696

697 YPA, SPN and AlM designed the project; YPA, KG, AO, CS and RH performed experiments; YPA,
698 ArM, KG, AC, YAY, AG and AlM analysed experiments; DC provided animals; AS set up and
699 supervised scRNA-seq analyses; YPA and AlM wrote the manuscript; all the authors edited and
700 approved the manuscript.

701

702 **CONFLICT OF INTEREST**

703 The authors declare no competing interests.

704 **FIGURE TITLES AND LEGENDS**

705

706 **Fig. 1. Cell type diversity in naïve and GL261 tumour-bearing mice at different tumour stages,**
707 **both from wild type and ACOD1/IRG1 knock-out mice. (A)** Flowchart depicting the overall design
708 of the study. Naïve- and macro-dissected brain tumour regions from both wild type and ACOD1/IRG1
709 knock-out mice were processed by scRNA-seq analyses. Samples were collected at different time points
710 (early: 5-10 mm3; intermediate: 20-25 mm3; late: 30-35 mm3) according to tumour volume measured
711 by magnetic resonance imaging (MRI). **(B)** 2D-tSNE representation of all single cells included in the
712 study (n = 5'659 cells) grouped within 12 cell clusters. **(C)** Cell type-specific markers allowing the
713 identification of stromal cell types: pericytes (*Dbi*$^+$), lymphocytes (*Trac*$^+$), ependymal cells (*Ttr*$^+$),
714 endothelial cells (*Pecam1*$^+$), astrocytes (*Slc1a2*$^+$), oligodendrocytes (*Plp1*$^+$), oligodendrocyte precursor
715 cells (OPCs, *Pdgfra*$^+$), neural stem cells (NSCs, *Meg3*$^+$), myeloid cells 1 (*Itgam*$^+$) and myeloid cells 2
716 (*Itgam*$^+$). See **Fig. S1** for additional cell type-specific markers used for clusters annotation. **(D)** 2D-
717 tSNE representation showing naïve (in black) and tumour-associated (in red) cells. **(E)** Up-regulated
718 genes in tumour-associated clusters compared to corresponding naïve cell types (myeloid cells,
719 endothelial cells, oligodendrocytes and astrocytes). **(F)** Examples of the most up-regulated genes (p
720 value < 0.01, logFC > 0.5) per cell type in tumour-bearing mice.

721

722 **Fig. 2. Microglia- (TAM I) and macrophage-like (TAM II) subsets display discrete functional**
723 **adaptation in the GBM syngeneic GL261 murine model. (A)** Colour-coded 2D-tSNE representation
724 showing three distinct myeloid cell subsets in WT mice: naïve, TAM I and TAM II clusters. **(B)** 2D-
725 tSNE representation showing the expression of microglia homeostatic genes (*Gpr34*, *Hexb*, *P2ry12*,
726 *Siglech* and *Sparc*) and macrophage-like markers (*Arg1, Ccr2, Ly6c2, Mrc1 and Tgfbi*). **(C)** Percentage
727 of CD11b+ P2ry12+ cells in naïve and tumour-bearing mice quantified by flow cytometry in naïve and
728 tumour-bearing mice. **(D)** Heat-map representation of two-way hierarchical clustering analyses of the
729 top 40 differentially expressed genes based on the p-value rank (rows) for each myeloid cluster: naïve,
730 TAM I and TAM II (columns). Genes represented were present at least in one of the three comparisons

731 (TAM I versus naïve; TAM II versus naïve and TAM I versus TAM II, **Table S2**). Red: up-regulation;
732 blue: down-regulation. **(E)** Number of differentially expressed genes for TAM I versus naïve (n = 574
733 up-regulated; n = 17 down-regulated) and for TAM II versus naïve (n = 943 up-regulated; n = 110
734 down-regulated). **(F)** Gene ontology functional network of TAM I (upper graph) and TAM II (bottom
735 graph) versus naïve microglia. Node size correlates to gene set numbers and annotated nodes were
736 defined as containing ≥ 15 genes. **(G)** Kaplan-Meier survival analysis in GBM patients (TCGA-LGG
737 and TCGA-GBM databases) with high and low TAM I enriched signature.
738 Statistical analysis for (**C**) Unpaired Student *t* test (WT = 4, *Acod1* KO n = 3), mean ± SEM, ** p <
739 0.01.
740
741 **Fig. 3. TAM subsets spatial and temporal characterisation along Glioblastoma development. (A)**
742 Myeloid tSNE plot colour coded representation for tumour progression (green: early; blue:
743 intermediate; purple: late stage). **(B)** Number of up-regulated and down-regulated genes (p-value <
744 0.01, FC > ± 0.5) between TAM II and TAM I along GBM progression. **(C)** Relative proportions of
745 TAM I and TAM II subsets at early and late GBM stages obtained by scRNA-seq analysis. **(D)** Venn
746 diagram representation showing TAM I shared (n = 228) and exclusively up-regulated genes at early (n
747 = 112) and late (n = 329) stages versus naïve microglia. **(E)** Single-cell bar plots showing selected top
748 differentially expressed genes in TAM I between early and late GBM stages. **(F)** Venn diagram
749 representation showing TAM II shared (n = 403) and exclusively up-regulated genes at early (n = 262)
750 and late (n = 77) stages versus naïve microglia. **(G)** Single-cell bar plots showing selected top
751 differentially expressed genes in TAM II between early and late GBM stages. **(H)** RNA-seq profiles of
752 laser-microdissected regions of GBM patients for microglia (*BIN1, CX3CR1, P2RY12*) and peripheral
753 monocyte-derived cell (*IL1RN, TGFBI, THBSI*) marker genes. Data extracted from the Ivy
754 Glioblastoma Atlas Project (PCAN: pseudopalisading cells around necrosis; MvP: microvascular
755 proliferation). **(I)** Representative immunofluorescence pictures of Iba1 positive cells in the tumour
756 margin and core in murine brain sections. **(J)** Quantification of Iba1 surface area in the tumour margin
757 and tumour core at early and late stages. **(K-L)** Representative immunofluorescence pictures and

758 quantification for (**K**) MHC-II and (**L**) CD74 staining in the tumour margin and core at early and late
759 stages.
760 Statistical analysis for (**J**) Two-way ANOVA with Sidak's multiple comparison corrections (early n =
761 3 and late n = 3), (**K-L**) Two-way ANOVA with Sidak's multiple comparison corrections (early n ≥ 3
762 and late n = 4), mean ± SEM, * $p < 0.05$; ** $p < 0.01$; *** $p < 0.001$; ns = not significant. Scale bars in
763 I, K and L = 50µm. TAM I, tumour-associated microglia, TAM II, tumour-associated macrophage;
764 PCAN, Pseudopalisading cells around necrosis; MvP, Microvascular proliferation; T.margin, tumour
765 margin; T.core, tumour core; Iba1, Allograft inflammatory factor 1; MHC-II, Major histocompatibility
766 complex class II molecules; CD74, HLA class II histocompatibility antigen gamma chain.
767
768 **Fig. 4. *Acod1* expression is induced in TAMs and its deficiency affects their recruitment. (A)** *Acod1*
769 expression levels in naïve and tumour-bearing TAM I (logFC 0,44) and TAM II (logFC 0,46) cells at
770 early and late stage of GBM progression by scRNA-seq. **(B)** Expression levels of *Acod1* gene in
771 BMDMs from WT and *Acod1* KO mice upon co-culture with GL261 tumour cells at 24 and 48h. Dash
772 line represents baseline expression at time zero. **(C)** Myeloid tSNE plot colour coded (brown: WT;
773 orange: *Acod1* KO) and respective percentage of microglia-like and macrophage-like cells according to
774 the genotype. **(D)** Total number of CD11b+ cells isolated from WT and *Acod1* KO tumour-bearing
775 mouse brains at late stage. **(E)** Immunofluorescence pictures depicting Iba1 positive cells in the tumour
776 margin (left) and core (right). Number of Iba1 positive cells were quantified in WT and *Acod1* KO mice
777 at early GBM stage. **(F)** Venn diagram representation showing shared and exclusive up-regulated genes
778 in *Acod1* KO TAM I (n = 3) and TAM II (n = 41) at early stage versus their respective counterparts in
779 age-matched WT cells (**Table S4**). Notch plot representation of selected genes exclusively up-regulated
780 by TAM II in *Acod1* KO mice in comparison to WT mice at early stage. Statistical analysis for (**A**)
781 pairwise Wilcoxon test with p-value adjusted with Benjamini Hochberg method; (**B**) Two-way ANOVA
782 with Sidak's corrections (WT = 2, *Acod1* KO n= 2); (**D**) Unpaired Student *t* test (WT = 8, *Acod1* KO
783 n= 5); (**E**) Unpaired Student *t* test (WT early n = 4; *Acod1* KO early n ≥ 2), mean ± SEM. *** $p < 0.001$.
784 Scale bars in E = 50µm. WT, wild-type; KO, knock-out; *Acod1*, aconitate decarboxylase 1; TAM I,
785 tumour-associated microglia; TAM II, tumour-associated macrophage; BMDMs, bone marrow-derived

786 macrophages; Iba1, Allograft inflammatory factor 1; *Ccr2*, C-C chemokine receptor type 2; *Mif*,
787 Macrophage migration inhibitory factor; *Ldha*, Lactate dehydrogenase A; *Tspo*, Translocator protein.
788
789 **Fig. 5. TAMs under *Acod1* deficiency display higher antigen presenting cell programmes**
790 **associated with increased lymphocytic recruitment at late GBM stage. (A)** Venn diagram
791 representation showing shared (n = 15) and exclusive up-regulated genes in *Acod1* KO TAM I (n = 9)
792 and TAM II (n = 68) at late stage versus their respective counterparts in age-matched WT cells (**Table**
793 **S4**). Corresponding notch plot representations of selected shared or unique genes up-regulated in TAM
794 I and TAM II cells in *Acod1* KO mice compared to age-matched WT mice at late stage. **(B)** Expression
795 levels of *Cd74, H2-Ab1, H2-Aa* and *Irf1* genes in CD11b+ cells isolated from WT and *Acod1* KO mice
796 at late stages. **(C)** Immunofluorescence pictures (left) and quantification (right) of IRF1 expression in
797 Iba1+ cells in the tumour core region at late stage in *Acod1* KO and WT mouse brain sections. **(D)**
798 Representative overlay histogram (left) and quantification (right) of MHC-II expression in TAMs
799 analysed in WT and *Acod1* KO mice at late stage by flow cytometry. **(E)** Immunofluorescence pictures
800 (left) and quantification (right) of CD74 expression in Iba1+ cells in the tumour core region at late stage
801 in *Acod1* KO and WT mouse brain sections. **(F)** Percentage of CD11b- CD45+ lymphocytes at late
802 stage quantified by flow cytometry. **(G)** Single cell trajectory inference analysis of 335 myeloid cells
803 from WT naïve and tumour-bearing mice (upper graph) and 501 myeloid cells from *Acod1* KO naïve
804 and tumour-bearing mice (bottom graph). Statistical analysis for (**B**) Unpaired Student t test (WT n =
805 4, *Acod1* KO n = 2); (**C**) Unpaired Student t test (WT n = 3, *Acod1* KO n = 3); (**D**) Unpaired Student t
806 test (WT n = 7, *Acod1* KO n = 3), (**E**) Unpaired Student t test (WT n = 4, *Acod1* KO n = 3), (**F**) Unpaired
807 Student t test (WT n = 5, *Acod1* KO n = 3), mean ± SEM, * $p < 0.05$; ** $p < 0.01$; *** $p < 0.001$. Scale
808 bars = 50µm and 20µm in (**C**). *Cxcl9*, C-X-C Motif Chemokine Ligand 9; *Cd36*, CD36 Molecule;
809 *Clec7a*, C-Type Lectin Domain Containing 7A; *Cd74*, CD74 Molecule; *H2-Ab1*, Major
810 Histocompatibility Complex, Class II; *Stat1*, Signal Transducer And Activator Of Transcription 1; *Irf1*,
811 Interferon Regulatory Factor 1; *H2-K1*, Major Histocompatibility Complex, Class I, A; *H2-T23*, Major
812 Histocompatibility Complex, Class I, E; *H2-Aa*, Major Histocompatibility Complex, Class II; WT,

813 wild-type; KO, knock-out; TAM I, tumour-associated microglia; TAM II, tumour-associated
814 macrophage.

REFERENCES

1. Lathia, J.D., et al., *Deadly teamwork: neural cancer stem cells and the tumor microenvironment.* Cell Stem Cell, 2011. **8**(5): p. 482-5.
2. Venkatesan, S. and C. Swanton, *Tumor Evolutionary Principles: How Intratumor Heterogeneity Influences Cancer Treatment and Outcome.* Am Soc Clin Oncol Educ Book, 2016. **35**: p. e141-9.
3. Quail, D.F. and J.A. Joyce, *The Microenvironmental Landscape of Brain Tumors.* Cancer Cell, 2017. **31**(3): p. 326-341.
4. Ginhoux, F., et al., *Fate mapping analysis reveals that adult microglia derive from primitive macrophages.* Science, 2010. **330**(6005): p. 841-5.
5. Schulz, C., et al., *A lineage of myeloid cells independent of Myb and hematopoietic stem cells.* Science, 2012. **336**(6077): p. 86-90.
6. Glass, R. and M. Synowitz, *CNS macrophages and peripheral myeloid cells in brain tumours.* Acta Neuropathol, 2014. **128**(3): p. 347-62.
7. Hambardzumyan, D., D.H. Gutmann, and H. Kettenmann, *The role of microglia and macrophages in glioma maintenance and progression.* Nat Neurosci, 2016. **19**(1): p. 20-7.
8. Bowman, R.L., et al., *Macrophage Ontogeny Underlies Differences in Tumor-Specific Education in Brain Malignancies.* Cell Rep, 2016. **17**(9): p. 2445-2459.
9. Muller, S., et al., *Single-cell profiling of human gliomas reveals macrophage ontogeny as a basis for regional differences in macrophage activation in the tumor microenvironment.* Genome Biol, 2017. **18**(1): p. 234.
10. Friebel, E., et al., *Single-Cell Mapping of Human Brain Cancer Reveals Tumor-Specific Instruction of Tissue-Invading Leukocytes.* Cell, 2020. **181**(7): p. 1626-1642 e20.
11. Szulzewsky, F., et al., *Glioma-associated microglia/macrophages display an expression profile different from M1 and M2 polarization and highly express Gpnmb and Spp1.* PLoS One, 2015. **10**(2): p. e0116644.
12. Zeiner, P.S., et al., *Distribution and prognostic impact of microglia/macrophage subpopulations in gliomas.* Brain Pathol, 2018.
13. Gabrusiewicz, K., et al., *Glioblastoma-infiltrated innate immune cells resemble M0 macrophage phenotype.* JCI Insight, 2016. **1**(2).
14. Macosko, E.Z., et al., *Highly Parallel Genome-wide Expression Profiling of Individual Cells Using Nanoliter Droplets.* Cell, 2015. **161**(5): p. 1202-1214.
15. Shalek, A.K., et al., *Single-cell transcriptomics reveals bimodality in expression and splicing in immune cells.* Nature, 2013. **498**(7453): p. 236-40.
16. Tang, F., et al., *mRNA-Seq whole-transcriptome analysis of a single cell.* Nat Methods, 2009. **6**(5): p. 377-82.
17. Jordao, M.J.C., et al., *Single-cell profiling identifies myeloid cell subsets with distinct fates during neuroinflammation.* Science, 2019. **363**(6425).
18. Darmanis, S., et al., *Single-Cell RNA-Seq Analysis of Infiltrating Neoplastic Cells at the Migrating Front of Human Glioblastoma.* Cell Rep, 2017. **21**(5): p. 1399-1410.
19. Michelucci, A., et al., *Immune-responsive gene 1 protein links metabolism to immunity by catalyzing itaconic acid production.* Proc Natl Acad Sci U S A, 2013. **110**(19): p. 7820-5.
20. Mills, E.L., et al., *Itaconate is an anti-inflammatory metabolite that activates Nrf2 via alkylation of KEAP1.* Nature, 2018. **556**(7699): p. 113-117.
21. Hooftman, A. and L.A.J. O'Neill, *The Immunomodulatory Potential of the Metabolite Itaconate.* Trends Immunol, 2019. **40**(8): p. 687-698.
22. Dominguez-Andres, J., et al., *The Itaconate Pathway Is a Central Regulatory Node Linking Innate Immune Tolerance and Trained Immunity.* Cell Metab, 2019. **29**(1): p. 211-220 e5.
23. Weiss, J.M., et al., *Itaconic acid mediates crosstalk between macrophage metabolism and peritoneal tumors.* J Clin Invest, 2018. **128**(9): p. 3794-3805.

866 24. Pires-Afonso, Y., S.P. Niclou, and A. Michelucci, *Revealing and Harnessing Tumour-Associated*
867 *Microglia/Macrophage Heterogeneity in Glioblastoma.* Int J Mol Sci, 2020. **21**(3).
868 25. Qiu, X., et al., *Reversed graph embedding resolves complex single-cell trajectories.* Nat
869 Methods, 2017. **14**(10): p. 979-982.
870 26. Trapnell, C., et al., *The dynamics and regulators of cell fate decisions are revealed by*
871 *pseudotemporal ordering of single cells.* Nat Biotechnol, 2014. **32**(4): p. 381-386.
872 27. Buttini, M., et al., *Expression of human apolipoprotein E3 or E4 in the brains of Apoe-/- mice:*
873 *isoform-specific effects on neurodegeneration.* J Neurosci, 1999. **19**(12): p. 4867-80.
874 28. Oh, T., et al., *Immunocompetent murine models for the study of glioblastoma immunotherapy.*
875 J Transl Med, 2014. **12**: p. 107.
876 29. Aslan, K., et al., *Heterogeneity of response to immune checkpoint blockade in hypermutated*
877 *experimental gliomas.* Nat Commun, 2020. **11**(1): p. 931.
878 30. Fecci, P.E., et al., *Systemic CTLA-4 blockade ameliorates glioma-induced changes to the CD4+*
879 *T cell compartment without affecting regulatory T-cell function.* Clin Cancer Res, 2007. **13**(7):
880 p. 2158-67.
881 31. Qian, J., et al., *TLR2 Promotes Glioma Immune Evasion by Downregulating MHC Class II*
882 *Molecules in Microglia.* Cancer Immunol Res, 2018. **6**(10): p. 1220-1233.
883 32. Khalsa, J.K., et al., *Immune phenotyping of diverse syngeneic murine brain tumors identifies*
884 *immunologically distinct types.* Nat Commun, 2020. **11**(1): p. 3912.
885 33. Tasic, B., et al., *Adult mouse cortical cell taxonomy revealed by single cell transcriptomics.* Nat
886 Neurosci, 2016. **19**(2): p. 335-46.
887 34. Cahoy, J.D., et al., *A transcriptome database for astrocytes, neurons, and oligodendrocytes: a*
888 *new resource for understanding brain development and function.* J Neurosci, 2008. **28**(1): p.
889 264-78.
890 35. Tabula Muris, C., et al., *Single-cell transcriptomics of 20 mouse organs creates a Tabula Muris.*
891 Nature, 2018. **562**(7727): p. 367-372.
892 36. Sankowski, R., et al., *Mapping microglia states in the human brain through the integration of*
893 *high-dimensional techniques.* Nat Neurosci, 2019. **22**(12): p. 2098-2110.
894 37. Venteicher, A.S., et al., *Decoupling genetics, lineages, and microenvironment in IDH-mutant*
895 *gliomas by single-cell RNA-seq.* Science, 2017. **355**(6332).
896 38. Patel, A.P., et al., *Single-cell RNA-seq highlights intratumoral heterogeneity in primary*
897 *glioblastoma.* Science, 2014. **344**(6190): p. 1396-401.
898 39. Szatmari, T., et al., *Detailed characterization of the mouse glioma 261 tumor model for*
899 *experimental glioblastoma therapy.* Cancer Sci, 2006. **97**(6): p. 546-53.
900 40. Schaaf, M.B., A.D. Garg, and P. Agostinis, *Defining the role of the tumor vasculature in*
901 *antitumor immunity and immunotherapy.* Cell Death Dis, 2018. **9**(2): p. 115.
902 41. Liu, S., et al., *Molecular and clinical characterization of CD163 expression via large-scale*
903 *analysis in glioma.* Oncoimmunology, 2019. **8**(7): p. 1601478.
904 42. Ochocka, N., et al., *Single-cell RNA sequencing reveals functional heterogeneity of glioma-*
905 *associated brain macrophages.* Nat Commun, 2021. **12**(1): p. 1151.
906 43. Pombo Antunes, A.R., et al., *Single-cell profiling of myeloid cells in glioblastoma across species*
907 *and disease stage reveals macrophage competition and specialization.* Nat Neurosci, 2021.
908 **24**(4): p. 595-610.
909 44. Sousa, C., et al., *Single-cell transcriptomics reveals distinct inflammation-induced microglia*
910 *signatures.* EMBO Rep, 2018. **19**(11).
911 45. Pinton, L., et al., *The immune suppressive microenvironment of human gliomas depends on*
912 *the accumulation of bone marrow-derived macrophages in the center of the lesion.* J
913 Immunother Cancer, 2019. **7**(1): p. 58.
914 46. Alban, T.J., et al., *Global immune fingerprinting in glioblastoma patient peripheral blood*
915 *reveals immune-suppression signatures associated with prognosis.* JCI Insight, 2018. **3**(21).

47. Zhao, E., et al., *Cancer mediates effector T cell dysfunction by targeting microRNAs and EZH2 via glycolysis restriction.* Nat Immunol, 2016. **17**(1): p. 95-103.
48. Woroniecka, K.I., et al., *T-cell Dysfunction in Glioblastoma: Applying a New Framework.* Clin Cancer Res, 2018. **24**(16): p. 3792-3802.
49. Puchalski, R.B., et al., *An anatomic transcriptional atlas of human glioblastoma.* Science, 2018. **360**(6389): p. 660-663.
50. Chen, Z., J.L. Ross, and D. Hambardzumyan, *Intravital 2-photon imaging reveals distinct morphology and infiltrative properties of glioblastoma-associated macrophages.* Proc Natl Acad Sci U S A, 2019. **116**(28): p. 14254-14259.
51. Cordes, T., A. Michelucci, and K. Hiller, *Itaconic Acid: The Surprising Role of an Industrial Compound as a Mammalian Antimicrobial Metabolite.* Annu Rev Nutr, 2015. **35**: p. 451-73.
52. Lampropoulou, V., et al., *Itaconate Links Inhibition of Succinate Dehydrogenase with Macrophage Metabolic Remodeling and Regulation of Inflammation.* Cell Metab, 2016. **24**(1): p. 158-66.
53. Muri, J., et al., *Electrophilic Nrf2 activators and itaconate inhibit inflammation at low dose and promote IL-1beta production and inflammatory apoptosis at high dose.* Redox Biol, 2020. **36**: p. 101647.
54. Klemm, F., et al., *Interrogation of the Microenvironmental Landscape in Brain Tumors Reveals Disease-Specific Alterations of Immune Cells.* Cell, 2020. **181**(7): p. 1643-1660 e17.
55. Chen, Z., et al., *Cellular and Molecular Identity of Tumor-Associated Macrophages in Glioblastoma.* Cancer Res, 2017. **77**(9): p. 2266-2278.
56. Zhang, J., et al., *A dialog between glioma and microglia that promotes tumor invasiveness through the CCL2/CCR2/interleukin-6 axis.* Carcinogenesis, 2012. **33**(2): p. 312-9.
57. Calandra, T. and T. Roger, *Macrophage migration inhibitory factor: a regulator of innate immunity.* Nat Rev Immunol, 2003. **3**(10): p. 791-800.
58. Guda, M.R., et al., *Pleiotropic role of macrophage migration inhibitory factor in cancer.* Am J Cancer Res, 2019. **9**(12): p. 2760-2773.
59. Taniguchi, T., et al., *IRF family of transcription factors as regulators of host defense.* Annu Rev Immunol, 2001. **19**: p. 623-55.
60. Borden, E.C., et al., *Interferons at age 50: past, current and future impact on biomedicine.* Nat Rev Drug Discov, 2007. **6**(12): p. 975-90.
61. Ogasawara, K., et al., *Requirement for IRF-1 in the microenvironment supporting development of natural killer cells.* Nature, 1998. **391**(6668): p. 700-3.
62. Lohoff, M., et al., *Interferon regulatory factor-1 is required for a T helper 1 immune response in vivo.* Immunity, 1997. **6**(6): p. 681-9.
63. Alsamman, K. and O.S. El-Masry, *Interferon regulatory factor 1 inactivation in human cancer.* Biosci Rep, 2018. **38**(3).
64. Thorsson, V., et al., *The Immune Landscape of Cancer.* Immunity, 2018. **48**(4): p. 812-830 e14.
65. Ashton-Rickardt, P.G., *An emerging role for Serine Protease Inhibitors in T lymphocyte immunity and beyond.* Immunol Lett, 2013. **152**(1): p. 65-76.
66. O'Neill, L.A.J. and M.N. Artyomov, *Itaconate: the poster child of metabolic reprogramming in macrophage function.* Nat Rev Immunol, 2019. **19**(5): p. 273-281.
67. Reardon, D.A., et al., *Effect of Nivolumab vs Bevacizumab in Patients With Recurrent Glioblastoma: The CheckMate 143 Phase 3 Randomized Clinical Trial.* JAMA Oncol, 2020. **6**(7): p. 1003-1010.

965 **SUPPLEMENTARY INFORMATION**

966

967 **Supplementary Fig. 1. Gene expression of distinct cell-types identified by scRNA-seq in the**
968 **GL261 syngeneic murine model and naïve mice.**

969

970 **Supplementary Fig. 2. Expression of tumour cell oncogenes in the GL261 GBM murine model.**

971

972 **Supplementary Fig. 3. Gene expression of distinct cell-types present in naïve and tumour-bearing**
973 **mice. (A)**

974

975 **Supplementary Fig. 4. Microglia- versus macrophage-like features in GBM. (A)**

976

977 **Supplementary Fig. 5. Differential microglia and monocytic-derived macrophage transcriptional**
978 **adaptation along GBM progression.**

979

980 **Supplementary Fig. 6. TAM signatures under *Acod1* deficiency.**

981

982 **Supplementary Fig. 7. TAM II cellular state diversity under Acod1 deficiency.**

983

984 **Supplementary Table 1. Differentially expressed genes in tumour-associated clusters (astrocytes,**
985 **endothelial, oligodendrocytes, myeloid) versus correspondent naïve cells (pvalue<0.01 and logFC**
986 **> 0.5).**

987

988 **Supplementary Table 2. Top 40 differentially expressed genes among the three myeloid clusters**
989 **(Naïve, TAM I and TAM II) (pvalue<0.01).**

990

991 **Supplementary Table 3. Upregulated differentially expressed genes at early and late stages for**
992 **TAM I and TAM II versus naïve cells (pvalue < 0.001 and logFC> 0.5).**
993
994 **Supplementary Table 4. Upregulated differentially expressed genes at late stage for TAM I KO**
995 **and TAM II KO versus correspondent WT cells (pvalue < 0,001 and logFC> 0,5).**

Figure 1

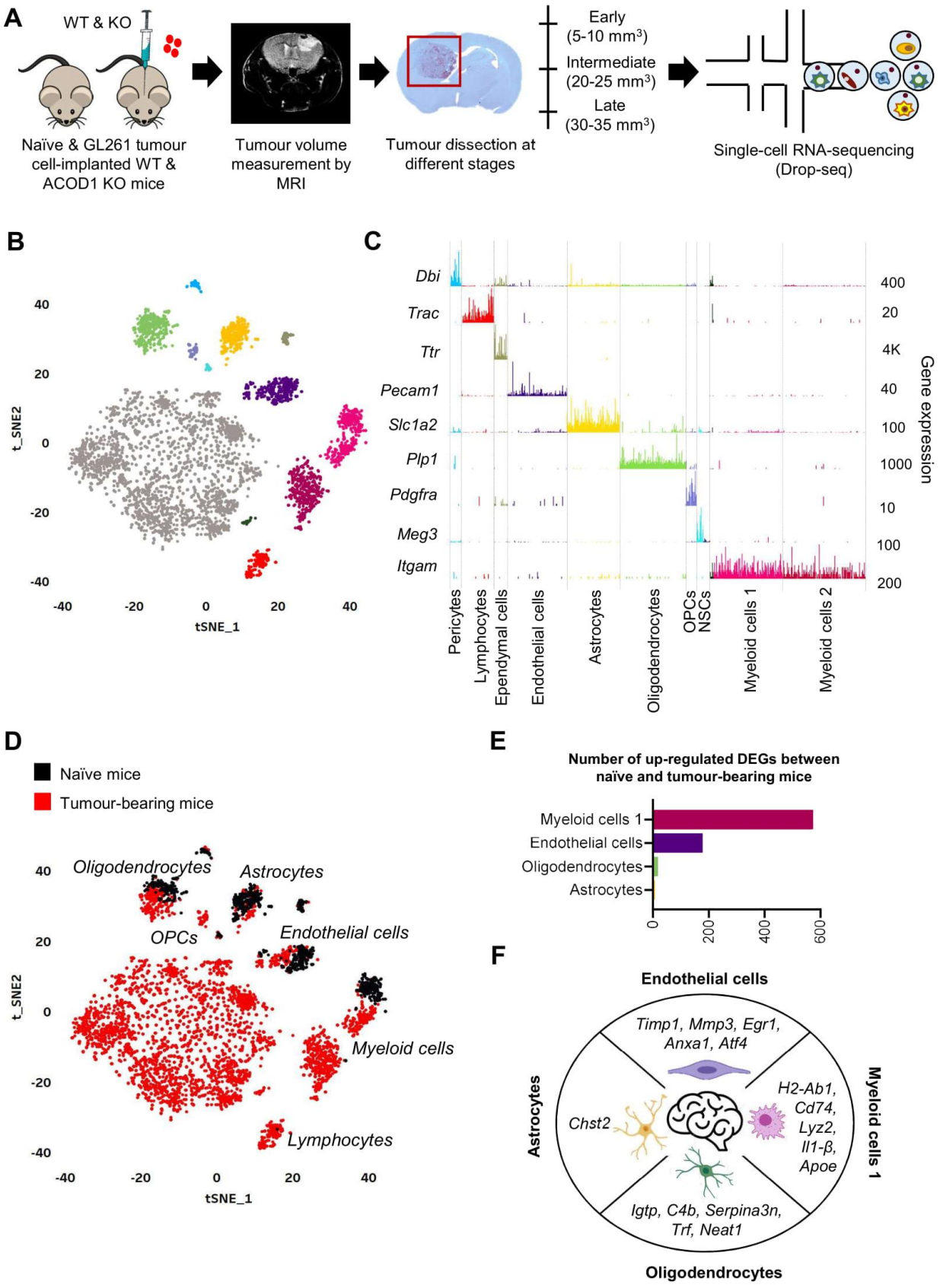
A
WT & KO
Naïve & GL261 tumour cell-implanted WT & ACOD1 KO mice
Tumour volume measurement by MRI
Tumour dissection at different stages
Early (5-10 mm³)
Intermediate (20-25 mm³)
Late (30-35 mm³)
Single-cell RNA-sequencing (Drop-seq)
B
t_SNE2
tSNE_1
C
Dbi
Trac
Ttr
Pecam1
Slc1a2
Plp1
Pdgfra
Meg3
Itgam
Gene expression
Pericytes
Lymphocytes
Ependymal cells
Endothelial cells
Astrocytes
Oligodendrocytes
OPCs NSCs
Myeloid cells 1
Myeloid cells 2
D
Naïve mice
Tumour-bearing mice
Oligodendrocytes
Astrocytes
OPCs
Endothelial cells
Myeloid cells
Lymphocytes
t_SNE2
tSNE_1
E
Number of up-regulated DEGs between naïve and tumour-bearing mice
Myeloid cells 1
Endothelial cells
Oligodendrocytes
Astrocytes
F
Endothelial cells
Timp1, Mmp3, Egr1, Anxa1, Atf4
Astrocytes
Chst2
Myeloid cells 1
H2-Ab1, Cd74, Lyz2, Il1-β, Apoe
Igtp, C4b, Serpina3n, Trf, Neat1
Oligodendrocytes

Figure 2

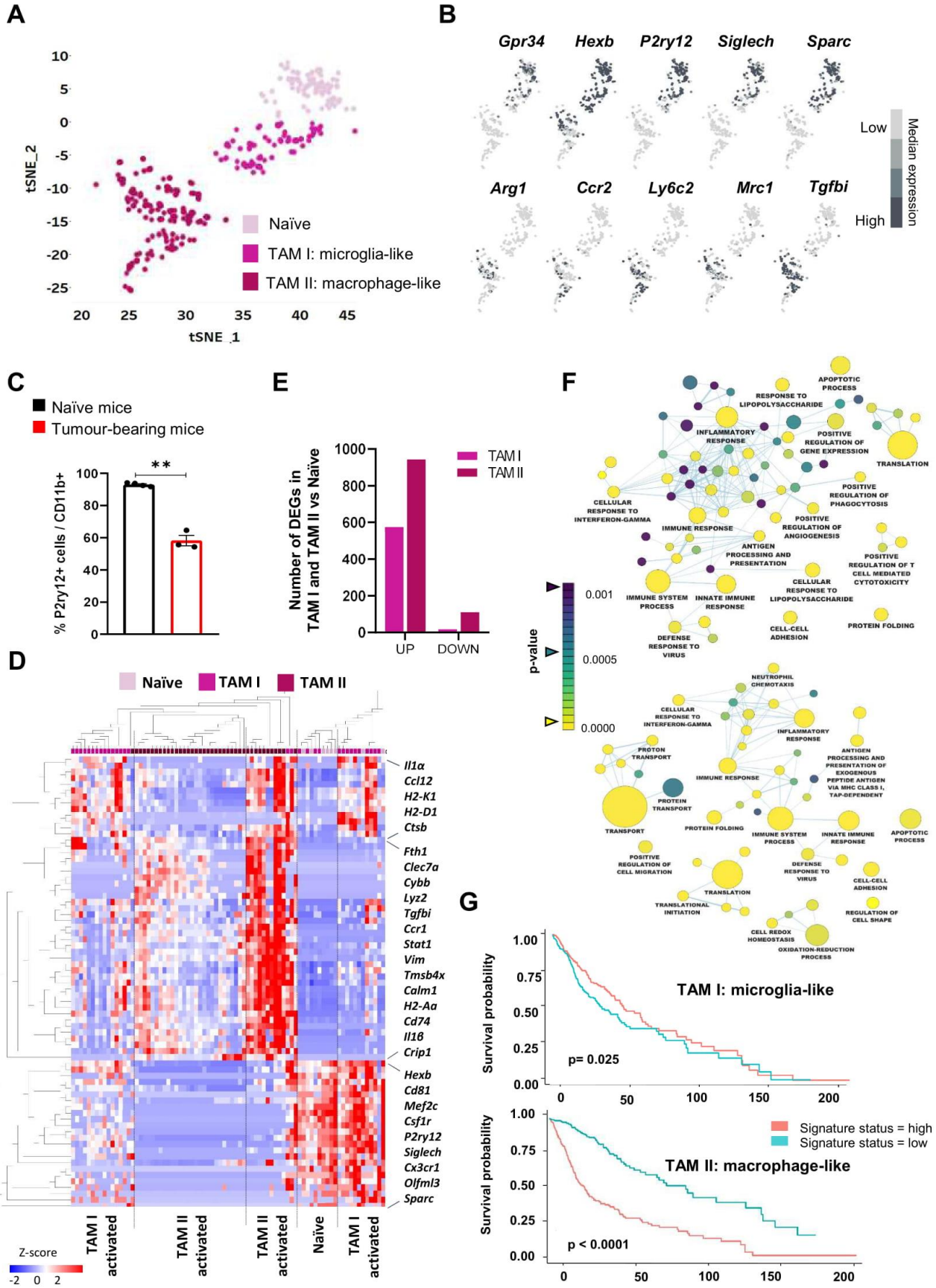
A
tSNE_2
tSNE_1
Naïve
TAM I: microglia-like
TAM II: macrophage-like
B
Gpr34
Hexb
P2ry12
Siglech
Sparc
Arg1
Ccr2
Ly6c2
Mrc1
Tgfbi
Low
High
Median expression
C
Naïve mice
Tumour-bearing mice
% P2ry12+ cells / CD11b+
**
E
Number of DEGs in TAM I and TAM II vs Naïve
TAM I
TAM II
UP
DOWN
F
p-value
0.001
0.0005
0.0000
INFLAMMATORY RESPONSE
IMMUNE RESPONSE
TRANSLATION
IMMUNE SYSTEM PROCESS
INNATE IMMUNE RESPONSE
PROTEIN FOLDING
TRANSPORT
D
Naïve
TAM I
TAM II
Il1α
Ccl12
H2-K1
H2-D1
Ctsb
Fth1
Clec7a
Cybb
Lyz2
Tgfbi
Ccr1
Stat1
Vim
Tmsb4x
Calm1
H2-Aa
Cd74
Il1β
Crip1
Hexb
Cd81
Mef2c
Csf1r
P2ry12
Siglech
Cx3cr1
Olfml3
Sparc
TAM I activated
TAM II activated
TAM II activated
Naïve
TAM I activated
Z-score
G
Survival probability
TAM I: microglia-like
p= 0.025
Signature status = high
Signature status = low
TAM II: macrophage-like
p < 0.0001

Figure 3

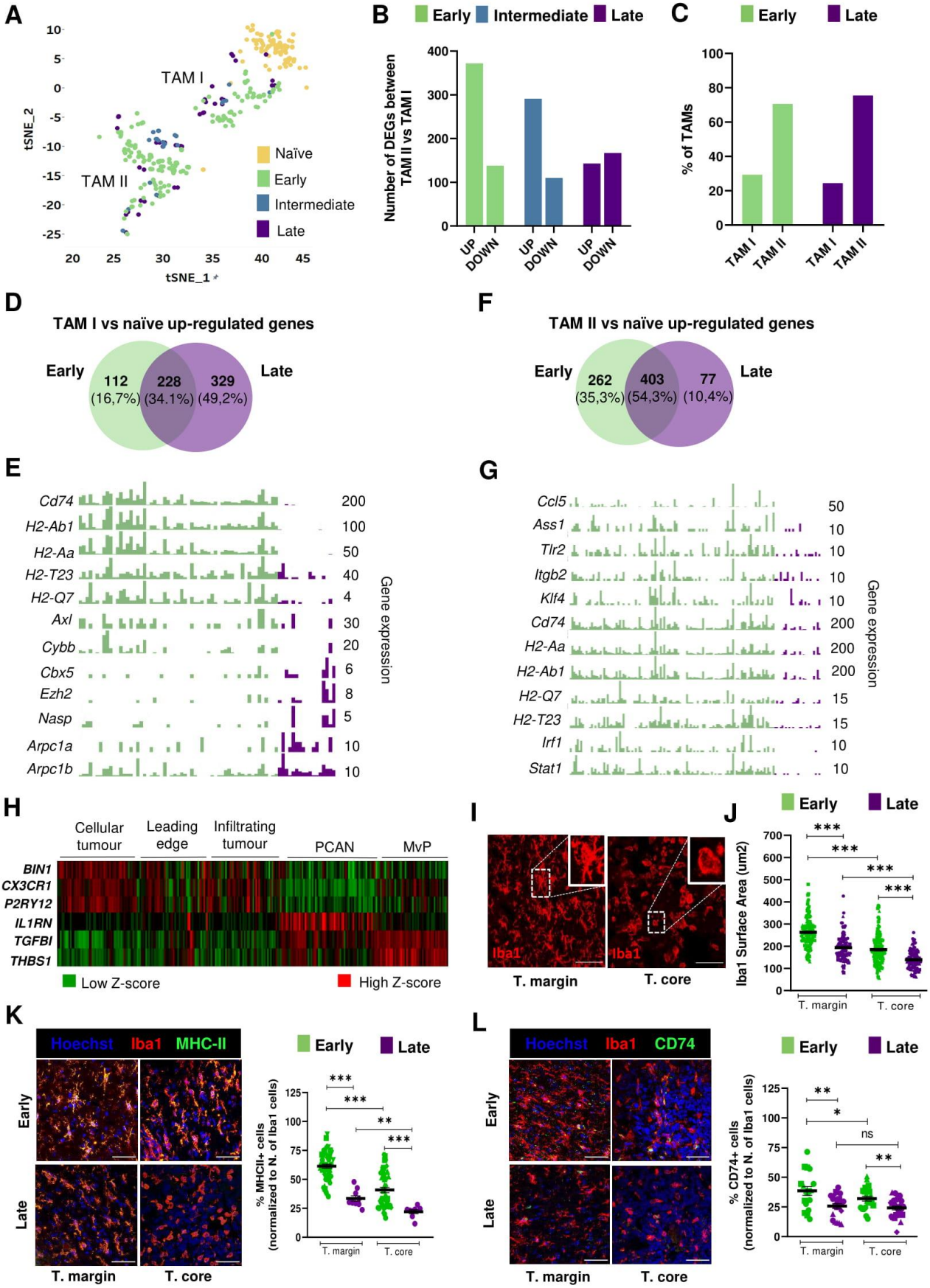
A
TAM I
TAM II
Naïve
Early
Intermediate
Late
tSNE_1
tSNE_2
B
Early Intermediate Late
Number of DEGs between TAM II vs TAM I
UP DOWN
C
Early Late
% of TAMs
TAM I TAM II
D
TAM I vs naïve up-regulated genes
Early 112 (16,7%) 228 (34.1%) 329 (49,2%) Late
F
TAM II vs naïve up-regulated genes
Early 262 (35,3%) 403 (54,3%) 77 (10,4%) Late
E
Cd74
H2-Ab1
H2-Aa
H2-T23
H2-Q7
Axl
Cybb
Cbx5
Ezh2
Nasp
Arpc1a
Arpc1b
Gene expression
G
Ccl5
Ass1
Tlr2
Itgb2
Klf4
Cd74
H2-Aa
H2-Ab1
H2-Q7
H2-T23
Irf1
Stat1
Gene expression
H
Cellular tumour
Leading edge
Infiltrating tumour
PCAN
MvP
BIN1
CX3CR1
P2RY12
IL1RN
TGFBI
THBS1
Low Z-score
High Z-score
I
Iba1
T. margin
T. core
J
Early Late
Iba1 Surface Area (um2)
T. margin
T. core
K
Hoechst Iba1 MHC-II
Early
Late
T. margin
T. core
% MHCII+ cells (normalized to N. of Iba1 cells)
L
Hoechst Iba1 CD74
Early
Late
T. margin
T. core
% CD74+ cells (normalized to N. of Iba1 cells)

Figure 4

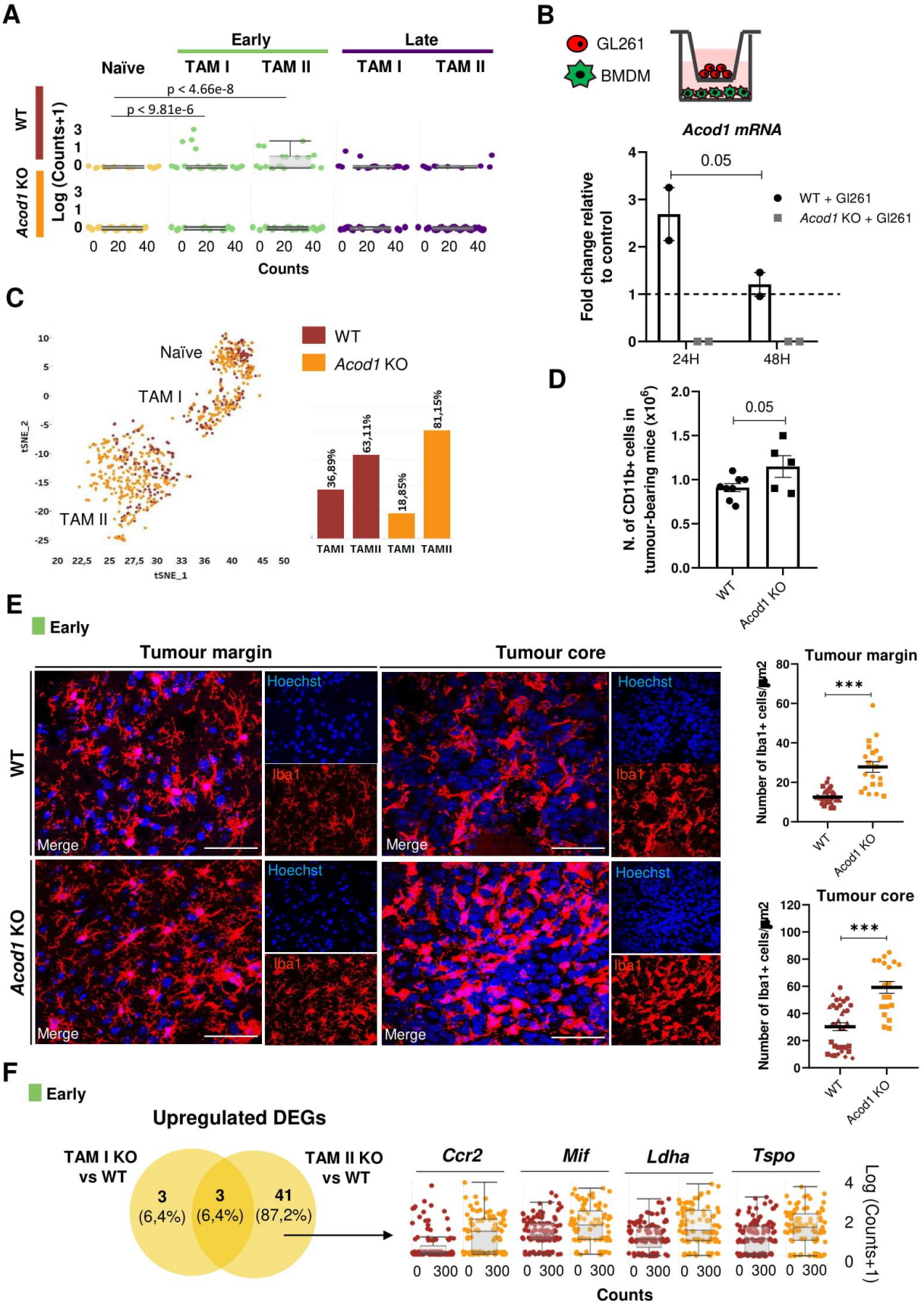
A
Early
Late
Naïve
TAM I
TAM II
TAM I
TAM II
p < 4.66e-8
p < 9.81e-6
WT
Acod1 KO
Log (Counts+1)
Counts
B
GL261
BMDM
Acod1 mRNA
0.05
Fold change relative to control
WT + Gl261
Acod1 KO + Gl261
24H
48H
C
Naïve
TAM I
TAM II
tSNE_1
tSNE_2
WT
Acod1 KO
36,89%
63,11%
18,85%
81,15%
TAMI
TAMII
TAMI
TAMII
D
0.05
N. of CD11b+ cells in tumour-bearing mice (x10^6)
WT
Acod1 KO
E
Early
Tumour margin
Tumour core
WT
Acod1 KO
Hoechst
Iba1
Merge
Tumour margin
Tumour core
Number of Iba1+ cells/µm2
***
WT
Acod1 KO
F
Early
Upregulated DEGs
TAM I KO vs WT
TAM II KO vs WT
3 (6,4%)
3 (6,4%)
41 (87,2%)
Ccr2
Mif
Ldha
Tspo
Log (Counts+1)
Counts

Figure 5

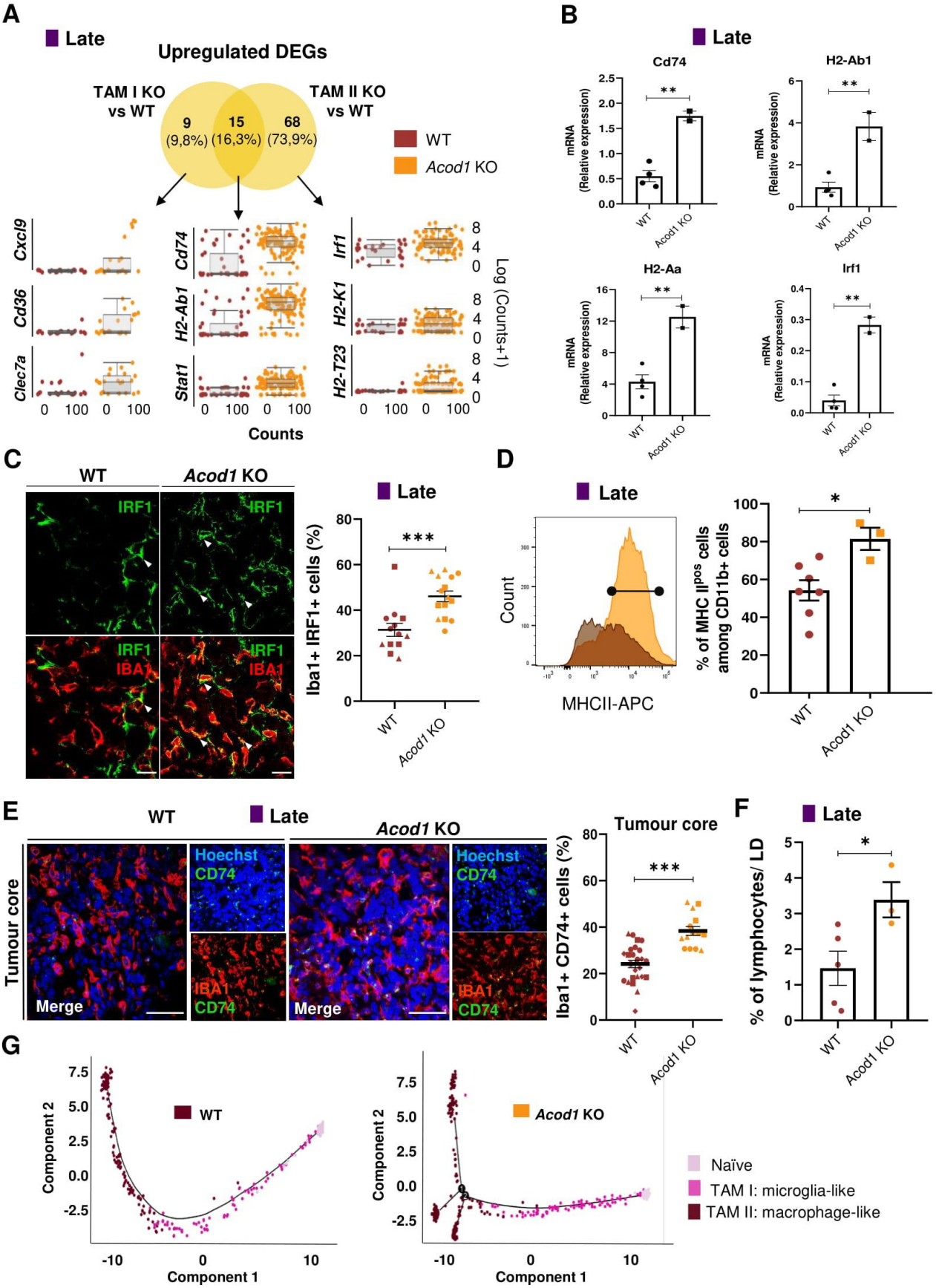
A
Late
Upregulated DEGs
TAM I KO vs WT
TAM II KO vs WT
9 (9,8%)
15 (16,3%)
68 (73,9%)
WT
Acod1 KO
Cxcl9
Cd36
Clec7a
Cd74
H2-Ab1
Stat1
Irf1
H2-K1
H2-T23
Counts
Log (Counts+1)
B
Late
Cd74
H2-Ab1
H2-Aa
Irf1
mRNA (Relative expression)
WT
Acod1 KO
C
WT
Acod1 KO
IRF1
IBA1
Late
Iba1+ IRF1+ cells (%)
D
Late
Count
MHCII-APC
% of MHC IIpos cells among CD11b+ cells
E
WT
Late
Acod1 KO
Tumour core
Hoechst
CD74
IBA1
Merge
Iba1+ CD74+ cells (%)
F
Late
% of lymphocytes/ LD
G
WT
Acod1 KO
Component 1
Component 2
Naïve
TAM I: microglia-like
TAM II: macrophage-like

Supplementary Figure 1

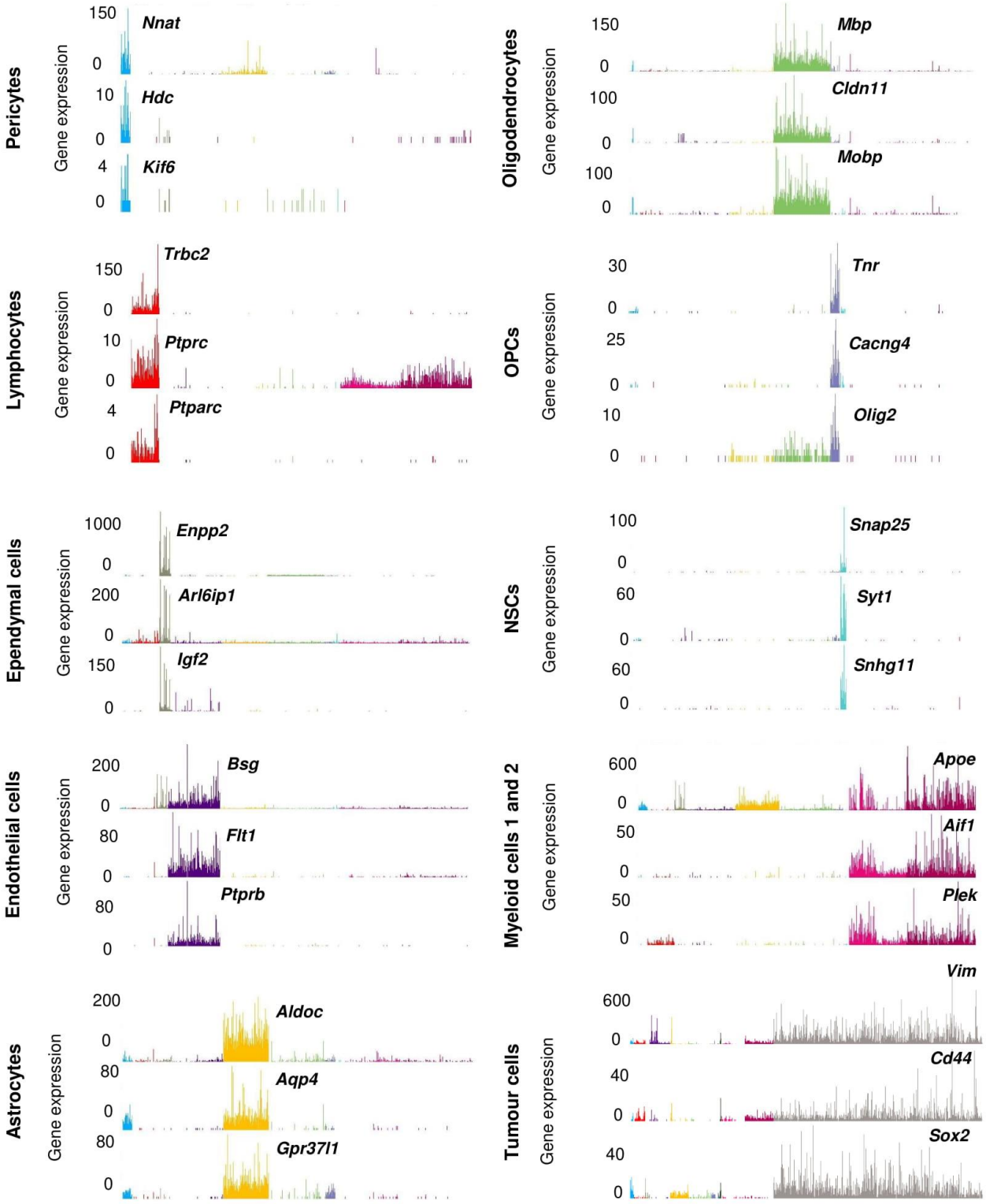

Supplementary Figure 1. Gene expression of distinct cell-types identified by scRNA-seq in the GL261 syngeneic murine model and naïve mice, related to Fig. 1.

Bar plots of additional cell type-specific markers. Pericytes (*Nnat, Hdc, Kif6*), lymphocytes (*Trbc2, Ptprcap, Ptprc*), ependymal (*Enpp2, Arl6ip1, Igf2*), endothelial (*Bsg, Flt1, Ptprb*), astrocytes (*Aldoc, Aqp4, Gpr37l1*), oligodendrocytes (*Mbp, Cldn11, Mobp*), OPCs (*Tnr, Cacng4, Olig2*), NSCs (*Snap25, Syt1, Snhg11*), myeloid cells 1 and 2 (*Apoe, Aif1, Plek*). Abbreviations: OPCs, Oligodendrocyte precursor cells; NSCs, Neural stem cells.

Supplementary Figure 2

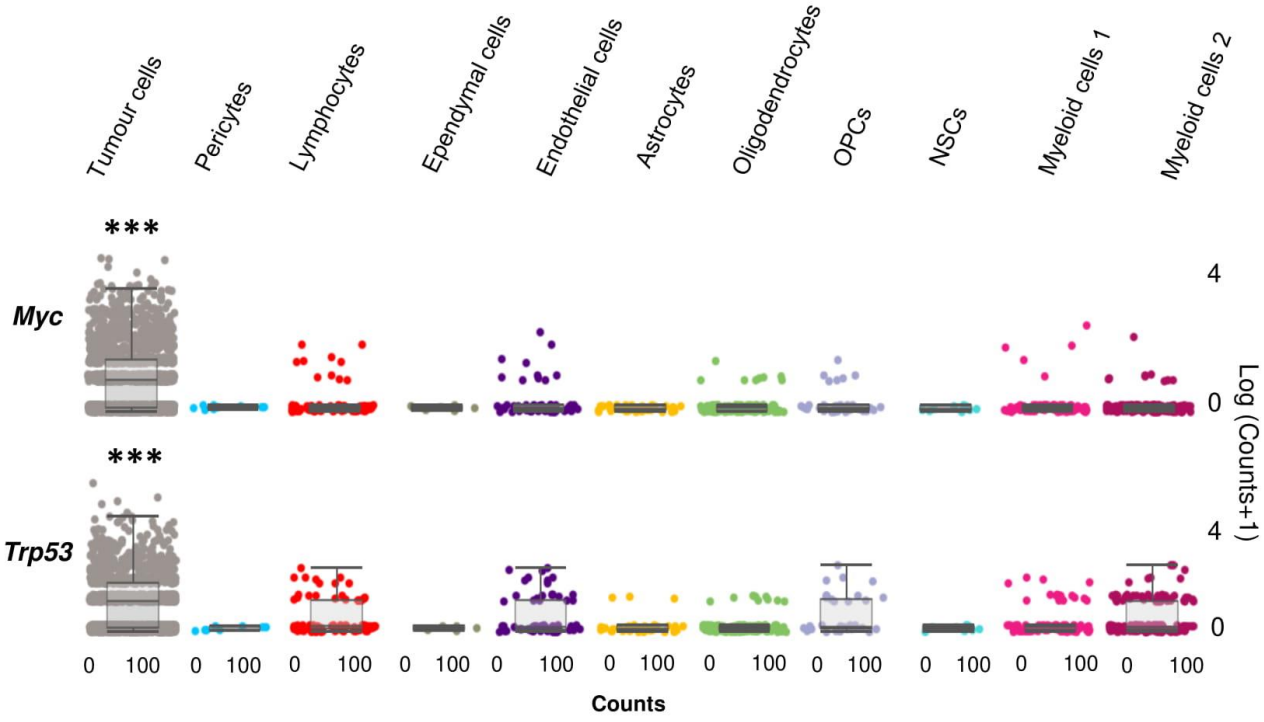

Supplementary Figure 2. Expression of tumour cell oncogenes in the GL261 GBM murine model, related to figure 1.

Myc and *Trp53* gene expression levels across the main 10 stromal cell-types identified by scRNA-seq. Data are represented as mean ± SEM, *** $p < 0.001$.

Supplementary Figure 3

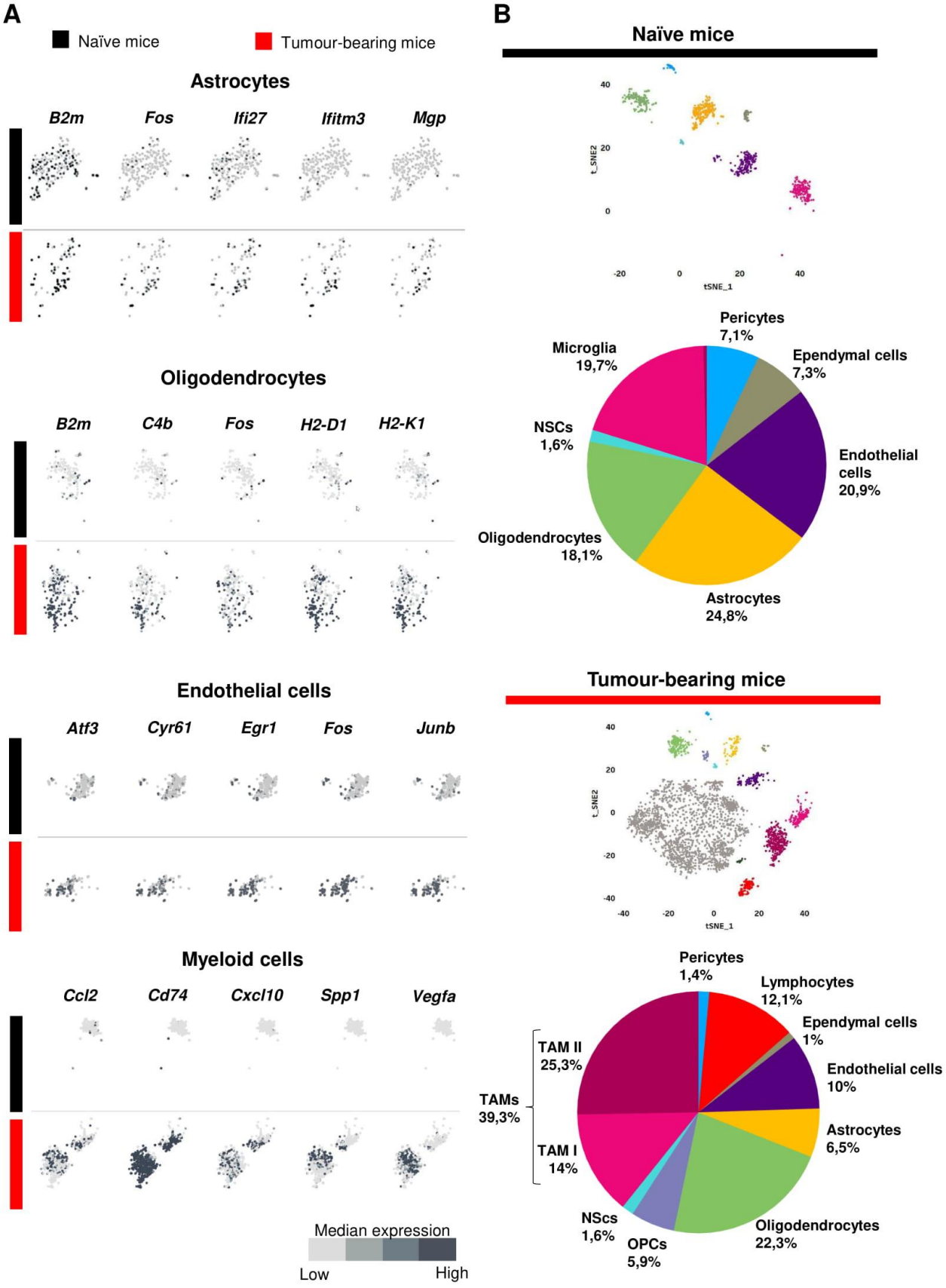

Supplementary Figure 3. Gene expression of distinct cell-types present in naïve and tumour-bearing mice, related to Fig, 1.

(A) tSNE representation of the top up-regulated genes in tumour-associated clusters (astrocytes, oligodendrocytes, endothelial cells, myeloid cells) compared to their naïve counterparts. **(B)** tSNE plot and respective cell-type proportion shown in pie chart of 2'282 isolated cells from naïve samples (upper panels) and 5'659 isolated cells from tumour-bearing samples (lower panels).

Supplementary Figure 4

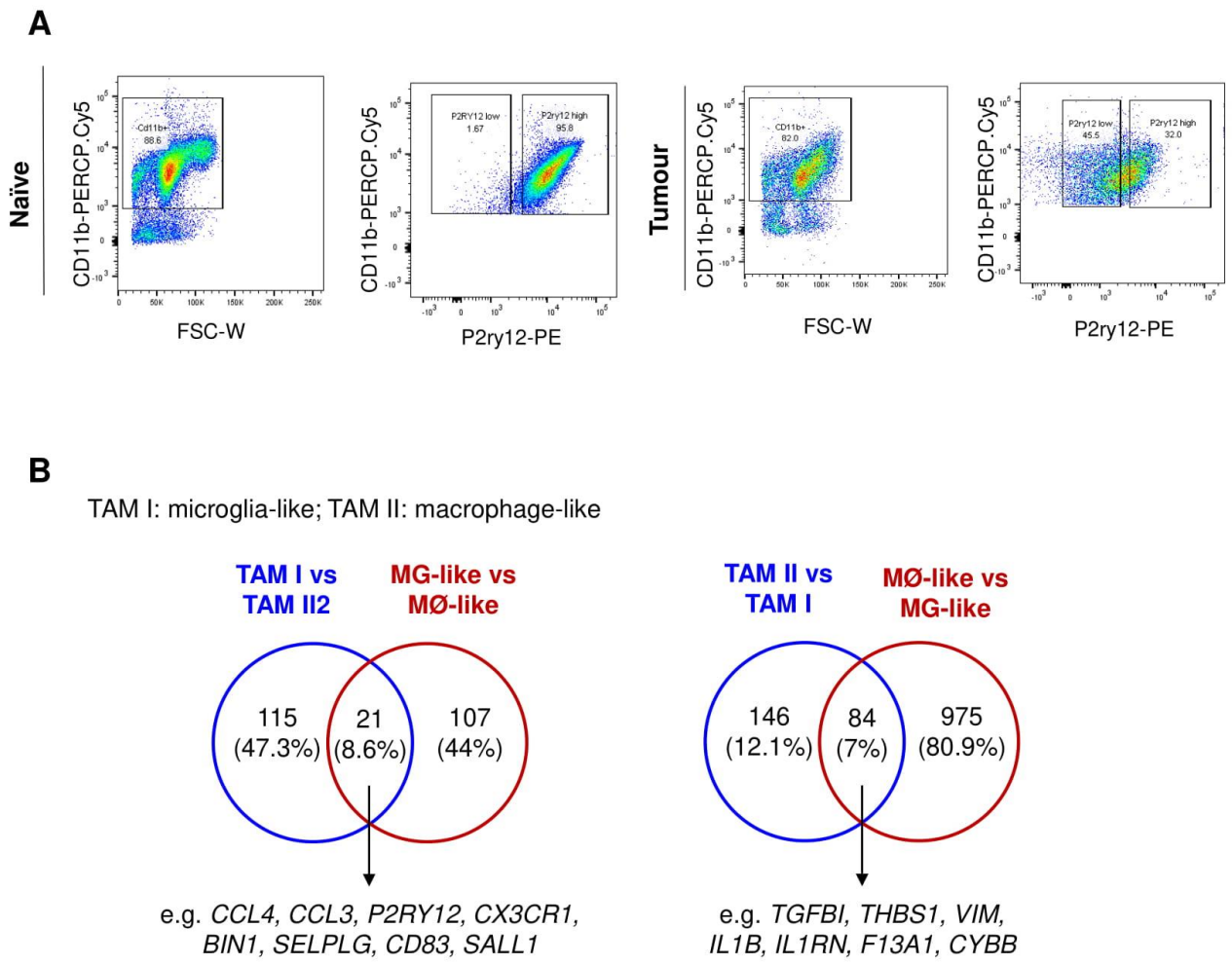

Supplementary Figure 4. Microglia- versus macrophage-like features in GBM, related to Fig. 2.

(A) Gating strategy used to discriminate CD11b+ P2ry12+ and CD11b+ P2ry12-/low cells in naïve and syngeneic GL261 tumour-bearing mice by flow cytometry. **(B)** Comparison of up-regulated genes in microglia-like (TAM I) and macrophage-like (TAM II) cells with putative corresponding cell types described in GBM patients (Muller et al., 2017). Shared and unique genes are represented in Venn diagrams and a selection of genes is annotated.

Supplementary Figure 5

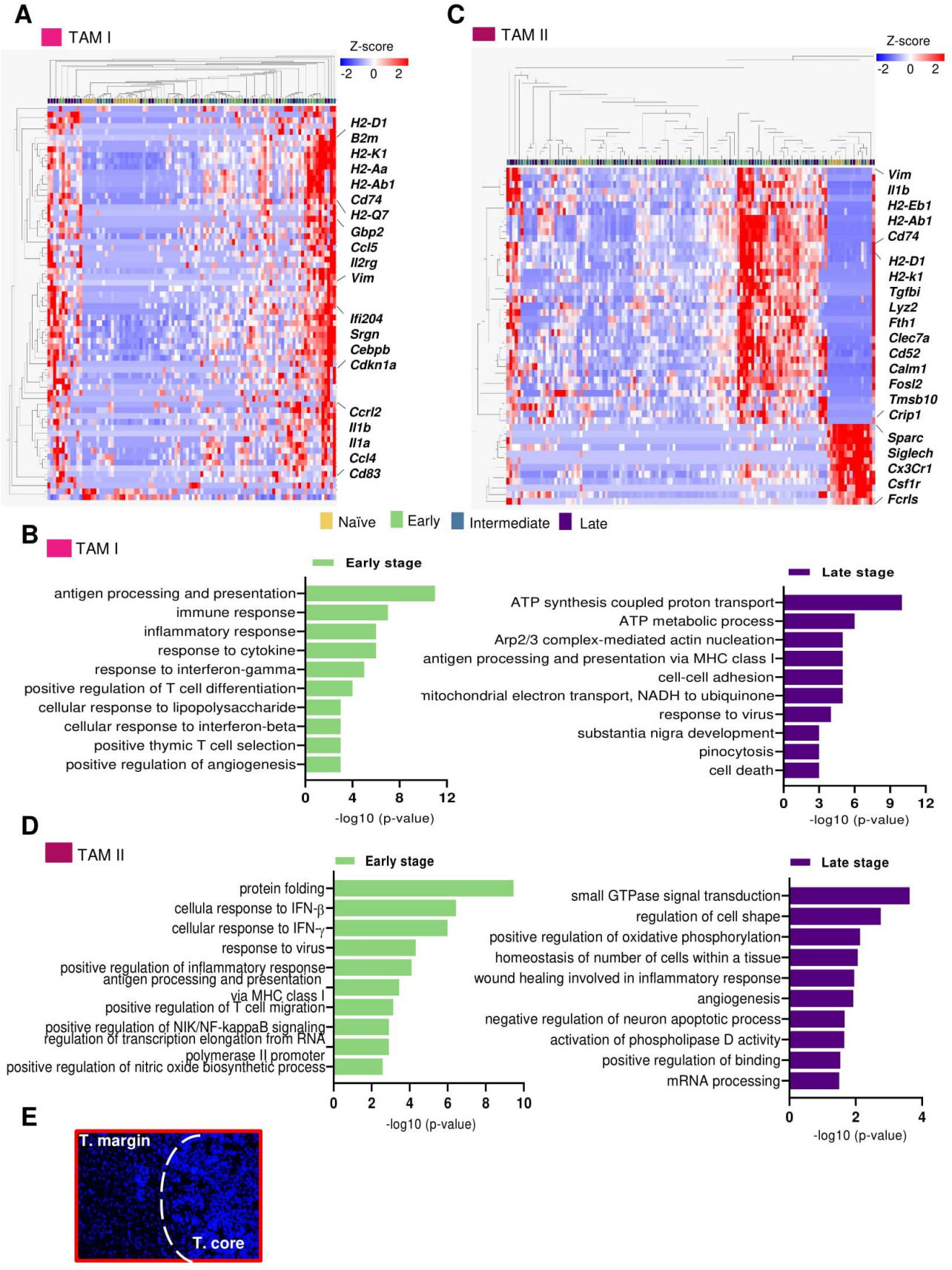

Supplementary Figure 5. Differential microglia and monocytic-derived macrophage transcriptional adaptation along GBM progression, related to Fig. 3.

(A) Two-way hierarchical heat-map clustering analyses of the most differentially expressed genes (based on p-value rank) in TAM I along tumour progression. Red: up-regulation; blue: down-regulation. **(B)** Gene ontology terms of TAM I exclusive up-regulated genes at early (left) and late (right) GBM stages. **(C)** Two-way hierarchical heat-map clustering analyses of the most differentially expressed genes (based on p-value rank) in TAM II along tumour progression. Red: up-regulation; blue: down-regulation. **(D)** Gene ontology terms of TAM II exclusive up-regulated genes at early (left) and late (right) GBM stages. See **S8 Data** for TAM I and TAM II gene list signatures and functional annotations. **(E)** Picture representing Hoechst-stained nuclei used to discriminate tumour margin and core in mouse brain sections. Colour coding in (**B** and **D**) is consistent with **Fig 3A**.

Supplementary Figure 6

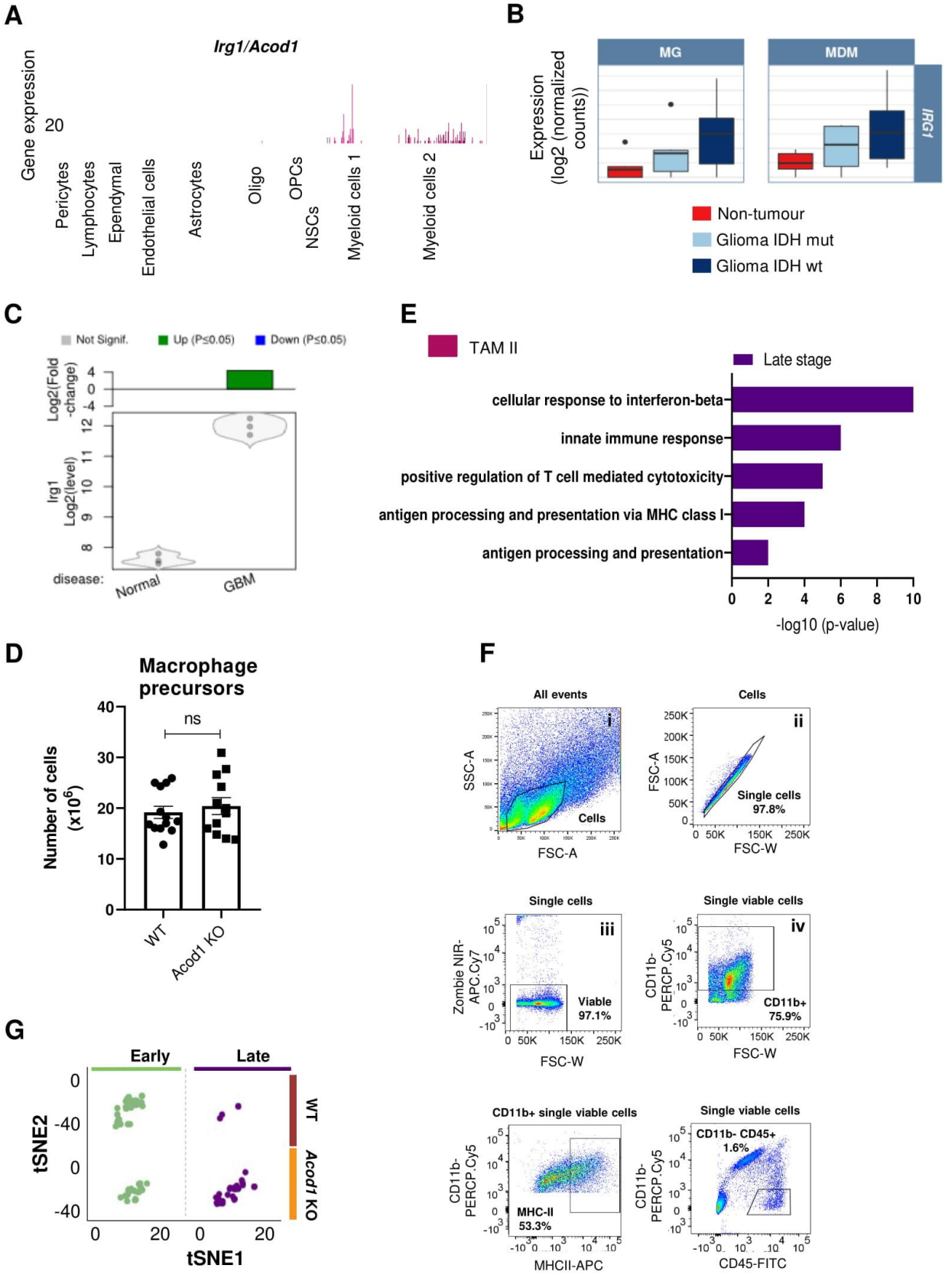

Supplementary Figure 6. TAM signatures under *Acod1* deficiency, related to Fig. 5.

(A) *Irg1/Acod1* expression levels across the main 10 stromal cell-types identified by scRNA-seq. **(B)** *IRG1/ACOD1* expression in both microglia (MG) and macrophages (MDM) in GBM patients from the Brain Tumor Immune Micro Environment dataset (Klemm et al., 2020). **(C)** *Irg1/Acod1* expression in CD11b+ cells isolated from naïve and GL261-implanted mice (E-MTAB-2660 dataset) (Szulzewsky et al., 2015). **(D)** Total number of bone marrow precursor cells flushed from the legs of WT and *Acod1* KO mice. Data are represented as mean ± SEM. n.s., not significant. **(E)** Gene set enrichment analysis of TAM II uniquely up-regulated genes in *Acod1* KO mice versus WT mice at late stages. **(F)** Flow cytometry gating strategy. (i) Cells of interest were gated based on forward (FSC) and side scatter (SSC). (ii) Doublets were excluded based on the forward scatter height (FSC-H) versus forward scatter area (FSC-A). (iii) Zombie NIR-APC.cy7 was used to discriminate living cells. (iv) CD11b-PERCP.cy5 was used to gate the myeloid compartment. Lastly, we gated MHC-II-expressing cells and lymphocytes (CD11b-CD45+). **(G)** tSNE representation of the lymphocytic population detected at early and late stage by scRNA-seq.

Supplementary Figure 7

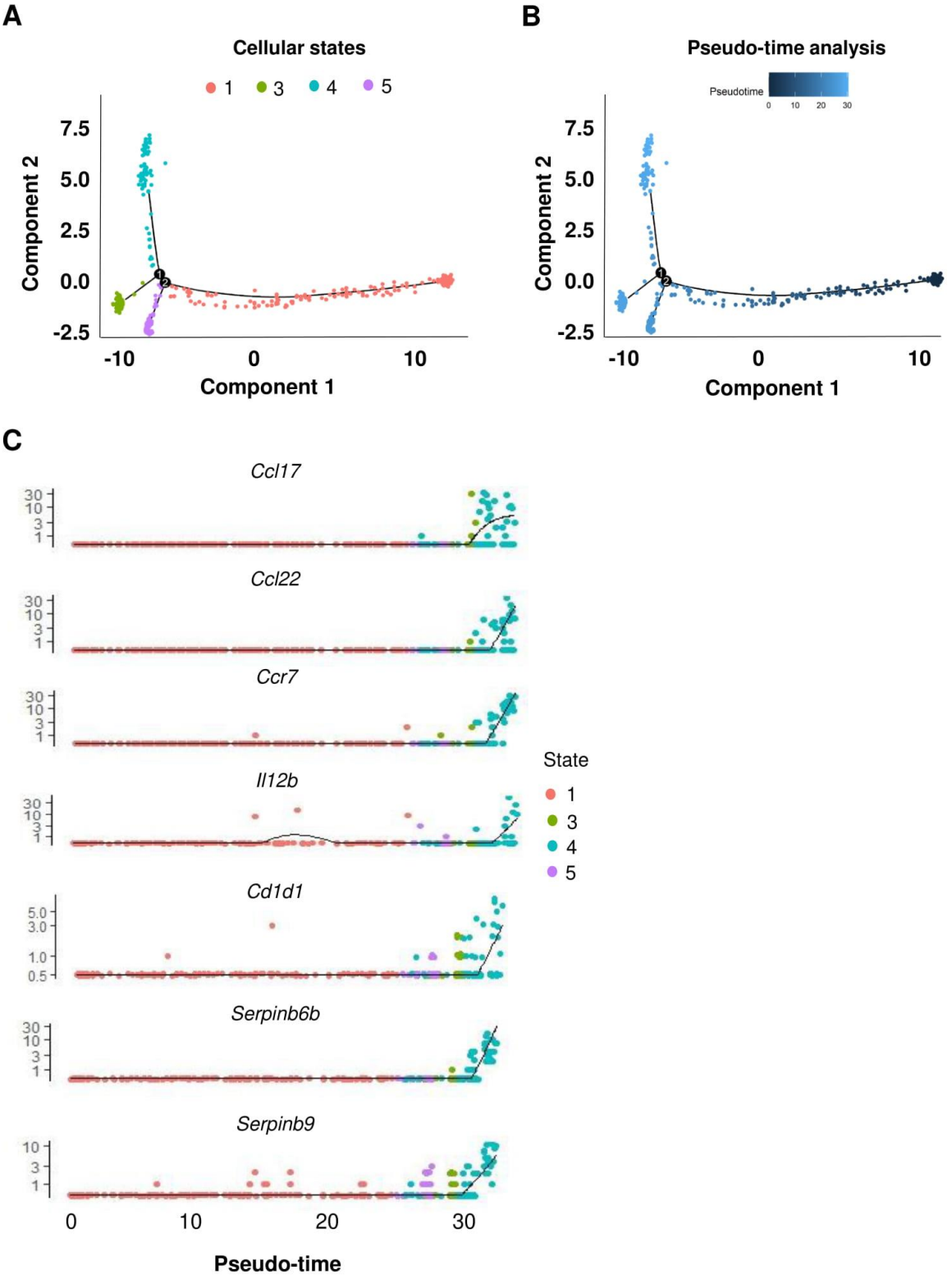

Supplementary Figure 7. TAM II cellular states diversity under *Acod1* deficiency, related to Fig. 5. (A) Pseudo-time analysis of TAM II from *Acod1* KO by Monoclone 2 leads to four distinct cellular states in a two-dimensional state space (see Materials and Methods). **(B)** Monocle estimated a pseudo-time for each cell along the inferred cell trajectory state. **(C)** Relative expression of exclusive genes driving the correspondent cellular state in TAM II subset under *Acod1* deficiency.

PAPER 3: Research article.

Co-authored publication (not subject for thesis defence)

Scientific Report

SOURCE DATA TRANSPARENT PROCESS OPEN ACCESS

EMBO reports

Single-cell transcriptomics reveals distinct inflammation-induced microglia signatures

Carole Sousa[1,2,3], Anna Golebiewska[1], Suresh K Poovathingal[2,4], Tony Kaoma[5], Yolanda Pires-Afonso[1,3], Silvia Martina[2], Djalil Coowar[2], Francisco Azuaje[5], Alexander Skupin[2,6], Rudi Balling[2], Knut Biber[7,8], Simone P Niclou[1,9] & Alessandro Michelucci[1,2,*]

Abstract

Microglia are specialized parenchymal-resident phagocytes of the central nervous system (CNS) that actively support, defend and modulate the neural environment. Dysfunctional microglial responses are thought to worsen CNS diseases; nevertheless, their impact during neuroinflammatory processes remains largely obscure. Here, using a combination of single-cell RNA sequencing and multicolour flow cytometry, we comprehensively profile microglia in the brain of lipopolysaccharide (LPS)-injected mice. By excluding the contribution of other immune CNS-resident and peripheral cells, we show that microglia isolated from LPS-injected mice display a global downregulation of their homeostatic signature together with an upregulation of inflammatory genes. Notably, we identify distinct microglial activated profiles under inflammatory conditions, which greatly differ from neurodegenerative disease-associated profiles. These results provide insights into microglial heterogeneity and establish a resource for the identification of specific phenotypes in CNS disorders, such as neuroinflammatory and neurodegenerative diseases.

Keywords heterogeneity; lipopolysaccharide; microglia; neuroinflammation; single-cell RNA-seq

Subject Categories Immunology; Methods & Resources; Neuroscience

DOI 10.15252/embr.201846171 | Received 23 March 2018 | Revised 17 August 2018 | Accepted 22 August 2018 | Published online 11 September 2018

EMBO Reports (2018) 19: e46171

Introduction

The healthy brain hosts distinct and specialized populations of tissue-resident macrophages strategically placed in the parenchyma, perivascular spaces, meninges and choroid plexus where they coordinate homeostatic and immune surveillance functions [1]. As the only parenchymal-resident immune cells of the central nervous system (CNS), microglia act as critical effectors and regulators of changes in the CNS during development and adult homeostasis. Their ontogeny, together with the absence of turnover from the periphery and the exceptional environment of the CNS, makes microglia a unique immune cell population [2]. By sensing any disruption of CNS homeostasis, microglia rapidly change their gene expression programmes and functional profiles. Recent genome-wide transcriptional studies revealed a unique molecular signature selectively expressed in homeostatic microglia [3–6] that is lost in disease and during ageing [4,7–17]. Microglia coordinate immune responses between the periphery and the CNS as they perceive and propagate inflammatory signals initiated outside the CNS [18]. A multitude of signals received from the CNS environment as well as from the periphery induce microglial responses towards phenotypes that ultimately may support or harm neuronal health [2,19]. Although neuroinflammation and its associated immune responses are often linked to neurodegeneration, the inflammatory response *per se* provides a primary, transient and self-limiting defence mechanism, by which harmful stimuli are resolved and tissue damage is repaired [20]. Disruption of CNS homeostasis, neuronal deterioration and inflammation are common pathophysiological features of several neurodegenerative diseases. In this context, chronic inflammation is likely to be triggered by abnormal protein deposition, by signals elicited by injured neurons and synapses or by impaired pro- and anti-inflammatory regulatory mechanisms that ultimately exacerbate the neurodegenerative process [21]. Dysfunctional microglial responses are believed to worsen CNS diseases [22]; nevertheless, their impact during the neuroinflammatory processes remains largely obscure.

1 NORLUX Neuro-Oncology Laboratory, Department of Oncology, Luxembourg Institute of Health, Luxembourg, Luxembourg
2 Luxembourg Centre for Systems Biomedicine, University of Luxembourg, Esch-Belval, Luxembourg
3 Doctoral School of Science and Technology, University of Luxembourg, Esch-sur-Alzette, Luxembourg
4 Single Cell Analytics & Microfluidics Core, Vlaams Instituut voor Biotechnologie-KU Leuven, Leuven, Belgium
5 Proteome and Genome Research Unit, Department of Oncology, Luxembourg Institute of Health, Luxembourg, Luxembourg
6 National Centre for Microscopy and Imaging Research, University of California San Diego, La Jolla, CA, USA
7 Section Molecular Psychiatry, Department for Psychiatry and Psychotherapy, Laboratory of Translational Psychiatry, Medical Center - University of Freiburg, Faculty of Medicine, University of Freiburg, Freiburg, Germany
8 Section Medical Physiology, Department of Neuroscience, University Medical Center Groningen, University of Groningen, Groningen, The Netherlands
9 Department of Biomedicine, KG Jebsen Brain Tumour Research Center, University of Bergen, Bergen, Norway
*Corresponding author. Tel: +352 26970 263; E-mail: alessandro.michelucci@lih.lu

In recent years, single-cell RNA sequencing investigations have emerged as a remarkable method to depict heterogeneous cell populations and measure cell-to-cell expression variability of thousands of genes [23–25]. In the murine and human brains, single-cell RNA sequencing analyses have revealed neural and glial cell heterogeneity [26–30]. Similarly, the complexity of immune cell types has been recently unravelled [31]. However, although recent studies have elucidated microglia signatures associated with inflammatory conditions at the bulk level [4,16,32], it is still not clear whether all microglial cells uniformly react to the inflammatory stimuli.

To elucidate the heterogeneity of microglial responses towards systemic inflammation, we here analysed the effect of a peripheral injection of the Gram-negative bacterial endotoxin lipopolysaccharide (LPS) in 3- to 4-month-old C57BL/6N mice using a combination of multicolour flow cytometry and single-cell RNA sequencing analyses. LPS is a well-known immunostimulant used to mimic inflammatory and infectious conditions inducing immune responses associated with sickness behaviour in mice and humans [33,34]. Notably, it has been shown that repeated peripheral injections of LPS in mice induce neurodegeneration, while a single-dose injection of LPS induces acute inflammatory, but not neurodegenerative processes [35]. By our approach, we have identified distinct microglial activated profiles under acute inflammatory conditions, which differ from the recently described disease-associated phenotypes [14].

Understanding the specific molecular triggers and the subsequent genetic programmes defining microglia under homeostatic, inflammatory and neurodegenerative conditions at the single-cell level is a fundamental step to further uncover the multifaceted nature of microglia, thus opening new windows to design novel therapeutic strategies to restore, for example, efficient inflammatory immune responses in CNS diseases.

Results and Discussion

Acutely isolated CD11b$^+$CD45^{int} cells express high levels of microglial homeostatic genes and represent a specific resident immune cell population

Cell-specific transcriptomic analyses are critically dependent on isolation protocols to obtain pure populations resembling their physiological profiles. To characterize microglia close to their proper environment, mouse brains were mechanically dissociated into single-cell suspension with all the steps performed at 4°C [36]. Since microglia in the mouse brain represent only 10% of the cells, CD11b$^+$CD45^{int} microglia were purified from other CNS and immune cells, including CD11b$^+$CD45^{high} macrophages and CD11b$^-$CD45^{high} lymphocytes, by FACS, as described previously (Figs 1A and EV1) [37]. To verify accurate microglial enrichment, we compared gene expression levels of specific CNS cell type markers between RNA extracted from unsorted total brain cells and CD11b$^+$CD45^{int} sorted microglia (Fig 1B). We analysed the expression levels of microglial homeostatic genes (*Olfml3*, *Fcrls*, *Tmem119*, *Siglech*, *Gpr34*, *P2ry12*) as well as astrocytic (*Gfap*, *Gjb6*, *Ntsr2*, *Aldh1l1*), oligodendrocytic (*Mobp*, *Mog*, *Cldn11*) and neuronal (*Tubb3*, *Vglut1*, *NeuN*) markers. As expected, microglial markers were highly expressed in CD11b$^+$CD45^{int} sorted cells, whereas astrocytic, oligodendrocytic and neuronal markers were undetectable or detectable at background levels (Figs 1B and EV1). We next investigated whether CD11b$^+$CD45^{int} population contained resident non-parenchymal macrophages, such as perivascular macrophages. This was inferred using CD206 as an additional marker for resident macrophages [38]. Under homeostatic conditions, CD11b$^+$CD45^{int} microglia contained only 0.04 ± 0.02% CD206$^+$ cells, while CD11b$^+$CD45^{high} cells contained 24.7 ± 3.8% CD206$^+$ resident macrophages (Fig 1C and D). Similar results were obtained for the dendritic cell marker CD11c and the monocytic markers Ly6C and CCR2 (Fig EV1). Taken together, these results show that our approach highly discriminates pure and not activated microglial populations from other resident CNS cells.

Microglia isolated from LPS-injected mice show a classical activated pro-inflammatory profile accompanied by a decreased homeostatic signature

The response of microglia towards specific pro- or anti-inflammatory cues *in vitro* has been extensively studied [39]. Treatment of primary microglial cells with TGF-β, LPS or IL-4 generates, respectively, the so-called M0 homeostatic, M1 pro-inflammatory and M2 anti-inflammatory states defined by specific gene signatures [5,40]. However, our understanding towards the reaction of microglia under inflammatory conditions *in vivo* is only starting to emerge. To comprehensively investigate the effect of a systemic inflammatory and/or infectious state on microglia, we peripherally injected mice with LPS (4 μg/g body) 24 h prior analysis. It has been shown that a single-dose injection of LPS induces acute inflammatory, but not neurodegenerative processes [35]. We isolated CD11b$^+$CD45^{int} cells from LPS-injected mice and compared mRNA levels of specific genes

Figure 1. Characterization of acutely isolated CD11b$^+$CD45^{int} cells.

A FACS gating strategy representative of five independent experiments adopted to sort CD11b$^+$CD45^{int} microglia distinctly from CD11b$^+$CD45^{high} resident macrophages and CD11b$^-$CD45^{high} lymphocytes.

B Analysis of relative transcript levels of CD11b$^+$CD45^{int} FACS-sorted microglia compared with whole brain tissue by qPCR. Gene expression levels of microglia (*Olfml3*, *Fcrls*, *Tmem119*, *Siglech*, *Gpr34*, *P2ry12*), astrocyte (*Gfap*, *Gjb6*, *Ntsr2*, *Aldh1l1*), oligodendrocyte (*Mobp*, *Mog*, *Cldn1*) and neuron (*Tubb3*, *Vglut1*, *NeuN*) markers. Bars represent mean (n = 4; pool of one female and one male per biological replicate) of relative expression (*Gapdh* as housekeeping gene) ± SEM (*P < 0.05; **P < 0.01 by two-tailed Student's t-test). N.D., not detected.

C Representative quantification of CD206 expression in CD11b$^+$CD45^{int} microglia and CD11b$^+$CD45^{high} resident macrophages. Values denote the percentage of the mean ± SEM of five independent experiments.

D Representative images of two independent experiments showing microglia, resident macrophages and lymphocytes acquired with ImageStream imaging cytometer (Amnis) based on CD45, CD11b and CD206 expression levels (scale bar represents 7 μm).

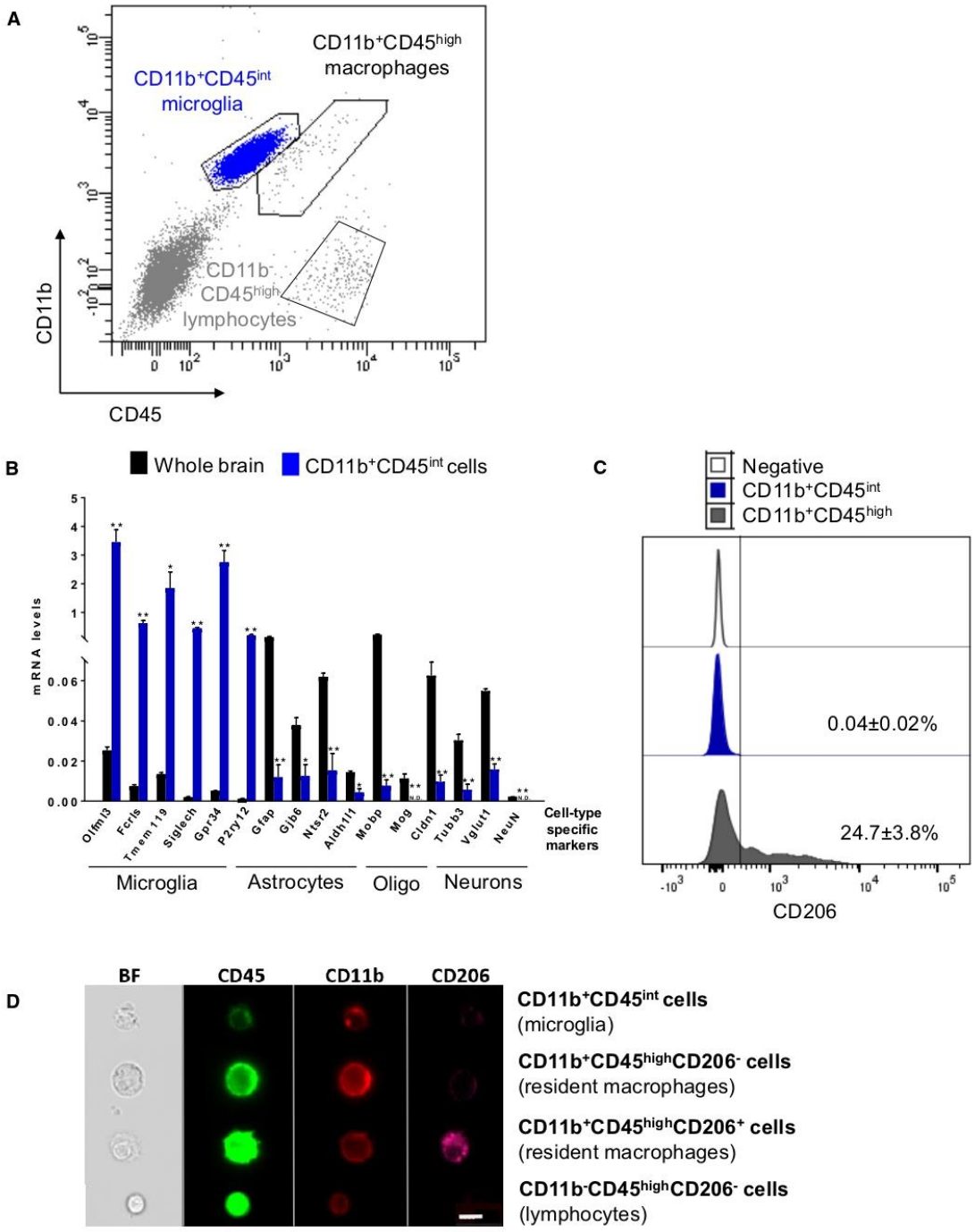

Figure 1.

to the corresponding cells isolated from saline-injected control mice by qPCR. In agreement with previous studies [32,41], the expression levels of homeostatic (e.g. *Olfml3*, *Fcrls*, *Tmem119*, *Siglech*, *Gpr34*, *P2ry12*, *Mef2c*), phagocytic (*Tyrobp* and *Trem2*) and anti-inflammatory genes (e.g. *Mrc1* and *Arg1*) were highly decreased in microglia isolated from LPS-injected mice compared to untreated mice, while the classical pro-inflammatory genes (e.g. *Il1b*, *Tnf* and *Ccl2*) were markedly increased (Figs 2A and EV2). Notably, it has been recently shown that signals from the CNS microenvironment have considerable influence in shaping, maintaining and reinforcing microglial identity by regulating expression and establishing distinct chromatin landscapes surrounding enhancer regions [42–44]. Changes in chromatin remodelers associate with changes in the expression of nearby genes. Specifically, MEF2C binding sites were shown to be over-enriched in enhancer regions of microglial-specific genes [42] and the loss of MEF2C was associated with priming of microglia [45]. In line with these observations, *Mef2c* expression levels were highly decreased in microglia isolated from LPS-injected mice compared to naïve mice.

We verified that this signature is microglia-specific, and it is not affected by LPS-activated immune peripheral cells, such as lymphocytes ($CD11b^{-}CD45^{high}$ cells) and peripheral monocytes/macrophages ($CD11b^{+}CD45^{high}$ cells), as no significant differences were detected between cellular populations present in brains of saline- and LPS-injected mice (Figs 2B and EV2). Importantly, $CD11b^{+}CD45^{int}$ FACS-gated cells contained very rare (< 0.25%) $Ly6C^{+}$ putative monocytes and (< 0.1%) $CD206^{+}$ putative resident macrophages (Fig 2C). Also, the expression of monocytic markers *Ly6c1* and *Ccr2* was very low in $CD11b^{+}CD45^{int}$ microglia compared to bone marrow-isolated monocytes with no significant differences under LPS exposure (Figs 2D and EV2). In order to further assess that the decrease in the homeostatic signature under inflammatory conditions is not due to the presence of other immune cell types, but it is an intrinsic property of microglial cells, we also analysed the effect of LPS on cultivated microglial from adult and neonatal mice. As expected, the expression level of the homeostatic genes was markedly decreased in cultivated cells when compared to acutely isolated microglia (Fig EV2) [5]. Thus, we cultivated adult microglia in the presence of TGF-β (50 μg/ml) and M-CSF (10 ng/ml) or neonatal cells with TGF-β 24 h prior treatment with LPS to induce the expression of the homeostatic genes, although at a lower extent than in *ex vivo* isolated cells (Fig EV2). Cells treated with LPS (1 ng/ml) for 6 h showed a dramatic decrease of the expression levels of the homeostatic gene markers, such as *Olfml3*, *Tmem119* and *Gpr34*, accompanied by enhanced expression levels of inflammatory marker genes, such as *Il1b*, *Tnf* and *Ccl2* both in adult and in neonatal microglia when compared to cells treated with TGF-β only (Fig 2E). In the healthy brain, TGF-β is expressed at low levels by both neurons and glial cells [46,47], while its expression is increased upon injury [48,49], hypoxia–ischaemia [50] and neurodegeneration [51,52]. SMAD and signal transducer and activator of transcription (STAT) proteins are key signal transducers and transcription factors controlling TGF-β downstream signalling [53]. Specifically, STAT3 and suppressor of cytokine signalling 3 (SOCS3) regulate inflammatory responses [54]. The binding of SOCS3 to both JAK kinase and the cytokine receptor results in the inhibition of STAT3 activation. In our analysis, microglial cells treated with LPS showed increased amounts of STAT3 phosphorylation along with upregulation of *Socs3* expression levels compared to untreated cells (Appendix Fig S1). Taking advantage of the "harmonizome" collection of databases [55], we attested that more than 1/3 of the top 100 sensome genes [4] possess STAT3-binding sites in their promoter region. Hence, we hypothesized that the SOCS3-STAT3 antagonistic signalling may be responsible for the suppression of the homeostatic microglia signature and the concomitant shift towards the inflammatory profile [56].

These results show that microglia isolated from LPS-injected mice display a classical activated pro-inflammatory profile associated with a decrease in the expression of the homeostatic genes. The decrease in the homeostatic signature under inflammatory conditions is an inherent facet of microglial *in vivo* and *in vitro*.

Single-cell mRNA sequencing of $CD11b^{+}CD45^{int}$ microglia isolated from LPS-injected mice reveals a global transcriptional shift and increased heterogeneity compared to steady state conditions

Based on the observed differences in the targeted qPCR approach under steady state and LPS conditions, we next aimed to investigate microglial states at the genome-wide level and infer their transcriptomic heterogeneity at single-cell resolution, since studying a population of cells masks the differences among individual cells. For this purpose, FACS-sorted $CD11b^{+}CD45^{int}$ cells from saline- or LPS-injected mice were analysed using the recently developed high-throughput droplet-based Drop-seq method [23]. In Drop-seq, single cells and functionalized barcoded beads as cell identifiers are co-encapsulated into droplets followed by cDNA synthesis,

Figure 2. LPS stimulation induces an intrinsic loss of the microglia homeostatic signature.

A–D Three- to four-month-old C57BL/6N mice were treated with an acute dose of LPS (4 μg/g body) or vehicle (saline). Microglia (pool of two mice per group per replicate; one female and one male) were FACS-sorted 24 h later. (A) Gene expression levels of microglial homeostatic (*Olfml3*, *Fcrls*, *Tmem119*, *Siglech*, *Gpr34*, *P2ry12*, *Mef2c*), phagocytic (*Tyrobp*, *Trem2*) and inflammatory (*Il1b*, *Tnf*, *Ccl2*, *Mrc1*, *Arg1*) markers were analysed by qPCR. Bars represent mean of relative expression (% of saline; *Gapdh* as housekeeping gene) ± SEM (*$P < 0.05$; **$P < 0.01$ by two-tailed Student's *t*-test; $n = 4$). (B) Representative multicolour flow cytometry analysis of five independent experiments showing CD11b- and CD45-positive populations in single viable cells in saline or LPS-injected mouse brains. (C) Representative multicolour flow cytometry analysis showing the percentage of the mean ± SEM of five independent experiments of Ly6C- and CD206-expressing cells in $CD11b^{+}CD45^{int}$ cells from saline or LPS-injected mice. (D) Gene expression levels of the monocytic markers *Ly6c1* and *Ccr2* in purified microglia ($n = 4$) and isolated bone marrow monocytes ($n = 2$) by qPCR. Bars represent mean of relative expression (*Gapdh* as housekeeping gene) ± SEM (**$P < 0.01$ by two-tailed Student's *t*-test).

E Primary adult microglia were cultivated in the presence of TGF-β (50 μg/ml) and M-CSF (10 ng/ml), while neonatal cells were stimulated for 24 h with TGF-β (50 μg/ml) followed by 6 h of stimulation with LPS (1 ng/ml) or left untreated. Expression levels of microglial homeostatic (*Olfml3*, *Tmem119*, *Gpr34*) and inflammatory (*Il1b*, *Tnf*, *Ccl2*) genes were analysed by qPCR. Bars represent mean of relative expression (*Gapdh* as housekeeping gene) ± SEM (*$P < 0.05$; **$P < 0.01$ by two-tailed Student's *t*-test).

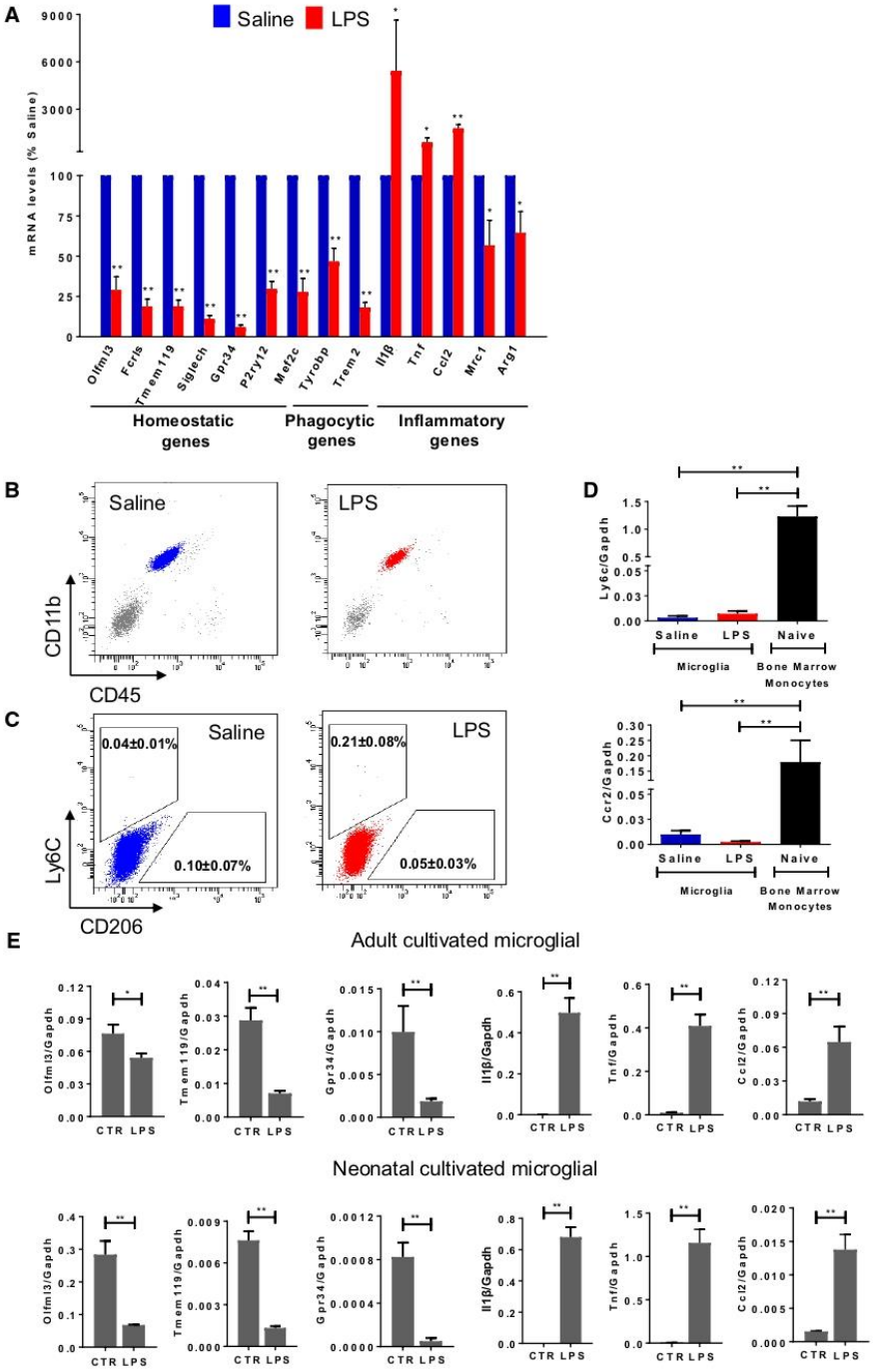
A
Saline
LPS
mRNA levels (% Saline)
Olfml3
Fcrls
Tmem119
Siglech
Gpr34
P2ry12
Mef2c
Tyrobp
Trem2
Il1β
Tnf
Ccl2
Mrc1
Arg1
Homeostatic genes
Phagocytic genes
Inflammatory genes
B
Saline
LPS
CD11b
CD45
C
Saline
LPS
0.04±0.01%
0.10±0.07%
0.21±0.08%
0.05±0.03%
Ly6C
CD206
D
Ly6c/Gapdh
Ccr2/Gapdh
Saline
LPS
Naive
Microglia
Bone Marrow Monocytes
E
Adult cultivated microglial
Neonatal cultivated microglial
Olfml3/Gapdh
Tmem119/Gapdh
Gpr34/Gapdh
Il1β/Gapdh
Tnf/Gapdh
Ccl2/Gapdh
CTR
LPS

Figure 2.

amplification, library preparation and next-generation sequencing. First, we sought for differentially expressed genes between all LPS and all naïve/saline cells using MAST [57]. We identified 2,405 differentially expressed genes between these two conditions with a false discovery rate (FDR) cut-off of 5% (Dataset EV1) and exemplified the top 100 differentially expressed genes in a heatmap (Fig 3A). Second, principal component analysis followed by two-dimensional *t*-distributed stochastic neighbour embedding (2D-tSNE) of the overall gene expression data of 1,247 analysed cells identified two main cell clusters that were independent of the 2D-tSNE parameters and library sizes (Appendix Fig S2). Microglia isolated from LPS-injected mice distinctly clustered from the corresponding steady state microglia presenting discrete gene expression signatures (Fig 3B; Dataset EV1). Intriguingly, we noticed from both analyses that, although most of the activated cells clustered together, a small group of cells assembled closer to the control cells, thus highlighting the existence of potential subpopulations under inflammatory conditions, which we characterized later. Gene set enrichment analysis (GO) of upregulated genes in microglia isolated from LPS-injected mice using DAVID [58,59] uncovered significant involvement ($P < 2.5 \times 10^{-9}$) in "translation", "protein folding", "ribosome biogenesis" and "immune system process", thus reflecting highly activated cells. On the other hand, GO of the corresponding downregulated genes identified, among others, significant enrichment ($P < 4.9 \times 10^{-5}$) in "regulation of transforming growth factor beta receptor signalling pathway", thus reflecting that TGF-β signalling is among the most affected pathways in microglia exposed to LPS (Appendix Fig S3). In line with gene expression results obtained at the bulk level, microglial homeostatic genes (e.g. *Tmem119*, *Mef2c*, *P2ry13*, *P2ry12*, *Siglech*) were among the top downregulated genes and classical pro-inflammatory genes (e.g. *Ccl2*, *Gpr84*, *Nfkbia*) were mainly upregulated also at the single-cell level (Appendix Fig S2). We further investigated individual gene expressions at single-cell level using 2D-tSNE to show specific homeostatic and inflammatory gene expression levels. For example, *Tmem119*, *Siglech* and *P2ry12* genes were consistently expressed under steady state, but were downregulated in microglia isolated from LPS-injected mice, while *Ccl2* and *Gpr84* were largely upregulated in most of the cells exposed to LPS compared to saline conditions (Fig 3C; Appendix Fig S4). Notably, a prominent decrease in TMEM119 and P2RY12 expression was further confirmed at the protein level by flow cytometry (Fig 3D).

Although microglial activation is a common hallmark under inflammatory and neurodegenerative conditions [22], microglia transcriptional signatures have been shown to be different. For example, Chiu *et al* [16] demonstrated that acutely isolated microglia from the $SOD1^{G93A}$ mouse model of amyotrophic lateral sclerosis (ALS) differed from LPS-activated microglia, defining an ALS-specific phenotype. Following the recent description of a novel disease-associated microglial (DAM) phenotype identified under neurodegenerative conditions at single-cell resolution [14], we here compared our inflammatory-associated microglia (IAM) signature to DAM. The scatterplot showing the fold change of genes between microglia isolated from LPS-injected mice (2,405 genes; Dataset EV1) versus DAM (1,660 genes; Dataset EV2) compared to homeostatic microglia (FDR < 0.05) disclosed 1,826 unique genes affected by the LPS treatment (e.g. *Tnf*, *Irf1*), 1,081 distinct genes in DAM (e.g. *Itgax*, *Axl*) and 579 shared genes between the two populations (e.g. *Gpr84*, *Tmem119*), thus highlighting that these cells mainly display a unique expression profile (Fig EV3). Specifically, only 215 upregulated genes (12.1%) and 364 downregulated genes (21.2%) were shared between the two groups (Fig EV3). Gene set enrichment analysis (GO) and identification of key genes being discriminative between inflammatory microglia and DAM revealed a high inflammatory reactivity upon LPS treatment and a phagocytic/lysosomal gene signature in DAM (Fig EV3). For instances, *Trem2* and *Tyrobp* expression levels were highly decreased in IAM, whereas an elevation of both genes was reported in DAM. TREM2 associates with the immunoreceptor tyrosine-based activation motif (ITAM)-containing adaptor protein TYROBP (DAP12), in which signalling involves the recruitment of tyrosine kinase Syk that further phosphorylates downstream pathways inducing cell activation. TREM2 is required for phagocytosis of apoptotic neurons, microglial proliferation and survival [56,60–62]. These subtle differences in perceiving different signals induced by CNS perturbations support the microglial critical role in modulating specific functional activities. In fact, it is intuitive to consider that sensing inflammatory environments to maintain a homeostatic neuronal network (e.g. through the expression of *Clec4a* and *Clec5a* genes that are exclusively upregulated in our dataset) or recognizing and clearing pathogenic factors (e.g. by expressing *Clec7a/Dectin-1* in DAM), such as β-amyloid aggregates in AD, require distinct activated phenotypes. In a different context, it has been recently shown that myelin pieces are gradually released from ageing myelin sheaths and are subsequently cleared by microglia [63]. Age-related myelin fragmentation is substantial, leading to lysosomal storage and contributing to microglial senescence and immune dysfunction in ageing [63]. It could be then hypothesized that a similar accentuated mechanism may be encountered by microglia surrounding β-amyloid plaques, which become dystrophic at a late stage of the disease [64]. Interestingly, genes described to be associated with neurological diseases, such as *Cd33*, *Cd9*, *Sod1*, *Ctsd*, and *Hif1a*, were also downregulated in our signature in comparison with DAM.

Taken together, these results suggest that microglia under acute systemic inflammation present a highly activated state, which is heterogeneous and distinct from neurodegenerative disease-associated profiles.

Microglia present distinct activated signatures under inflammatory conditions

Next, we aimed to elucidate whether the response to LPS was heterogeneous across microglial cells. Based on our previous observation (Figs 3A and B), we further analysed the identified subclusters by 2D-tSNE representation (Fig 4A). Based on the obtained 2D representation, a specific LPS subgroup ("subset LPS", in yellow) distinct from the core LPS cluster ("main LPS", in red) was identified closer to naïve microglial cluster. Thus, we hypothesized that these cells may correspond to a microglial subset that is less sensitive to inflammatory stimuli or a cluster of cells which already partly recovered from their activated state following the prominent pro-inflammatory immune response. We obtained differentially expressed genes between the "main LPS" (Dataset EV3) and the "subset LPS" (Dataset EV4) clusters compared to the corresponding control conditions (FDR < 0.05). We represented the top 100

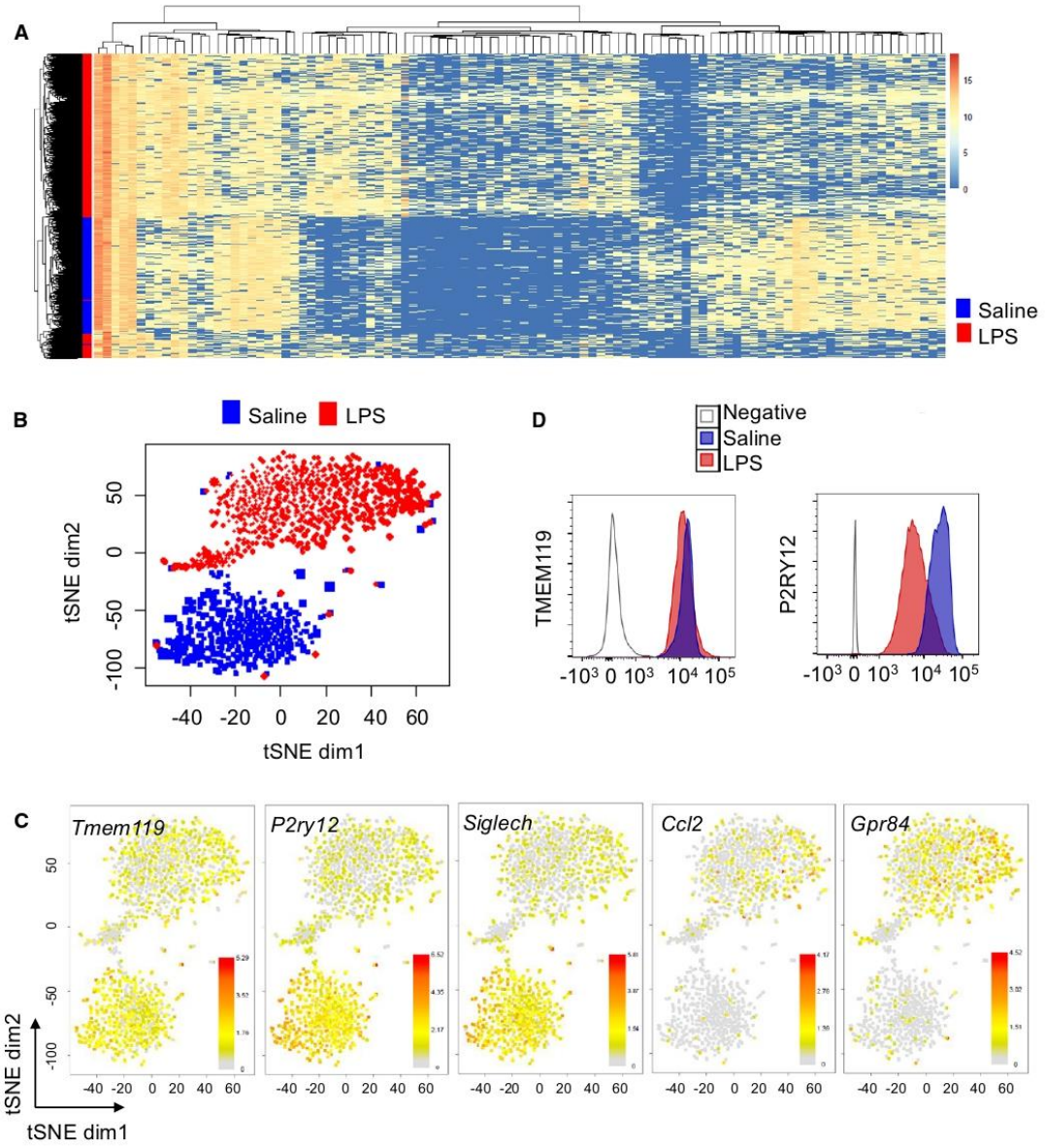

Figure 3. Characterization of microglial activation at the single-cell level.

A Heatmap showing clustering analysis of 1,247 single cells, featuring 100 most variable genes (FDR < 0.05). Single-cell RNA-seq results are obtained from two mice per group (one female and one male each). Values denote a score based on gene expression rank.

B 2D-tSNE representation of all single cells included in the study (n = 1,247) depicting the separation of microglia isolated from LPS-injected mice (770 cells in red) and steady state (477 cells in blue) in two main clusters.

C Expression of specific homeostatic (*Tmem119*, *P2ry12*, *Siglech*) and inflammatory (*Ccl2*, *Gpr84*) genes overlaid on the 2D-tSNE space. Bars represent log2 (Count + 1).

D Representative multicolour flow cytometry analysis of two independent experiments showing TMEM119 and P2RY12 expression levels in $CD11b^{+}CD45^{int}$ microglia of saline or LPS-injected mouse brains. For the unconjugated TMEM119 antibody, negative stands for primary antibody without secondary antibody. For P2RY12 antibody, negative represents isotype PE control.

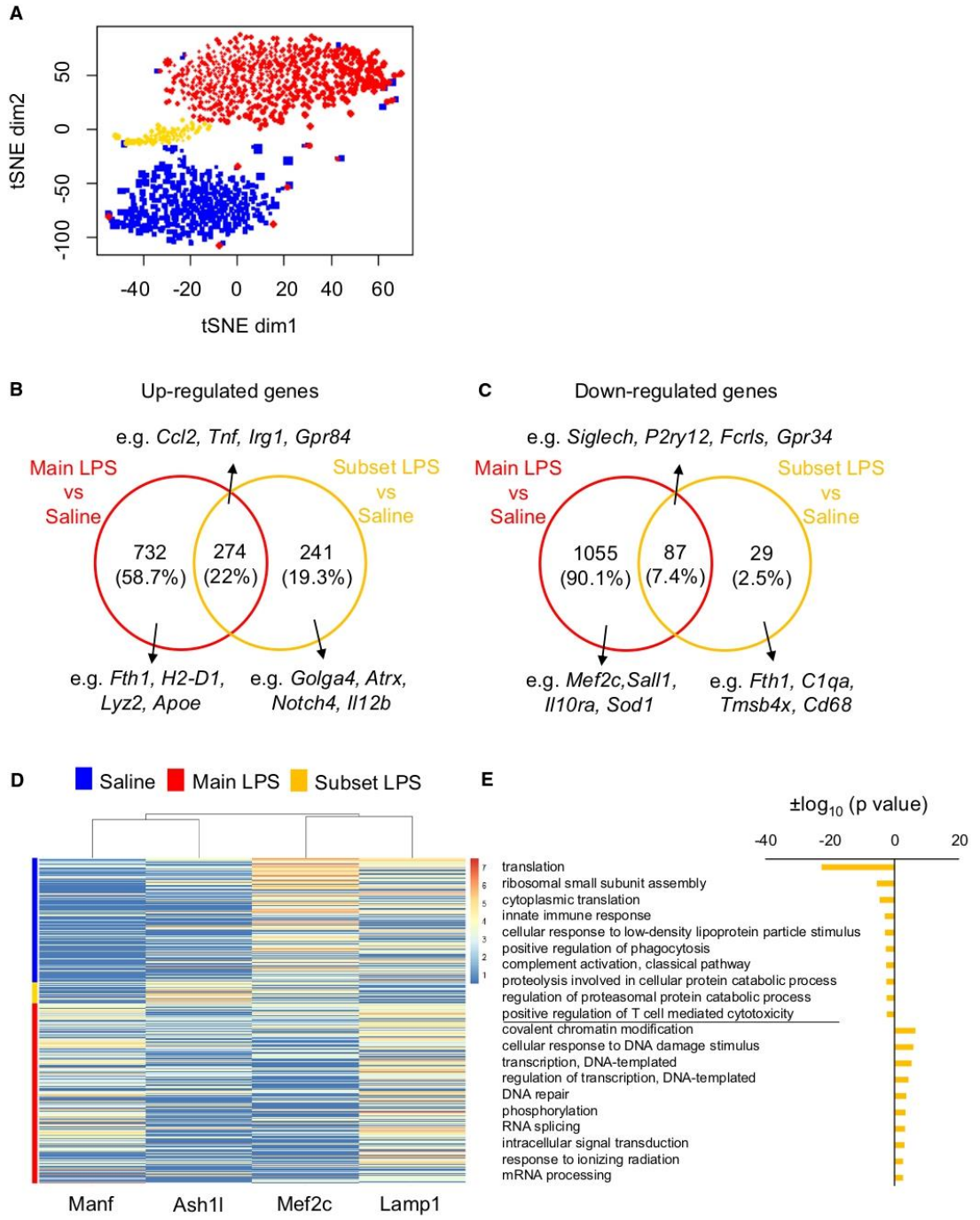

Figure 4.

Figure 4. Identification of microglial subpopulations under inflammatory conditions.

A 2D-tSNE representation of 1,247 single cells isolated from naïve (blue)- and LPS-treated mice showing two distinct subpopulations among the 770 cells isolated from LPS-injected mice (n = 703, red; n = 67, yellow).

B Venn diagram showing 732 genes uniquely upregulated in the "main LPS" cluster (red) and 241 genes exclusively increased in the "subset LPS" (yellow) compared to their corresponding controls (blue) (FDR < 0.05). A total of 274 genes were shared between the two LPS populations.

C Venn diagram showing 1,055 genes uniquely downregulated in the "main LPS" cluster (red) and 29 genes exclusively decreased in the "subset LPS" (yellow) compared to their corresponding controls (blue) (FDR < 0.05). A total of 87 genes were shared between the two LPS populations.

D Heatmap showing examples of specific genes mainly upregulated in "main LPS" (*Manf*) or "subset LPS" (*Ash1l*) and downregulated in "main LPS" (*Mef2c*) or "subset LPS" (*Lamp1*) overlaid on the 2D-tSNE space. Bars represent log2 (Count + 1).

E Gene set enrichment analysis (GO, top 10 biological processes) of 99 downregulated and 397 upregulated genes distinguishing cells in "subset LPS" versus "main LPS" (FDR < 0.05).

differentially expressed genes among the identified clusters in a heatmap (FDR < 0.05; Appendix Fig S5). To elucidate the transcriptional signature of the LPS subgroups, we showed differentially expressed genes between "main LPS" and "subset LPS" clusters compared to the corresponding control conditions (FDR < 0.05). In line with their activated state, the main pro-inflammatory genes (e.g. *Ccl2, Tnf, Irg1, Gpr84*) were upregulated (Fig 4B) and the microglial homeostatic genes (e.g. *Siglech, P2ry12, Fcrls, Gpr34*) were downregulated in both populations (Fig 4C), although at a lesser extent in "subset LPS", compared to steady state conditions. Investigation of the top differentially expressed genes unique to "main LPS" or "subset LPS" compared to naïve cells (FDR < 0.05; Log2FC ≥ 3 or Log2FC ≤ −3; Table 1) identified, for example, *Manf* (a growth factor that promotes neuroprotection and tissue repair [65]) and *C5ar1* among the top upregulated genes in "main LPS" and *Stab 1* as well as *Ash1l* (which suppresses the production of pro-inflammatory mediators, such as IL-6 and TNF [66]), among the enhanced genes in "subset LPS". Downregulated genes were, for example, the homeostatic gene marker *Mef2c*, which restrains the microglial inflammatory response [45] in "main LPS" and genes associated with endosomes/lysosomes in both "main LPS" (*Maf*) and "subset LPS" (*Lamp1*) (Figs 4D and EV4), thus potentially providing some mechanistic insights regarding the less activated state of "subset LPS" compared to the "main LPS" cluster. Further analysis of unique differentially expressed genes (FDR < 0.05) characterizing the two LPS subpopulations based on microglial functions and properties showed a dramatic increase in genes associated with the major histocompatibility complex (e.g. *H2-D1* and *H2-K1*) exclusively in the "main LPS" group and a decrease in the complement system (e.g. *C1qa*, *C1qb* and *C1qc*) in the "subset LPS" group when compared to steady state (Table EV1).

Table 1. List of top differentially expressed genes unique to "main LPS" or "subset LPS" versus PBS (FDR < 0.05; upregulated genes, Log2FC ≥ 3; downregulated genes, Log2FC ≤ −3).

Top upregulated genes		Top downregulated genes	
"Main LPS"	"Subset LPS"	"Main LPS"	"Subset LPS"
Rplp0	Gm26924	Tanc2	Lamp1
Rps2	Golga4	Pde3b	Gm17087
Cd52	Zfc3h1	Maf	Cd68
Cd63	RP24-312B12.1	Rasgrp3	Rps14
Ctsl	Stab 1	Zfhx3	C1qc
Manf	Cacna1d	4632428N05Rik	Itm2c
Pdia4	Ash1l	Mef2c	Eif1
Calm1	Ascc3	Qk	H3f3b
Rps19	Atrx	Ivns1abp	Cd81
Fth1	Ptprc	Pmepa1	Ubb
Rps5	Ttc14		Lrrc58
Pdia6	Chd7		
C5ar1	Myo9a		
Ptplb			
Rpl32			
Gnl3			

Notably, we characterized membrane markers corresponding to specific genes identified at single-cell resolution by flow cytometry to analyse the expression levels of markers upregulated in both LPS groups (e.g. CD44), only in "main LPS" (e.g. CD274) or only in "subset LPS" (e.g. NOTCH4). Although three markers used simultaneously did not allow to clearly discriminate the "subset LPS" from the "main LPS" population, changes in the proportion of marker-positive cells were in line with the scRNA-seq data. Upon LPS treatment, a smaller proportion of NOTCH4-positive cells (saline 5.4%; LPS 18.9%) compared to CD44 (saline 65.2%; LPS 97.5%) and CD274 (saline 48.7%; LPS 88.1%) were detected (Fig EV5). We confirmed this pattern by immunohistochemistry, showing that NOTCH4-positive cells were evenly distributed throughout the brain, thus indicating that these cells were not associated with a specific brain region (Fig EV5).

Gene set enrichment analysis of downregulated genes characterizing "subset LPS" compared to "main LPS" confirmed "innate immune response" and "complement activation, classical pathway" as decreased terms, thus highlighting a less pronounced activated state of the "subset LPS". Intriguingly, these cells revealed significant over-representation (P < 0.05) of "covalent chromatin modification" and "DNA repair" that may indicate cells recovering from their acute activated state or a subset of cells with specific chromatin states and DNA repair properties conveying an attenuated activated phenotype than the main population (Fig 4E). In order to further corroborate the existence of the identified microglial subpopulations under inflammatory conditions, the corresponding 770 cells were subjected to the "SC3" method [67]. With two clusters, we found a very high concordance between the subcluster obtained with "SC3" and the LPS subset identified by 2D-tSNE, thus supporting the existence of the detected subpopulations. We represented the top 50 differentially expressed genes driving the segregation of cells into the two clusters in a heatmap (adjusted P-value < 0.05; Appendix Fig S6).

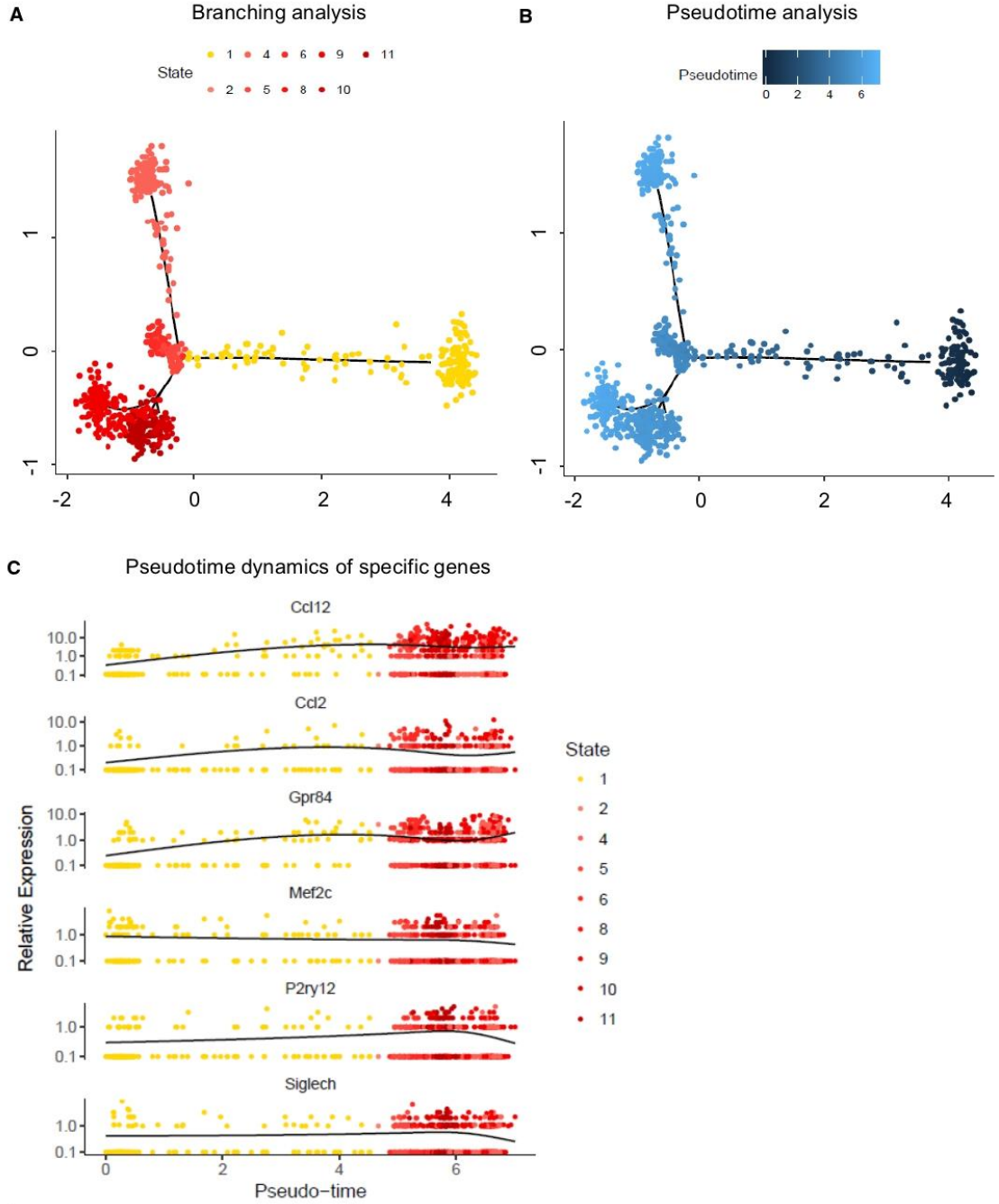

Figure 5.

Figure 5. Pseudotime analysis.

A Branching analysis of LPS-activated microglia by Monocle 2 leads to nine distinct clusters in a two-dimensional state space inferred by generalized regression modelling (see Materials and Methods) showing the major difference of "subset LPS" (in yellow) compared to the other clusters corresponding to "main LPS" (in red).

B Monocle estimated a pseudotime for each cell along the inferred cell trajectory within the state space showing a delayed activation pattern of "subset LPS" compared to the other fractions.

C Pseudotime dynamics of inflammatory (*Ccl12*, *Ccl2*, *Gpr84*) and homeostatic (*Mef2c*, *P2ry12*, *Siglech*) genes in dependence on inferred cell states.

Lastly, we used Venn diagrams to show unique and common upregulated and downregulated (Fig EV5) genes among "main LPS" cluster, "subset LPS" and DAM (FDR < 0.05). Among the deregulated genes, for example, *Spp1*, *Il1b* and *Tlr2* were commonly upregulated, while *Fcrls*, *Tgfbr1* and *Siglech* were downregulated in the three groups. Intriguingly, genes of the complement system (e.g. *C1qa*, *C1qb* and *C1qc*) were downregulated in both "subset LPS" and DAM, but not in "main LPS". Further analysis of the top differentially expressed genes unique to the three groups compared to naïve cells (FDR < 0.05; Log2FC ≥ 3 or Log2FC ≤ −3; Appendix Table S1) showed that the previously identified genes, such as *Manf* and *C5ar1* are uniquely upregulated in "main LPS", while *Stab 1* as well as *Ash1l* is among the increased genes only in "subset LPS".

Overall, these results highlight the existence of specific microglial subpopulations under inflammatory conditions, which are distinct from neurodegenerative-associated phenotypes. These findings emphasize heterogeneity of microglial activated states *in vivo* reflecting specific functional activities related to their corresponding environment.

Pseudotime analysis of LPS-activated microglia uncovers "subset LPS" as an intermediate activated state

Although further analyses at different time points should be performed in the future to resolve the dynamic process of activation, to further investigate the activation process, the heterogeneity within LPS-activated microglia and, specifically, the properties of "subset LPS" compared to "main LPS", we applied branch expression analysis modelling (BEAM) and corresponding pseudotime analysis implemented in Monocle 2 [68]. Since the more subtle differences during the activation process would be dominated by the large differences between naïve and LPS conditions, we applied the branching analysis to the LPS-activated microglia only. This more sensitive analysis revealed nine different states, with the largest difference of "subset LPS" to all others, in accordance with the previous tSNE and "SC3" analyses. Interestingly, cells assigned to "subset LPS" exhibit a dense core, but also a significant number of cells towards the other main clusters (Fig 5A). Given this more sensitive clustering and corresponding pseudotime analysis, we then investigated the characteristics of "subset LPS" with respect to their activation state and their relation with the other states. For this purpose, we plotted the estimated pseudotime of each cell in the state space indicating a delayed activation pattern of "subset LPS" (Fig 5B). Lastly, we investigated inflammatory (e.g. *Ccl12*, *Ccl2*, *Gpr84*) and homeostatic (e.g. *Mef2c*, *P2ry12*, *Siglech*) gene expression profiles in dependence on pseudotime, further indicating the delayed activation state of "subset LPS" by smaller pseudotimes (Fig 5C). By comparing the dynamics of the inflammatory and homeostatic genes along the activation process, we observed that inflammatory genes were upregulated first, while the homeostatic markers were only subsequently downregulated. Thus, "subset LPS" may correspond to an intermediate state where the gene expression levels of the inflammatory mediators are increased, but the homeostatic gene markers, such as *Mef2c*, are still partly preserved. In conclusion, from this analysis, we hypothesized that these cells may correspond to a microglial subpopulation that is less sensitive to inflammatory stimuli.

In summary, our work elucidated an extensive picture of microglial profiles in steady state and upon inflammatory conditions, including unforeseen heterogeneity in their states of activation. We believe that our findings, together with the recent single-cell RNA sequencing studies of microglia in Alzheimer's disease [14], present a comprehensive transcriptomic view of microglia under acute inflammatory conditions and a comparison with neurodegenerative processes. These results could then pave the way to design new therapeutic approaches to restore abnormal or detrimental microglial phenotypes found in several CNS disorders.

Materials and Methods

Animals

Three- to four-month-old C57BL/6N male and female mice were obtained from Charles River Laboratories (France). Mice were housed in 12-h light/dark cycle, with sterile food and water *ad libitum*. All animal procedures were approved by the University of Luxembourg Animal Experimentation Ethics Committee and by appropriate government agencies. The animal work of the present study has been conducted and reported in accordance with the ARRIVE (Animal Research: Reporting of *In Vivo* Experiments) guidelines to improve the design, analysis and reporting of research using animals, maximizing information published and minimizing unnecessary studies.

Acute microglial isolation and purification by multicolour flow cytometry

Mice were treated with a single intraperitoneal injection of LPS (4 μg LPS/g body weight) or with PBS (saline) as vehicle control. Twenty-four hours later, mice were deeply anaesthetized with a combination of ketamine (100 mg/ml; Nimatek Vet)–dorbene (medetomidine hydrochloride; 1 mg/ml; Dorbene Vet) and perfused transcardially with ice-cold PBS. Further processing was performed at 4°C and no-break centrifugations. Brains were rapidly removed, stored in ice-cold HBSS (Gibco/Life Technologies) with 1 M HEPES (Gibco/Life Technologies) and 0.5% D-(+)-glucose (Sigma-Aldrich), mechanically homogenized in a potter homogenizer and centrifuged at 900 rpm for 10 min. Myelin was removed from cell suspension with the Myelin Removal Kit (Miltenyi Biotec) according to the manufacturer's protocol. Prior to the FACS, the cell suspension was

resuspended in ice-cold HBSS with 2% FBS and 10 mM HEPES, pH 7.4 and filtered through a 70-μm nylon mesh (CellTrics). For multicolour staining, cells were incubated for 15 min with Fc receptor binding inhibitor (anti-mouse CD16/CD32 monoclonal antibody; 1:100; eBioscience) to reduce binding of non-specific Fc-gamma receptors, and then stained with fluorochrome-conjugated antibodies (Appendix Table S2) or their corresponding isotopic controls for 45 min at 4°C in dark. After washing, cells were pelleted at 300 *g* for 10 min at 4°C and resuspended in 200 μl of the appropriated buffer. Hoechst (0.1 μg/ml; Sigma) or Sytox Red (1:1,000; Thermo Fisher Scientific) were added shortly before flow cytometry measurements for dead cell discrimination. Cells were sorted with FACSAria™ SORP cytometer (BD Biosciences) fitted with a 640 nm (30 mW) red laser, a 355 nm (60 mW) UV laser, a 405 nm (50 mW) violet laser, a 488 nm (100 mW) blue laser and a 561 nm (50 mW) yellow/green laser. Data were analysed with FACSDiva software (Becton Dickinson) and FlowJo software (version 7.6.5; Tree Star). Imaging flow cytometry was performed with an ImageStream imaging cytometer (Amnis) fitted with a 375 UV laser, a 488 blue laser, a 561 yellow-green laser, a 642 red laser and a 785 nm infrared laser. Acquisition was performed with the INSPIRE® software, and analysis was performed using IDEAS® image analysis software. Pictures were taken at 60× magnification at low speed, high sensitivity mode.

Isolation of bone marrow monocytes

Monocytes were isolated from mouse bone marrow cells by using the Monocyte Isolation Kit (Miltenyi Biotec) according to the manufacturer's protocol.

Primary adult mouse microglial culture

Adult microglia were isolated from brains of C57BL/6N mice at age 6–10 weeks by magnetic separation. Mice were transcardially perfused with ice-cold PBS under anaesthesia, and brains were dissociated using the Neural Dissociation Kit P (MACS Miltenyi Biotec) according to the manufacturer's instruction. Microglia were enriched by magnetic separation using $CD11b^+$ beads (MACS Miltenyi Biotec). Briefly, 1×10^7 cells were resuspended in 90 μl of MACS buffer [Hank's balanced salt solution (HBSS); Lonza] supplemented with 0.5% BSA (Sigma-Aldrich) and 2 mM EDTA and 10 μl of CD11b MicroBeads (MACS Miltenyi Biotec). The cell suspension was incubated at 4°C for 20 min, washed and pelleted in 500 μl of MACS buffer at a density of 1×10^8 cells. The cell suspension was applied into LS columns (MACS Miltenyi Biotec), and the $CD11b^+$ fraction was eluted. Primary adult microglia were plated in 24-well plates coated in poly-L-lysine (0.1 mg/ml solution; Sigma-Aldrich) at a density of 2×10^5 cells/ml and grown in microglial culture medium [Dulbecco's modified Eagle's medium (DMEM-F12 w/L-glutamine w/15 mM HEPES; Biowest)] supplemented with 10% foetal bovine serum (FBS; Gibco/Life Technologies), pen-strep (100 U/ml/100 μg/ml; Gibco/Life Technologies), human recombinant TGF-β (PeproTech) at a final concentration of 50 μg/ml and mouse recombinant M-CSF (R&D Systems) at a final concentration of 10 ng/ml. Cells were cultured for 5 days without changing media. After 9 days of culture, cells were stimulated with lipopolysaccharide (LPS from *Escherichia coli* 055:B5; Sigma-Aldrich) at a final concentration of 1 ng/ml for 6 h.

Primary newborn mouse microglial culture

Murine primary microglial cells were isolated from newborn (P1–P4) C57BL/6N mouse brains as previously described [69]. Brains were dissected on ice. Subsequently, meninges and large blood vessels were carefully removed and brains were pooled and minced in cold Dulbecco's phosphate buffered saline (PBS; Lonza). Tissue dissociation was completed by 10 min of incubation in 2 mM EDTA (Sigma-Aldrich). Cells were washed, centrifuged, seeded into six-well plates coated with poly-L-lysine and allowed to attach and grow in complete medium DMEM (Gibco/Life Technologies) supplemented with 10% FBS and pen-strep at 37°C in a water-saturated atmosphere containing 5% CO_2. The culture medium was renewed after 3 days of culture. After 10 days, when cells reached confluence, the mixed glial monolayer was trypsinated (0.05% Trypsin–EDTA; Gibco/Life Technologies) and microglial cells were purified by magnetic cell sorting (MACS Miltenyi Biotec) following the manufacturer's instructions. Primary microglia were plated in 12-well plates coated with poly-L-lysine (Sigma-Aldrich) at a density of 4 × 105 cells/ml. Twenty-four hours after plating, cells were activated with different compounds: LPS at a final concentration of 1 ng/ml, TGF-β at a final concentration of 50 μg/ml and M-CSF at a final concentration of 10 ng/ml.

RNA isolation and RT–PCR

$CD11b^+CD45^{int}$ cells were FACS-sorted directly to TRIzol® LS, and total RNA was extracted according to the manufacturer's protocol (Life Technologies). RNA from primary cells was extracted using the RNeasy Mini Kit (QIAGEN), according to the manufacturer's instructions. RNA concentration was quantified by NanoDrop (NanoDrop Technologies) and the quality assessed by the quotient of the 28S to 18S ribosomal RNA electropherogram peak using a bioanalyser (Agilent 2100; Agilent Technologies) using a RNA Pico Chip (Agilent Technologies; only samples with RIN ≥ 7 were further analysed). For cDNA synthesis, RNA was reverse-transcribed using SuperScript™ III reverse transcriptase (10,000 U; Invitrogen/Life Technologies) with 1 μl (50 μM)/reaction oligo(dT)20 (25 μM; Invitrogen/Life Technologies) as primer according to the manufacturer's instructions. Reverse transcription was performed at 50°C for 60 min. Gene expression reaction mixtures contained 2 μl of diluted cDNA, 10 μl of Fast SYBR Green Master Mix (Applied Biosystems/Thermo Fisher Scientific) and 0.5 μl of each 10 μM forward and reverse primers. PCRs were carried out in 96-well plates on a ViiA™ 7 real-time PCR system (Applied Biosystems/Thermo Fisher Scientific) using the following programme: 95°C for 20 s, 40 cycles at 95°C for 1 s and 60°C for 20 s. The sequences of the primers designed using Primer-Blast tool are listed in Appendix Table S3. Samples were run in duplicates, and the mean C_t (threshold cycle) values were used to calculate the relative amount of product by the $\Delta\Delta C_t$ method using *Gapdh* as housekeeping gene.

Immunohistochemistry

Under deep ketamine–dorbene anaesthesia, mice were transcardially perfused with ice-cold PBS, post-fixed in 4% paraformaldehyde (PFA) for 48 h and stored at 4°C in 0.02% sodium azide/PBS as preservative. Serialized parasagittal free-floating 50-μm-thick

sections were generated with a vibratome (Leica; VT-1000S) and collected in cryoprotective medium [PBS containing 1-1 ethylene glycol (Sigma-Aldrich) and 1% w/v polyvinylpyrrolidone (Sigma-Aldrich)]. Sections were stored at −20°C in tubes, each containing a series of every 4th section.

For immunofluorescence, a standard protocol was used with minor modifications [70]. Briefly, sections were washed (PBS with 0.1% Triton X-100), permeabilized (PBS with 1.5% Triton X-100), blocked (PBS with 5% BSA) and incubated with primary antibodies (PBS with 0.3% Triton X-100 and 2% BSA): rabbit anti-Iba1 (1:1,000; Wako) and pre-conjugated PE anti-mouse Notch4 (1:80; BioLegend). Iba1 antibody was visualized using goat anti-rabbit IgG Molecular Probes Alexa Fluor 555 (Thermo Fisher Scientific) secondary antibody. Cell nuclei were counterstained with Hoechst (1 μg/ml; Sigma). Sections were mounted on glass slides cover-slipped using Fluoromount™ Aqueous Mounting Medium (Sigma). Microscopic images were obtained using confocal microscopy (Zeiss LSM880).

SDS–PAGE and Western Blotting analysis

Heat-denatured protein samples were separated on 4–12% BisTris–polyacrylamide gel electrophoresis followed by transfer to nitrocellulose membranes 0.2 μm (Bio-Rad). After blocking with 5% (wt/vol) dry milk in TBST for STAT3 and 3% BSA in TBST for Phospho-STAT3, respectively, the membrane was incubated overnight at 4°C in primary anti-STAT3 antibody from mouse (Cell Signaling) diluted 1:1,000 in 5% (wt/vol) dry milk in TBST and in primary anti-Phospho-STAT3 antibody (Cell Signaling) diluted 1:500 in 3% BSA in TBST with constant shaking. After three washing steps with TBS containing 0.1% Tween-20, the membrane was incubated with anti-rabbit antibody or anti-mouse respectively, coupled to horseradish peroxidase and revealed by chemoluminescence using the Pierce™ ECL detection reagents (Thermo Fisher Scientific).

Single-cell RNA sequencing using Drop-seq

Cell preparation

FACS-sorted $CD11b^{+}CD45^{int}$ cells were collected in pre-cooled HBSS and 0.5% BSA and transferred directly for subsequent Drop-seq analysis. The cells were stored on ice until the start of the Drop-seq experiment (tissue harvest to running of Drop-seq was < 1 h). Prior to cell loading on the Drop-seq chips, the cell viability was verified and the concentration was adjusted to ~150 cells/μl. This was optimal based on Poissonian statistics to achieve single-cell encapsulation within each droplet of ~800–900 pl droplet size. All samples analysed in this work had a cell viability > 95%.

Microfluidics fabrication

Microfluidics devices were generated using a previously published design [23]. Soft lithography was performed using SU-8 2050 photoresist (MicroChem) on 4" silicon substrate to obtain a feature aspect depth of 100 μm. After overnight silanization (using chlorotrimethylsilane; Sigma), the wafer masks were used for microfluidics fabrication. Drop-seq chips were fabricated using silicon-based polymerization chemistry, with the previously published protocol [71]. Briefly, polydimethylsiloxane (PDMS) base and cross-linker (Dow Corning) were mixed at a 10:1 ratio, mixed and degassed before pouring onto the Drop-seq master template. PDMS was cured on the master template, at 80°C for 2 h. After incubation and cooling, PDMS monoliths were cut and the inlet/outlet ports were punched with 1.25-mm biopsy punchers (World Precision Instruments). The PDMS monolith was plasma-bonded to a clean microscopic glass slide using a Harrick plasma cleaner. Immediately after pairing the plasma-treated surfaces of the PDMS monolith and the glass slide, flow channels of the Drop-seq chip were subjected to a hydrophobicity treatment using 1H,1H,2H,2H-perfluorodecyltrichlorosilane (in 2% v/v in FC-40 oil; Alfa Aesar/Sigma). After 5 min of treatment, excessive silane was blown through the inlet/outlet ports. Chips were further incubated at 80°C for 15 min.

Single-cell droplet encapsulation

Experiments followed the original Drop-seq protocol [23] with minor changes described below. Synthesized barcoded beads (ChemGenes Corp., USA) were co-encapsulated with cells inside the droplets containing lysis reagents using an optimal bead concentration of 200 beads/μl in Drop-seq Lysis buffer medium. Cellular mRNA was captured on the beads via barcoded oligo (dT) handles synthesized on the surface.

For cell encapsulation, bead suspensions and cell suspension were loaded into 3-ml syringes (BD). To keep beads in homogenous suspension, a micro-stirrer was used (VP Scientific). The QX200 carrier oil (Bio-Rad) used as continuous phase in the droplet generation was loaded into a 20-ml syringe (BD). For droplet generation, 3.6 ml/h and 13 ml/h flowrates were used in KD Scientific Legato Syringe Pumps for the dispersed and continuous phase flows, respectively. After stabilization of droplet formation, the droplet suspension was collected into a 50-ml Falcon tube. Collection of the emulsion was carried out until 1 ml of the single-cell suspension was dispensed. Droplet consistency and stability were evaluated by bright-field microscopy using INCYTO C-Chip Disposable Hemacytometer (Thermo Fisher Scientific). Bead occupancy within droplets was carefully monitored to avoid multiple beads per droplet.

The subsequent steps of droplet breakage, bead harvesting, reverse transcription and exonuclease treatment were carried out in accordance with the Drop-seq method [23]. RT buffer contained 1× Maxima RT buffer, 4% Ficoll PM-400 (Sigma), 1 μM dNTPs (Thermo Fisher Scientific), 1 U/ml RNase Inhibitor (Lucigen), 2.5 μM Template Switch Oligo [23] and 10 U/ml Maxima H-RT (Thermo Fisher Scientific). After Exo-I treatment, the bead counts were estimated using INCYTO C-Chip Disposable Hemacytometer, and 5,000–8,000 beads were aliquoted in 0.2 ml Eppendorf PCR tubes. PCR mix was dispensed in a volume of 50 μl using 1× HiFi HotStart ReadyMix (Kapa Biosystems) and 0.8 mM Template Switch PCR primer. The thermocycling programme for the PCR amplification was modified for the final PCR cycles by 95°C (3 min), four cycles of 98°C (20 s), 65°C (45 s), 72°C (3 min) and 16 cycles of 98°C (20 s), 67°C (20 s), 72°C (3 min), followed by a final extension step of 72°C for 5 min. After PCR amplification, libraries were purified with 0.6× Agencourt AMPure XP beads (Beckman Coulter), according to the manufacturer's protocol. Finally, the purified libraries were eluted in 20 μl RNase/DNase-free Molecular Grade Water. Quality and concentration of the sequencing libraries were assessed using Bioanalyzer High Sensitivity Chip (Agilent Technologies).

NGS preparation for Drop-seq libraries

The 3′ end enriched cDNA libraries were prepared by tagmentation reaction of 600 pg cDNA library using the standard Nextera XT tagmentation kit (Illumina). Reactions were performed according to the manufacturer's instructions. The PCR amplification cycling programme used was 95°C 30 s, and fourteen cycles of 95°C (10 s), 55°C (30 s) and 72°C (30 s), followed by a final extension step of 72°C (5 min). Libraries were purified twice to reduce primers and short DNA fragments with 0.6× and 1× Agencourt AMPure XP beads (Beckman Coulter), respectively, in accordance with the manufacturer's protocol. Finally, purified libraries were eluted in 15 μl Molecular Grade Water. Quality and quantity of the tagmented cDNA library were evaluated using Bioanalyzer High Sensitivity DNA Chip. The average size of the tagmented libraries prior to sequencing was between 400 and 700 bps.

Purified Drop-seq cDNA libraries were sequenced using Illumina NextSeq 500 with the recommended sequencing protocol except for 6pM of custom primer (GCCTGTCCGCGGAAGCAGTGGTATCAACG CAGAGTAC) applied for priming of read 1. Paired-end sequencing was performed for the read 1 of 20 bases (covering the random cell barcode 1–12 bases and the rest 13–20 bases of random unique molecular identifier (UMI) and for read 2 of 50 bases of the genes.

Bioinformatics processing and data analysis

The FASTQ files were assembled from the raw BCL files using Illumina's bcl2fastq converter and ran through the FASTQC codes (Babraham bioinformatics; https://www.bioinformatics.babraham.ac.uk/projects/fastqc/) to check for consistency in library qualities. The monitored quality assessment parameters were (i) quality per base sequence (especially for the read 2 of the gene), (ii) per base N content, (iii) per base sequence content, and (iv) over-represented sequences. Libraries that showed significant deviation were re-sequenced. The FASTQ files were then merged and converted into binaries using PICARD's FastqToSam algorithm. The sequencing reads were converted into a digital gene expression matrix using the Drop-seq bioinformatics pipeline [23].

Data analysis was done in R. Cells with less than 1,000 counts and genes with zero count in all cells were excluded from subsequent analyses, resulting in 1,247 cells (477 from the saline control and 770 from LPS-injected mice) and 12,369 genes. PCA (*prcomp* function *with scaling*) was used for dimensionality reduction, and PCA results were projected onto a two-dimensional (2D) space using *t*-distributed stochastic neighbour embedding (tSNE, *tsne package*, v.0.1-3). As the first principal component was strongly correlated to the total number of UMI (reads) per cell, it was not included in the 2D-tSNE analysis. Differential expression analysis was performed with MAST [57]. *P*-values were adjusted for multiple testing using false discovery rate (FDR) [72]. Prior to MAST analysis, counts were converted into counts per million and log2-transformed. For subpopulation identification, two approaches were used: (i) based on visual inspection of 2D-tSNE plot, cells were divided into three clusters: one cluster contained almost exclusively cells isolated from control mice, another cluster contained mainly cells harvested from LPS-injected mice, and the last cluster was constituted of a small subset of LPS-derived cells. Clusters were pruned to keep only cells coming from the predominant sample in the group. Comparisons of gene expression between different groups were done with the Kruskal–Wallis *H*-test. *P*-values were corrected with FDR [72]; (ii) each condition was analysed separately with the "SC3" package [67]. Branching analysis was performed by Monocle 2.4.0 in R (version 3.4.4) with standard parameters [68,73]. The branching method orders cells along an estimated cell trajectory within a gene expression state space based on gene expression similarities estimated by generalized linear regression models.

Statistical analysis

Statistical analyses for qPCRs and FACS experiments were performed using GraphPad Prism 7 software. Comparisons of two groups were performed with a two-tailed Student's *t*-test. Comparisons involving more than two groups were performed using one-way ANOVA followed by the Bonferroni correction for multiple testing. All differences were considered significantly different at $P < 0.05$. Further statistical analysis details are reported in the figure legends.

Data availability

Single-cell RNA sequencing data have been deposited in Gene Expression Omnibus (GEO) database under the accession number GSE115571 (https://www.ncbi.nlm.nih.gov/geo/query/acc.cgi?acc=GSE115571).

Expanded View for this article is available online.

Acknowledgements

We thank Dr. Coralie Guérin and Dr. Léa Guyonnet for helping with flow cytometry experiments as well as Eliane Klein for Western blot analyses. We are grateful to Dr. Tony Heurtaux for technical assistance with cultivated microglial as well as Oihane Uriarte and Dr. Manuel Buttini for immunohistochemistry analyses. C.S. was supported by the Luxembourg National Research Fund (AFR project reference 6916713) and the Fondation du Pélican de Mie et Pierre Hippert-Faber Under the Aegis of Fondation de Luxembourg. Y.P.A. and S.M. were supported by the Luxembourg National Research Fund (PRIDE15/10675146 and PRIDE16/10907093, respectively). A.S. was supported by the C14/BM/7975668/CaSCAD project as well as by the National Biomedical Computation Resource (NBCR) through the NIH P41 GM103426 grant from the National Institutes of Health. We acknowledge financial support by the Luxembourg Institute of Health (MIGLISYS) and the Luxembourg Centre for Systems Biomedicine.

Author contributions

CS and AM designed the project; KB, RB and SPN involved in the experimental design; CS, SKP, YP-A and AM performed experiments; CS, AG, SKP, TK, SM, AS and AM analysed experiments; DC provided animals; FA supervised the bioinformatics analyses of the single-cell RNA-seq; CS and AM wrote the manuscript; and AG, SKP, TK, DC, YP-A, SM, FA, AS, RB, KB and SPN edited and approved the manuscript.

Conflict of interest

The authors declare that they have no conflict of interest.

References

1. Prinz M, Priller J (2014) Microglia and brain macrophages in the molecular age: from origin to neuropsychiatric disease. *Nat Rev Neurosci* 15: 300 – 312

2. Sousa C, Biber K, Michelucci A (2017) Cellular and molecular characterization of microglia: a unique immune cell population. *Front Immunol* 8: 198
3. Gautier EL, Shay T, Miller J, Greter M, Jakubzick C, Ivanov S, Helft J, Chow A, Elpek KG, Gordonov S *et al* (2012) Gene-expression profiles and transcriptional regulatory pathways that underlie the identity and diversity of mouse tissue macrophages. *Nat Immunol* 13: 1118 – 1128
4. Hickman SE, Kingery ND, Ohsumi TK, Borowsky ML, Wang LC, Means TK, El Khoury J (2013) The microglial sensome revealed by direct RNA sequencing. *Nat Neurosci* 16: 1896 – 1905
5. Butovsky O, Jedrychowski MP, Moore CS, Cialic R, Lanser AJ, Gabriely G, Koeglsperger T, Dake B, Wu PM, Doykan CE *et al* (2014) Identification of a unique TGF-beta-dependent molecular and functional signature in microglia. *Nat Neurosci* 17: 131 – 143
6. Zhang Y, Chen K, Sloan SA, Bennett ML, Scholze AR, O'Keeffe S, Phatnani HP, Guarnieri P, Caneda C, Ruderisch N *et al* (2014) An RNA-sequencing transcriptome and splicing database of glia, neurons, and vascular cells of the cerebral cortex. *J Neurosci* 34: 11929 – 11947
7. Butovsky O, Jedrychowski MP, Cialic R, Krasemann S, Murugaiyan G, Fanek Z, Greco DJ, Wu PM, Doykan CE, Kiner O *et al* (2015) Targeting miR-155 restores abnormal microglia and attenuates disease in SOD1 mice. *Ann Neurol* 77: 75 – 99
8. Elliott R, Li F, Dragomir I, Chua MM, Gregory BD, Weiss SR (2013) Analysis of the host transcriptome from demyelinating spinal cord of murine coronavirus-infected mice. *PLoS One* 8: e75346
9. Holtman IR, Raj DD, Miller JA, Schaafsma W, Yin Z, Brouwer N, Wes PD, Moller T, Orre M, Kamphuis W *et al* (2015) Induction of a common microglia gene expression signature by aging and neurodegenerative conditions: a co-expression meta-analysis. *Acta Neuropathol Commun* 3: 31
10. Lewis ND, Hill JD, Juchem KW, Stefanopoulos DE, Modis LK (2014) RNA sequencing of microglia and monocyte-derived macrophages from mice with experimental autoimmune encephalomyelitis illustrates a changing phenotype with disease course. *J Neuroimmunol* 277: 26 – 38
11. Olah M, Amor S, Brouwer N, Vinet J, Eggen B, Biber K, Boddeke HW (2012) Identification of a microglia phenotype supportive of remyelination. *Glia* 60: 306 – 321
12. Verheijden S, Beckers L, Casazza A, Butovsky O, Mazzone M, Baes M (2015) Identification of a chronic non-neurodegenerative microglia activation state in a mouse model of peroxisomal beta-oxidation deficiency. *Glia* 63: 1606 – 1620
13. Wang Y, Cella M, Mallinson K, Ulrich JD, Young KL, Robinette ML, Gilfillan S, Krishnan GM, Sudhakar S, Zinselmeyer BH *et al* (2015) TREM2 lipid sensing sustains the microglial response in an Alzheimer's disease model. *Cell* 160: 1061 – 1071
14. Keren-Shaul H, Spinrad A, Weiner A, Matcovitch-Natan O, Dvir-Szternfeld R, Ulland TK, David E, Baruch K, Lara-Astaiso D, Toth B *et al* (2017) A unique microglia type associated with restricting development of Alzheimer's disease. *Cell* 169: 1276 – 1290 e17
15. Krasemann S, Madore C, Cialic R, Baufeld C, Calcagno N, El Fatimy R, Beckers L, O'Loughlin E, Xu Y, Fanek Z *et al* (2017) The TREM2-APOE pathway drives the transcriptional phenotype of dysfunctional microglia in neurodegenerative diseases. *Immunity* 47: 566 – 581 e9
16. Chiu IM, Morimoto ET, Goodarzi H, Liao JT, O'Keeffe S, Phatnani HP, Muratet M, Carroll MC, Levy S, Tavazoie S *et al* (2013) A neurodegeneration-specific gene-expression signature of acutely isolated microglia from an amyotrophic lateral sclerosis mouse model. *Cell Rep* 4: 385 – 401
17. Orre M, Kamphuis W, Osborn LM, Jansen AHP, Kooijman L, Bossers K, Hol EM (2014) Isolation of glia from Alzheimer's mice reveals inflammation and dysfunction. *Neurobiol Aging* 35: 2746 – 2760
18. Norden DM, Godbout JP (2013) Review: microglia of the aged brain: primed to be activated and resistant to regulation. *Neuropathol Appl Neurobiol* 39: 19 – 34
19. Crotti A, Ransohoff RM (2016) Microglial physiology and pathophysiology: insights from genome-wide transcriptional profiling. *Immunity* 44: 505 – 515
20. Fullerton JN, Gilroy DW (2016) Resolution of inflammation: a new therapeutic frontier. *Nat Rev Drug Discov* 15: 551 – 567
21. Wyss-Coray T, Mucke L (2002) Inflammation in neurodegenerative disease–a double-edged sword. *Neuron* 35: 419 – 432
22. Glass CK, Saijo K, Winner B, Marchetto MC, Gage FH (2010) Mechanisms underlying inflammation in neurodegeneration. *Cell* 140: 918 – 934
23. Macosko EZ, Basu A, Satija R, Nemesh J, Shekhar K, Goldman M, Tirosh I, Bialas AR, Kamitaki N, Martersteck EM *et al* (2015) Highly parallel genome-wide expression profiling of individual cells using nanoliter droplets. *Cell* 161: 1202 – 1214
24. Shalek AK, Satija R, Adiconis X, Gertner RS, Gaublomme JT, Raychowdhury R, Schwartz S, Yosef N, Malboeuf C, Lu D *et al* (2013) Single-cell transcriptomics reveals bimodality in expression and splicing in immune cells. *Nature* 498: 236 – 240
25. Tang F, Barbacioru C, Wang Y, Nordman E, Lee C, Xu N, Wang X, Bodeau J, Tuch BB, Siddiqui A *et al* (2009) mRNA-Seq whole-transcriptome analysis of a single cell. *Nat Methods* 6: 377 – 382
26. Tasic B, Menon V, Nguyen TN, Kim TK, Jarsky T, Yao Z, Levi B, Gray LT, Sorensen SA, Dolbeare T *et al* (2016) Adult mouse cortical cell taxonomy revealed by single cell transcriptomics. *Nat Neurosci* 19: 335 – 346
27. Mathys H, Adaikkan C, Gao F, Young JZ, Manet E, Hemberg M, De Jager PL, Ransohoff RM, Regev A, Tsai LH (2017) Temporal tracking of microglia activation in neurodegeneration at single-cell resolution. *Cell Rep* 21: 366 – 380
28. Dulken BW, Leeman DS, Boutet SC, Hebestreit K, Brunet A (2017) Single-cell transcriptomic analysis defines heterogeneity and transcriptional dynamics in the adult neural stem cell lineage. *Cell Rep* 18: 777 – 790
29. Chen R, Wu X, Jiang L, Zhang Y (2017) Single-cell RNA-seq reveals hypothalamic cell diversity. *Cell Rep* 18: 3227 – 3241
30. Artegiani B, Lyubimova A, Muraro M, van Es JH, van Oudenaarden A, Clevers H (2017) A single-cell RNA sequencing study reveals cellular and molecular dynamics of the hippocampal neurogenic niche. *Cell Rep* 21: 3271 – 3284
31. Jaitin DA, Weiner A, Yofe I, Lara-Astiaso D, Keren-Shaul H, David E, Salame TM, Tanay A, van Oudenaarden A, Amit I (2016) Dissecting immune circuits by linking CRISPR-pooled screens with single-cell RNA-seq. *Cell* 167: 1883 – 1896 e15
32. Bennett ML, Bennett FC, Liddelow SA, Ajami B, Zamanian JL, Fernhoff NB, Mulinyawe SB, Bohlen CJ, Adil A, Tucker A *et al* (2016) New tools for studying microglia in the mouse and human CNS. *Proc Natl Acad Sci USA* 113: E1738 – E1746
33. Qin L, Wu X, Block ML, Liu Y, Breese GR, Hong JS, Knapp DJ, Crews FT (2007) Systemic LPS causes chronic neuroinflammation and progressive neurodegeneration. *Glia* 55: 453 – 462
34. Dantzer R (2001) Cytokine-induced sickness behavior: mechanisms and implications. *Ann N Y Acad Sci* 933: 222 – 234
35. Bodea LG, Wang Y, Linnartz-Gerlach B, Kopatz J, Sinkkonen L, Musgrove R, Kaoma T, Muller A, Vallar L, Di Monte DA *et al* (2014)

Neurodegeneration by activation of the microglial complement-phagosome pathway. *J Neurosci* 34: 8546 – 8556
36. Ransohoff RM (2016) A polarizing question: do M1 and M2 microglia exist? *Nat Neurosci* 19: 987 – 991
37. Sedgwick JD, Schwender S, Imrich H, Dorries R, Butcher GW, ter Meulen V (1991) Isolation and direct characterization of resident microglial cells from the normal and inflamed central nervous system. *Proc Natl Acad Sci USA* 88: 7438 – 7442
38. Goldmann T, Wieghofer P, Jordao MJ, Prutek F, Hagemeyer N, Frenzel K, Amann L, Staszewski O, Kierdorf K, Krueger M *et al* (2016) Origin, fate and dynamics of macrophages at central nervous system interfaces. *Nat Immunol* 17: 797 – 805
39. Michelucci A, Heurtaux T, Grandbarbe L, Morga E, Heuschling P (2009) Characterization of the microglial phenotype under specific pro-inflammatory and anti-inflammatory conditions: effects of oligomeric and fibrillar amyloid-beta. *J Neuroimmunol* 210: 3 – 12
40. Beutner C, Linnartz-Gerlach B, Schmidt SV, Beyer M, Mallmann MR, Staratschek-Jox A, Schultze JL, Neumann H (2013) Unique transcriptome signature of mouse microglia. *Glia* 61: 1429 – 1442
41. Haynes SE, Hollopeter G, Yang G, Kurpius D, Dailey ME, Gan WB, Julius D (2006) The P2Y12 receptor regulates microglial activation by extracellular nucleotides. *Nat Neurosci* 9: 1512 – 1519
42. Gosselin D, Link VM, Romanoski CE, Fonseca GJ, Eichenfield DZ, Spann NJ, Stender JD, Chun HB, Garner H, Geissmann F *et al* (2014) Environment drives selection and function of enhancers controlling tissue-specific macrophage identities. *Cell* 159: 1327 – 1340
43. Lavin Y, Winter D, Blecher-Gonen R, David E, Keren-Shaul H, Merad M, Jung S, Amit I (2014) Tissue-resident macrophage enhancer landscapes are shaped by the local microenvironment. *Cell* 159: 1312 – 1326
44. Matcovitch-Natan O, Winter DR, Giladi A, Vargas Aguilar S, Spinrad A, Sarrazin S, Ben-Yehuda H, David E, Zelada Gonzalez F, Perrin P *et al* (2016) Microglia development follows a stepwise program to regulate brain homeostasis. *Science* 353: aad8670
45. Deczkowska A, Matcovitch-Natan O, Tsitsou-Kampeli A, Ben-Hamo S, Dvir-Szternfeld R, Spinrad A, Singer O, David E, Winter DR, Smith LK *et al* (2017) Mef2C restrains microglial inflammatory response and is lost in brain ageing in an IFN-I-dependent manner. *Nat Commun* 8: 717
46. Flanders KC, Ludecke G, Engels S, Cissel DS, Roberts AB, Kondaiah P, Lafyatis R, Sporn MB, Unsicker K (1991) Localization and actions of transforming growth factor-beta s in the embryonic nervous system. *Development* 113: 183 – 191
47. Hamby ME, Hewett JA, Hewett SJ (2010) Smad3-dependent signaling underlies the TGF-beta1-mediated enhancement in astrocytic iNOS expression. *Glia* 58: 1282 – 1291
48. Lindholm D, Castren E, Kiefer R, Zafra F, Thoenen H (1992) Transforming growth factor-beta 1 in the rat brain: increase after injury and inhibition of astrocyte proliferation. *J Cell Biol* 117: 395 – 400
49. Wang X, Chen W, Liu W, Wu J, Shao Y, Zhang X (2009) The role of thrombospondin-1 and transforming growth factor-beta after spinal cord injury in the rat. *J Clin Neurosci* 16: 818 – 821
50. Klempt ND, Sirimanne E, Gunn AJ, Klempt M, Singh K, Williams C, Gluckman PD (1992) Hypoxia-ischemia induces transforming growth factor beta 1 mRNA in the infant rat brain. *Brain Res Mol Brain Res* 13: 93 – 101
51. Flanders KC, Ren RF, Lippa CF (1998) Transforming growth factor-betas in neurodegenerative disease. *Prog Neurobiol* 54: 71 – 85
52. Dobolyi A, Vincze C, Pal G, Lovas G (2012) The neuroprotective functions of transforming growth factor beta proteins. *Int J Mol Sci* 13: 8219 – 8258
53. Wang G, Yu Y, Sun C, Liu T, Liang T, Zhan L, Lin X, Feng XH (2016) STAT3 selectively interacts with Smad3 to antagonize TGF-beta. *Oncogene* 35: 4388 – 4398
54. Carow B, Rottenberg ME (2014) SOCS3, a major regulator of infection and inflammation. *Front Immunol* 5: 58
55. Rouillard AD, Gundersen GW, Fernandez NF, Wang Z, Monteiro CD, McDermott MG, Ma'ayan A (2016) The harmonizome: a collection of processed datasets gathered to serve and mine knowledge about genes and proteins. *Database (Oxford)* 2016: baw100
56. Colonna M, Butovsky O (2017) Microglia function in the central nervous system during health and neurodegeneration. *Annu Rev Immunol* 35: 441 – 468
57. Finak G, McDavid A, Yajima M, Deng J, Gersuk V, Shalek AK, Slichter CK, Miller HW, McElrath MJ, Prlic M *et al* (2015) MAST: a flexible statistical framework for assessing transcriptional changes and characterizing heterogeneity in single-cell RNA sequencing data. *Genome Biol* 16: 278
58. Huang DW, Sherman BT, Lempicki RA (2008) Systematic and integrative analysis of large gene lists using DAVID bioinformatics resources. *Nat Protoc* 4: 44
59. Huang DW, Sherman BT, Lempicki RA (2009) Bioinformatics enrichment tools: paths toward the comprehensive functional analysis of large gene lists. *Nucleic Acids Res* 37: 1 – 13
60. Hsieh CL, Koike M, Spusta SC, Niemi EC, Yenari M, Nakamura MC, Seaman WE (2009) A role for TREM2 ligands in the phagocytosis of apoptotic neuronal cells by microglia. *J Neurochem* 109: 1144 – 1156
61. Takahashi K, Rochford CD, Neumann H (2005) Clearance of apoptotic neurons without inflammation by microglial triggering receptor expressed on myeloid cells-2. *J Exp Med* 201: 647 – 657
62. Zheng H, Jia L, Liu CC, Rong Z, Zhong L, Yang L, Chen XF, Fryer JD, Wang X, Zhang YW *et al* (2017) TREM2 promotes microglial survival by activating Wnt/beta-Catenin pathway. *J Neurosci* 37: 1772 – 1784
63. Safaiyan S, Kannaiyan N, Snaidero N, Brioschi S, Biber K, Yona S, Edinger AL, Jung S, Rossner MJ, Simons M (2016) Age-related myelin degradation burdens the clearance function of microglia during aging. *Nat Neurosci* 19: 995 – 998
64. Streit WJ, Braak H, Xue QS, Bechmann I (2009) Dystrophic (senescent) rather than activated microglial cells are associated with tau pathology and likely precede neurodegeneration in Alzheimer's disease. *Acta Neuropathol* 118: 475 – 485
65. Neves J, Zhu J, Sousa-Victor P, Konjikusic M, Riley R, Chew S, Qi Y, Jasper H, Lamba DA (2016) Immune modulation by MANF promotes tissue repair and regenerative success in the retina. *Science* 353: aaf3646
66. Xia M, Liu J, Wu X, Liu S, Li G, Han C, Song L, Li Z, Wang Q, Wang J *et al* (2013) Histone methyltransferase Ash1 l suppresses interleukin-6 production and inflammatory autoimmune diseases by inducing the ubiquitin-editing enzyme A20. *Immunity* 39: 470 – 481
67. Kiselev VY, Kirschner K, Schaub MT, Andrews T, Yiu A, Chandra T, Natarajan KN, Reik W, Barahona M, Green AR *et al* (2017) SC3: consensus clustering of single-cell RNA-seq data. *Nat Methods* 14: 483 – 486
68. Qiu X, Hill A, Packer J, Lin D, Ma YA, Trapnell C (2017) Single-cell mRNA quantification and differential analysis with Census. *Nat Methods* 14: 309 – 315
69. Losciuto S, Dorban G, Gabel S, Gustin A, Hoenen C, Grandbarbe L, Heuschling P, Heurtaux T (2012) An efficient method to limit

microglia-dependent effects in astroglial cultures. *J Neurosci Methods* 207: 59 – 71

70. Buttini M, Orth M, Bellosta S, Akeefe H, Pitas RE, Wyss-Coray T, Mucke L, Mahley RW (1999) Expression of human apolipoprotein E3 or E4 in the brains of Apoe-/- mice: isoform-specific effects on neurodegeneration. *J Neurosci* 19: 4867 – 4880
71. Mazutis L, Gilbert J, Ung WL, Weitz DA, Griffiths AD, Heyman JA (2013) Single-cell analysis and sorting using droplet-based microfluidics. *Nat Protoc* 8: 870 – 891
72. Benjamini Y, Hochberg Y (1995) Controlling the false discovery rate: a practical and powerful approach to multiple testing. *J R Stat Soc B Methodol* 57: 289 – 300
73. Trapnell C, Cacchiarelli D, Grimsby J, Pokharel P, Li S, Morse M, Lennon NJ, Livak KJ, Mikkelsen TS, Rinn JL (2014) The dynamics and regulators of cell fate decisions are revealed by pseudotemporal ordering of single cells. *Nat Biotechnol* 32: 381 – 386

PAPER 4: Research article.

Co-authored publication (not subject for thesis defence)

frontiers in Immunology

ORIGINAL RESEARCH
published: 29 March 2021
doi: 10.3389/fimmu.2021.639613

Single-Cell Transcriptomics and *In Situ* Morphological Analyses Reveal Microglia Heterogeneity Across the Nigrostriatal Pathway

*Oihane Uriarte Huarte[1,2], Dimitrios Kyriakis[1], Tony Heurtaux[2,3], Yolanda Pires-Afonso[4,5], Kamil Grzyb[1], Rashi Halder[1], Manuel Buttini[1,2], Alexander Skupin[1,6], Michel Mittelbronn[1,2,7,8] and Alessandro Michelucci[1,4]**

[1] Luxembourg Centre for Systems Biomedicine (LCSB), University of Luxembourg, Esch-sur-Alzette, Luxembourg, [2] Luxembourg Center of Neuropathology (LCNP), Luxembourg, Luxembourg, [3] Department of Life Sciences and Medicine (DLSM), University of Luxembourg, Esch-sur-Alzette, Luxembourg, [4] Neuro-Immunology Group, Department of Oncology (DONC), Luxembourg Institute of Health (LIH), Luxembourg, Luxembourg, [5] Faculty of Science, Technology and Medicine, University of Luxembourg, Belvaux, Luxembourg, [6] National Center for Microscopy and Imaging Research, University of California San Diego, La Jolla, CA, United States, [7] Department of Oncology (DONC), Luxembourg Institute of Health (LIH), Luxembourg, Luxembourg, [8] National Center of Pathology (NCP), Laboratoire National de Santé (LNS), Dudelange, Luxembourg

OPEN ACCESS

Edited by:
Jennifer K. Dowling, Royal College of Surgeons in Ireland, Ireland

Reviewed by:
Björn Spittau, Bielefeld University, Germany
Daniel Erny, University of Freiburg Medical Center, Germany

***Correspondence:**
Alessandro Michelucci
alessandro.michelucci@lih.lu

Specialty section:
This article was submitted to Multiple Sclerosis and Neuroimmunology, a section of the journal Frontiers in Immunology

Received: *09 December 2020*
Accepted: *11 March 2021*
Published: *29 March 2021*

Citation:
Uriarte Huarte O, Kyriakis D, Heurtaux T, Pires-Afonso Y, Grzyb K, Halder R, Buttini M, Skupin A, Mittelbronn M and Michelucci A (2021) Single-Cell Transcriptomics and in Situ Morphological Analyses Reveal Microglia Heterogeneity Across the Nigrostriatal Pathway. Front. Immunol. 12:639613. doi: 10.3389/fimmu.2021.639613

Microglia are the resident immune effector cells of the central nervous system (CNS) rapidly reacting to various pathological stimuli to maintain CNS homeostasis. However, microglial reactions in the CNS may also worsen neurological disorders. Hence, the phenotypic analysis of microglia in healthy tissue may identify specific poised subsets ultimately supporting or harming the neuronal network. This is all the more important for the understanding of CNS disorders exhibiting regional-specific and cellular pathological hallmarks, such as many neurodegenerative disorders, including Parkinson's disease (PD). In this context, we aimed to address the heterogeneity of microglial cells in susceptible brain regions for PD, such as the nigrostriatal pathway. Here, we combined single-cell RNA-sequencing with immunofluorescence analyses of the murine nigrostriatal pathway, the most affected brain region in PD. We uncovered a microglia subset, mainly present in the midbrain, displaying an intrinsic transcriptional immune alerted signature sharing features of inflammation-induced microglia. Further, an *in situ* morphological screening of inferred cellular diversity showed a decreased microglia complexity in the midbrain when compared to striatum. Our study provides a resource for the identification of specific microglia phenotypes within the nigrostriatal pathway, which may be relevant in PD.

Keywords: microglia, nigrostriatal pathway, single-cell transcriptomics, cellular heterogeneity, immune alerted, cell morphology, Parkinson's disease

INTRODUCTION

Microglia are the resident immune effectors of the brain that arise from the yolk sac and colonize the brain early during embryonic development (1). Under homeostatic conditions, both during development and in the adult brain, microglia play key roles shaping the neuronal network through synaptic pruning and phagocytosis of apoptotic neurons (2–5). In addition, microglia scan the adult brain and can rapidly react to threatening conditions to mainly maintain the brain homeostasis. In this context, improper immune responses, such as weakened or exaggerated microglia reactions, can play a critical role in the development and progression of neurological diseases with an immunological component (6–8). Thus, specific microglial poised subsets ultimately supporting or harming the neuronal network may contribute to the development and progression of CNS disorders exhibiting regional-specific and cellular pathological hallmarks, such as many neurodegenerative disorders, including Parkinson's disease (PD).

PD is the second most common neurodegenerative disease of aging and the most frequent movement disorder (9). The presence of intracellular inclusions of misfolded alpha-synuclein (α-syn) and the loss of dopaminergic neurons in the substantia nigra pars compacta (SNc), a basal ganglia structure located in the midbrain, characterize the brain of PD patients. In the healthy brain, the dopaminergic neurons in the SNc mainly support the basal ganglia circuit by supplying the striatum with dopamine. Consequently, dopamine levels in the dorsal striatum of PD patients are decreased, triggering the impairment of the nigrostriatal pathway leading to various non-motor and classical motor dysfunctions, including bradykinesia, tremor, posture impairment or rigidity (10–12). Importantly, α-syn aggregation and loss of dopaminergic neurons are associated with neuroinflammation, which also constitutes a hallmark of PD (13). However, the effective role of the neuroinflammatory processes in PD is still unclear. For example, it has not yet been elucidated if specific microglia subsets within the nigrostriatal pathway may play a causative or a protective role for the development and progression of PD (14–16).

In the recent years, microglia heterogeneity in the healthy brain is emerging (17–19). Specifically, microglia diversity across various brain regions has been described at the level of their density, morphology and transcriptional programs (20–22). Further, single-cell RNA-sequencing studies enabled to detect microglia heterogeneity beyond region specificity, unraveling specific microglia subsets within different brain regions (23). Still, none of the previous studies has addressed the heterogeneity of microglial cells in susceptible brain regions for PD, such as the nigrostriatal pathway, at single-cell resolution.

Here, we conducted single-cell RNA-sequencing of the midbrain and striatum in 6-month-old female mice and identified specific microglia subsets characterized by different immune programs. Among them, we detected a subset, mainly composed by microglial cells isolated from the midbrain, displaying an intrinsic immune alerted state sharing genes characterizing microglia under inflammatory conditions (24). Further, we combined single-cell RNA-sequencing analyses with morphological and protein screening of inferred cellular diversity taking cortical microglia as a paradigm for the homeostatic resting state and cerebellar microglia as cells displaying an immune alerted state (21). In line with the single-cell transcriptomics results and their typical resting state, microglia from the cortex and striatum showed higher ramification length and increased branching points compared to microglia from the cerebellum and midbrain. Lastly, we found heterogeneity of microglial cell density within midbrain sub-regions, with the number of Iba1+ cells being higher in the substantia nigra pars reticulata (SNr), similarly to cortex and striatum, while being lower in the SNc and ventral tegmental area (VTA), comparable to cerebellum.

Taken together, our results shed light on the complexity of microglial cell diversity in the nigrostriatal pathway and establish a resource for the identification of specific phenotypes, which might be relevant for the development of PD.

MATERIALS AND METHODS

Animals

C57BL/6J female mice were housed in individually ventilated cages (IVC) in a conventional animal facility at the University of Luxembourg in agreement to the EU Directive 2010/63/EU and Commission recommendation 2007/526/EC. Mice were kept in groups under a dark-light cycle with *ad libitum* access to water and food. The animal work of the present study has been conducted and reported in accordance with the ARRIVE (Animal Research: Reporting of In Vivo Experiments) guidelines to improve the design, analysis and reporting of research using animals, maximizing information published and minimizing unnecessary studies.

Microglia Isolation, RNA Extraction and RT-PCR

Six-month-old C57BL/6J female mice were euthanized in deep anesthesia (intraperitoneal injection of medetomidine 1 mg/kg and ketamine 100 mg/kg) and perfused with PBS. Mouse brains were manually dissected into cortex, cerebellum, midbrain and striatum and tissue was dissociated with Adult Brain Dissociation Kit (Miltenyi Biotec). Microglia were subsequently isolated by magnetic separation. Briefly, a total of $1x10^7$ cells was incubated with 90 µl of MACS buffer and 10 µl of CD11b microbeads antibody (Milteny Biotec) for 20 min at 4°C. Total RNA was extracted from eluted microglial cells using NucleoSpin RNA Plus XS (Macherey-Nagel) for samples containing less than 100.000 CD11b+ cells, whereas the kit innuPREP RNA Mini Kit 2.0 (Analytik Jena) was used for samples constituted by more than 100.000 CD11b+ cells. We measured the RNA concentration and quality by Nanodrop (Nanodrop technologies) and we performed reverse transcription using the ImProm-II reverse Transcription System (Promega) according to manufacturer's instructions. Reverse transcription was performed at 25°C for 5 min, followed by 42°C for 60 min and 70°C for 15 min. For the RT-PCR conducted in 96-well plates,

2 µl of cDNA were mixed with 10 µl of iQ SYBR Green Supermix (Biorad) and 0.5 µl of 10 µM primers. A total volume of 20 µl was added to a LigthCycler 480 Multiwell Plate 96 white (Roche) and RT-PCR was performed in the LigthCycler 480 II (Roche) using the following program: 95°C for 3 min, 40 cycles at 95°C for 3 sec, 60°C for 3 sec and 72°C for 3 sec. For the RT-PCR conducted in 384-well plates, 1 µl of cDNA was mixed with 2.5 µl of SYBR Green Mastermix (Applied Biosystems) with 1.25 µl of water and 0.125 µl of 10 µM primers. A total volume of 5 µl was added to a MicroAmp Optical 384 well-reaction plate (Applied Biosystems) and RT-PCR was performed in the QuantStudio Design & Analysis software (Applied Biosystems) using the following program: 95°C for 3 min, 40 cycles at 95°C for 3 sec, 60°C for 3 sec and 72°C for 3 sec. The primer sequences were as follows. *Gapdh* forward: TGCGACTTCAACAGCAACTC, *Gapdh* reverse: CTTGCTCAGTGTCCTTGCTG; *Cx3cr1* forward: CCTGCCCTTGCTTATCAT, *Cx3cr1* reverse: GCCTTCTTGC GATTCTTG; *Fcrls* forward: TTCTGGTCTTCGCTCCTGTC, *Fcrls* reverse: ACCGCGTCTTGCATTCCTAA; *P2ry12* forward: GTGCAAGGGGTGGCATCTA, *P2ry12* reverse: TGGAACTTGCAGACTGGCAT. The threshold cycle of each gene was determined as PCR cycles at which an increase in reporter fluorescence above a baseline signal was measured. The difference in threshold cycles between the target gene and reference gene *Gapdh* yielded the standardized expression level (dC_T). The expression level of each gene was calculated with the formula 2^{-dCT}. Data are represented as mean ± standard error of the mean (SEM) from three independent experiments. All statistical analyses were performed using GraphPad Prism 8.0 (GraphPad Software, Inc., San Diego, CA). The significance was analyzed by a one-way ANOVA followed by a post-hoc Tukey's test. Differences between groups were considered as significant when p values were less than 0.05 (* $p<0.05$, ** $p< 0.01$, *** $p<0.005$).

Single-Cell RNA-Sequencing

Tissue Dissection and Library Preparation

Six-month-old C57BL/6J female mice were euthanized in deep anesthesia by intraperitoneal injection of medetomidine (1 mg/kg) and ketamine (100 mg/kg) and perfused transcardially with phosphate-buffered saline (PBS). We manually dissected and isolated striatum and midbrain from mouse brains on ice. We separately dissected those brain regions using Adult Brain Dissociation Kit (Miltenyi Biotec). Cells were re-suspended in 0.5% BSA and the single cell RNA libraries were captured using the Drop-seq method (24). The 3'end enriched cDNA libraries were prepared by tagmentation reaction of 600 pg cDNA sample library using the standard Nextera XT tagmentation kit (Illumina). Reactions were performed according to the manufacturer's instructions. The PCR amplification cycling program used was 95°C for 30 sec, and twelve cycles at 95°C for 10 sec, 55°C for 30 sec and 72°C for 30 sec, followed by a final extension step at 72°C for 5 min. Libraries were purified twice to reduce primers and short DNA fragments with 0.6× and 1× Agencourt AMPure XP beads (Beckman Coulter), respectively. Lastly, purified libraries were eluted in 10 µl Molecular Grade Water. Quality and quantity of the tagmented cDNA library were evaluated using Bioanalyzer High Sensitivity DNA Chip. The average size of the tagmented libraries before sequencing was between 400 and 700 bps.

Purified Drop-Seq cDNA libraries were pulled together and sequenced using Illumina NextSeq 500 with the recommended sequencing protocol except for 6 pM of custom primer (GCCTGTCCGCGGAAGCAGTGGTATCAACG CAGAGTAC) applied for priming of read 1. Paired-end sequencing was performed for the read 1 of 20 bases (covering the random cell barcode 1–12 bases and the rest 13–20 bases of random unique molecular identifier) and for read 2 of 60 bases of the mRNAs. Raw reads were further de-multiplexed and processed using the Drop-seq computational pipeline (24).

Single-Cell RNA-Sequencing Data Analysis, Reads Filtering, Alignment and Mapping Quality

We adopted the Drop-seq method as previously described (24). The identification of the low quality cells was done separately in each data set. In order to select only the highest quality data, we sorted the cells by the cumulative gene expression. A subset of cells with the highest cumulative expression was considered for the analysis (25). Additional to this filtering, we defined cells as low-quality, based on three criteria for each cell. The number of expressed genes is higher than 200 with 2 median-absolute-deviations (MADs) above the median, the total number of counts is 2 MADs above or below the median and the percentage of counts to mitochondrial genes is 1.5 MADs above the median. Cells failing at least two criteria were considered as low quality cells and filtered out from further analysis. Similar to the cell filtering, we filtered out the low abundant genes being expressed in less than 5 cells in the data. Moreover, we excluded the mitochondrial and ribosomal genes from the rest of the analysis. The integration of the filtered matrices of the different tissues was performed using Seurat v3.1 (26). The final gene expression matrix, which we used for downstream analyses, consisted of 1,337 cells and 15,446 genes. The filtered count matrix was normalized for library size per cell, whereby the expression level of each gene was divided by the cell's total library size, multiplying this by a scale factor (10,000 default), and natural-log transformed the result, using log1p. Principal component analysis (PCA) was computed using the 5000 most variable genes on the aligned data. The clustering of data was performed using Louvain clustering. The resolution of the clustering was selected based on the best silhouette score of the different resolutions (27). The clusters were identified using the graph-based clustering algorithm implemented in Seurat. Then, differential expression analysis was used to identify whether this clustering segregated the expected cell types in the brain. A short list of manually curated markers was used to infer the identity of the different clusters. Cells assigned as "microglia" were re-projected in two dimensions using again the 5,000 most variable genes of this subset. Next, we performed differential expression analysis on the clusters of these projected microglia populations. For this, we used the function FindAllMarkers on the normalized counts using MAST (28) as test with the total number of transcripts in each

cell as a covariate (LogFC threshold = 0, min pct = 0) and the Bonferroni correction to correct for multiple hypothesis testing (Padj). From this differential gene expression analysis, one small population was annotated as oligodendrocytes. This cluster was filtered out for further analysis. A new PCA was performed using the normalized count matrix of the remaining "purified microglia" population. The new clusters were checked for difference in gene expression levels. We performed differential expression analysis using a generalized linear method with linear predictors adding as covariate the total number of transcripts in each cell using Monocle2 (29). The Benjamini-Hochberg correction was applied to correct for multiple hypothesis testing (here q values were used as more advanced adjusted p-values, which not only consider the sample size, but also take into account an optimized FDR).

Flow Cytometry Analyses

Single-cell suspensions were obtained as previously described for single-cell RNA-seq analyses. Cells were re-suspended in ice-cold HBSS with 2% FBS and 10 mM HEPES (FACS buffer) and filtered through a 70 µm nylon mesh (CellTrics). For multicolor phenotyping, cells were blocked with Fc receptor binding inhibitor (anti-mouse CD16/CD32 monoclonal antibody; 1:100; eBioscience) for 15 min at 4°C to reduce binding of non-specific Fc-gamma receptors, and then stained with fluorochrome-conjugated antibodies (anti-mouse CD45-FITC antibody; 1:1000; eBioscience; anti-mouse CD11b-PERCP_Cy5.5; 1:20; eBioscience; anti-mouse CD83-PE; 1:500; Biolegend; anti-mouse CD206-APC; 1:50; Biolegend) for 30 min at 4°C in the dark. Unstained (control) and stained cells were washed and re-suspended in 100 µL of FACS buffer prior acquisition. Before acquisition, the performance of the instrument was assessed using CS&T beads according to the manufacturer's instructions. Single-stain controls were prepared with UltraComp eBeads (eBioscience) following the manufacturer's instructions and thus used to calculate the compensation matrix. Hoechst (0.1 µg/ml, Bisbenzimide, 33342; Sigma) was added for dead cell discrimination. Samples were run on FACSAria IIu SORP cytometer (Becton Dickinson) and flow cytometry data were analyzed using FlowJo software (v. 10.6.1, Becton Dickinson).

Immunohistochemistry Analyses

Brains were fixed in 4% PFA for 24h and kept in PBS with 0.1% NaN_3. They were cut with vibratome (VT1000S from Leica) into 50 µm sagittal free-floating sections and kept at -20°C in a cryoprotective medium (1:1 v/v PBS/Ethylene Glycol, 10g.L^{-1} Polyvinyl Pyrrolidone). For immunohistochemistry, sections were washed (PBS), permeabilized (PBS with 3% H_2O_2 and 1.5% Triton X-100) and blocked (PBS with 5% BSA). Sections were then incubated overnight (PBS with 0.3% Triton X-100 and 2% BSA) with IBA1 (1:1000; Wako) and tyrosine hydroxylase (TH; 1:1000; ab76442) antibodies. IBA1 was visualized using donkey anti-rabbit IgG Molecular Probes Alexa Fluor 647, while TH using goat anti-chicken IgG Molecular Probes Alexa Fluor 488 (Thermo Fisher). Sections were mounted on glass slides using DAPI-Fluoromount-G (SouthernBiotech). Sections were imaged at 20x using Zeiss Confocal LSM-710. For microglial morphological analyses, Z-stack pictures were taken and at least 12 cells per region in four mice were analyzed using IMARIS software (Bitplane). Lastly, we used GraphPad Prism 8 software for statistical analyses. For parametric groups (cell density and process length), we applied one-way ANOVA with post-hoc Tukey's test. We analyzed non-parametric groups (number of branching points and number of segments) by using Kruskal-Wallis followed by post-hoc Dunn's test.

RESULTS

Single-Cell Transcriptomics Identifies Cellular Diversity of the Midbrain and Striatum

To analyze the cellular and molecular heterogeneity of the nigrostriatal pathway at single-cell resolution, we manually dissected the midbrain and striatum from five 6 month-old C57Bl/6J female mice and used the microfluidic Drop-seq method for single-cell transcriptomics analyses (30) (**Figure 1A**). Unsupervised-clustering and t-distributed stochastic neighbor-embedding (*t*-SNE) projection represented single cells separated into individual clusters. Among 1,337 cells considered for subsequent analyses, 480 cells were from the midbrain and 857 cells from the striatum (**Figure 1B**). Differential expression analysis featuring 15,446 most variable genes between the clusters (FDR<0.05) identified nine specific groups. To gather the resultant identity of the clusters, we analyzed the expression levels of the top genes in each cluster (**Table S1**). We annotated them based on cell type-specific gene markers (31, 32). Specifically, we identified four main clusters, corresponding respectively to astrocytes (e.g. *Gja1*, *Plpp3*, *Slc1a2*, *Aqp4*), microglia (e.g. *P2ry12*, *Hexb*, *Cx3cr1*, *Siglech*), oligodendrocytes (e.g. *Plp1*, *Mbp*, *Mobp*, *Trf*) and endothelial cells (e.g. *Ly6c1*, *Cldn5*, *Pltp*, *Pecam1*). Four smaller clusters were represented by ependymal cells (e.g. *Ccdc153*, *Tmem212*, *Dynlrb2*, *Rsph4a*), choroid plexus cells (*Kcnj13*, *Flor1*, *Clic6*, *Kl*) mainly constituted by striatal cells, neurons/neural stem cells (*Meg3*, *Snhg11*, *Ndrg4*, *Snap25*) and pericytes (e.g. *Cald1*, *Vtn*, *Notch3*, *Snap25*). Lastly, we identified a hybrid cluster represented by a mix of cell-types, including cells expressing neuronal (*Scn7a*, *Map2*) or oligodendrocyte precursor cell (*C1ql1*, *Pdgfra*) markers (**Figure 1C**; **Figure S1**). Next, following the comprehensive characterization of the clusters (**Figure 1D**), we verified that identities, markers, and proportions of cell types matched previous single-cell droplet-based sequencing data from mouse brain tissue (**Figure 1E**) (33), indicating that our results were robust for analyses. Lastly, we showed that cell type distribution was similar across midbrain and striatum, confirming that both cell suspensions contained the brain cell types described above (**Figure 1F**).

Overall, our single-cell approach enabled to identify in an unbiased manner different cell types present in the nigrostriatal pathway, allowing studying them separately and at single-cell resolution.

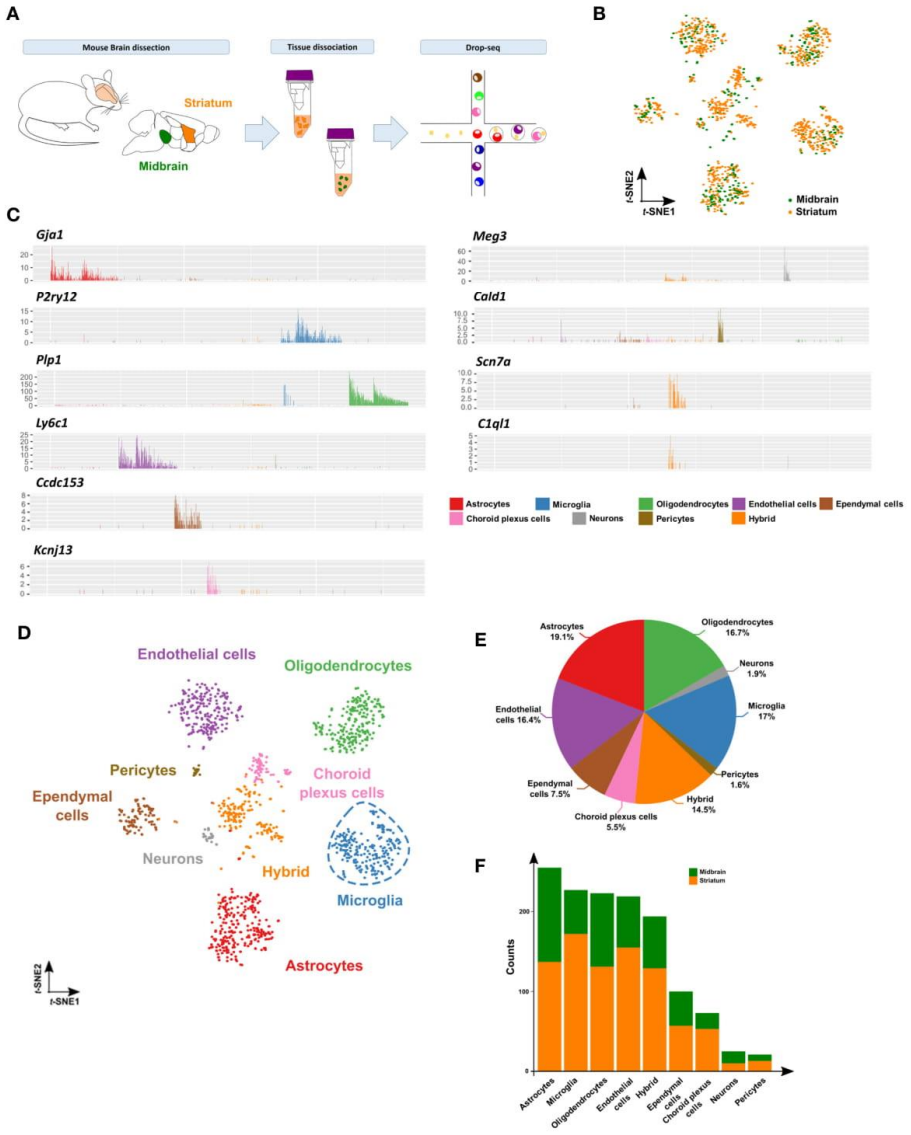

FIGURE 1 | Single-cell transcriptomics identifies cellular diversity of the midbrain and striatum. **(A)** Schematic representation of the experimental approach. Tissue dissected and dissociated from midbrain (in green) and striatum (in orange) of six months-old C57BL/6J mice (pool of 5 mice) analyzed by Drop-seq. **(B)** *t*-SNE projection of 1,337 single cells included in the study showing 480 cells isolated from midbrain (in green) and 857 cells from striatum (in orange). **(C)** Bar plots of representative cell type-specific markers across nine identified clusters: microglia (*P2ry12*), astrocytes (*Gja1*), oligodendrocytes (*Plp1*), endothelial cells (*Ly6c1*), hybrid (*Scn7a* and *C1ql1*), ependymal cells (*Ccdc153*), choroid plexus cells (*Kcnj13*), neurons/neuronal stem cells (*Meg3* and *Snhg11*) and pericytes (*Cald1*, *Vtn*, *Notch3*) clusters. See **Figure S1** and **Table S1** for additional cell type-specific markers used for cluster annotation. **(D)** Annotated clusters in the *t*-SNE map showing nine specific groups identified by differential expression analysis featuring 15,446 total genes (FDR<0.05): microglia (in blue), astrocytes (in red), oligodendrocytes (in green), endothelial cells (in purple), hybrid (orange), ependymal cells (brown), choroid plexus cells (in pink), neurons/neuronal stem cells (in grey) and pericytes (in pale brown). **(E)** Pie chart depicting the percentage of the identified cell types. **(F)** Bar plot showing proportion of cell types within midbrain (in green) and striatum (in orange).

Microglia Within the Nigrostriatal Pathway Segregate Into Specific Immune Subsets

As we were interested to elucidate the heterogeneity of microglial cells, we selected the corresponding cluster for downstream analyses. First, by testing the purity of the microglia-associated cluster, we identified few cells expressing oligodendrocytic markers, such as *Mbp*, *Mag* or *Plp1*, thus we discarded these cells for subsequent analyses (**Figure S2**). Uniform Manifold Approximation and Projection (UMAP) representation of 210 uncontaminated microglial cells, with 169 cells harvested from the striatum and 41 cells from the midbrain, revealed four different subsets, namely homeostatic, intermediate 1 and 2 and immune alerted (**Figure 2A**). They all contained striatal microglial cells, with a higher proportion of cells in the homeostatic and intermediate subsets, while microglia from the midbrain mostly clustered to the immune alerted subset (**Figure 2B).** To detect transcriptional differences between the four subsets, we first performed differential expression analysis and identified 78 genes (q value < 0.05) (**Figure 2C**; **Table S2**). Corresponding gene ontology analysis using DAVID (34, 35) revealed biological processes associated to "inflammatory response", "cytokine-mediated signaling pathway", "antigen processing and presentation" and "response to lipopolysaccharide" (**Figure 2D**). In line with these terms, KEGG analysis revealed pathways underlying microglia activation, such as TNF, MAPK, Toll-like receptor and NFκB signaling pathways (**Figure 2E**; **Table S3**). Indeed, among the differentially expressed genes, inflammatory markers, such as *Nfkbiz, Ccl4, Cd83, Adamts1, Il1b, Icam1, Fth1, Casp4, Lyz1, Gpr84, Cd14, Socs3* were up-regulated in the immune alerted subset (**Figure 2F**). We confirmed increased amounts of CD83+ cells among CD11b+CD45int cells, representing microglia, in the midbrain (7.58 ± 0.7%) compared to cortex (2.15 ± 1.1%) and striatum (2.42 ± 0.4%) by flow cytometry analyses (**Figure 2G**; **Figure S3**). Additionally, antigen presenting cell markers, including *H2-aa*, *H2-ab1* or *Cd74* were specifically up-regulated in the immune alerted subset (**Figure 2H**), while this subset expressed lower levels of the microglia homeostatic genes, such as *Hexb, Cx3cr1, P2ry12, C1qa* and *Fcrls* (**Figure 2I**). This is reminiscent of the decrease of homeostatic genes in reactive microglia under inflammatory conditions, suggesting that cells belonging to this cluster display an immune alerted-like state. We considered the two intermediate subsets as transitions between homeostatic and immune alerted microglia (**Figure 2A**). To exclude that the immune alerted subset could be, at least partially, constituted by non-parenchymal macrophages that mediate immune responses at brain boundaries, namely border-associated macrophages (BAMs), we verified the expression levels of their recently described specific markers (36–40). Except for *Cd74* and *H2-Ab1*, which are known genes to be also expressed by activated microglia (41), additional specific BAM markers were not detected (e.g. *Lyve1* and *Ccr2*) or expressed by few cells not pertaining to the immune alerted cluster (e.g. *Mrc1*) (**Figure S3**), thus indicating that the identified microglia subsets were mainly constituted by microglial cells. Flow cytometry analyses aimed at examining the expression of CD206 (encoded by *Mrc1*) in CD11b+CD45+ cells (approximately 2-3%) did not detect differences across the analyzed brain regions, hence showing that the midbrain is not enriched with BAMs when compared to striatum and cortex (**Figure S3**).

A recent study described microglia in the cerebellum to be more immune vigilant than cortical microglia (21). Therefore, we examined the expression of microglia homeostatic genes in freshly isolated microglia from midbrain or striatum and compared them with microglia harvested from cortex and cerebellum. For this, we manually dissected the cortex, cerebellum, striatum and midbrain from 6-month C57Bl/6J mouse females and extracted RNA from MACS-isolated CD11b+ cells. In agreement with previous observations (21), microglia isolated from the cerebellum expressed lower levels of the homeostatic genes (e.g. *Cx3cr1, Fcrls, P2ry12)* when compared to the cortex. In line with the results obtained at single-cell resolution, we detected a trend to a decrease of the homeostatic genes in the midbrain compared to the striatum, although these differences did not reach statistical significance (**Figure S3**), probably due to the heterogeneity that we detected within these brain regions at single-cell resolution.

Lastly, besides differences in their immune phenotype, microglial cells in the immune alerted subset exhibited an up-regulation of genes related to TGF-β signaling (*Atf3*, *Egr1*), epigenetic functions (*H3f3b*, *Chd4*), proliferation (*Btg2*), reactive oxygen species-mediated cell death (*Gpx1*), energy production (*Atp5a1*) and autophagy-linked genes (*Vps29*) (**Table S2**).

Taken together, our data suggests that microglial cells in the striatum and midbrain display different immune phenotypes, with the latter enriched by immune alerted microglia. Further, bulk analyses strengthen the importance of single-cell transcriptomics studies, which enabled to detect unprecedented transcriptional microglia subsets across the nigrostriatal pathway.

Midbrain-Enriched Immune Alerted Microglia Show Transcriptional Similarities to Inflammation-Associated Microglia and May Be Supported by Other CNS Glial Cells

Next, to further characterize the immune transcriptional profile of midbrain-enriched immune alerted microglia, we compared its signature with microglia under acute systemic inflammatory conditions gathering the corresponding dataset from our recent study conducted at single-cell resolution using the Drop-seq technology (24). Intriguingly, our previous gene ontology analysis detected biological processes related to "response to lipopolysaccharide". In this context, the comparison of midbrain-enriched immune alerted microglia signature with microglia from lipopolysaccharide-injected mice identified 50% (39 out of 78) of shared differential expressed genes (e.g. *Nfkbia*, *Cd74*, *Socs3* or *Il1a*) (**Figure 3A**). Among these genes, 72% (28 out of 39) were up- or down-regulated in both immune alerted and inflammation-associated microglia populations. Specifically, genes such as *Cd14*, *Gpr84*, *Il1b* and *Fth1* were upregulated in both populations, while *Ccl4*, *Cd83*, *H2-ab1*, *Casp4* were exclusively overexpressed in the immune alerted subset (**Figure 3B**). Further, genes like *Cx3cr1, Hexb, Fcrls* and *P2ry12* were

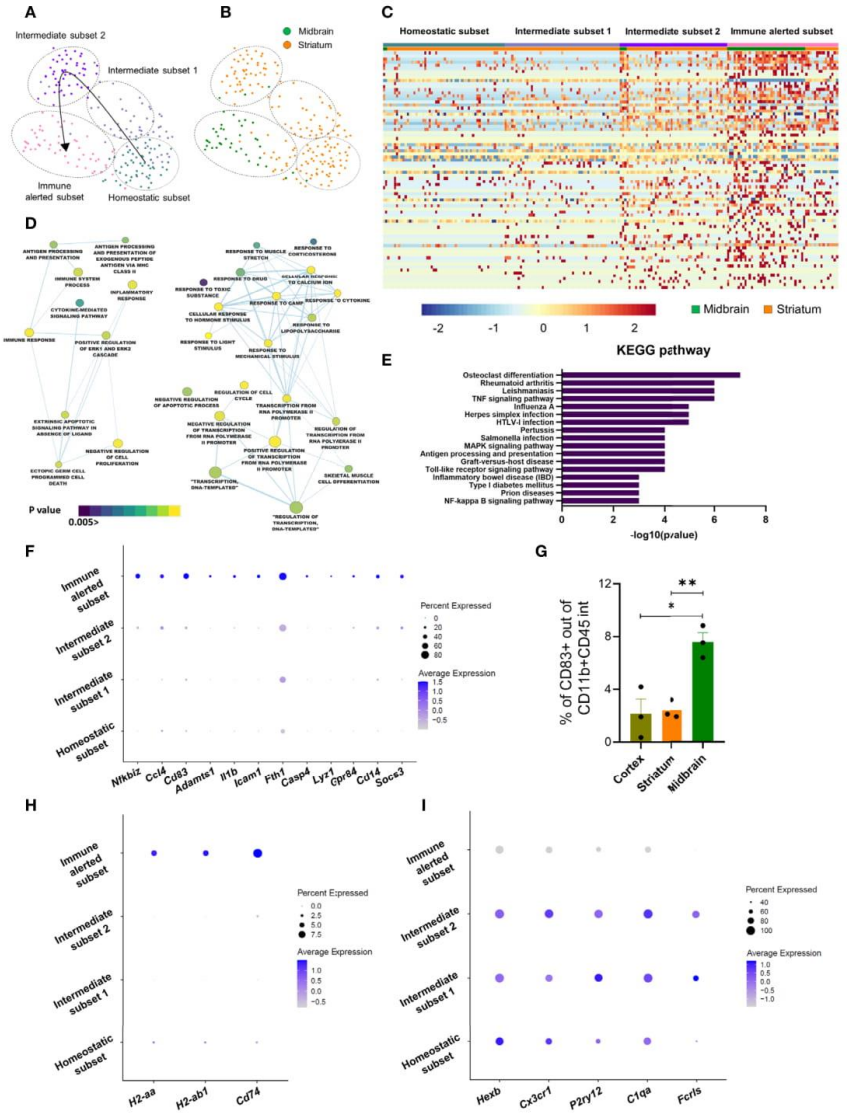

FIGURE 2 | Microglia within the nigrostriatal pathway segregate into specific immune subsets. **(A)** UMAP plot of the re-projected microglia cluster showing four distinct subsets: homeostatic (in grey), intermediate 1 (in pale blue), intermediate 2 (in purple) and immune alerted (in pink). **(B)** UMAP representation showing 210 microglial cells, with 41 cells from the midbrain (in green) and 169 cells from striatum (in orange). **(C)** Heatmap showing clustering analysis of single cells, featuring 78 differential expressed genes across the four subsets (q value < 0.05). Color bar represents z-scores (from low z-score in blue to high z-score in red) (**Table S2**). **(D)** Cytoscape network analysis of gene ontology terms identified by DAVID analysis (p value < 0.05, node cut off q value < 0.1) of the 78 differentially expressed genes across microglia subsets (**Table S3**). **(E)** Top 17 KEGG pathways identified by DAVID resulting from 78 differentially expressed genes (**Table S3**). **(F)** Dot plot representing the expression of inflammatory genes across the microglia subsets. Circle diameter denotes percent expression; color code indicates average expression levels. **(G)** Percentage of CD83+ cells within the CD11b+CD45int population quantified by flow cytometry. Bars represent mean ± SEM (cortex in pale green; striatum in orange; midbrain in green). Unpaired Student t test (n = 3) (*p < 0.05, **p < 0.01). **(H–I)** Dot plots representing **(H)** antigen presenting cell markers and **(I)** homeostatic genes across the microglia subsets. Circle diameter denotes percent expression; color code indicates average expression levels.

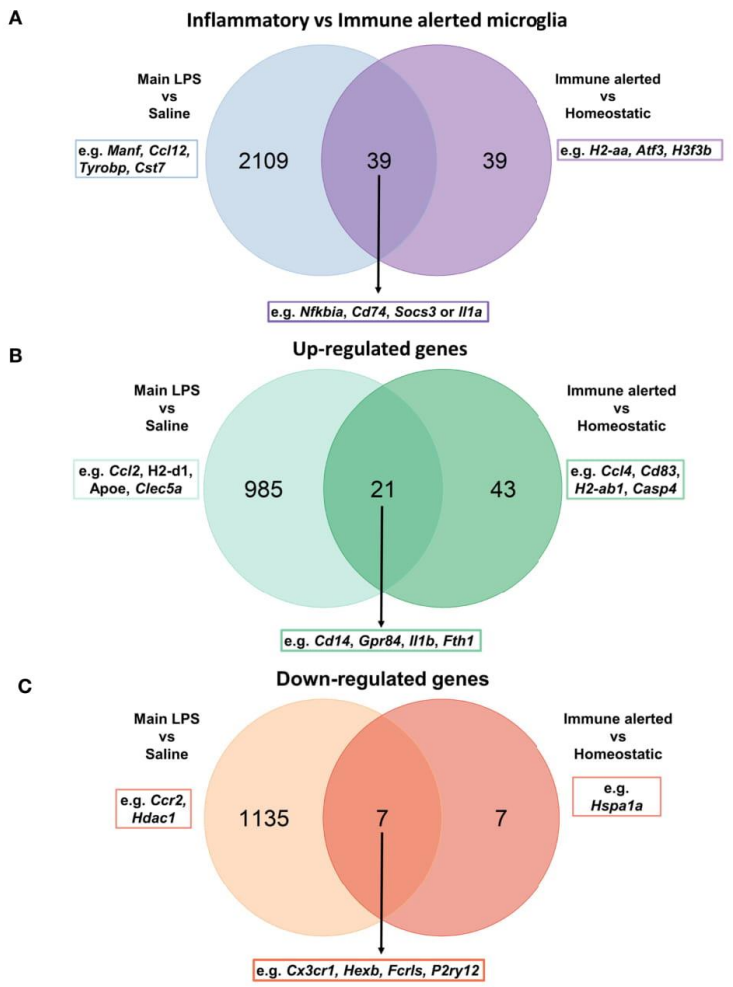

FIGURE 3 | Midbrain-enriched immune alerted microglia show transcriptional similarities to inflammation-associated microglia. **(A–C)** Venn diagrams showing the comparison between 78 differentially expressed genes across midbrain/striatum microglia subsets and 2,148 genes characterizing inflammation-associated microglia (24).

downregulated in both microglia populations, whereas *Hspa1a* was solely decreased in the midbrain-enriched microglia population (**Figure 3C**).

In the CNS, the intense crosstalk of microglial cells with neurons and the other glial cells, including astrocytes, oligodendrocytes and ependymal cells, is critical for the acquisition of the microglial phenotype. Hence, we sought to analyze differentially expressed genes between midbrain and striatum within the corresponding cell clusters (**Table S4**). The low number of neurons isolated with our protocol did not enable us to analyze their differentially expressed genes between the two regions. In contrast, we detected differentially expressed genes across the other glial cells, especially in astrocytes and ependymal cells. When focusing on highly up-regulated genes (logFC > 1; adj p value < 0.05), the expression levels of *Vwa1, Xpr1, H2-T3* and *Foxb1* in astrocytes were increased in the midbrain compared to striatum. Interestingly, *H2-T3* gene, coding for H-2 class I histocompatibility antigen, has been shown to be up-regulated in murine astrocytes under IFNγ exposure (42). On a side note, supporting the accuracy of our dissected brain regions, high expression levels of the transcription factor *Foxb1* (forkhead box B1) in the midbrain are in line with its specific expression in

diencephalic brain regions, such as the *substantia nigra* (43). In this perspective, the *Ttr* gene coding for transthyretin, a protein that in the brain is mainly produced in the choroid plexus (44), was overexpressed in all the main identified cell types of the striatum (**Table S4**). In ependymal cells, the expression levels of *Car9, Fam81b, Atp5f1, Sparcl1, Cfap36* and *Fos* genes were up-regulated in the midbrain. Of note, *Atp5f1* gene encodes a subunit of mitochondrial ATP synthase, the enzyme that catalyzes the production of ATP. Microglia are able to sense and catabolize extracellular ATP, which triggers the recruitment of microglial protrusions and is converted into AMP and adenosine (45).

Taken together, we show that midbrain-enriched immune alerted microglia share transcriptional features of inflammatory and reactive microglia. Transcriptional differences of other glial cells may support the identified "immune alerted" phenotype of microglia in the midbrain.

Microglial Density and Morphology Across Midbrain and Striatum Are Heterogeneous

Then, we studied microglial cell density and morphology across the previously analyzed brain regions. Anatomically, two main subregions, namely the caudoputamen (CP) and the nucleus accumbens (NA), constitute the mouse striatum (**Figure 4A**), whereas three subregions, the SNc, SNr and VTA, compose the midbrain (**Figure 4B**). To link morphology to functionality, we also included cortex and cerebellum in our analyses since microglia from these two brain regions have been previously described to have different immunological phenotypes (21). We used IBA1 antibody to study microglia and tyrosine hydroxylase (TH) to localize the different brain regions and subregions in the mouse tissue by immunofluorescence analyses. We identified different patterns of microglial cell density, with CP, NA and SNr subregions composed by similar shapes than cortex, whereas microglia density in the SNc and VTA was closer to cerebellum. Notably, we observed significant differences between SNc and SNr, with the latter having more IBA1 + cells than SNc (p value<0.005) (**Figure 4C**). Then, to address the complexity of microglia morphology, we analyzed three different parameters: total process length, number of branching points and number of segments. We first confirmed that even though all microglial cells in the mouse brain have a spindle-shaped-like morphology, cells in the cortex are far more complex than cerebellar cells. By applying this analysis to our regions of interest, we observed that microglia morphology in the striatum was similar to the corresponding cells in the cortex, whereas the lower microglia complexity detected in the cerebellum was similar to midbrain (**Figures 4D–G**). We did not detect significant morphological microglia sub-regional variation within midbrain and striatum (**Table S5**).

Taken together, our results confirm the spatial heterogeneity of microglia across different brain regions and further demonstrate organizational and morphological diversities between midbrain and striatum, thus supporting the transcriptional signatures identified at single-cell resolution suggesting that microglia functionality within these regions may be heterogeneous.

DISCUSSION

Neuroinflammation linked to chronic or abnormal microglia activation is supposed to contribute to the loss of dopaminergic neurons in PD (46–48). Microglia actively contribute to PD pathology by reacting to α-syn (49). However, it is still not clear if different microglial cell populations in the healthy brain might be more prone to aberrant activation, which might consequently induce and sustain neurodegeneration under threatening conditions. To address this question, transcriptomic differences of microglia across specific brain regions have been studied over the last years (17, 50). For example, various bulk approaches elucidated microglia features across cortex, cerebellum, hippocampus or the basal ganglia (21, 22, 51). These studies confirmed the diversity of microglia across these brain regions, with microglia in the hippocampus and cerebellum displaying a marked immune vigilant status when compared to cortex and basal ganglia. However, bulk analyses are not suitable to identify specific cellular subsets, since they merely represent the average of specific cellular programs. To overcome this difficulty, single-cell approaches aided to detect, for example, a higher microglia heterogeneity during development (23, 52). In the adult brain, heterogeneity has been primarily linked to specialized microglial cells displaying different predisposition to be activated (23, 50, 52–55). Here, we applied the Drop-seq method (30) to elucidate microglia heterogeneity within the nigrostriatal pathway, the main affected path in PD. First, we took advantage of this technique to decipher the cell taxonomy across midbrain and striatum, revealing the identity of all the main brain cells in line with other studies identifying similar cell types in the cortex, hippocampus or striatum (32, 56, 57). Intriguingly, we detected few cells originally included in the microglia cluster expressing oligodendrocytic markers that we discarded for further analysis. We are currently investigating the biological or technical relevance of these detected cells.

When focusing on microglia heterogeneity in our studied regions, we identified a special subset prevalently composed by cells of the midbrain. The corresponding upregulated genes were mainly related to immune and inflammatory response, thus indicating that this subset display an "immune alerted" phenotype. Notably, microglial activation and inflammation have been reported to contribute to neurodegeneration in *in vivo* models of PD by directly affecting the dopaminergic neurons (47, 58). In addition, midbrain-enriched immune alerted microglial cells were enriched for toll-like receptor (TLR) signaling pathways, which have been linked to neurodegeneration (59). Specifically, TLR4 is involved in microglia activation linked to PD and the lack of *Tlr4* in a PD-like model of MPTP resulted in a reduced microglia activation and a decreased neurodegeneration (60). Further, it has been shown that TLR4 is necessary for α-syn uptake by microglia and their subsequent activation (61). We also identified enrichment expression of antigen processing and presentation markers, including MHC-II signaling pathway. MHC-II is upregulated by microglia in post-mortem brains of PD patients (62) and *in vitro* models have shown its relation between microglia activation and further neurodegeneration (63), thus indicating that MHC-II may be a mediator directly involved in PD pathogenesis.

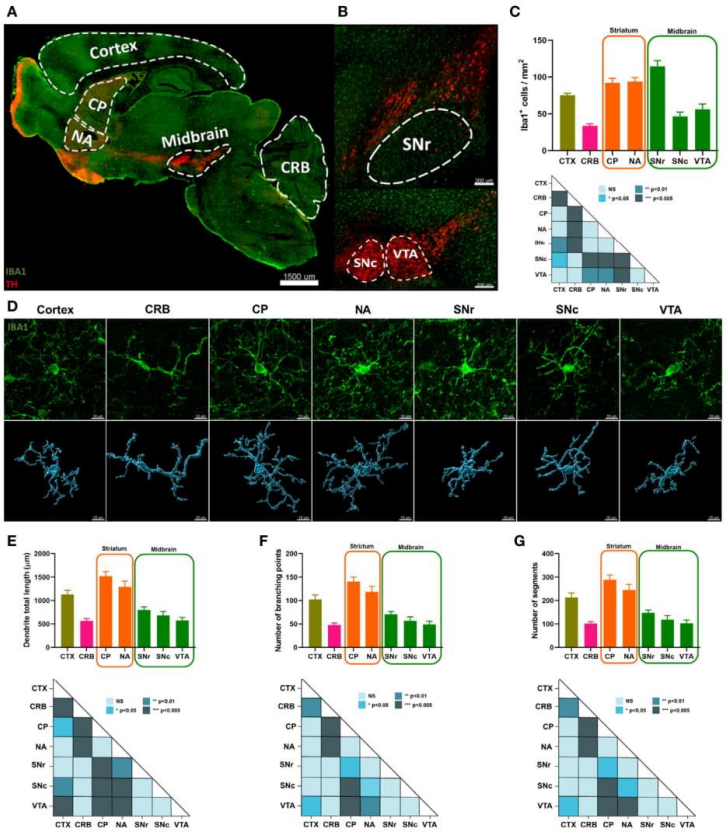

FIGURE 4 | Microglial density and morphology across striatum and midbrain are heterogeneous. **(A)** Representation of different areas analyzed for microglia density and morphology. TH was employed to identify the brain regions, while IBA1 was used to visualize microglia. Scale bar, 1500 µm (CP, caudoputamen; NA, nucleus accumbens; CRB, cerebellum). **(B)** Tile pictures showing midbrain sub-regions in sagittal mouse brain. Scale bar, 200 µm (SNr, substantia nigra pars reticulata; SNc; substantia nigra pars compacta; VTA, ventral tegmental area). **(C)** Quantification of microglial cell density in the different brain areas, cortex (in pale green), cerebellum (in pink), striatum (in orange) and midbrain (in green). Bars represent the mean ± standard error of the mean (SEM) from four independent mice. One-way ANOVA with post-hoc Tukey's test was used for statistical test (*$p < 0.05$, **$p < 0.01$, ***$p < 0.005$). **(D)** 3D reconstruction of representative microglial cells across different brain regions. Scale bar, 10 µm (CRB, cerebellum; CP caudoputamen; NA, nucleus accumbens; SNr, substantia nigra pars reticulata; SNc, substantia nigra pars compacta; VTA, ventral tegmental area). **(E-G)** Quantification of microglial cell complexity across brain regions. Bars represent the mean ± standard error of the mean (SEM) from twelve independent Iba1+ cells. One-way ANOVA with post-hoc Tukey's test was used for statistical test for process total length, whereas Kruskal-Wallis followed by post-hoc Dunn's test was used as statistical test for number of branching points and number of segments (NS not significant, *$p < 0.05$, **$p < 0.01$, ***$p < 0.005$) (**Table S5**). CTX, cortex; CRB, cerebellum; CP caudoputamen; NA, nucleus accumbens; SNr, substantia nigra pars reticulata; SNc, substantia nigra pars compacta; VTA, ventral tegmental area.

Experimentally, peripheral injection of lipopolysaccharide (LPS) in the mouse has been related to neurodegeneration (64) by contributing to the aggregation of different proteins such as α-syn (65). In addition, the consecutive injection of LPS aggravate the loss of dopaminergic neurons, which occurs *via* the activation of the microglial complement-phagosome pathway (47). Taken together, this might indicate that the immune alerted phenotype, mainly displayed by midbrain microglia and few striatal microglia, might turn detrimental in the long term or under specific cues, contributing to dopaminergic neuronal loss triggering PD-like pathogenesis. For example, aged microglia exhibit a primed state characterized by a hyper-reactive response towards threatening conditions. As a consequence, primed microglia release higher amounts of cytokines and chemokines that could turn neurotoxic, thus contributing to disease progression (66). Intriguingly, following LPS administration, midbrain microglia show an immunosuppressive response when compared to microglia from other brain regions, including the

cortex, striatum or hippocampus, indicating that microglia in the midbrain display a dampened response towards an inflammatory insult, hence presenting a tolerogenic and not a primed phenotype (67). Further, the analysis of microglia phenotypes associated with chronic inflammation in a TNF transgenic mouse model recently revealed distinct signatures across different brain regions, including the cortex, striatum, hippocampus, thalamus and cerebellum. More specifically, microglial cells located within the cortex, striatum and thalamus were characterized by the overexpression of inflammatory genes, such as *Cxcl13*, *Ccl2*, *C3* and *C4b*, thus suggesting a more pronounced reactive state of microglia under persistent inflammation in these specific regions when compared to hippocampus and cerebellum (68). These results are in line with our observations since it has been previously shown that, at baseline, hippocampal and cerebellar microglia exist in a more immune-vigilant state (21). Hence, the intrinsic immune-alerted phenotype in the midbrain evidenced by our results as well as the previously described immune-vigilant state in the hippocampus and cerebellum seem to confer microglia the ability to react to an inflammatory stimulus at a lesser extent compared to the corresponding cells in other analyzed brain regions. In the midbrain, whether this putative reduced response might be detrimental for the underlying dopaminergic neuronal network as, for example, threatening conditions cannot be efficiently resolved, remains a matter of investigation. In addition, whether midbrain microglia will similarly respond to a PD-like insult, such as α-syn aggregation or neuronal loss, requires further analyses.

Concomitantly to transcriptional adaptations, morphological changes of microglia also underlie their activated state. Briefly, amoeboid microglia with shorter or thicker ramifications are linked to an activated state, whereas highly ramified phenotypes are associated to classical homeostatic microglia (69–71). In this context, microglia complexity has been described to vary depending on the localization of the cells across specific brain regions (72). Indeed, microglia from cortex, hippocampus and striatum are more complex than microglia from cerebellum (54, 73). In addition, microglia density decreases during the rise of dystrophic and degenerating cells in the aging mouse nigrostriatal pathway (74). In these perspectives, the development of computational and machine learning approaches recently enabled the identification of 9 microglia subsets based on 62 morphological features in the murine hippocampus (75). To complement our analyses, it will be critical to use these approaches to further unraveling clusters of cells across the analyzed brain regions.

Lastly, the recently described heterogeneity of neuronal populations in the nigrostriatal pathway supports our results on microglia diversity in the corresponding brain region. For example, seven subsets of dopaminergic neurons have been identified in the mouse brain, which are also present in humans (76, 77). These studies also highlight the importance of investigating cellular heterogeneity in the murine nigrostriatal pathway, since this region is mainly conserved across mouse and human species.

The combination of single-cell transcriptomics and *in situ* morphological approaches to study microglia phenotypes across the nigrostriatal pathway at baseline enabled us to detect a small subset of cells, mainly constituted by microglia in the midbrain, displaying an immune alerted phenotype, which might have implications in PD. Whether those immune alerted microglia are sustained by specific cues in the midbrain environment, such as mediators released by the highly active dopaminergic neuronal network, or they are ontogenetically different compared to other brain regions needs further investigations. Additional studies elucidating microglia immune phenotypes in relevant PD mouse models and patients, both in males and females, using single-cell transcriptional and imaging approaches, such as imaging mass cytometry, will be critical to understand how different subsets of cells might be beneficial or detrimental during the development and progression of the disease.

DATA AVAILABILITY STATEMENT

The datasets presented in this study can be found in online repositories. The names of the repository/repositories and accession number(s) can be found at: https://www.ncbi.nlm.nih.gov/geo/ GSE148393.

ETHICS STATEMENT

The animal study was reviewed and approved by Animal Experiment Ethics Committee of the University of Luxembourg and the responsible Luxembourg government authorities (Ministry of Health, Ministry of Agriculture).

AUTHOR CONTRIBUTIONS

OUH, MB, MM, and AM designed project. AS set up single-cell analysis. OUH, TH, KG, YP-A, and RH performed experiments. OUH, DK, TH, KG, YP-A, RH, AS, MM, and AM analyzed experiments. MB, AS, MM, and AM supervised research. OUH and AM wrote the manuscript. All authors contributed to the article and approved the submitted version.

FUNDING

OUH was supported by Art2Cure Foundation. DK was supported by the Luxembourg National Research Fund (FNR) through PRIDE17/12244779/PARK-QC. YP-A was supported by the FNR through PRIDE15/10675146/CANBIO and by the Fondation du Pélican de Mie et Pierre Hippert-Faber (Fondation de Luxembourg). AS and KG were supported by the FNR through the C14/BM/7975668/CaSCAD and INTER/DFG/17/11583046 projects as well as by the National Biomedical Computation Resource (NBCR) through the NIH P41 GM103426 grant from the National Institutes of Health. MM would like to thank the FNR for the support (PEARL P16/BM/11192868 grant). Rotary Club Luxembourg in the framework of its initiative "Espoir-en-tête" supported MB, AS, and AM. We acknowledge

financial support by the Luxembourg Institute of Health and the Luxembourg Centre for Systems Biomedicine (MIGLISYS).

ACKNOWLEDGMENTS

We thank Kristopher Schmit for the Venn Diagrams' code and Thomas Cerutti for the precious support with flow cytometry analyses.

SUPPLEMENTARY MATERIAL

The Supplementary Material for this article can be found online at: https://www.frontiersin.org/articles/10.3389/fimmu.2021.639613/full#supplementary-material

Supplementary Figure 1 | Cellular taxonomy across midbrain and striatum. **(A)** Heatmap showing clustering analysis featuring 15 most variable genes per cluster (FDR < 0.05). Color bar represents z-scores (from low z-score in blue to high z-score in red). **(B)** t-SNE representation of cell-type representative genes. Color bar represents z-scores (high z-score in red).

Supplementary Figure 2 | Enrichment of microglial cells across midbrain and striatum. **(A)** Left panel: UMAP representation of microglial cells from the midbrain (in green) and striatum (in orange); right panel: UMAP representation showing four distinct subsets with few microglial cells (in purple) clustering independently. **(B)** Heatmap showing the corresponding microglial cells expressing oligodendrocytic markers (padj < 0.05).

Supplementary Figure 3 | Immune phenotypes across specific brain regions. **(A)** Flow cytometry gating strategy. (i) Cells of interest were gated based on forward-scatter area (FSC-A) and side-scatter area (SSC-A). (ii) Doublets were excluded based on forward-scatter area (FSC-A) versus forward-scatter height (FSC-H). (iii) Hoechst was used to discriminate dead and live cells. (iv) CD45-FITC and CD11b-PERCP_cy5.5 antibodies were used to gate microglia. (v) CD83-PE antibody was used to quantify CD83 expression. (vi) CD45-FITC and CD11b-PERCP_cy5.5 antibodies were used to gate the myeloid compartment. (vii) CD206-APC antibody was used to quantify CD206 expression. **(B)** *t*-SNE and UMAP plots showing *Mrc1* expression across cell types (left) and microglia (right), respectively. Color bars represent z-scores (from low z-score in grey to high z-score in red). **(C)** Percentage of CD206+ cells within the CD11b+CD45+ population quantified by flow cytometry. Bars represent mean ± SEM (cortex in pale green; striatum in orange; midbrain in green). Unpaired Student t test (n = 3). **(D)** Expression levels of microglia homeostatic gene markers in microglia isolated from cortex (in pale green), cerebellum (in pink), striatum (in orange) and midbrain (in green) analyzed by qPCR. *Gapdh* was used as housekeeping gene. Bars represent the mean ± standard error of the mean (SEM) from three independent experiments. One-way ANOVA followed by a post-hoc Tukey's test was used to infer statistical differences between groups (*p < 0.05).

REFERENCES

1. Ginhoux F, Greter M, Leboeuf M, Nandi S, See P, Gokhan S, et al. Fate mapping analysis reveals that adult microglia derive from primitive macrophages. *Science* (2010) 330(6005):841–5. doi: 10.1126/science.1194637
2. Paolicelli RC, Bolasco G, Pagani F, Maggi L, Scianni M, Panzanelli P, et al. Synaptic pruning by microglia is necessary for normal brain development. *Science* (2011) 333(6048):1456–8. doi: 10.1126/science.1202529
3. Sierra A, Abiega O, Shahraz A, Neumann H. Janus-faced microglia: beneficial and detrimental consequences of microglial phagocytosis. *Front Cell Neurosci* (2013) 7:6. doi: 10.3389/fncel.2013.00006
4. Salter MW, Stevens B. Microglia emerge as central players in brain disease. *Nat Med* (2017) 23(9):1018–27. doi: 10.1038/nm.4397
5. Kettenmann H, Kirchhoff F, Verkhratsky A. Microglia: new roles for the synaptic stripper. *Neuron* (2013) Jan 977(1):10–8. doi: 10.1016/j.neuron.2012.12.023
6. Michelucci A, Mittelbronn M, Gomez-Nicola D. Microglia in Health and Disease: A Unique Immune Cell Population. *Front Immunol* (2018) 9:1779. doi: 10.3389/fimmu.2018.01779
7. Colonna M, Butovsky O. Microglia Function in the Central Nervous System During Health and Neurodegeneration. *Annu Rev Immunol* (2017) 35:441–68. doi: 10.1146/annurev-immunol-051116-052358
8. Prinz M, Priller J, Sisodia SS, Ransohoff RM. Heterogeneity of CNS myeloid cells and their roles in neurodegeneration. *Nat Neurosci* (2011) 14(10):1227–35. doi: 10.1038/nn.2923
9. Mhyre TR, Boyd JT, Hamill RW, Maguire-Zeiss KA. Parkinson's disease. *Subcell Biochem* (2012) 65:389–455. doi: 10.1007/978-94-007-5416-4_16
10. Spillantini MG, Schmidt ML, Lee VM, Trojanowski JQ, Jakes R, Goedert M. Alpha-synuclein in Lewy bodies. *Nature* (1997) 388(6645):839–40. doi: 10.1038/42166
11. Bridi JC, Hirth F. Mechanisms of α-Synuclein Induced Synaptopathy in Parkinson's Disease. *Front Neurosci* (2018) 12:80. doi: 10.3389/fnins.2018.00080
12. Lang AE, Lozano AM. Parkinson's Disease. *New Engl J Med* (1998) 339(16):1130–43. doi: 10.1056/NEJM199810153391607
13. Tansey MG, Romero-Ramos M. Immune system responses in Parkinson's disease: Early and dynamic. *Eur J Neurosci* (2019) 49(3):364–83. doi: 10.1111/ejn.14290
14. Duffy MF, Collier TJ, Patterson JR, Kemp CJ, Luk KC, Tansey MG, et al. Lewy body-like alpha-synuclein inclusions trigger reactive microgliosis prior to nigral degeneration. *J Neuroinflammation* (2018) 15(1):129. doi: 10.1186/s12974-018-1202-9
15. Eidson LN, Kannarkat GT, Barnum CJ, Chang J, Chung J, Caspell-Garcia C, et al. Candidate inflammatory biomarkers display unique relationships with alpha-synuclein and correlate with measures of disease severity in subjects with Parkinson's disease. *J Neuroinflammation* (2017) 14(1):164. doi: 10.1186/s12974-017-0935-1
16. Yang X, Ren H, Wood K, Li M, Qiu S, Shi F-D, et al. Depletion of microglia augments the dopaminergic neurotoxicity of MPTP. *FASEB J* (2018) 32(6):3336–45. doi: 10.1096/fj.201700833RR
17. Silvin A, Ginhoux F. Microglia heterogeneity along a spatio-temporal axis: More questions than answers. *Glia* (2018) 66(10):2045–57. doi: 10.1002/glia.23458
18. De Biase LM, Bonci A. Region-Specific Phenotypes of Microglia: The Role of Local Regulatory Cues. *Neuroscientist* (2019) 25(4):314–33. doi: 10.1177/1073858418800996
19. Stratoulias V, Venero JL, Tremblay M-È, Joseph B. Microglial subtypes: diversity within the microglial community. *EMBO J* (2019) 0238(17):e101997. doi: 10.15252/embj.2019101997
20. Doorn KJ, Brevé JJP, Drukarch B, Boddeke HW, Huitinga I, Lucassen PJ, et al. Brain region-specific gene expression profiles in freshly isolated rat microglia. *Front Cell Neurosci* (2015) 9:84. doi: 10.3389/fncel.2015.00084
21. Grabert K, Michoel T, Karavolos MH, Clohisey S, Baillie JK, Stevens MP, et al. Microglial brain region–dependent diversity and selective regional sensitivities to aging. *Nat Neurosci* (2016) 19(3):504–16. doi: 10.1038/nn.4222
22. De Biase LM, Schuebel KE, Fusfeld ZH, Jair K, Hawes IA, Cimbro R, et al. Local Cues Establish and Maintain Region-Specific Phenotypes of Basal Ganglia Microglia. *Neuron* (2017) 95(2):341–56.e6. doi: 10.1016/j.neuron.2017.06.020
23. Masuda T, Sankowski R, Staszewski O, Bottcher C, Amann L, Sagar n, et al. Spatial and temporal heterogeneity of mouse and human microglia at single-cell resolution. *Nature* (2019) 566(7744):388–92. doi: 10.1038/s41586-019-0924-x
24. Sousa C, Golebiewska A, Poovathingal SK, Kaoma T, Pires-Afonso Y, Martina S, et al. Single-cell transcriptomics reveals distinct inflammation-induced microglia signatures. *EMBO Rep* (2018) 19(11):e46171. doi: 10.15252/embr.201846171
25. James NA, Matteson DS. ecp: An R Package for Nonparametric Multiple Change Point Analysis of Multivariate Data. *J Stat Software* (2015) 62(1):1–25. doi: 10.18637/jss.v062.i07

26. Butler A, Hoffman P, Smibert P, Papalexi E, Satija R. Integrating single-cell transcriptomic data across different conditions, technologies, and species. *Nat Biotechnol* (2018) 36(5):411–20. doi: 10.1038/nbt.4096
27. Rousseeuw PJ. Silhouettes: A graphical aid to the interpretation and validation of cluster analysis. *J Comput Appl Mathematics* (1987) 20:53–65. doi: 10.1016/0377-0427(87)90125-7
28. Finak G, McDavid A, Yajima M, Deng J, Gersuk V, Shalek AK, et al. MAST: a flexible statistical framework for assessing transcriptional changes and characterizing heterogeneity in single-cell RNA sequencing data. *Genome Biol* (2015) 16(1):278. doi: 10.1186/s13059-015-0844-5
29. Qiu X, Hill A, Packer J, Lin D, Ma Y-A, Trapnell C. Single-cell mRNA quantification and differential analysis with Census. *Nat Methods* (2017) 14 (3):309–15. doi: 10.1038/nmeth.4150
30. Macosko EZ, Basu A, Satija R, Nemesh J, Shekhar K, Goldman M, et al. Highly Parallel Genome-wide Expression Profiling of Individual Cells Using Nanoliter Droplets. *Cell.* (2015) 161(5):1202–14. doi: 10.1016/j.cell.2015.05.002
31. Cahoy JD, Emery B, Kaushal A, Foo LC, Zamanian JL, Christopherson KS, et al. A Transcriptome Database for Astrocytes, Neurons, and Oligodendrocytes: A New Resource for Understanding Brain Development and Function. *J Neurosci* (2008) 28(1):264–78. doi: 10.1523/JNEUROSCI.4178-07.2008
32. Tasic B, Menon V, Nguyen TN, Kim TK, Jarsky T, Yao Z, et al. Adult mouse cortical cell taxonomy revealed by single cell transcriptomics. *Nat Neurosci* (2016) 19(2):335–46. doi: 10.1038/nn.4216
33. Schaum N, Karkanias J, Neff NF, May AP, Quake SR, Wyss-Coray T, et al. Single-cell transcriptomics of 20 mouse organs creates a Tabula Muris. *Nature.* (2018) 562(7727):367–72. doi: 10.1038/s41586-018-0590-4
34. Huang DW, Sherman BT, Lempicki RA. Systematic and integrative analysis of large gene lists using DAVID bioinformatics resources. *Nat Protoc* (2009) 4 (1):44–57. doi: 10.1038/nprot.2008.211
35. Huang DW, Sherman BT, Lempicki RA. Bioinformatics enrichment tools: paths toward the comprehensive functional analysis of large gene lists. *Nucleic Acids Res* (2009) 37(1):1–13. doi: 10.1093/nar/gkn923
36. Prinz M, Masuda T, Wheeler MA, Quintana FJ. Microglia and Central Nervous System-Associated Macrophages-From Origin to Disease Modulation. *Annu Rev Immunol* (2021). doi: 10.1146/annurev-immunol-093019-110159
37. Utz SG, See P, Mildenberger W, Thion MS, Silvin A, Lutz M, et al. Early Fate Defines Microglia and Non-parenchymal Brain Macrophage Development. *Cell* (2020) 181(3):557–73.e18. doi: 10.1016/j.cell.2020.03.021
38. Van Hove H, Martens L, Scheyltjens I, De Vlaminck K, Pombo Antunes AR, De Prijck S, et al. A single-cell atlas of mouse brain macrophages reveals unique transcriptional identities shaped by ontogeny and tissue environment. *Nat Neurosci* (2019) 22(6):1021–35. doi: 10.1038/s41593-019-0393-4
39. Jordão MJC, Sankowski R, Brendecke SM, Sagar, Locatelli G, Tai Y-H, et al. Single-cell profiling identifies myeloid cell subsets with distinct fates during neuroinflammation. *Science* (2019) 363(6425):eaat7554. doi: 10.1126/science.aat7554
40. Goldmann T, Wieghofer P, Jordão MJC, Prutek F, Hagemeyer N, Frenzel K, et al. Origin, fate and dynamics of macrophages at central nervous system interfaces. *Nat Immunol* (2016) 17(7):797–805. doi: 10.1038/ni.3423
41. Mathys H, Adaikkan C, Gao F, Young JZ, Manet E, Hemberg M, et al. Temporal Tracking of Microglia Activation in Neurodegeneration at Single-Cell Resolution. *Cell Rep* (2017) 21(2):366–80. doi: 10.1016/j.celrep.2017.09.039
42. Kudriaeva A, Galatenko VV, Maltseva DV, Khaustova NA, Kuzina E, Tonevitsky AG, et al. The Transcriptome of Type I Murine Astrocytes under Interferon-Gamma Exposure and Remyelination Stimulus. *Molecules* (2017) 22(5):808. doi: 10.3390/molecules22050808
43. Zhao T, Szabó N, Ma J, Luo L, Zhou X, Alvarez-Bolado G. Genetic mapping of Foxb1-cell lineage shows migration from caudal diencephalon to telencephalon and lateral hypothalamus. *Eur J Neurosci* (2008) 28 (10):1941–55. doi: 10.1111/j.1460-9568.2008.06503.x
44. Richardson SJ, Wijayagunaratne RC, D'Souza DG, Darras VM, Van Herck SLJ. Transport of thyroid hormones via the choroid plexus into the brain: the roles of transthyretin and thyroid hormone transmembrane transporters. *Front Neurosci* (2015) 9:66. doi: 10.3389/fnins.2015.00066
45. Badimon A, Strasburger HJ, Ayata P, Chen X, Nair A, Ikegami A, et al. Negative feedback control of neuronal activity by microglia. *Nature* (2020) 586(7829):417–23. doi: 10.1038/s41586-020-2777-8
46. Cunningham C. Microglia and neurodegeneration: The role of systemic inflammation. *Glia* (2013) 61(1):71–90. doi: 10.1002/glia.22350
47. Bodea L-G, Wang Y, Linnartz-Gerlach B, Kopatz J, Sinkkonen L, Musgrove R, et al. Neurodegeneration by activation of the microglial complement-phagosome pathway. *J Neurosci* (2014) 34(25):8546–56. doi: 10.1523/JNEUROSCI.5002-13.2014
48. Tansey MG, Goldberg MS. Neuroinflammation in Parkinson's disease: its role in neuronal death and implications for therapeutic intervention. *Neurobiol Dis* (2010) 37(3):510–8. doi: 10.1016/j.nbd.2009.11.004
49. Su X, Maguire-Zeiss KA, Giuliano R, Prifti L, Venkatesh K, Federoff HJ. Synuclein activates microglia in a model of Parkinson's disease. *Neurobiol Aging* (2008) 29(11):1690–701. doi: 10.1016/j.neurobiolaging.2007.04.006
50. Prinz M, Jung S, Priller J. Microglia Biology: One Century of Evolving Concepts. *Cell* (2019) 3179(2):292–311. doi: 10.1016/j.cell.2019.08.053
51. de Haas AH, Boddeke HWGM, Biber K. Region-specific expression of immunoregulatory proteins on microglia in the healthy CNS. *Glia* (2008) 56(8):888–94. doi: 10.1002/glia.20663
52. Li Q, Cheng Z, Zhou L, Darmanis S, Neff NF, Okamoto J, et al. Developmental Heterogeneity of Microglia and Brain Myeloid Cells Revealed by Deep Single-Cell RNA Sequencing. *Neuron* (2019) 101(2):207–23.e10. doi: 10.1016/j.neuron.2018.12.006
53. Hammond TR, Dufort C, Dissing-Olesen L, Giera S, Young A, Wysoker A, et al. Single-Cell RNA Sequencing of Microglia throughout the Mouse Lifespan and in the Injured Brain Reveals Complex Cell-State Changes. *Immunity* (2019) 50(1):253–271.e6. doi: 10.1016/j.immuni.2018.11.004
54. Geirsdottir L, David E, Keren-Shaul H, Weiner A, Bohlen SC, Neuber J, et al. Cross-Species Single-Cell Analysis Reveals Divergence of the Primate Microglia Program. *Cell* (2019) 179(7):1609–22. doi: 10.1016/j.cell.2019.11.010
55. Masuda T, Sankowski R, Staszewski O, Prinz M. Microglia Heterogeneity in the Single-Cell Era. *Cell Rep* (2020) 30(5):1271–81. doi: 10.1016/j.celrep.2020.01.010
56. Zeisel A, Muñoz-Manchado AB, Codeluppi S, Lönnerberg P, Manno GL, Juréus A, et al. Cell types in the mouse cortex and hippocampus revealed by single-cell RNA-seq. *Science* (2015) 347(6226):1138–42. doi: 10.1126/science.aaa1934
57. Gokce O, Stanley GM, Treutlein B, Neff NF, Camp JG, Malenka RC, et al. Cellular Taxonomy of the Mouse Striatum as Revealed by Single-Cell RNA-Seq. *Cell Rep* (2016) 16(4):1126–37. doi: 10.1016/j.celrep.2016.06.059
58. Hirsch EC, Hunot S. Neuroinflammation in Parkinson's disease: a target for neuroprotection? *Lancet Neurol* (2009) 8(4):382–97. doi: 10.1016/S1474-4422(09)70062-6
59. Fiebich BL, Batista CRA, Saliba SW, Yousif NM, de Oliveira ACP. Role of Microglia TLRs in Neurodegeneration. *Front Cell Neurosci* (2018) 12:329. doi: 10.3389/fncel.2018.00329
60. Noelker C, Morel L, Lescot T, Osterloh A, Alvarez-Fischer D, Breloer M, et al. Toll like receptor 4 mediates cell death in a mouse MPTP model of Parkinson disease. *Sci Rep* (2013) 3:1393. doi: 10.1038/srep01393
61. Fellner L, Irschick R, Schanda K, Reindl M, Klimaschewski L, Poewe W, et al. Toll-like receptor 4 is required for alpha-synuclein dependent activation of microglia and astroglia. *Glia* (2013) 61(3):349–60. doi: 10.1002/glia.22437
62. Imamura K, Hishikawa N, Sawada M, Nagatsu T, Yoshida M, Hashizume Y. Distribution of major histocompatibility complex class II-positive microglia and cytokine profile of Parkinson's disease brains. *Acta Neuropathol* (2003) 106(6):518–26. doi: 10.1007/s00401-003-0766-2
63. Martin HL, Santoro M, Mustafa S, Riedel G, Forrester JV, Teismann P. Evidence for a role of adaptive immune response in the disease pathogenesis of the MPTP mouse model of Parkinson's disease. *Glia* (2016) 64(3):386–95. doi: 10.1002/glia.22935
64. Brown GC. The endotoxin hypothesis of neurodegeneration. *J Neuroinflammation* (2019) 16(1):180. doi: 10.1186/s12974-019-1564-7
65. Kim C, Lv G, Lee JS, Jung BC, Masuda-Suzukake M, Hong C-S, et al. Exposure to bacterial endotoxin generates a distinct strain of α-synuclein fibril. *Sci Rep* (2016) 046:30891. doi: 10.1038/srep30891

66. Holtman IR, Raj DD, Miller JA, Schaafsma W, Yin Z, Brouwer N, et al. Induction of a common microglia gene expression signature by aging and neurodegenerative conditions: a co-expression meta-analysis. *Acta Neuropathologica Commun* (2015) 3(1):31. doi: 10.1186/s40478-015-0203-5
67. Abellanas MA, Zamarbide M, Basurco L, Luquin E, Garcia-Granero M, Clavero P, et al. Midbrain microglia mediate a specific immunosuppressive response under inflammatory conditions. *J Neuroinflammation* (2019) 16 (1):233. doi: 10.1186/s12974-019-1628-8
68. Süß P, Hoffmann A, Rothe T, Ouyang Z, Baum W, Staszewski O, et al. Chronic Peripheral Inflammation Causes a Region-Specific Myeloid Response in the Central Nervous System. *Cell Rep* (2020) 30(12):4082–95. doi: 10.1016/j.celrep.2020.02.109
69. Kettenmann H, Hanisch U-K, Noda M, Verkhratsky A. Physiology of Microglia. *Physiol Rev* (2011) 91(2):461–553. doi: 10.1152/physrev.00011.2010
70. Graeber MB, Streit WJ. Microglia: biology and pathology. *Acta Neuropathol* (2010) 119(1):89–105. doi: 10.1007/s00401-009-0622-0
71. Sierra A, de Castro F, Del Rio-Hortega J, Rafael Iglesias-Rozas J, Garrosa M, Kettenmann H. The 'Big-Bang' for modern glial biology: Translation and comments on Pío del Río-Hortega 1919 series of papers on microglia. *Glia* (2016) 64(11):1801–40. doi: 10.1002/glia.23046
72. Lawson LJ, Perry VH, Dri P, Gordon S. Heterogeneity in the distribution and morphology of microglia in the normal adult mouse brain. *Neuroscience* (1990) 39(1):151–70. doi: 10.1016/0306-4522(90)90229-W
73. Verdonk F, Roux P, Flamant P, Fiette L, Bozza FA, Simard S, et al. Phenotypic clustering: a novel method for microglial morphology analysis. *J Neuroinflammation* (2016) 13(1):153. doi: 10.1186/s12974-016-0614-7
74. Sharaf A, Krieglstein K, Spittau B. Distribution of microglia in the postnatal murine nigrostriatal system. *Cell Tissue Res* (2013) 351(3):373–82. doi: 10.1007/s00441-012-1537-y
75. Salamanca L, Mechawar N, Murai KK, Balling R, Bouvier DS, Skupin A. MIC-MAC: An automated pipeline for high-throughput characterization and classification of three-dimensional microglia morphologies in mouse and human postmortem brain samples. *Glia* (2019) 67(8):1496–509. doi: 10.1002/glia.23623
76. Tiklová K, Björklund ÅK, Lahti L, Fiorenzano A, Nolbrant S, Gillberg L, et al. Single-cell RNA sequencing reveals midbrain dopamine neuron diversity emerging during mouse brain development. *Nat Commun* (2019) 10(1):1–12. doi: 10.1038/s41467-019-08453-1
77. La Manno G, Gyllborg D, Codeluppi S, Nishimura K, Salto C, Zeisel A, et al. Molecular Diversity of Midbrain Development in Mouse, Human, and Stem Cells. *Cell* (2016) 167(2):566–80.e19. doi: 10.1016/j.cell.2016.09.027

Conflict of Interest: The authors declare that the research was conducted in the absence of any commercial or financial relationships that could be construed as a potential conflict of interest.